Investigations into Nanostructured Materials for Water Splitting and Direct Solar Energy Harvesting

Thèse N° 9424

Filip Mateusz PODJASKI

2019

EPFL
ÉCOLE POLYTECHNIQUE
FÉDÉRALE DE LAUSANNE

Schläft ein Lied in allen Dingen,
Die da träumen fort und fort
Und die Welt hebt an zu singen,
Triffst du nur das Zauberwort.

Joseph Freiherr von Eichendorff

Acknowledgements

First of all, I would like to express my deepest gratitude to my thesis advisors Bettina Lotsch and Anna Fontcuberta i Morral for the great opportunity to do research together with you and in the framework of the Max-Planck-EPFL center. Thank you for your supervision and great support during my entire PhD. The liberty you gave me and the fruitful discussions with both of you made this time an exciting experience. Furthermore, you allowed me to broaden my horizon in a way I could not have expected. The interdisciplinary environment I could learn from and contribute to, thanks to you, was the most valuable gift a young scientist like me could receive.

Furthermore, I want to thank all other friends, collaborators and scientists that helped me during the past PhD years, providing helpful points of view and sharing their profound knowledge. Among these, Esther Alarcón-Lladó and Rotraut Merkle were particularly important – thank you for your instructions, advice and patience. Furthermore, I'd like to thank Leslie Schoop, Florian Pielnhofer and Vincent Wing-hei Lau, representing our post-docs, for additional guidance and support. Thank you Hernàn Miguez, Juan Lopez and Alberto for the enriching time with photoluminescence studies in Sevilla. I also want to thank all scientific members and employees at the MPI FKF who helped at lot at various occasions and with whom it is such a pleasure to work – making MPI FKF probably one of the best and most comfortable places to do research. Thanks to all the scientific facilities (chemical and IT service, glass blowers, electronics and mechanical workshops, nanostructuring lab and surface analysis groups) for the excellent and fast help with all

kinds of questions and issues. Besides, I want to thank Mr. Kuhnke and everyone else in the administration of MPI and the MPS-EPFL-center for making science so nice at this institute and outside of it. Viola Duppel, Roland Eger, Sigrid Fuhrmann, Willi Hölle, Claudia Kamella, Jürgen Köhler, Marie-Luise Schreiber – thank you also for making life in the Lotsch group so adorable and easy going.

Furthermore, many co-students and post-docs enriched the everyday PhD life in the Lotsch group a lot. Our post-docs Vincent, Vijay, Leslie, Tanmay, Sourav, Florian, Alberto, Rao, Bishnu, Doug, Tanja and Nella – it has always been very nice to work or to talk with you, to learn from you and to spend time outside the institute with some of you. Especialy the latter will remain unforgotten! My fellow PhD-students: Thanks Tanja and Katharina for your positive attitude and your motivation to organize events as well as for your often very amusing company at various discussions and breaks. Thanks to Pirmin, Katalin and Marie for being so kind-hearted. Thanks to our crazy-large COF-group for being so patient with me as a physicist and for insightful discussions about the boundaries between chemistry and physics (Linus, Freddi, Gök, Kerstin, Sebastian, Johannes, Alex and Lars) - with and without beer. Thanks to Dan for your enthusiasm that always motivated me and for all kinds of enriching exchange of ideas as well as your assistance with basic solid state chemistry. Thank you Anna for not leaving me alone with electrochemistry and thanks Leo and Hendrik for being such nice and easy-going photocatalysis colleagues. Thank you Sophia and Claudia for all the fun in and especially around common projects. Thank you Hugo for the Spanish lessons, fruitful discussions about photocatalysis reactors and for being a good friend. And to everyone else - thanks for adding to the nice atmosphere and high level of knowledge and research in our group. Last but not least - thank you Brian and Julia. Not only have you been amazing office mates, but you also became true friends and there are too many things to be listed here. And thanks you Julia for corrections in papers and this thesis. My interns, HiWis and master students: Thank you Marie-Claire, Philip and Andi for being so productive, helpful and for all the funny moments apart from work.

Thanks also to all the other students and scientists from other groups at the MPI and EPFL that allowed me for insights outside my comfort zone in physics and many unforgettable moments, not only related to science. This accounts especially for our PhD representatives community (Eren, Pinar, Werner, Anna and Tomasz, Pascal, Luzia, Max, Kai, Nikolai etc.) and the MPS-EPFL center people.

Apart from the institute, one of the most beautiful and lovable WGs in Stuttgart made live a true pleasure. Thanks to all my former and current flat mates for the great time making me feel at home in Stuttgart. Thanks also to Alania and especially to Marc. And thank you all my friends in- and outside Stuttgart for sharing so many beautiful and important moments with me, especially Agnès, Alyssa, Basti, Jenni, Lena, Natalia and Pia. Furthermore I'd like to thank everyone else who was and is part of my life. My friends from Göttingen, such as "the 12" and from Sugambria: life in, around and outside science and university has always been a pleasure thanks to you. I hope it will stay like this forever.

My family: Droga rodzinko, dziękuje wam wszystkim za wielkie wsparcie przez całe moje życie. Zawsze byliście i będziecie dla mnie najawaźniejsi. Z tak wspaniałą rodziną jak wy można żyć bez prawdziwych trosk i obaw. Dziękuję wam za wszystko.

Last but not least – thanks to those people who helped me to discover how interesting, enriching and beautiful life, science and research can be, bringing me here and teaching me so many things. Most importantly – how to think and how to solve problems: My parents and my brother Alan, Thomas Teich, Leo Sunderdiek, Rainer Wittenberg, Thierry Biben and Michael Seibt.

I hope that the research I could and will be able to do will one day contribute to giving something back to you, too.

Stuttgart, 30.12.2018

Filip Podjaski

Abstract

This thesis deals with different aspects of renewable energy transformation and storage concepts and connects them. Although renewable energy installations are growing worldwide, their use is limited by storage technologies. As such, water splitting for hydrogen production and battery technologies are research areas with high potential impact in the 21st century. Especially earth abundant material solutions and integrated technologies that combine solar energy absorption and transformation *operando* such as photoelectrochemical cells or solar batteries are highly promising concepts.

The technical feasibility of large scale electrochemical renewable fuel generation is most limited by overpotential losses at catalysts, their often low abundance, and limited stability. The most active and most widely used materials for the hydrogen and oxygen evolution reaction (HER and OER) are still Pt and Ru, which are very expensive and scarce. For this purpose, we studied delafossite oxides, making use of an intrinsically expanded noble metal sublattice. We observed an *operando* increasing activity for the materials with the lowest stability in acidic media, outperforming even bulk Pt in the interesting low overpotential region. Detailed investigations into the growth of the corrosion induced cap layers revealed substrate induced strain effects, modifying the ability of Pd to catalyze the hydrogen evolution reaction efficiently. The kinetically facilitated and stabilized phase transition to β-PdH$_x$ appears to be induced by these strain effects, opening up an alternative materials perspective for HER and an interesting pathway to modify material properties and phase transition barriers.

Second, we studied the photocatalytic activity origins of covalent organic frameworks (COFs). This fairly new family of crystalline porous polymers enables a bottom-up design of periodic organic structures. As such, they are a promising material class for engineering opto-electronic properties on the molecular level. One possible application is the direct photocatalytic production of solar fuels. Besides the need of co-catalysts deposited on the surface to drive the respective reactions, their description often lacks knowledge about intrinsic optoelectronic properties, which consequently rely on calculations. This work is one of the first in the field addressing these issues and actually measuring photocurrents, which are related to photocatalytic activities. Besides, these currents were used to adapt band position determination theories, which were used for classical semiconductors, to COFs for the first time. Besides, a Nernstian pH dependence of band positions could be proven, which was questioned for these materials.

Third, we investigated and explained the direct solar energy storage properties of new, 2D carbon nitrides (CN_x), namely cyanamide (NCN^-)-functionalized poly(heptazine imide) polymers (NCN-PHI). CN_x are organic based semiconductors showing promise in photocatalytic applications. After having shown that photocatalytic hydrogen evolution could be triggered with significant time delays, we revealed the storage process of this material and have shown that it is suitable for new types of direct solar batteries, where the absorber and the storage medium are combined in the very same material. Besides this conceptual novelty, which has never been shown on organic based materials, we reveal many interesting material features, such as light induced conductivity increase, the compatibility with different earth abundant ions and the interesting use as a (solar) battery electrode in aqueous media, where the material allows for larger potential windows of water based batteries, affecting energy densities positively. Most of these effects are attributed to increasing densities of states above RHE, which are intrinsically stable against decay by HER when no co-catalyst is present.

Keywords: Catalysis, water splitting, hydrogen evolution, delafossites, dealloying, strain, phase transition, β-Palladium, covalent organic framework, DFT calculations, photocatalysis, photo-current, π-stacking, carbon nitrides, pseudocapacitance, solar batteries, solar energy conversion

Zusammenfassung

Diese Doktorarbeit behandelt und verbindet verschiedene Aspekte zur Umwandlung und Speicherung erneuerbarer Energien. Obwohl weltweit immer mehr Infrastruktur zu Nutzung erneuerbare Energiequellen geschaffen wird, ist ihre Verwendung vor allem durch fehlende Speichermöglichkeiten limitiert. Die Forschung an neuen Batterietechnologien und an der Wasserspaltung zur Produktion von Wasserstoff als chemischen Energieträger bekommt daher im 21. Jahrhundert eine immer größer werdende Bedeutung. Besonders erfolgversprechende Konzepte basieren dabei auf der Verwendung von reichhaltig verfügbaren Ressourcen und integrierten Technologien, bei denen die Absorption von Licht direkt zur Transformation der Energie in eine speicherbare Form führt. Beispiele hierfür sind fotoelektrochemische Zellen oder Sonnenbatterien.

Technisch ist die großskalige Umsetzbarkeit einer Produktion von sog. solaren Brennstoffen vor allem durch die Katalysatormaterialien selbst limitiert – etwa durch energetische Verluste (Überspannungen) bei der Reaktion, eine mangelnde Stabilität oder ihr seltenes Vorkommen in der Erdkruste. Die aktivsten und weitverbreitetsten Katalysatoren für die elektrochemische Wasserstoff- und Sauerstoffentwicklung sind nach wie vor Pt und Ru, die beide sehr teuer und selten sind. Aus diesem Grund haben wir Delafossit-Oxide genauer studiert, die aufgeweitete Atomabstände in dem 2D Untergitter der Edelmetalle aufweisen. Bei den Materialien, die die geringste Stabilität in sauren Elektrolyten aufweisen, haben wir eine *operando* ansteigende Aktivität beobachtet, die so weit reicht, dass selbst Pt in der für Anwendungen interessanten Region niedriger Überspannungen übertroffen wird. De-

taillierte Untersuchungen des Wachstums einer korrosionsinduzierten Oberflächenschicht haben substrat-induzierte Spannungseffekte nachgewiesen, die die Fähigkeit von Pd, die Wasserstoff-Reaktion zu katalysieren, effizient beeinflussen. Durch die Spannungseffekte in den Oberflächenlagen wird der Übergang zu einer katalytisch höchst aktiven β-PdH$_x$-Phase stabilisiert und kinetisch begünstigt. Dieser Ansatz eröffnet neue Materialperspektiven für die Wasserstoffentwicklung und weist zugleich einen interessanten Weg auf, Materialeigenschaften und Energiebarrieren an Phasenübergängen zu beeinflussen.

Im zweiten Teil der Arbeit stellen wir eine Studie vor, die die Ursachen der fotokatalytischen Aktivität von kovalenten organischen Netzwerken (engl. covalent organic framework, COF) näher beleuchtet. Diese neuere Familie kristalliner und poröser Polymere erlaubt es, periodische organische Strukturen von Grund auf zu designen. Daher stellen sie eine interessante Materialklasse dar, bei der optoelektronische Eigenschaften auf molekularer Ebene gezielt beeinflusst und angepasst werden können. Ein Anwendungsbeispiel ist hierbei die direkte fotokatalytische Herstellung solarer Brennstoffe. Abgesehen davon, dass diese Materialien zusätzlich Co-Katalysatoren benötigen, die auf der Oberfläche deponiert werden, um die gewünschten Reaktionen ablaufen zu lassen, fehlen der Beschreibung und Erklärung ihrer Aktivität oft Kenntnisse über intrinsische, optoelektronische Eigenschaften, für die daher oft nur theoretische Berechnungen herangezogen werden. Diese Arbeit ist eine der ersten in diesem Feld, die diese Problematik angeht und Fotoströme untersucht, die mit der katalytischen Aktivität eng verwandt sind. Diese Fotoströme wurden zudem dazu herangezogen, um Techniken, die bei klassischen Halbleitern zur Bandlagenbestimmung verwendet werden, zu erweitern und anzupassen, um somit zum ersten Mal auch auf COFs angewandt werden zu können. Zudem konnte hiermit eine nernstsche pH-Abhängigkeit der Bandlagen nachgewiesen werden, die für solche Materialien fragwürdig erschien.

Im dritten Teil haben wir die besondere Eigenschaft der direkten Sonnenenergiespeicherung innerhalb von neuartigen Kohlenstoffnitriden (CN$_x$), nämlich zwei-dimensionalen, mit Cyanamid-Gruppen funktionalisierten Poly(heptazinimid) (NCN-PHI), untersucht und erklärt. CN$_x$ sind Halbleiter, die auf organischen Bausteinen beruhen und sehr vielversprechend für fotokatalytische Anwendungen sind. Nachdem wir gezeigt hatten, dass die fotokatalytische Wasserstoffentwicklung mit signifikanter zeitlicher Verzögerung gezielt getriggert werden kann, haben wir nun den Speicherprozess aufgeklärt und dargelegt, dass dieses Material auch für neuartige Typen von direkten Sonnenbatterien genutzt wer-

den kann. Hierbei werden die beiden notwendigen Teilschritte der Lichtabsorption und der Energiespeicherung in ein und demselben Material vereinigt. Neben der konzeptionellen Neuheit dieses Ansatzes, der noch nie mit organisch basierten Materialien verfolgt wurde, decken wir dabei viele interessante Eigenschaften auf. Darunter fallen die lichtinduzierte Verbesserung der Leitfähigkeit, die Kompatibilität mit verschiedenen, reichhaltig verfügbaren Ionen und die spannende Verwendungsmöglichkeit als (Solar-)Batterieelektrode in wässrigen Elektrolyten, bei denen dieses Material es erlaubt, das Spannungsfenster in wasserbasierten Batterien zu erhöhen, was sich positiv auf ihre Energiedichte auswirkt. Die meisten dieser Effekte werden einer ansteigenden Zustandsdichte im Leitungsband des Materials, oberhalb des reversiblen Wasserstoffelektrodenpotenzials, zugeschrieben. Diese Zustände sind intrinsisch stabil gegenüber der Wasserstoffentwicklungsreaktion, sofern kein Co-Katalysator vorhanden ist.

Stichworte: Katalyse, Wasserspaltung, Wasserstoffentwicklung, Delafossite, dealloying, Verdehnung, Phasenübergänge, β-Palladium, kovalante organische Netzwerke, DFT Berechnungen, Fotokatalyse, Fotoströme, π-Stapelung, Kohlenstoffnitride, Pseudokapazität, Sonnenbatterien, Sonnenenergiekonversion

Contents

List of Publications

The majority of the work presented herein has been published in peer reviewed journals. The publication data is reproduced in Chapter 4 and the Appendix A, with the permission of the publishers. Publication **A-I** has been submitted to a peer reviewed journal. For the publications **A-I** and **A-III** presented herein, I prepared the thin film samples after bulk synthesis from collaborators. Furthermore, I have designed and assembled the experimental setup used to characterize the materials (photo)electrochemically, designed, planned and performed most of the measurements, evaluated the results and have written the manuscripts. For publication **A-II**, I developed sample criteria for suitable and reproducible photoelectrochemical measurements. After thin film growth on suitable substrates by collaborators, I measured and analyzed all photoelectrochemical properties and contributed to the manuscript in all parts being affected by my results with discussions, Figures and text passages.

A-I **F. Podjaski**, D. Weber, S. Zhang, L. Diehl, R. Eger, V. Duppel, E. Alarcon-Llado, G. Richter, F. Haase, A. Fontcuberta i Morral, C. Scheu, B. V. Lotsch (*submitted*). Title: "Rational Strain Engineering in Delafossite Oxides for Highly Efficient Hydrogen Evolution Catalysis in Acidic Media"

A-II L. Stegbauer, S. Zech, G. Savasci, T. Banerjee, **F. Podjaski**, K. Schwingham-mer, C. Ochsenfeld, B.V. Lotsch. *Adv. Energy Mater.* **2018**, *8*, 1703278. Title: "Tailor-made Photoconductive Pyrene-based Covalent Organic Frameworks for Visible-Light Driven Hydrogen Generation"

A-III **F. Podjaski**, J. Kröger, B.V. Lotsch. *Adv. Mater.* **2018**, *30*, 1705477. Title: "Toward an Aqueous Solar Battery: Direct Electrochemical Storage of Solar Energy in Carbon Nitrides"

In the course of my thesis, I also contributed to a variety of projects related to the study of materials for photo- and electro-catalysis. This work included the sample prepara-tion, measurement of photocatalytic hydrogen and oxygen evolution, optical and SEM characterization, photoluminescence studies and various (photo)electrochemical measure-ments, which partially also required the development of stable and suitable measurement conditions. As a result, I am co-author of the following publications:

B-I S. Laha, Y. Lee, **F. Podjaski**, D. Weber, V. Duppel, L. M. Schoop, F. Pielnhofer, C. Scheurer, K. Müller, U. Starke, K. Reuter, B. V. Lotsch. *Adv. Energy Mater.* **2019**, 1803795. Title: "Ruthenium Oxide Nanosheets for Enhanced Oxygen Evolution Catalysis in Acidic Medium"

B-II D. Weber, L. M. Schoop, D. Wurmbrand, S. Laha, **F. Podjaski**, V. Duppel, K. Müller, U. Starke, B. V. Lotsch. *J. Mater. Chem. A* **2018**, *6*, 21558–21566. Title: "IrOOH nanosheets as acid stable electrocatalysts for the oxygen evolution reaction"

B-III T. Wang, H.-K. Kim, Y. Liu, W. Li, J. Griffiths, Y. Wu, S. Laha, K. Fong, **F. Podjaski**, C. Yun, R. Kumar, B.V. Lotsch, A. Cheetham, S. Smoukov. *J. Am. Chem. Soc.* **2018**, *140*, 6130–6136. Title: "Bottom-up Formation of Carbon-based Structures with Multilevel Hierarchy from MOF-guest Polyhedra"

B-IV C. Ziegler, T. K. Dennenwaldt, D. Weber, V. Duppel, C. Kamella, **F. Podjaski**, B. Tuffy, I. Moudrakovski, C. Scheu, B.V. Lotsch. *Z. Anorg. Allg. Chem.* **2017**, *643*, 1668–1680. Title: "Functional engineering of perovskite nanosheets: Impact of lead substitution on exfoliation in the solid solution $RbCa_{2-x}Pb_xNb_3O_{10}$"

B-V V. W.-h. Lau, D. Klose, H. Kasap, **F. Podjaski**, M.-C. Pignié, E. Reisner, G. Jeschke, B.V. Lotsch. *Angew. Chem. Int. Ed.* **2017**, *56*, 510–514. Title: "Dark photocatalysis: Storage of solar energy in carbon nitride for time-delayed hydrogen generation"

B-VI S. Betzler, **F. Podjaski**, M. Beetz, K. Handloser, A. Wisnet, M. Handloser, A. Hartschuh, B.V. Lotsch, C. Scheu. *Chem. Mater.* **2016**, *28*, 7666-7672. Title: "Titanium doping and its effect on the morphology of three-dimensional hierarchical $Nb_3O_7(OH)$ nanostructures for enhanced light-induced water splitting"

B-VII V.S. Vyas, F. Haase, L. Stegbauer, G. Savasci, **F. Podjaski**, C. Ochsenfeld, B.V. Lotsch *Nat. Commun.* **2015**, *6*, 8508. Title: "A tunable azine covalent organic framework platform for visible light-induced hydrogen generation"

List of Figures

List of Acronyms

A-TEBPY   azine-1,3,6,8-tetrakis(4-ethynylbenzaldehyde)-pyrene

A-TENPY   azine-1,3,6,8-tetrakis(6-ethynylnicotinaldehyde)-pyrene

A-TEPPY   azine-1,3,6,8-tetrakis(2-ethynylpyrimidin-5-carbaldehyde)pyrene

BSE   back scattered electron

CA   chronoamperometric measurement

CB   conduction band

CN$_x$ carbon nitride

COF   covalent organic framework

CP   chronopotentiometric measurement

CV   current-voltage measurement

DC   direct current

DOS   density of states

DP   diffraction pattern

ECSA   electrochemical surface area

EDS, EDX energy dispersive X-ray spectroscopy

EELS electron energy loss spectroscopy

EIS electrochemical impedance spectroscopy

FIB focussed ion beam

FFT fast Fourier transform

FTO fluorine doped tin oxide

HER hydrogen evolution reaction

HOMO highest occupied molecular orbita

HOR hydrogen oxidation reaction

ITO indium doped tin oxide

KSCN potassium thiocyanate

LUMO lowest unoccupied molecular orbital

NCN cyanamide

NHE normal hydrogen electrode

OCP open circuit potential

OER oxygen evolution reaction

ORR oxygen reduction reaction

PEC photoelectrochemical

PHI poly(heptazine imide)

PTI poly(triazine imide)

RHE reversible hydrogen electrode

SE secondary electron

SECM scanning electrochemical microscope

SEM   scanning electron microscope

SIMS   secondary ion mass spectroscopy

STH   solar to hydrogen conversion efficiency

TEM   transmission electron microscope

TON   turnover number

VB   valence band

XPS   X-ray photoemission spectroscopy

XRD   X-ray diffraction

1

Introduction & Motivation

Nowadays, in 2019, we approach a world where almost all kinds of labor can be taken over or are severely facilitated by machines or electronics, which, once constructed, require basically only energy and maintenance to operate. This applies to all three economic sectors. Agriculture, mining, industrial production (especially the chemical industry) as well as transportation and all kinds of IT based work – their operation relies largely on only few raw materials, such as fertilizers, platform chemicals, metals and semiconductors. They are being continuously modified and thus are in principle recyclable in large parts. Besides these raw materials and know-how, the main production and operation requirement is energy. In most cases, this energy stems from fossil fuels, which are limited and being burned, and electricity. Besides a small contribution of renewable electricity sources and nuclear energy, electricity and heat production as well as transportation rely in large parts on fossil fuels and thus have the strongest impact on the global production of greenhouse gases, as shown in Fig. 1.1.

Our economy and society are thus very dependent on these fuels and the continuous economic growth, but on a finite world like our earth, an unlimited exploitation of resources has no future. [2–4] For this purpose, and for more and more strongly visible effects due to pollution and climate change, a transition towards more sustainable energy solutions is required, better sooner than later. The only two renewable energy sources being exploitable on a large scale are wind and sunlight. [5–9] While wind provides fluctuating electricity, such as sunlight in traditional photovoltaics, we still require chemical
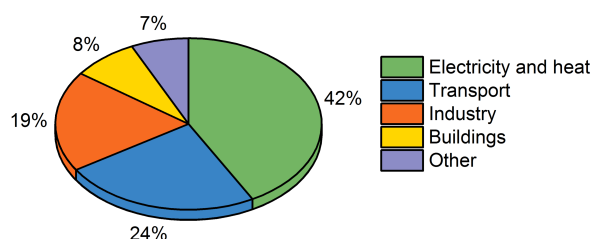
Figure 1.1: Global emission of CO_2 in 2016 by sector. Adapted from [1].

fuels that enable both, the storage of energy and energy intensive applications, such as heavy transportation or industrial manufacturing. For this purpose, photocatalytic fuel production is probably the most promising solution to our upcoming energy problems. (Photo)electrochemical processes enable the transformation of solar or electrical energy into chemical bonds, enabled by the reduction of N_2, CO_2 or by the splitting of water e.g. [10–12] The resulting products - ammonia, alcohols and other carbon based platform chemicals as well as hydrogen - are very energy rich, versatile and thus useful chemicals. Furthermore, their gravimetric energy density can outperform solid state energy storage devices and is close to that of traditional fossil fuels. [12] Since the storage of renewable electrical energy is actually what is limiting its implementation, investments into this research related to energy conversion and storage become more and more important.

Within this field, photocatalytic water splitting appears to become the most important factor. While water is very earth abundant, it is not even consumed by the conversion process into hydrogen and oxygen, since salt-free water is again the product of the highly efficient recombination-process in a fuel cell. Furthermore, hydrogen can blended from 5 to 15% into our existing gas infrastructure without significantly affecting the lifetime of the network and the safety of utilization. For a transition to a hydrogen economy this is very beneficial since production can be made rentable without the need to change the whole energy supply system in developed countries. [13] In countries of the Third World for example, sunlight is usually even more abundant than in our northern hemisphere, making the creation of an energy infrastructure based on photoelectrochemical reactions even more efficient and appealing. Another benefit of such a truly renewable technology is that many approaches, such as the herein presented use of suspended nanoparticles, for instance, require relatively little know-how and cost for maintenance and operation. [14] Such a relatively local production of fuels and energy would, besides all positive environ-

mental factors, further reduces its cost and decreases economic and political supra-regional dependences and conflicts. [2, 3, 15, 16] In addition to that, the implementation of such an infrastructure, often labeled "Hydrogen Economy" if based on hydrogen, is even more applicable in the growing Third World and in still developing countries, which otherwise have to rely on more and more expensive fossil fuels. Furthermore, all solutions for local fuel production and energy storage, which can also be operated easily, are beneficial for the economic, social and personal benefit of the majority of individuals of a society, as stated very clearly already in the 70's by Ernst Friedrich Schumacher in his forward-looking and still relevant book "Small is Beautiful: A Study of Economics as if People Mattered". [3] What hinders us so far from accepting the transition to a more sustainable infrastructure? The main factors are costs, confirmed habits and the fear of unestablished technologies, the requirement of possibly limited resources (e.g. Li and Co for batteries, rare earth elements for turbines, rare elements for catalysts, such as Pt) and pure convenience. For these purposes, research activities in the field of photocatalysis and energy storage are extremely important. They allow rendering these fairly new technologies cheaper, more efficient and stable, thus socially more accepted, and, if new material solutions are found, less based on limited raw materials.

This thesis approaches many of the before mentioned aspects with three publications trying to connect distinct, but related fields. As outlined above, photoelectrochemical energy conversion relies on electrochemical energy conversion as the last reaction step, which most often occurs on the surface of photocatalysts of photoelectrochemical devices. The first publication deals with such electrocatalysts for the hydrogen evolution reaction (HER). Electrocatalysts are used to drive the respective redox-reactions with low overpotentials, which is important to minimize losses not only in electrolyzers or fuel cells, but also by deposition of the electrocatalyst directly on photoabsorbers. In this case, they are called "co-catalysts", since they make the photoreaction, enabled by the photoabsorber, possible or more efficient, if the intrinsic overpotentials are too high, which is the case for most organic based and inorganic photocatalysts alone. At the moment, Pt is the most widely used electrocatalyst. Due to its low abundance, nanostructuring techniques to reduce the catalyst load or alternative materials are being looked for. [17–19] For this purpose, a new approach enhancing the activity of catalyst surface by *operando* induced strain is presented. This approach enables severe material savings on precious metals, since only a tiny fraction on the catalyst's surface is used, and allows for using other ele-

ments like Pd based catalysts, which so far seemed unsuitable for the HER. Furthermore, and most importantly, it opens a new pathway to catalyst fabrication and *operando* enhancement versus the traditionally observed decline or poisoning, using corrosion induced strain, which was shown to alter catalytic properties severely and thus is an important topic in today's catalyst research. [20]
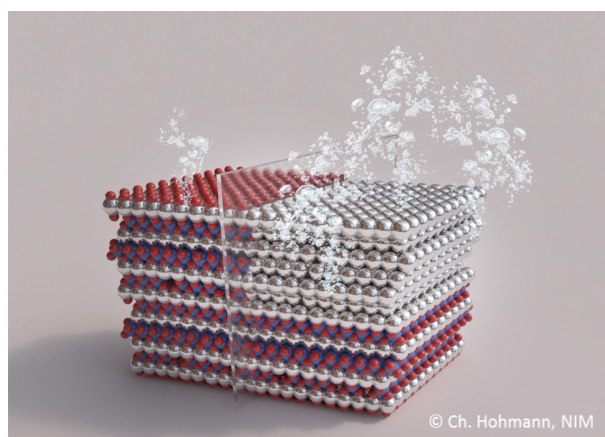

Figure 1.2: Illustration of the increased HER activity on Pd overlayers growing on $PdCoO_2$.

The second publication deals with carbon-based, photocatalytically active semiconductors that enable water splitting reactions. The most prominent material classes in this field, which can be tailored, are carbon nitrides (CN_x) and covalent organic frameworks (COFs), which are on the way to enable more stable and efficient, purely earth abundant solar water splitting. [21, 22] Since the discovery of the solar driven water splitting process on TiO_2 by Fujishima and Honda in 1972, [23] more and more efforts have been put into using inorganic semiconductors as light absorbers, decorated with efficient but expensive electrocatalysts, to drive the hydrogen evolution reaction (HER) and the oxygen evolution reaction (OER). [24–27] For a long time, these seemed to be the best and only solution in order to drive the respective water splitting reactions. The field drastically changed when Domen and Antonietti found out that graphitic carbon nitrides, which are organic based semiconductors compromising essentially C, N and H only, are also able to drive the respective half-reactions. [28] Since this discovery, many groups invested into other forms of organic based and biomimetic materials to do the job more efficiently. While

biomimetic systems tend to have a limited lifetime (and the catalysts a limited turnover number, TON), the more robust CN_x, and since recently, COFs keep showing promise, reaching high external quantum yields above 10%. [29,30] Although most of these materials have a large enough optical band gap ($> 2\,eV$) to achieve full water splitting ($1.23\,eV$ + overpotential losses), the large gap currently limits the efficient use of solar irradiation. But also this problem is being addressed by different synthesis techniques and the introduction of molecular building blocks or elemental dopants, as well as heterojunctions with other materials that enhance or share the light absorption and improve charge separation. [31,32]

The main problem of these organic materials is their rather low intrinsic conductivity, their need for cocatalysts deposited on the surface and their mostly unknown photophysical properties, which are hard to extract and thus difficult to optimize. For that reason, their photoelectrochemical properties need to be studied in more depth, understood and possibly tuned or enhanced by rational design. These optoelectronic properties are partially measured and addressed by the second publication in Chapter 4, which studies new types of covalent organic frameworks that enable sacrificial water reduction.

Last but not least, an unprecedented material solution for the direct storage of solar (and external electrical) energy within an organic based, photoabsorbing material is presented and explained. A direct storage of solar electricity is presented in the third publication. This concept not only bypasses the need for solar energy storage in chemical bonds, but also enables new generations of direct "solar batteries". Opposite to traditional nanodevices, where a photoabsorber charges a battery or a supercapacitor, the direct solar battery concept enables the storage of solar energy directly within the photoabsorber material. [33–36] The reported cyanamide-functionalized poly(heptazine-imide) (NCN-PHI) is a new, truly 2D and porous type of CN_x, opposite to the widely used 1D polymer melon. [37–39] The proposed solar battery solution based on the dual absorption and storage functionality offers a lot of advantages, such as reduced complexity and thus system costs, the operation in non-toxic, aqueous media, and the use of all earth abundant alkali metal ions, not only lithium. Since this carbon nitride is further a purely organic based material containing some salt, it points towards a possible transition to a fully earth abundant energy infrastructure.

© Ch. Hohmann, NIM

Figure 1.3: Illustration of the solar battery dual functionality of NCN-PHI.

The points addressed by these different publications highlight important and interesting developments in the area of (photo)catalytic energy conversion based on more abundant materials. Thus, they adumbrate new horizons, aiming for a fully sustainable world, which is also locally more self-sufficient.

This doctoral thesis is composed of five Chapters:

Chapter 1: Introduction & Motivation

In the first Chapter, the motivation for this field of research on nanostructured materials for renewable energy applications is presented. The different topics of this thesis are introduced and placed in a wider scientific and socio-economical context.

Chapter 2: Theory on Photoelectrochemical Energy Conversion and the Materials

In this Chapter, the optoelectronic properties of metallic and organic semiconductor nanostructures are reviewed and related to their applications for (solar) energy conversion and storage. We start with a brief overview of existing technologies for photoelectrochemical water splitting and then explain the properties of photocatalysts and co-catalysts or electrocatalysts, which enable the desired solar driven redox-reactions. In particular, we discuss factors that can be accessed by photoelectrochemical measurements. In the last part, we present the desired properties that enable charge storage in solar batteries and relate them to existing technologies. We also discuss several techniques to investigate the electrochemical properties of the organic semiconductors and electrocatalysts presented. The rest of the Chapter reviews the material classes employed.

Chapter 3: Experimental Methods

In the third Chapter, the experimental methods that are relevant for this thesis are presented. We start by explaining the material synthesis and preparation with different substrates and conditions. Then, we describe optical and electron microscopy based characterization techniques. In the last part, we describe the sample analysis using (photo)electrochemical techniques in aqueous media.

Chapter 4: Results & Discussion

This Chapter presents the main results of this thesis. These include *operando* modifications of delafossite oxide based electrocatalysts and the understanding of how their properties evolve, COF characterization as organic semiconductor for photocatalytic water reduction and finally, the use of 2D-CN_x for energy storage applications and fundamentally new solar battery concepts, which are enabled by the material's dual functionality. For every topic, we first discuss its motivation and relevance to the respective field before presenting the articles, which have been published in or are submitted to peer-reviewed scientific journals.

Chapter 5: Conclusion & Outlook

In this last Chapter, the topics are concluded and an outlook for further research is given.

2

Theory on Photoelectrochemical Energy Conversion and the Materials

In this Chapter, a general introduction into different processes and material properties enabling photoelectrochemical (PEC) energy conversion is presented. First, the factors enabling and contributing to PEC water splitting are presented and explained, which include also purely electrochemical water reduction and oxidation. Analogously, the theory behind photoelectrochemical energy storage in solar batteries is explained in the second part. The third part of this Chapter introduces the material classes that were employed and studied as photo- and electrocatalysts.

2.1 Photoelectrochemcial Water Splitting

The first report of photoelectric current generation in a liquid dates back to 1839 and was given by Edmond Becquerel. [40] Nevertheless, the use of light to drive the water splitting reactions was reported only in 1921. [41] In 1972, direct water splitting on a semiconductor electrode in contact to a catalytic material driving the HER was shown for the first time. [23] Since then, the field has been developing continuously and quickly. Probably the first comprehensive overview of materials and mechanisms enabling this process was given by A. Nozik six years later. [42]

In order to achieve a photoelectrochemical water splitting reaction, first, the thermo-
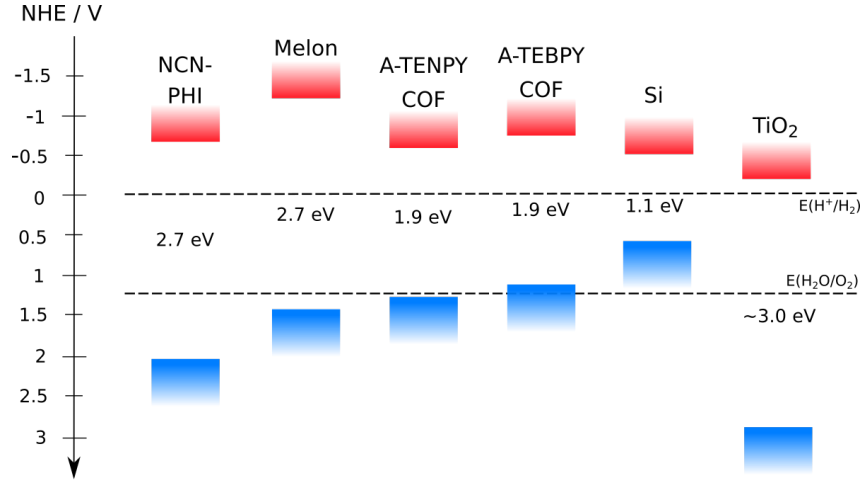
Figure 2.1: Band positions of CN$_x$ and COFs discussed in this thesis as well as two common semiconductors. [43]

dynamics have to be considered. Splitting a water molecule requires an energy input of 237 kJ/mol for the endothermic dissolution reaction. Since this process requires 2.46 eV in total and a transfer of two electrons, 1.23 eV have to be expended per charge carrier. The photoabsorber thus needs to have a band gap larger than 1.23 eV. Not only the gap itself, but also the energetic alignment of the conduction band (CB) and valence band (VB), or the respective molecular orbital energies (highest occupied molecular orbital (HOMO) and lowest unoccupied molecular orbital (LUMO)) energies, need to straddle the water reduction and oxidation potentials, as shown in Fig. 2.1.

Since the thermodynamic potential E for this reaction is pH-dependent, it follows a Nernstian relationship:

$$\begin{aligned} E &= E^0 + \frac{RT}{nF} log \frac{(c_{ox})^a}{(c_{red})^b} \\ E &= E^0 - 0.0592V \cdot pH \\ E_{RHE} &= E_{NHE} - 0.0592V \cdot pH \end{aligned} \qquad (2.1)$$

with E^0 being the equilibrium potential, R the natural gas constant, T the temperature in Kelvin, F the Faraday constant, n the number of electrons transferred, c_x the concentrations of the reduced and oxidized species and a, b their reaction coefficients. [44–46] While the equilibrium value for HER is given by the normal hydrogen electrode (NHE) (-4.5 V vs. the vacuum level), the pH-corrected value is given by the reversible hydrogen electrode (RHE). This has the consequence that the respective redox-potentials can actually be tuned by varying the pH.

2.1.1   Band Gap and Absorption

While large band gaps allow for higher driving forces for at least one reaction, they limit the absorption of light to photons above their bandgap. Small gaps on the other hand decrease the driving force (overpotential) for the respective water splitting reactions, but enhance absorption. Usually, the absorption process, enabled by the gap, needs to be balanced with the spectrum of the illumination source, i.e. the sun, in order to achieve the best possible Solar to Hydrogen (STH) conversion efficiencies. For this purpose, also tandem architectures or Z-schemes using two photoabsorbers are employed. The fraction of light that is absorbed defines the charge carrier generation efficiency, η_{Abs}, and enables all further processes. It is followed by the charge carrier separation and transport to the interface efficiency, η_{Trans}, and the reaction efficiency at the interface to the liquid, i.e. on the co-catalysts surface η_{Cat}, which are explained below. [45, 47] Overall, the STH efficiency is a product of the three major processes:

$$STH = \eta_{Abs} \cdot \eta_{Trans} \cdot \eta_{Cat} \tag{2.2}$$

An overview of optimal band gaps and resulting approaches for PEC water splitting including cost analysis was published in 2013. [48]

2.1.2 Charge Carrier Transport at the Solid-Liquid-Interface

If one looks at only one half reaction after photoabsorption, HER e.g., its driving force is not determined by the gap itself, but by the alignment of the semiconductor conduction band (or LUMO) and the RHE potential (see Fig. 2.1). If and only if a semiconductor has a well-defined Fermi energy (E_F) and mobile charge carriers, the Fermi energy of the semiconductor and the electrolyte will align, similar to metal-semiconductor contacts. Since the liquid usually presents the larger energetic reservoir, one can assume that the semiconductor always tries to align with the electrolyte. This process is illustrated in Fig. 2.2 for a n-type semiconductor and an aqueous electrolyte. The flow of charges, which equilibrates the Fermi levels, leads to an excess charge on the semiconductor side of the interface, which gives rise to a potential across the depletion region and thus bends the band structure at the surface. The barrier height, V_B, and the width W of the space charge region, depend in first approximation on the initial difference between the Fermi levels, the free charge carrier density in the semiconductor, N_D, and its dielectric constant, ε_r, which describes the polarizability of the material:

$$W = \sqrt{\frac{2\varepsilon_0\varepsilon_r V_B}{eN_D}} \tag{2.3}$$

ε_0 denotes the vacuum permittivity. In a traditional image, this band bending region defines the kind of surface reaction process taking place after light absorption on the interface to the semiconductor, since only the charge carriers that reach this band bending region will be separated and directed to the interface. As a consequence, downwards bent bands, which normally result from p-type doping, will carry electrons to the surface, which drive the reduction reaction (HER), while n-type materials, which have upwards bent bands, will drive the oxidation reaction by hole transfer to the electrolyte (OER). Consequently, a single semiconductor will never drive both, the HER and OER efficiently at a time. [42, 45, 49]

In the case of nanoparticles and many organic materials, it is not clear *a priori* if a band bending is present, since an equilibration of Fermi energies would require a charge flow, and many of organic materials are rather insulating with a bulk reduction or oxidation
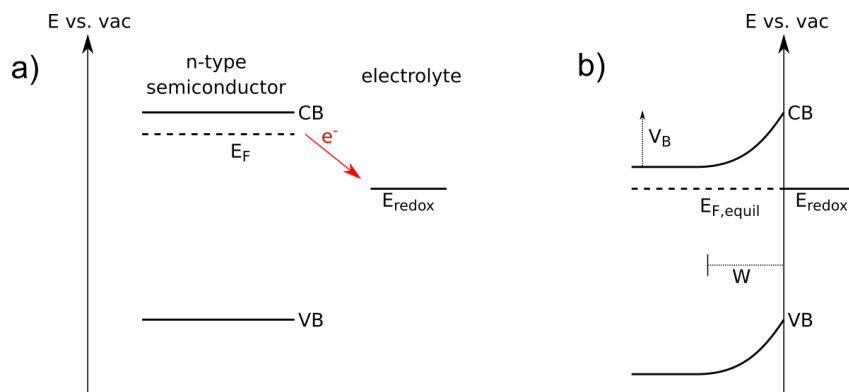
Figure 2.2: Band alignment in a semiconductor-liquid junction. a) Initial situation. b) After equilibration of the Fermi energies. Adapted from [42, 43].

being energetically unfavorable. Furthermore, if particle sizes are very small (in the nm range), no charge carrier gradient and resulting band bending is measurable and the material's energetic positions stay rather stable with respect to their vacuum levels (i.e. they do not necessarily vary with pH). In this case, it is important to have a large surface area and short distances from the region of absorption to the liquid interface. Since the light induced charge carriers have no additional driving force to reach the electrolyte, the reaction rate is governed by their intrinsic diffusion length and the tunneling probability, which depends on the energetic difference between the initial and final states, as well as the distance. Generally, 2 nm can be assumed as limit for a tunneling. For this purpose, high surface areas or porous structures in materials with limited conductivity are highly beneficial, since they shorten the pathways for the photogenerated charges to the surface or catalysts and hence reduce the rate of recombination. This especially applies to very small semiconductor nanoparticles, which do not have enough mobile charge carriers to align with the electrolyte, and to poorly conductive CN_x and COFs, which are usually suspended for photocatalytic applications. [47, 50–52]

A critical study comparing the technical feasibility of different concepts for PEC water was published in 2013. [14] It should be noted that for cost purposes, particulate systems such as CN_x or COFs are more interesting to be pursued, even if their efficiency is lower. A review of the developments in the field of particulate photocatalysts was published recently. [53]

2.1.3   Catalysis on the Surface

Once the charge carriers have reached the interface, they can drive the respective redox-reaction. Unfortunately, the kinetic barrier (overpotential) is very high for most catalyst surfaces, since reaction intermediates are not stabilized appropriately at the interface. In order to improve this, co-catalysts are usually deposited on the surface. They lower the respective overpotentials and thus enable an efficient reaction of the light induced carriers with the redox-medium.

These co-catalysts are most often metals like Pt. They have a large density of states (DOS) near the Fermi level, are very conductive and align energetically with the surrounding medium. As such, they can act as energetic sinks or short term reservoirs for light induced charge carriers generated in the photocatalyst before being consumed in redox-reactions on the co-catalysts surface. [51, 53]

Description of Reaction Rates on Catalyst Surfaces

To every reversible catalytic reaction, one can assign a respective redox potential. The redox potential of proton reduction e.g. per definition relates the redox-potentials used in electrochemistry to the absolute scale vs. vacuum used in physics (-4.5 V vs. vac = 0 V vs. NHE). The pH-dependence was described in Eq. 2.1. Every reaction has kinetic barriers that depend mostly on the energetic barriers related to the formation of intermediates and their ad- and desorption rates to the respective catalyst surface. The reaction rate or current j is related to the potential by the following Butler-Volmer equation, describing the respective potential dependent forward and backward reaction current:

$$ j \;\; = \;\; j_0 \left[exp\left(+\frac{\alpha_A nF}{RT}\eta\right) - exp\left(-\frac{\alpha_c nF}{RT}\eta\right) \right] \tag{2.4} $$

with j being the current density, j_0 the exchange current density, which relates to the intrinsic activity of a catalyst, $\alpha_{a,c}$ the anodic and cathodic charge transfer parameters, and η the overpotential applied to drive the reaction with respect to RHE. [54] At increasing overpotentials η, the back reaction in Eq. 2.4 can be neglected and it simplifies to the Tafel equation:
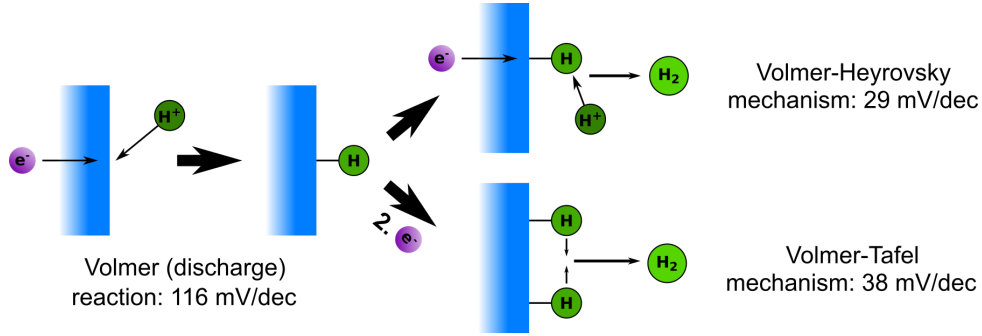
Figure 2.3: Intermediate reaction steps during HER in acidic media and the Tafel slopes for the respective rate-limiting reactions.

$$\eta \;=\; b \cdot log \; \frac{j}{j_0} \tag{2.5}$$

where b denotes the Tafel slope in mV/decade. [55] Regarding HER, different rate limiting steps can occur during the two-electron transfer in acidic and alkaline media. In this work, we focus on the processes dominating in acidic and neutral conditions. If the adsorption of protons is limiting (Volmer or discharge reaction), a Tafel slope of 116 mV/decade is obtained. Subsequently, the reaction towards hydrogen can take place via the reduction of another proton on the already adsorbed one (Volmer-Heyrovsky step, 38 mV/decade) or via the recombination of two adsorbed protons (Volmer-Tafel reaction, 29 mV/decade). [46, 54] These processes are illustrated in Fig. 2.3.

Articles reviewing state-of-the-art electrocatalysts for HER are given in [46, 56, 57]. The best alternatives to Pt are NiMo, NiMoCo, MoS_2, WS_2 and CoP. Still, their overpotentials η_{10} (required to achieve $10\,\text{mA/cm}^2$) are mostly $> 100\,\text{mV}$ and in all cases, besides NiMo, $> 50\,\text{mV}$. The exceptional activity in this material is in large parts due to its rough surface, which is increased by a factor of 1000 with respect to its geometrical surface area. Strategies to enhance the catalysts' activity usually aim at a maximized exposure of active sites, which can be the edges in the 2H phase or the planes in the 1T phase of the transition metal dichalcogenides for example. [58, 59]
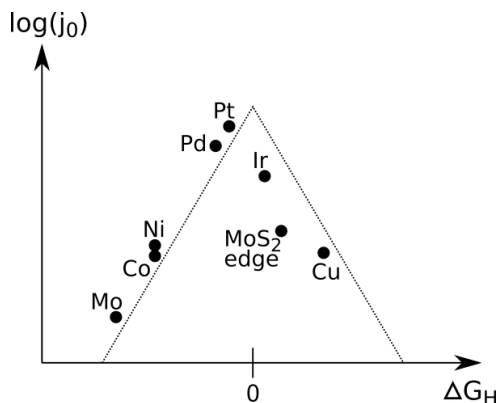
15

Figure 2.4: Volcano plot for HER catalysts relating adsorption enthalpy for hydrogen, ΔG_H to the surface activity of an electrocatalyst. Adapted from [46].

d-Band Theory

The catalytic HER often occurs by interactions with transition metal d-orbitals that enable the strongest interaction with protons or hydrogen and thus are predicted to be responsible for the reduction of protons and the adsorption of hydrogen. The intrinsic activity of a catalyst for HER, j_0, is thus directly related to the adsorption enthalpy for hydrogen, ΔG_H. Most beneficial is a slight stabilization of the intermediate hydrogen binding to the catalysts surface, whereas an energetically unfavorable or too strong binding of the intermediate limits the activity, following Sabatier's principle. This is illustrated in so called Volcano plots:

In many catalysts, the dominant interaction for HER results from the overlap of metal d-orbitals with the antibonding hydrogen σ^*-orbitals. [60] The material's density of states (DOS) at the Fermi energy E_F is thus an important factor for the HER reaction.

Strain

d-band theory further describes how strain within the catalyst particles changes the DOS in d-bands. [60–62] Kibler and Greeley predicted and measured that tensile strain on Pd overlayers increases the DOS in the d-bands. [62,63] Intrinsically, this broadening would result in a shift of the d-band center E_D, as shown in Fig. 2.5. Since the Fermi level of the metal aligns with the one of the electrolyte, the Fermi level is shifted up to the same level as without strain and an effectively increased DOS per surface area is obtained. As
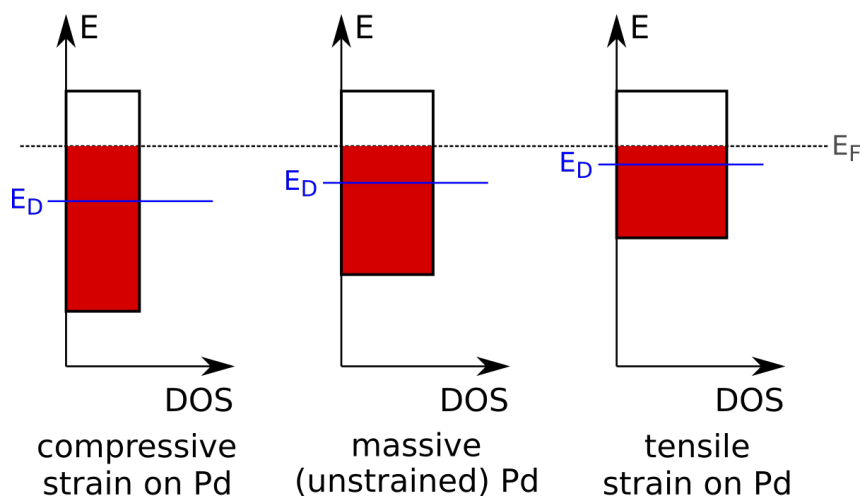
Figure 2.5: Influence of compressive and tensile strain on the DOS of Pd and its d-band center E_D. Adapted from 63.

a consequence, the interaction between the strained surface metal atoms and hydrogen strengthens. The ΔG_H is thus increased and the j_0 decreased. Compressive strain on the other hand can be beneficial for the j_0 of Pd.

Oxygen Evolution Reaction

The same principles affecting the exchange current densities and Tafel slopes can be applied to the OER and the oxygen reduction reaction (ORR). The four electron transfer reaction in this case has more intermediate steps that require a further oxidation of the surface. As such, the energetic levels of the intermediate states strongly depend on the crystal structure and its termination. For this purpose, insights into the catalytic mechanisms are more difficult to obtain and often rely on computation. Currently, the development of OER and ORR catalysts is the biggest challenge due to relatively high overpotentials for these reactions and due to only expensive Ir and Ru based catalysts being fairly stable in acidic media. [56, 57] For this purpose, water splitting reactions with high current densities were often restricted to alkaline media, while research for acid stable OER catalysts is ongoing, mostly driven by the development of proton exchange membrane (PEM) electrolyzers. [64, 65]

2.1.4 PEC out of Equilibrium: Quasi Fermi Levels under Illumination and Band Positions

In a PEC device, photoabsorbers are decorated with electrocatalysts. The photoabsorber converts solar energy into electrons and holes, which are subsequently used directly on the surface to drive the respective reactions, which is a continuous process out of equilibrium. While a semiconductor is illuminated with photon energies above its band gap, electrons and holes are generated continuously near the conduction and the valence band (or HOMO and LUMO). This process is limited and thus balanced by a continuous rate of recombination, giving rise to heat (non-radiative recombination) and photoluminescence (radiative recombination). The amount of charge carries persisting gives rise to a photovoltage, which is determined by the difference of the respective quasi Fermi Level of light induced electrons, $E_{F,n}$, and holes, $E_{F,n}$. [45, 50] The difference between both is equivalent to the photovoltage V_{Ph} (see Fig. 2.6).

Since the rate of recombination does not depend on the amount of charge carriers for most materials in first approximation, an increasing light intensity also increases the photovoltage until a maximum is reached. In this case, the bands are flattened and no current flows any more. This can be used to determine the flat band potential, which can be used to relate the band positions to a reference electrode, and the conductivity type of the material (negative shift for n-type semiconductors with upwards band bending, positive shift with p-type semiconductors). The flat band potential is then equivalent to the open circuit potential (OCP) measured. This state is illustrated in Fig. 2.6 c).

Even if no band bending is present, this technique can be used to determine the positions of the conduction or valence band with respect to an occurring photoreaction. If a bias is applied to a semiconducting material, its band positions are shifted with respect to the sign of the applied bias. If a bias decreasing the driving force of the conduction band is applied, the photocurrent (current induced by photoexcitation) ceases rapidly and stops at a point, where the charge carrier transport to the electrolyte is no longer thermodynamically favorable. [45] The CB position can then be extracted from the OCP.[1]

---

[1]The photocurrent may stop earlier and thus be offset if a high overpotential for the respective reaction is present. This effect can be reduced by suitable co-catalysts or more facile redox shuttles with lower overpotentials.
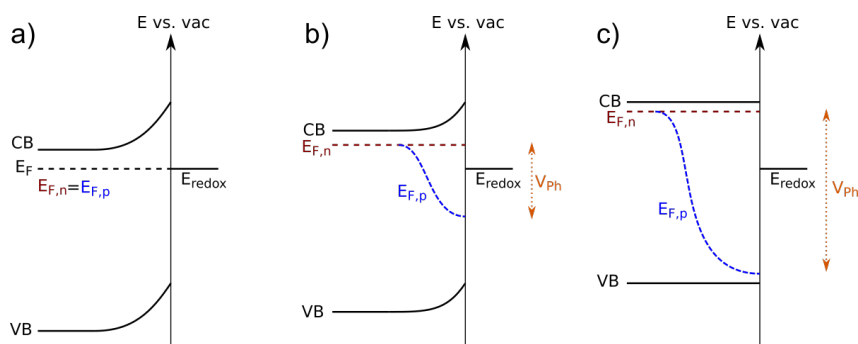
Figure 2.6: Band structure of an n-type semiconductor in contact with an electrolyte at different illumination conditions: a) In the dark. b) Under moderate illumination, creating a small V_{Ph}. c) Under intense illumination that flattens the bands. Adapted from 66 and 45.

A bias of opposite sign would increase the photocurrent up to a saturation value and lead to purely electrical current generation if η is large enough.

2.1.5 Sacrificial Hydrogen Evolution

In many cases, photocatalytically active materials are efficient at performing only one of the two redox reactions. This can be caused by unfavorable transport of either electrons or holes due to band bending, by different charge carrier mobilities and hence, diffusion lengths for electrons and holes, by different kinetic barriers for one of the two reactions or simply by inconvenient band alignment, which does not overcome the kinetic barrier or even renders the respective reaction thermodynamically impossible. To enable the study of only one (usually the desired) photoreaction on the material, sacrificial electron donors (or acceptors) can be used. They quench the photogenerated holes (or electrons) while overcoming the exciton binding energy, and simulate their extraction, which enables the study of the desired other half-reaction more efficiently. This applies mostly to suspended nanoparticles, such as CN_x or COFs, but also to more traditional materials, like TiO_2. In this case, the Fermi energy, which reflects the population of the majority carriers, can be measured directly and more efficiently by the OCP of the material. This potential, which is compared to a reference electrode while no current flows, reflects the energetic level of the conduction band (if electrons are the majority charge carriers or holes are quenched). The case of a p-type semiconductor, the valence band position is obtained (if the holes

are the majority carriers or electrons are quenched). This technique also applies to solar batteries, as explained in the following paragraph.

2.2 Photoelectrochemical Energy Storage

In order to circumvent the need for solar fuels to store energy, batteries can be used as storage medium for photovoltaics. Although the cost for photovoltaics is decreasing rapidly, the cost and convenience by using batteries is limiting this application. For this purpose, integrated devices, which enable the storage of the power provided by photoabsorbers, are developed more and more. Many examples appeared recently, which are mostly based on traditional photoabsorbers, such as TiO_2, silicon or the newly emerging hybrid perovskite solar cells, and storage devices, which are connected in parallel (see Fig. 2.7 a) and b) for separated and integrated device architectures). [33,34,67–70] Fast storage occurs by charge transfer to supercapacitors, while battery anode and cathode materials or redox flow battery electrolytes can be used for higher charge densities, on the cost of power density.

Most considerations for solar batteries are in-line with the requirements of PEC water splitting. The main difference lies in the fact that the photoabsorber potentials have to fit the storage electrodes while not allowing for reactions with the electrolyte. A common problem encountered is thus the efficient matching photovoltage and charging potentials. The same applies to photocurrents and charging currents that have to balanced, which is why supercapacitors are easier to employ than battery materials, where the charging reaction is kinetically limited. Furthermore, every conversion process is related to losses, which reduce the device efficiency. Since the energy also needs to be extracted further on, one more process is present. This back-conversion of chemical to electrical energy is achieved by external fuel cells in the case of PEC water splitting and thus not a limiting factor, while the gas storage itself may be one.

Due to possible intrinsic loss channels (self-discharge), the delay-time between photocharging and electrical discharging is also an important factor. Hence, a solar battery compromises between photovoltaics and batteries. As such, some more factors have to be adapted for the respective application of a solar battery device:

- cyclic stability

- coulombic efficiency

- capacity and charge retention time

- power and energy density for energy extraction

Akin to the above presented STH efficiency (see Eq. 2.2), the efficiency of a solar battery is determined by the absorption efficiency, the charge separation efficiency, the transport and storage efficiency, as well as the charge extraction efficiency and voltage losses occurring during the processes.

Most of these factors can be measured electrochemically. If the storage material (battery or supercapacitor) can be varied independently from the generation material (the photoabsorber) these four factors can be tuned independently and adapted for the given application. As in the case of photoelectrochemical energy conversion to solar fuels, the price and abundance of the last part in the chain, i.e. the storage material (vs. the electrocatalyst for solar fuels generation) is most often the limiting or expensive factor.

In the case of a coupled absorption and storage function, the charge transfer of at least one species is not necessary any more. This concept has been first proposed by G. Hodes in 1976 and followed by H. Tributsch in 1980 for inorganic, p-type semiconducting materials allowing for photo-intercalation. [35,71] Besides the technical advantages of reduced complexity, this has the drawback that the storage medium is intrinsically given and cannot be adapted any more. Furthermore, it may affect the semiconductor properties if the storage process modifies its structure and conductive properties, e.g. by intercalation. [72] The conceptual considerations based on such an approach including possible materials were summarized by Betz and Tributsch. [36] Only in the past years, numerous inorganic materials with a job-sharing property of light absorption and charge storage have been presented. [73–76] In all cases where Li intercalation is reported, the material acts as positive storage electrode. Upon hole storage, Li is driven out of the system, charging the electrodes positively. Unfortunately, it is often difficult to understand whether the materials show only photo-assisted charging while a bias is applied, or if they can be charged also purely radiatively. [77–79] Furthermore, it is not always made clear if the job-sharing architecture is not provided by a material composite made from an absorber
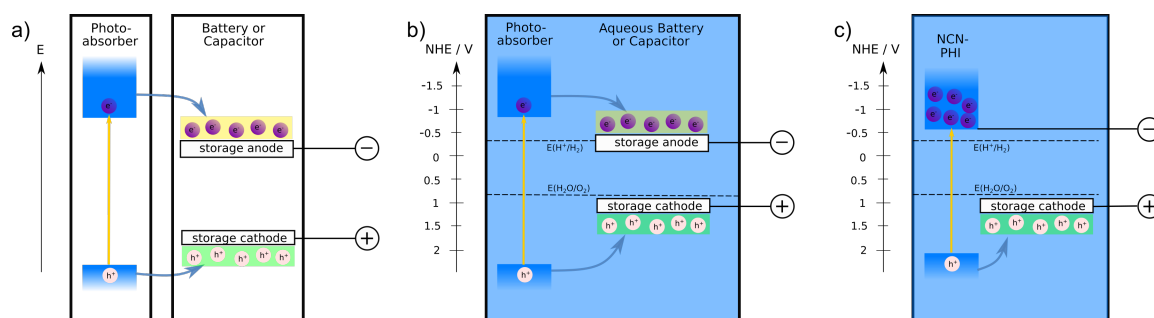
Figure 2.7: Three different approaches for solar batteries. a) A photoabsorber acts as power source for an external battery. b) An integrated device where the photoabsorber and the (possibly adjacent) storage device are in contact with an electrolyte (here: aqueous medium in neutral conditions). The storage potential is limited by the electrochemical stability window of the electrolyte. c) Direct solar battery based on the dual functionality of NCN-PHI enabling light absorption and electron storage in the very same material.

and a storage material, which corresponds to the concept of external charging.

2.2.1 Electrochemical Energy Storage

The storage of energy can be based on an induced change of potential energy (e.g. pumped hydropower), on kinetic energy (fly wheels), on heat, on mechanical deformations, phase transitions or electrochemical or electrostatic reactions. The latter three are of special interest because they are highly reversible, fairly easy to realize on all kinds of energy scales and directly accessible from electrical energy. Electrochemical storage is based on the transformation of an electrical potential that drives a chemical or surface adsorption reaction, modifying the chemical potential and thus the energetic state product, i.e. the battery or capacitor. There are three types of charge storage mechanisms being possible on the respective positive and negative storage electrodes:

- electrostatic surface charging

- intercalation capacitance

- conversion capacitance

(Super)capacitors rely on electrostatic surface processes only, which are comparably fast. [80] Pseudocapacitors and batteries on the other hand are modified in their volume, i.e.

a bulk process is taking place. The transition between both concepts is continuous, especially in porous materials. [81–83] To distinguish between a surface and a bulk process, scanrate dependent capacity measurements can be used. [84, 85] Intercalation reactions, which occur most often with alkali metal ions, are relatively fast and highly reversible. As such, they offer high energy densities and hence, are more interesting for direct solar batteries. The intercalation causes a volume change and modifies the chemical potential μ_0 of the material. [36, 86]

Conversion reactions are further used to maximize the energy density in battery electrodes. [87, 88] In redox flow batteries a charge storage electrolyte (anolyte and catholyte for the anode and cathode, respectively) is reduced or oxidized. Since the storage medium is in principle mobile in this case, the energy density limitations of such batteries are not so severe, offering high flexibility. [33, 89]

2.3 Materials

2.3.1 Noble Metal Delafossite Oxides

Delafossite oxides are layered materials with an ABO_2 stochiometry. The A-atoms form a 2D hexagonal lattice, while the B-atoms are coordinated octahedrally by O atoms in-between the A-atom layers. In this work, we focus on $PdCrO_2$, $PdCoO_2$, and $PtCoO_2$, although many structures with different A and B atoms exist. The structure is illustrated in Fig. 2.8 on the example of $PdCoO_2$. The A-metal sublattice has extended atomic distances in comparison to the respective pure metal phases. Since the periodic structure contains two metal atoms per oxygen, the formal oxidation state of the metals is $+1$, which is not commonly encountered for noble metals like Pd or Pt. In 1971, the synthesis and the material properties were reported for the first time. [90–92] Subsequently, high interest in these and related materials arose due to anisotropic electronic properties that stem from the layered structure, since the strained A-metal sublattice can be assumed as electronically decoupled from the octahedral structure. [93, 94] Recently, evidence for hydrodynamic electron flow in $PdCoO_2$ has been given. [95]
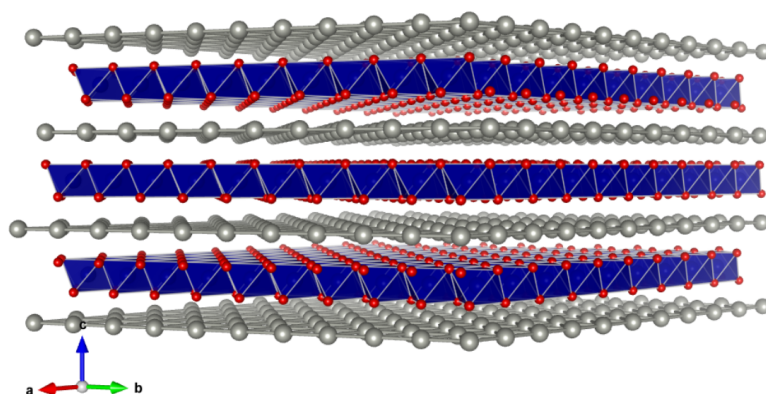
Figure 2.8: Structure of ABO_2 delafossites based on the example of $PdCoO_2$. Grey: Pd sublattice. Red and blue: O and Co atoms forming octahedra.

2.3.2 Carbon Nitrides

Carbon nitrides (CN_x) are organic based, polymeric and typically layered materials which are formed from linked heptazine or triazine units, as shown in Fig. 2.9. As such, they essentially are comprised of strictly alternating C and N atoms with no C-C or C-H bonds. The polymeric archetype was discovered by Jacob Berzelius in 1834 and named melon by Justus v. Liebig. [96] Since this 1D polymer actually orders in a 2D graphite-like fashion, it is often called *graphitic* carbon nitride (in analogy to graphene). [37, 97]

Melon type CN_x typically have a band gap of around 2.7 eV, with CB and VB positions at -1.1 and +1.6 eV vs NHE, being chemically stable in most solvents, acids, bases and water. They can be easily synthesized by thermal condensation from different nitrogen containing precursor molecules. [31] Since the discovery of moderate visible light photo-catalytic water splitting based CN_x, [28] research on these materials led to progress in the design, including morphological optimizations, band gap engineering and the fabrication of CN_x - semiconductor composites. Besides, different sonication assisted exfoliation techniques have increased the specific surface area and shown that a deposition down to single atomic layers with a thickness of 0.4 nm is possible. [98] Since the material is a fairly poor conductor, the resulting shorter migration distances for charge carriers ensure a higher charge separation efficiency after photogeneration. This leads to higher photocurrents and to up to 75% decreased electron transfer resistance in exfoliated CN_x compared to bulk material [51, 52].

On the other hand, it has been reported that the charge transport in CN_x occurs par-

tially by hopping from plane to plane, perpendicular to the 2D structure. [99] As such, the optimum particle thickness results probably from a trade-off between resistive losses, stacking being required for charge transport, and a high surface area.

The polymeric structure of CN_x enables surface chemistry modifications and surface engineering, tuning optical and electronic properties without affecting the overall composition significantly. The use of different precursors, copolymers and an adopted control of reaction parameters, affecting also the C/N ratio, provides a surface area range from $8\,m^2/g$ up to $288\,m^2/g$ and band gaps from 1.58 eV to 2.89 eV. [31, 100] Further doping and heterojunction possibilities with CN_x are summarized in review articles. [101–103]

2D trazine based CN_x can be obtained by ionothermal synthesis that requires a LiCl/KCl salt melt. The structure obtained is an imide bridged, triazine based polymer, called Poly(triazine imide) (PTI). [104] Since the structure is not fully condensed, ions can reside in the pores, which align perpendicular to the sheet structure. These PTI CN_x have similar band gaps, but can reach up to fourfold HER rates compared to melon. [105]

True 2D heptazine based CN_x were first reported in 2009, followed by another structural solution proposed in 2017. [38, 39, 106, 107] Their ionothermal synthesis is similar to the ones used for PTI, yielding a comparable structure based on heptazine units (see Fig. 2.9). The salt ions are also assumed to reside in the structural pores. The band gap of 2D PHI based CN_x is similar (2.7 eV), but the band positions are shifted to lower energies by 0.6-0.8 eV. [30, 38] Still, these PHI based materials show higher HER efficiencies than melon-type CN_x, ranging up to $2.8\,mmol\,g^{-1}h^{-1}$, which is among the highest values ever reported for CN_x. [108] The high efficiency is attributed to better exciton separation, electron stabilization or an enhanced charge transfer to the co-catalyst. [38, 108, 109] The stabilization of anion radicals on these CN_x, first reported in 2016, [109] could be used to drive the HER with significant time delays after illumination in the presence of a sacrificial electron donor, overcoming the intermittency of day and night. [30] To trigger the HER, a co-catalyst needed to be added. This observation has set the basis for the solar battery investigations presented in Section 4.3.
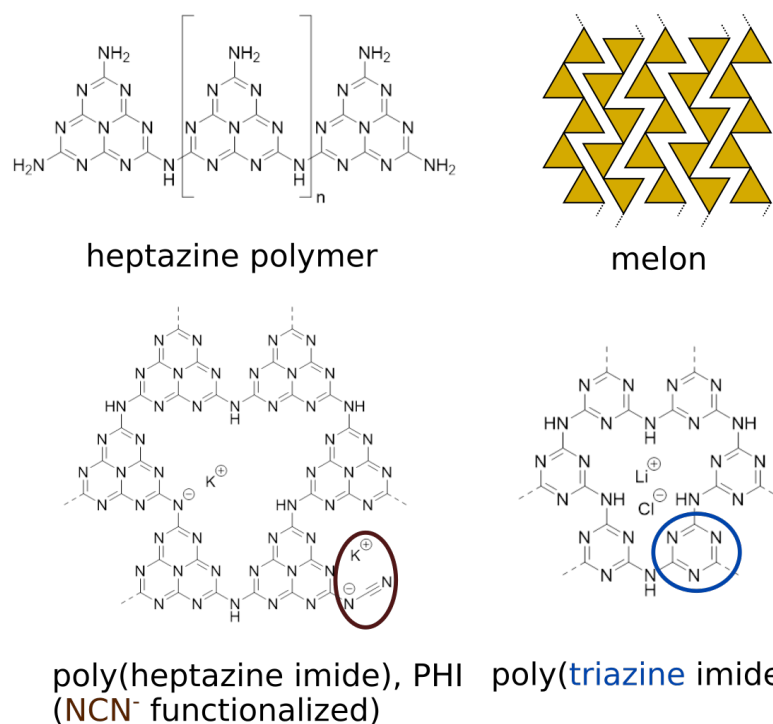
Figure 2.9: Structures of CN_x composed of heptazine and triazine units. Melon is a 1D heptazine based polymer where the chains arrange in a 2D manner.

2.3.3 Covalent Organic Frameworks

While CN_x are invariably composed of heptazine or triazine units, the closely related class of 2D or 3D covalent organic frameworks (COFs) offers a higher chemical versatility and modularity by the use of different molecular building blocks (see Fig. 2.10). COFs are based on light elements only (H, B, C, N, O and S). The building blocks, a linear (ditopic) and a crossing (often tritopic) linker, are synthesized by classical organic chemistry. Afterwards, they are reacted under reversible solvothermal conditions, which has the advantage of possible defect healing during the crystallization process. [110] As such, they often yield a better crystallinity and higher porosity and hence, specific surface area than CN_x.

The first COF was synthesized in the group of O. Yaghi back in 2005. [111] Since then, the field developed quickly offering various new structures for different applications, such as gas separation and storage, sensing and catalysis. [112–114] Many COFs are linked by boronate ester bonds or imine groups, which can be hydrolized. [115] Other COF ex-

amples are based on imide and hydrazone linkages, although the latter are less prone to hydrolysis and have shown to be exfoliated in 2D multilayers [116]. Reviews of possible structures and building block is given in [117–119].

In 2014, Stegbauer *et al.* have shown that hydrazone based COFs are active for visible light hydrogen production (in the presence of Pt as electrocatalyst). [120] The 3.8 nm wide pores provide a surface are of $1600\,\mathrm{m^2/g}$, which was the highest reported for hydrazone COFs. Although its optical band gap is estimated for 2.8 eV, the absorption tail ranges up to 600 nm and the hydrogen evolution rates of $1970\,\mu\mathrm{mol\,g^{-1}h^{-1}}$ are more than twice as high as for most CN_x at that time. The triazine moieties, which are likewise present in CN_x (see Fig. 2.9), are suspected to play an active role in the HER.

The choice of particularly electron rich or electron poor building block further allows for tuning charge stabilization and transfer properties. They also affect the layer stacking and hence, the crystallinity. [121–123] The high porosity and surface area of COFs further allows for anchoring nanoparticles or molecular co-catalysts to the COF matrix. [29, 124] The junction formed tends to stabilize photoelectrons or enhance the charge transfer to the co-catalyst thus boosting the HER significantly compared to each constituent. Since the bottom-up approach enables tuning optical and electrical properties towards tailored photoactive organic materials and combination possibilities with other co-catalysts are numerous, more examples of COFs being used for photocatalytic HER are being published. [125–129]

Besides, COFs have been reported as highly active HER and OER electrocatalysts, showing also promise for CO_2 reduction applications. [130–133] Recently, even light assisted charging of a COF solar battery photocathode has been reported, showing promise for applications similar to NCN-PHI. [79]
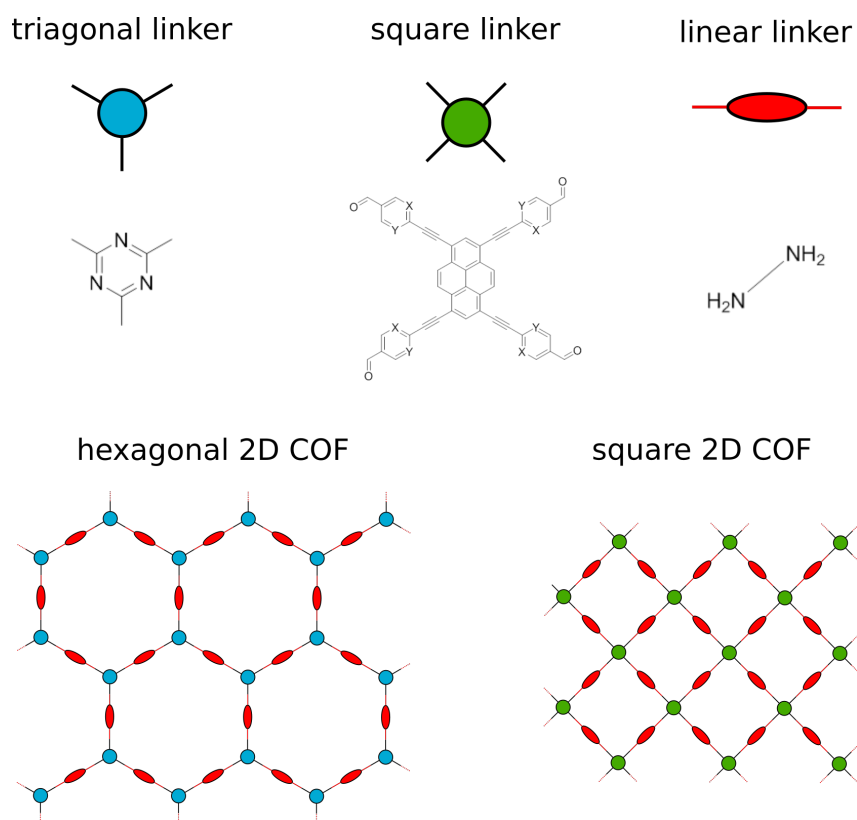
Figure 2.10: Illustration of different linkers to form hexagonal and square 2D COFs. A trigonal linker can be triazine-derived. The square linker shown here are pyrene based aldehydes. They are called 1,3,6,8-tetrakis(4-ethynylbenzaldehyde)-pyrene (TE**B**PY) if X,Y=CH; 1,3,6,8-tetrakis(6-ethynylnicotinaldehyde)-pyrene (TE**N**PY) if X=N, Y=CH; 1,3,6,8-tetrakis(2-ethynylpyrimidin-5-carbaldehyde)pyrene (TE**P**PY) if X,Y=N. The linear linker example is hydrazine.

3

Experimental Methods

In this Chapter, the most important techniques and procedures for the preparation of the different sample types are presented and followed by characterization methods. Besides optical and structural characterization, the photoelectrochemical methods employed are explained.

3.1 Material Synthesis

The **ABO$_2$-structured delafossites** were synthesized following a reported solid state synthesis technique by Daniel Weber, Roland Eger and Leo Diehl in the Lotsch group. [90] PtCoO$_2$ was synthesized from PtCl$_2$ and CoO, PdCrO$_2$ from PdCl$_2$ and LiCrO$_2$, PdCoO$_2$ from PdCl$_2$ and CoO, following also another procedure for larger crystals. [134] Subsequently, they were studied for their electrocatalytic performance in the paper presented in Ch. 4.1.

The **Covalent Organic Frameworks (COFs)** presented in Ch. 4.2 were prepared by Linus Stegbauer following a condensation reaction of hydrazine and pyrene based aldehydes. The details can be found in the Appendix A.2

2D **NCN-PHI** based **Carbon Nitrides (CN$_x$)** were synthesized by mixing melon and potassium thiocyanate (KSCN) and subsequent heating in an oven under an argon at-

29

mosphere. The excess KSCN is washed out afterwards. More detailed information can be found in literature. [30] The samples used for the publication presented in Section 4.3 were synthesized by Julia Kröger.

3.2 Optical Characterization

Optical imaging was performed to visualize the samples before and after (photo)catalytic measurements and to determine the geometrical sample surface area. The images were taken with a *Keyence VHX-600* digital microscope. The surface area was extracted with the program *ImageJ*.

Optical bands gaps were extracted from UV-VIS absorbance measurements carried out on an *Agilent Carry 5000 UV-Vis-NIR* spectrophotometer. Since the materials were strongly scattering, the absorbance was calculated based on the sample's reflectance using the Kubelka-Munck-function: [45]

$$f(R) = \frac{(1-R)^2}{2R} \tag{3.1}$$

3.3 Structural Characterization by Electron Microscopy

Electron microscopy was used to image the respective material's surface structure as well as its composition. The acceleration of the electrons to the sample surface creates different secondary particles and photons and leads to electron-sample interactions that are often characteristic for the elements or the material.

Based on secondary electrons (SE) that are created due to scattering of the incident electron beam with electrons present in the material the materials surface can be imaged by scanning it.

Directly backscattered electrons (BSE) result from elastic scattering of incident electrons with the atoms of the material under investigation. The interaction cross section and thus the amount of BSE depends on the elemental mass. As such, contrast differences can thus be used to image elemental distributions.

The creation of secondary electrons leaves behind low-lying unoccupied states in the sam-

ple material. If other electrons at higher levels jump into these free states, characteristic X-rays are emitted that allow for elemental detection by energy dispersive X-ray spectroscopy (EDX or EDS). This can also be done while scanning to create elemental maps. Transmission electron microscopy (TEM) was used to determine the crystal structure locally. This was especially of importance for the characterization of the delafossite film, which modify their crystal structure during catalysis. The interaction of the electron beam with a thin sample ($<100\,\text{nm}$) allows direct imaging of the crystal structure due to different electron beam-sample interactions, like in a conventional electron microscope. The periodicity of the crystal structure creates an interference or diffraction-pattern, which corresponds to the (fast) Fourier transform (FFT) of the crystal lattice structure.

For elemental detection, electron energy loss spectroscopy (EELS) can further be used to determine elemental concentration based on element specific interactions with the electron beam. [135]

3.4 Photoelectrochemical Characterization

3.4.1 Sample Preparation

The sample preparation has an important influence on the measurements, since electrocatalytic measurements do probe the whole surface and sometimes the volume. As such, knowledge of the contacted material area (and the material mass for volume effects) is required.

Usually, smaller (single) crystals were obtained after the delafossite synthesis. Since individual contacting was impossible due to their size, such samples had to be deposited on a conductive substrate, which is chemically stable in the given measurement conditions and inactive in the respective reaction range studied. Due to very strong hydrogen evolution at the delafossite crystallites, their adhesion was severely limited due to the formation of bubbles. For this purpose, small amounts covering just the surface (usually $1.5\,\text{mg}$) of $0.2\,\text{cm}^2$ were slightly pressed into carbon-paste electrodes fabricated for this purpose. These electrodes consist of a Teflon-body with a wire contact. Into this body, a mix of carbon paste is pressed, consisting of $0.9\,\text{ml}$ paraffin-oil and $2.5\,\text{mg}$ graphite powder. [136] In case of large single crystals, an electrical contact between the sample and the potentiostat can be obtained by contacting the material directly at one part, e.g. by a wire or

another conductive (and sometimes transparent) substrate and silverpaste. All parasitic, especially metallic areas such as the silver paste are covered with an inert epoxy ($3M^{TM}$ Scotch-Weld^{TM} DP 410). For special mm-sized crystal sample measurements, which required higher manual precision, nailpolish was used as sealant to cover the silverpaste. The sample area was then determined by recording an image of the free sample area with a reference scale.

The preparation of C-paste electrodes for delafossites and a sealed single crystal are shown in Fig. 3.1.
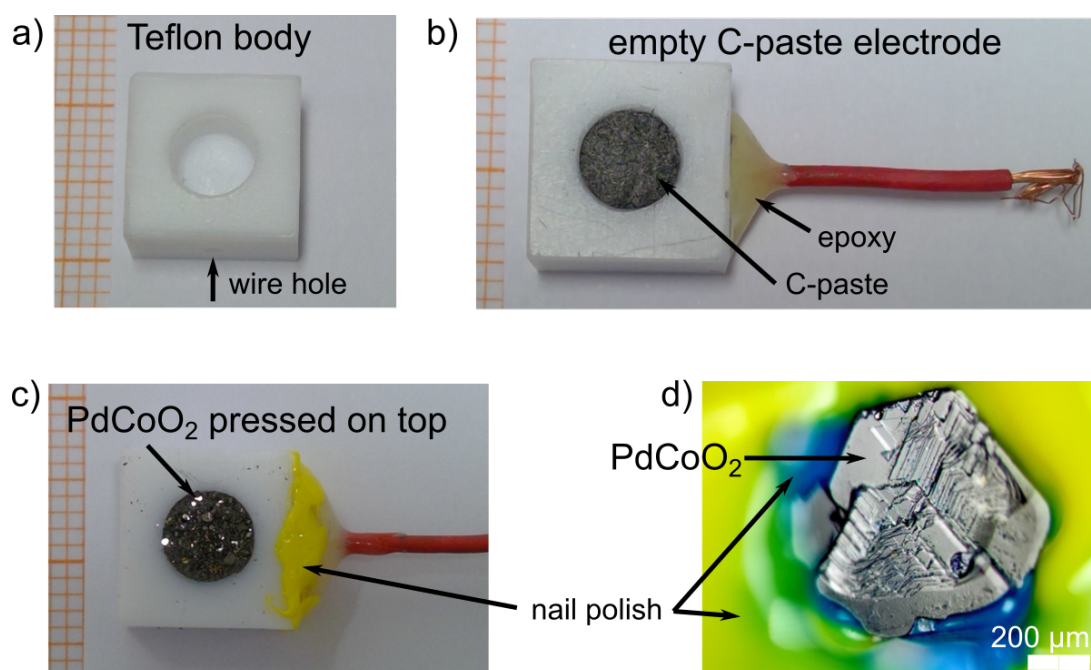
Figure 3.1: Electrode preparation for electrochemical characterization. a) Teflon body prior to adding a wire. b) Completely filled C-paste electrode with wire and sealing. c) Material deposited on top of the electrode. d) Larger single crystal of $PdCoO_2$ on FTO (invisible) sealed with nail polish.

In the case of semiconducting and macroscopically rather insulating CN_x or COFs, thin films of the materials had to be produced. Both materials were insoluble in all tested and suitable solvents. For this purpose, the powders of the materials ground for 2-10 min. Subsequently, they were dispersed in water or an alcohol evaporating faster. After sonication (2 min to 10 h, depending on the requirement), some samples were further size selected

and separated. For this purpose, the obtained opaque suspension was centrifuged three times with increasing time and speed to separate the larger particles. The obtained, dense suspensions were then partially dried and weighted on quartz crystal microbalance to determine the particle density. This liquid was then deposited on transparent indium- or fluorine doped tin oxide (ITO or FTO) glasses, which were contacted by silverpaste and sealed by epoxy. Besides drop-casting of the suspension, spin coating was used to obtain more uniform and mechanically stable films. A short plasma-treatment of 30 s-2 min improved the aqueous film formation due to an increased hydrophilicity. Sample adhesion was usually increased if the samples were dried at 60 °C in a hotplate overnight. If multiple deposition steps were necessary, which was the case for spin coating of CN_x, the samples were usually dried 10-15 min in-between spin coating steps. This allowed achieving a high enough surface coverage for measurements. The whole process is illustrated in Fig. 3.2. For COFs presented in this thesis, it was possible to grow the material directly on an FTO-substrate with a known thickness. After growth, the electrode was thus only contacted and sealed.
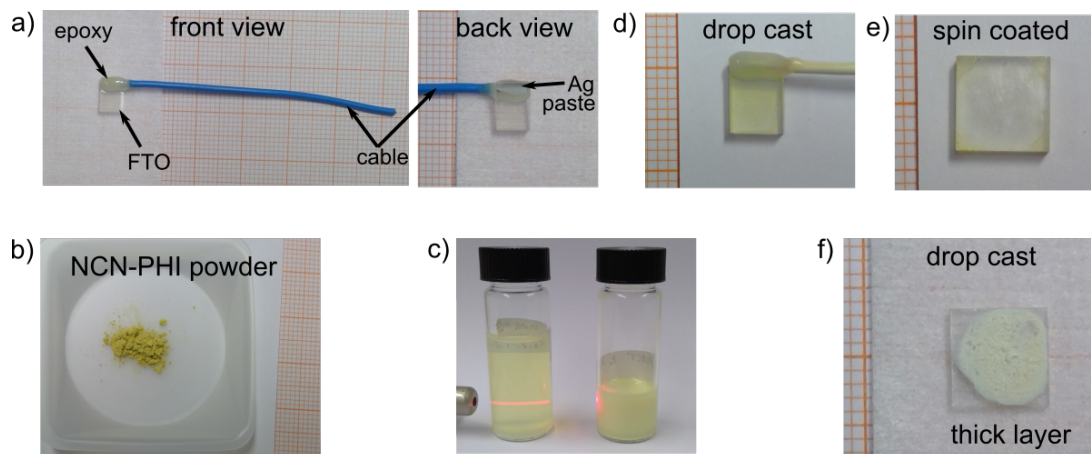

Figure 3.2: Electrode preparation for phtoelectrochemical characterization. a) Front and back view of a FTO sheet contacted with Ag paste to a wire and sealed. b) NCN-PHI after synthesis. c) Colloidal suspensions of NCN-PHI sheets (left) and larger particles (right) after sonication and separation by centrifugation. d) Image of a FTO electrode after deposition of 10 μg NCN-PHI sheets. e) Electrode after spin coating. f) Thick layer of NCN-PHI after drop casting the suspension with larger particles.

3.4.2   Measurement Setup

All (photo)electrochemical measurements were performed in a home-made glass reactor equipped with a quartz window for illumination (or in a glass beaker for pure electro-chemistry), as illustrated in Fig. 3.3. The electrochemical setup consists of a cylindrical glass chamber for the electrolyte, a frit to purge with gas and an outlet port as well as 3 ports for the electrodes (working, counter and reference electrode). Simulated solar sunlight (AM 1.5G) is provided by side-illumination with a *Sciencetech Solar LightLine A4* fiberized solar simulator through the front Quartz window, allowing also for automated chopping and intensity variation up to 7 sun. The measurements were recorded by a *Ivium CompactStat* potentiostat in a fume-hood that can be darkened, usually under stirring unless impedance was measured.
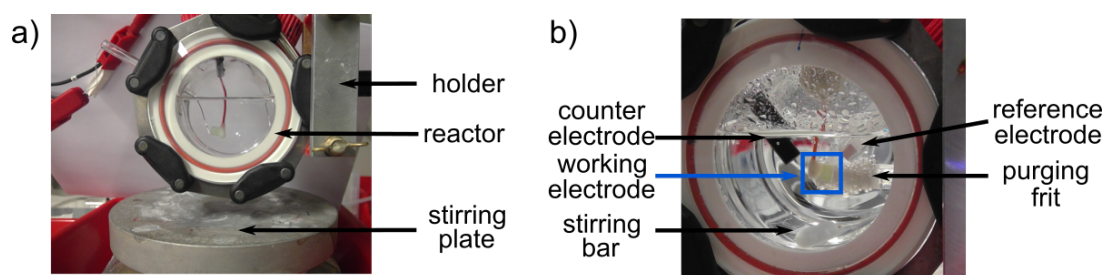

Figure 3.3: a) PEC setup for illumination from the front side. b) Operating PEC reactor with electrodes.

3.4.3   Electrochemical Measurements

To ensure the correct RHE potential before every measurement, the electrolyte was purged with hydrogen and cycled around the OCP with Pt. This is of high importance when materials are studied that are catalytically highly active like $PdCoO_2$. The activity for water reduction and oxidation was then extracted from cyclic current-voltage (CV) measurements in the desired gas purging conditions that simulate a saturation of the reaction product. Otherwise, the OCP values may be shifted. The CVs are then used to extract different values, such as redox-potentials, activities and the Tafel-parameters. Chopped light was use to extract the portion of light induced charge carriers as function of the applied potential. This allows the extraction of band positions and the photon-to-current efficiencies. Scanrate-dependent measurements enable to access the surface capacity and

thus to extract the active area.

Chronoamperometric (CA) measurements monitor the temporal evolution of the current at a constantly applied potential. They are mostly used to study the stability of the (photo)electrocatalytic materials and the electrodes as well as the products formed.[1] These measurements also allowed studying the Carbon Nitrides' internal and charge transfer resistance under light and in the dark if coupled to EIS. For direct solar batteries with a dual functionality of light absorption and charge storage, the charge generation cannot easily be separated from its storage. The charge storage properties can thus be best accessed by discharging the material chronoamperometically after illumination and comparing these to purely electrochemical charging- and discharging curves.

Chronopotentiometric (CP) measurements monitor the temporal evolution of the potential at a constantly applied current. As such, they can in principle be used in a similar fashion like CA measurements. Usually, the storage capacity and related energy is obtained by CP measurements with different constant currents. These define the Ragone diagrams comparing the energy density to the power density. [137] The change and saturation-value of the potential at zero current (open circuit potential, OCP) holds information about the conductivity type of a semiconductor and allows to access its flat band positions, see Section 2.1.4. To validate these values, a confirmation of Nernstian behavior in different pH-conditions is necessary. [45]

Electrochemical impedance spectroscopy (EIS) applies a sinusoidal wave at a desired potential with a defined amplitude and measures the sample's feedback, i.e. the change of phase and amplitude. Since the frequency of the excitation is varied over orders of magnitude (typically, MHz to mHz), information about sample properties in different time domains can be obtained. After fitting the respective data to appropriate equivalent circuit diagrams, electrochemical material properties can be extracted. Besides capacitive, inductive and resistive properties of different sample elements, the series resistance of a system can be extracted. This enables the correction of losses with respect to the potential applied to the investigated electrode. The corrected overpotential η is then used to fit Tafel-slopes. From Nyquist plots, describing the complex impedance plane, time dependent information about charge transfer and storage processes are extracted. Among these are the contributions of double layer and pseudocapacitance that can also be measured

---

[1]Before a gas analysis is run, the electrolyte as well as the headspace were purged with argon. For analysis, the reactor is closed and sealed.

under illumination. This knowledge can further be used to determine the electrochemical surface area (ECSA) and with that, to normalize for the surface roughness if a suitable reference is available. [138]

4
Results & Discussion

In this Chapter, the main results of the thesis are presented. While the first work was submitted to a peer-reviewed journal, the following two were already published. For every topic and respective publication, a specific introduction is given, followed by the article. For article 2, permission for reproduction is not required, since the article is available under the Creative Commons Attribution Non-Commercial License CC BY-NC, permitting non-commercial use, distribution and reproduction. Article 3 is reproduced with permission of the publisher.

4.1 Highly Efficient HER Catalysis based on Delafossite Oxides and *Operando* Induced Effects enabled by Strain

In this article, we study the catalytic activity of the ABO_2 structured delafossite oxides PdCrO2, $PdCoO_2$ and $PtCoO_2$ in acidic media. The most common HER catalyst employed is Pt. This material unites two beneficial properties. First, it has the highest j_0 of all pure elements, which is due to its beneficial ΔG_H, as discussed in Section 2.1.3. Second, the catalytic process on the surface is governed by the Volmer-Tafel mechanism, ensuring the fastest possible increase in the catalytic reaction rate with increasing potential. Since Pt is an expensive and rare metal, partial elemental substitutions enabling

material savings as well as the search for material alternatives with similar performances is still ongoing. [17, 56] This is especially interesting for Pd, which is a fairly poor HER catalyst, being used for oxidation reactions, ORR or organic synthesis e.g. [139–143] Its j_0 for HER is almost comparable to Pt, but the Tafel slope of $>100\,\mathrm{mV}$ hinders realistic HER applications.

The herein investigated delafossite oxides were already reported as good OER catalysts in 1980. [144] We decided to study their HER activity for their intrinsically strained metal sublattice with respect to the pure elements, [93] which was predicted to influence the catalytic activity severely, as discussed in Section 2.1.3. Examples of such strain induced enhanced catalytic activities are numerous, [20] being most often based on Pt and Pd in order to improve their intrinsic activity per surface area, in analogy to j_0. Interestingly, d-band theory (see Section 2.1.3) rather predicts a decreasing activity for HER if the metal-to-metal distances are extended by tensile strain. However, we observe an opposite effect, arising from different contributions at a time.

As discussed in Section 2.1.3, the HER is an electron transfer reaction, leading to reduction, which may also affect the material's stability towards reduction. Since this process is continuous, we also observed a continuous increase in the catalytic activity for the Co based materials. Faradaic efficiency measurements coupled to *operando* SECM investigations have evidenced a mostly faradaic nature of the HER currents. On the other hand, it can also be expected that the surface is partially reduced, as reported for many other catalysts created by dealloying. [145] In fact, this is also what we observe after electrochemical cycling. By SEM and EDX, we evidenced the growth of a capping layer on the Co based materials, which is in line with ICP investigations of dissolved Co in the electrolyte. XPS confirmed the formation of a pure noble metal surface. These corrosion effects occur with significantly different kinetics that depend mostly on the transition metal B in the ABO_2 structure. Since Cr has a lower dissolution rate constant than Co, [146] $PdCrO_2$ is rather stable under reductive conditions in acidic media, while the surfaces of $(Pt,Pd)CoO_2$ are transformed quickly to their metal structure. On the Pt based compound, the corroded surface is too thin to investigate it structurally, while on $PdCoO_2$, very fast dissolution of Co is observed, affecting almost 10% of the electrode material after 1000 cycles between RHE and $\eta = $ -110 mV.

Besides corrosion, templating effects arising most probably from the inherently strained $PdCoO_2$ substructure are observed by TEM. The lattice strain in the hexagonal sublat-

tice of $PdCoO_2$ (2.8% compared to Pd(111)) is partially transduced to the growing Pd capping layer, which itself is 2.3% strained versus bulk or nanosctrucured Pd at the interface to $PdCoO_2$ (3.98 Å in average). A significant surface roughening was observed by SEM, impedance spectroscopy and Tafel analysis, counteracting the possible decrease in surface specific activity in strained Pd overlayers that was observed and expected by d-band theory. [62, 63] As such, an increase in activity per geometrical electrode area is actually observed. Furthermore, Pd is a material that is very active for hydrogen sorption and whose HER activity has been found to depend on the fraction of hydrogenation. [147] In fact, a hydrogen rich but unstable β-Pd phase shows similar Tafel properties to Pt, as well as similar lattice constants to those observed for the Pd capping layer. Thus, the strain effects induced by the substrate are believed to facilitate a transformation of hydrogen poor α-phase to the hydrogen rich β-Pd (PdH_x, x>0.6), which otherwise is hindered by distinct lattice parameters (3.89 Å for α-Pd and 4.02 Å for β-Pd vs. 3.98 Å in the Pd capping layer). The transformation towards catalytically more active β-Pd is further evidenced by a shift of the OCP in CVs recorded with fast scan rates >25 mV/s and respective capacitive contributions. A complete analysis and discussion is presented in the manuscript below and in its Supplementary Information in the Appendix, Section A.1.

Rational Strain Engineering in Delafossite Oxides for Highly Efficient Hydrogen Evolution Catalysis in Acidic Media

Filip Podjaski[1,2], Daniel Weber[1,3], Siyuan Zhang[4], Leo Diehl[1,3], Roland Eger[1], Viola Duppel[1], Esther Alarcon-Llado[5], Gunther Richter[6], Frederik Haase[1,3], Anna Fontcuberta i Morral[2,7], Christina Scheu[4], Bettina V. Lotsch[1,3,8,9]

[1]Max-Planck-Institute for Solid State Research, Heisenbergstraße 1, 70569 Stuttgart, Germany. [2]Laboratory of Semiconductor Materials, Institute of Materials, Faculty of Engineering, Ecole Polytechnique Fédérale de Lausanne, Station 12, 1015 Lausanne, Switzerland. [3]Department of Chemistry, University of Munich (LMU), Butenandtstraße 5-13, 81377 München, Germany. [4]Max-Planck-Institut für Eisenforschung GmbH, Max-Planck-Straße 1, 40237 Düsseldorf, Germany. [5]AMOLF, Science Park 104, 1098 XG Amsterdam, The Netherlands. [6]Max-Planck-Institute for Intelligent Systems, Heisenbergstr. 3, 70569 Stuttgart, Germany. [7]Institute of Physics, Faculty of Basic Sciences, EPFL, 1015 Lausanne, Switzerland. [8]Nanosystems Initiative Munich (NIM), Schellingstraße 4, 80799 München, Germany. [9]Center for Nanoscience, Schellingstraße 4, 80799 München, Germany.

Keywords

Catalysis, water splitting, hydrogen evolution, delafossites, dealloying, strain, phase transition, beta-Palladium.

Abstract

The rational design of hydrogen evolution reaction (HER) electrocatalysts which are competitive with platinum is an outstanding challenge to make power-to-gas technologies economically viable. Here, we introduce the delafossites $PdCrO_2$, $PdCoO_2$ and $PtCoO_2$ as a new family of electrocatalysts for the HER in acidic media. We show that in $PdCoO_2$ the inherently strained Pd metal sublattice acts as a

1

pseudomorphic template for the growth of a strained (by +2.3%) Pd rich capping layer under reductive conditions. The surface modification continuously improves the electrocatalytic activity by simultaneously increasing the exchange current density j_0 from 2 to 5 mA/cm²$_{geo}$ and by reducing the Tafel slope down to 38 mV/decade, leading to overpotentials η_{10}< 15 mV for 10 mA/cm²$_{geo}$, superior to bulk platinum. The greatly improved activity is attributed to the in-situ stabilization of a β-palladium hydride phase with drastically enhanced surface catalytic properties with respect to pure or nanostructured palladium. These findings illustrate how *operando* induced electrodissolution can be used as a top-down design concept for rational surface and property engineering through the strain-stabilized formation of catalytically active phases.

Global warming and the decreasing availability of fossil fuels urge today's society to transition to more sustainable energy sources. While there is enough solar and wind power to satisfy our needs in terms of total energy, [1, 2] the available power fluctuates strongly and requires intermediate and long term storage. [3, 4] One viable option is the storage of the intermittent electrical energy in the form of chemical fuels such as hydrogen (power-to-X). Clean hydrogen can be produced by alkaline electrolyzers, which require constant and high current densities for a stable operation.[5] In acidic environments, more powerful and flexible proton exchange membrane (PEM) electrolyzers can be employed that allow for coupling with fluctuating energy sources such as wind and solar. [6, 7] As the most widely used electrocatalysts for the hydrogen evolution reaction (HER) is still platinum, an expensive and scarce material that is also poisoned easily, research into alternative or modified highly efficient and stable electrocatalysts under various conditions has been identified as a key goal in energy science.[8, 9, 10]

Strain effects have been discussed to be at the heart of enhanced intrinsic activities toward several catalytic reactions including the HER, as predicted and observed for example in Pd overlayers. [11, 12, 13] More recently, the scope of this concept has been widened and the direct strain control in substrate induced strain effects or in core-shell particles have been effectively used for the HER as well as the oxygen evolution reaction (OER) and the oxygen reduction reaction (ORR). [14, 15, 16, 17, 18, 19]

Here, we report the time evolution of the electrocatalytic activity of the ABO_2 delafossites $PdCrO_2$, $PdCoO_2$, and $PtCoO_2$ for the HER in acidic medium and show how inherent structural strain can be used to enhance the catalytic efficiency *operando*. Since their discovery and the observation of their unusually high and anisotropic conductivity in 1971, [20, 21, 22] these oxides have attracted renewed interest recently for their unusual electronic properties, [23, 24] anisotropic thermopower,[25] and most recently, for the discovery of hydrodynamic electron flow occurring in nanostructured $PdCoO_2$.[26]

A common property of the metallic Pd and Pt based delafossites is an inherently expanded hexagonal metal sublattice with extended nearest neighbour distances on the A site compared to the pure metals (2.830 Å in $PdCoO_2$ and 2.923 Å in $PdCrO_2$ vs. 2.751 Å in *fcc* Pd(111); 2.823 Å in $PtCoO_2$ vs. 2.775 Å in metallic Pt(111)). [20, 21, 22, 24] This sublattice is separated by a layer of edge-sharing MO_6 (M = Co, Cr) octahedra, see Fig. 1 a, which gives rise to anisotropic transport properties. So far, these and other delafossite oxides have been reported as highly efficient electrocatalysts for the OER in alkaline media. [27, 28, 29, 30] Furthermore, copper- and silver-based delafossites have been reported as photocathodes due to their large band gap. [31, 32, 33, 34] Apart from $AgRhO_2$ and $CuCrO_2$, the stability of these systems appears to be limited to basic, neutral or non-reductive conditions. [35, 36, 37]

In this work, we make use of the intrinsically strained metal sublattices and study the hydrogen evolution activity of the delafossite oxides $PdMO_2$ (M = Cr, Co) and $PtCoO_2$ for the first time, investigating the influence of strain on the catalytic activity. For $PdCoO_2$, our long-term studies reveal a gradual enhancement of the already excellent water reduction activity of the bulk material over time, putting the electrocatalytic activity of *operando* modified $PdCoO_2$ *en par* with that of the top-of-the-class HER electrocatalyst in acidic medium, platinum. We elucidate how the charge transfer properties as well as the high specific activity per surface area evolve, which we attribute to the strain-induced stabilization of *in-situ* formed, catalytically highly active β-palladium hydride (PdH_x, x~0.62-0.67).[38] Together with an apparent increase in exchange current density, these effects lead to a drastically reduced overpotential at 10 mA/cm²$_{geo}$ (η_{10}) < 15 mV and a Tafel slope of 30-40 mV/decade, enabling stable operation at current densities of 100 mA/cm²$_{geo}$ with less than 100 mV of applied (uncorrected) potential.

Results

Electrochemical characterization. Polycrystalline powders of the delafossites $PdCrO_2$, $PdCoO_2$ and $PtCoO_2$ were prepared according to previously reported procedures (for details, see the Method section). The crystal structure of the isostructural compounds (space group *R*-3*m*) was confirmed by powder XRD measurements (see Fig. S1) and is schematically displayed for $PdCoO_2$ in Fig. 1 a.[20, 39, 40, 41] The crystallite sizes were in the range from 1-3 µm for $PdCrO_2$, 10-30 µm for $PtCoO_2$ and up to 1 mm for $PdCoO_2$ as evidenced by electron microscopy (see Fig. 2). These microcrystals were subsequently pressed into a carbon paste electrode (see Methods for details) to study their activity towards HER in acidic media. The analysis was performed in hydrogen saturated 1M H_2SO_4 by means of cyclic voltammetry (CV), chronopotentiometry and –amperometry. The polarization curves in Fig. 1 b-d show the uncorrected cathodic currents per geometric surface area (in mA/cm²$_{geo}$) for the first 1000 cycles on all three materials, which all increase in efficiency in different ways. After correcting for the series resistance losses (*IR*-drop) extracted from impedance measurements before the respective cycles, the CVs can be fitted to the Tafel equation

$$\eta = b \log(i/j_0)$$

with η being the overpotential with respect to the reversible hydrogen electrode (RHE), while *b* denotes the Tafel slope (in mV/decade), which provides insight onto the electrocatalytic processes occurring on the surface, i being the current density and j_0 the exchange current density, which is a measure of the intrinsic activity per surface area.[42]

The activity of all delafossites is very high, requiring an overpotential η_{10} of far less than 100 mV for all systems. $PdCrO_2$ initially requires η_{10} of approx. 50 mV (Fig. 1 b and e). Subsequently, the current density decreases and stabilizes with increasing cycle number. $PdCoO_2$ (Fig. 1 c and e) initially also yields η_{10} at 50 mV vs. RHE for a similar loading and keeps improving for the first 1000 cycles down to 12(3)

mV. In contrast, $PtCoO_2$ initially shows a lower activity than the Pd based materials and quickly improves towards comparable activities of $PdCoO_2$ within 30-100 cycles. Afterwards, it stabilizes at η_{10} around 30-35 mV. Remarkably, the overpotentials of all the materials are very low after some initial cycles and especially the Co based delafossites outperform most catalysts already after 30 cycles ($\eta_{10} < 40mV$), particularly all oxides, in acidic media. [43, 44, 45, 46]

To better understand the curious evolution of the overpotential over time, we discriminate between the effects arising from the intrinsic activity and those induced *operando*, i.e. during the electrocatalytic process. In the first cycles, the cathodic currents are influenced by surface activation or hydrogen sorption, which is well known for Pt and Pd, respectively. [47, 48] This is clearly visible in the first cycle of $PdCrO_2$ (Fig. 1 b), where the apparent high activity occurs already at the RHE potential before hydrogen saturation at the surface is achieved. In the range of 10-1000 cycles, the catalytic mechanism on the surface evolves with increasing cycle number and the currents tend to stabilize. Interestingly, the overpotential is modified also by the catalytic process itself, which is reflected by the decreasing Tafel slopes for the Co based materials (Fig. 1f). The values between 70 and 38 mV/dec suggest a mixture between a reaction rate limited by the discharge reaction of protons at the surface (128 mV/dec, Volmer mechanism) and the Volmer-Tafel mechanism (38 mV/dec) where the recombination of adsorbed hydrogen is rate determining, which is observed after 1000 cycles on $PdCoO_2$. Pure Pd metal, which has a high Tafel slope of >100 mV/decade for current densities >1 mA/cm², is limited by the Volmer mechanism, in contrast to the delafossites presented herein, see Fig. S2. [42, 49, 50] The observed evolution of the activity described by η_{10} in the delafossite oxides further appears to be related to the activity of the catalysts per surface area, j_0, (Fig. 1g), which changes as a function of time and parallels the trends observed for the overpotentials shown in Fig. 1 e. While j_0 tends to slightly decrease for $PdCrO_2$, it increases for both Co containing materials, indicating an effective increase in the intrinsic activity or catalytically active area, or both. The values for j_0 evolving with time are all in the range of

1 mA/cm² and thus amongst the highest reported to date. For PdCoO$_2$, j_0 of up to 5(1.2) mA/cm² is even superior to those observed for both bulk Pt and Pd (2.3 and 0.9 mA/cm², respectively), as shown in Fig. S2.[42, 43, 51]

In order to obtain an estimate of the real surface area, impedance measurements were performed to extract the double layer capacitance C_{DL}, which is proportional to the electrochemical surface area (ECSA), and the pseudocapacitive contribution C_P (see discussion in the SI, section 3 and Fig. S3). Since due to their modified surface properties no references for the *operando* modified delafossites are available, the same capacitive response factors as for bulk Pd or Pt were assumed (see SI section 3 for details). We then obtain an ECSA normalized $j_{0,ECSA}$ of 0.14 mA/cm² for PdCrO$_2$ and 0.20 mA/cm² for (Pd,Pt)CoO$_2$ after 300 cycles (see Fig. S3 for details). These values are close to dealloyed Pd nanoparticles without normalization for real surface area (0.18 mA/cm²)[52] and reported surface normalized values of 0.14 mA/cm² for tensile strained Pd grown on Au or rough Pd surfaces (0.22 mA/cm²).[53, 54]
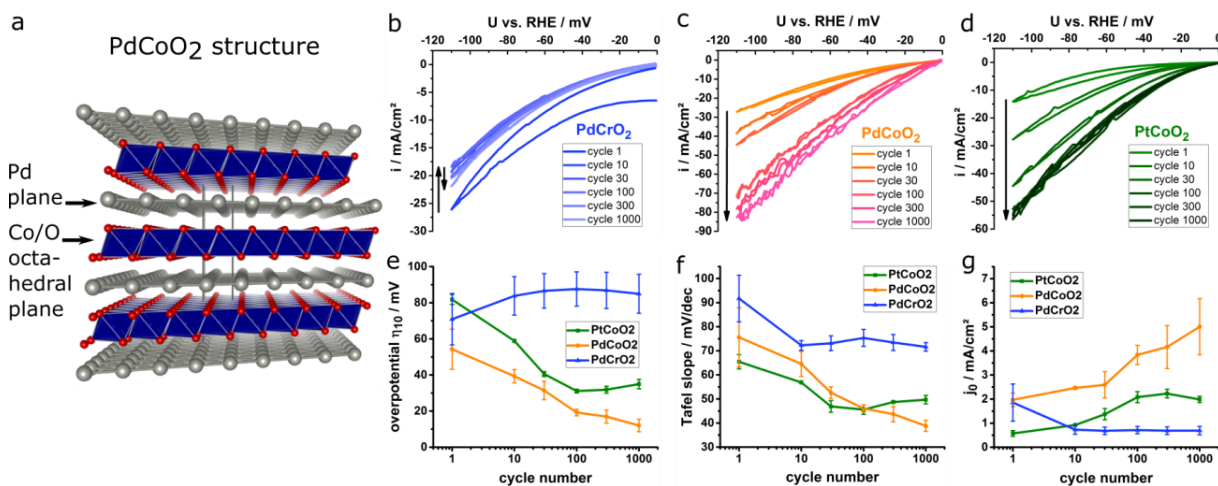
Figure 1: Crystal structure of the delafossites and the evolution of the electrochemical activity for HER. a: The layered delafossite structure using PdCoO$_2$ as a representative example, view along [100] (Pd: grey; oxygen: red, Co: blue octahedra). b-d: Uncorrected cathodic currents for PdCrO$_2$ (b), PdCoO$_2$ (c) and PtCoO$_2$ (d) in hydrogen saturated 1M H$_2$SO$_4$ during cathodic cycling (scan rate: 2 mV/s for displayed measurements, 25 mV/s for aging in-between the displaced cycles). d-f: The resulting

Tafel parameters (e: overpotential η_{10}, f: Tafel slope, and g: exchange current density for geometric surface area) after IR-correction and fitting in the region >1 mA/cm².

To provide insights into the origin of the currents observed in the electrocatalytic experiments, the evolution of hydrogen was investigated close to the surface by scanning electrochemical microscopy (SECM) measurements on $PdCoO_2$ single crystals *operando* (see Fig. S4 a & b for illustration). Although no site dependence could be mapped due to a tip-limited resolution >10 μm, the probing electrode feedback clearly shows the presence of hydrogen near the sample surface (~10 μm) when the sample is held at different cathodic sample potentials under weakly acidic conditions. Cyclic voltammograms reflecting the reductive SECM tip HER current for different sample potentials show a decrease when the $PdCoO_2$ sample HER current becomes competitive, and an increase in the hydrogen oxidation current at oxidative tip potentials (Fig. S4 c). Temporally, an increase in hydrogen production at the sample could be evidenced by increasing proton reduction currents at the tip (Fig. S4 d). This highlights the fact that pristine samples are HER active and improve over time, even without cycling. Furthermore, a comparison of the charge passed through a pre-aged $PdCoO_2$ single crystal (> 1000 cycles), referenced to a Pt wire, yielded stable Faradaic efficiencies towards hydrogen evolution of > 90%. In contrast, a pure Pd wire had a Faradaic efficiency of only 6%, probably due to large amounts of H_2 being incorporated into the Pd lattice, even after long coulometric measurements (see Fig. S5). [50, 51]

Surface modification analysis. Next, to understand the origin of the observed increase in catalytic activity over time, the modifications on the surface of the delafossites were tracked by analysis of the electrolyte composition by means of inductively coupled plasma optical emission spectrometry (ICP-OES) after the electrocatalytic experiments (see SI Table ST1). Almost no detectable amounts of Cr in the electrolyte suggest a high stability of this element in the $PdCrO_2$ surface (<0.08 at% of the Cr amount present in the electrode), while $PtCoO_2$ showed small amounts of Co in the electrolyte, corresponding to 0.24(3) at% of the electrode element. No dissolved Pt was evidenced in all cases. In contrast, $PdCoO_2$

shows increased amounts of Co in the electrolyte, indicating a much faster dissolution of Co, which progresses at a rate two orders of magnitude faster than Cr dissolution.[55] After 1000 cycles, 9.35(90) at% of the Co has leached out from $PdCoO_2$.

Consequently, we expect the formation of a Pd rich surface layer on $PdCoO_2$. Indeed, direct evidence of the surface transformation is obtained by optical microscopy and scanning electron microscopy (SEM) on the surfaces of the delafossites after catalysis. While $PdCrO_2$ does not show any obvious signs of corrosion (Fig. 2 a-b), the surface of $PtCoO_2$ is slightly modified, which is elucidated by a slight roughening and accumulation of heavier elements as shown by the back scattered electron (BSE) detector image (Fig. 2 c-d vs e-f). In contrast, the surface of $PdCoO_2$ is strongly modified, as shown in Fig. 2 g-l and mirrored by the significant Co dissolution and a stronger change in catalytic properties. Inspection under an optical microscope (Fig. 2 g-h) reveals a large area surface modification and roughening. A more detailed SEM analysis of the surface (Fig. 2 i vs j) shows the formation of a continuous capping layer with a higher concentration of heavy elements than the pristine, underlying material. Energy dispersive X-ray spectroscopy (EDS) maps on the modified surface further underline the enrichment of Pd in this topmost capping layer. The formation of cracks and nanoparticles within the capping layer (Fig. 2 j-l) suggests a release of strain still present in the remaining capping structure after Co and O are dissolved near the surface (*vide infra*). These cracks can also be related to potential dependent hydrogen loading and unloading into the catalysts during electrocatalytic cycling, which results in dynamically modified lattice parameters.[56] Also, small amounts of Pd were found in the electrolyte after catalysis, which can be explained by partial detachment of the strained capping layer (Fig. S6 a-c). [56]
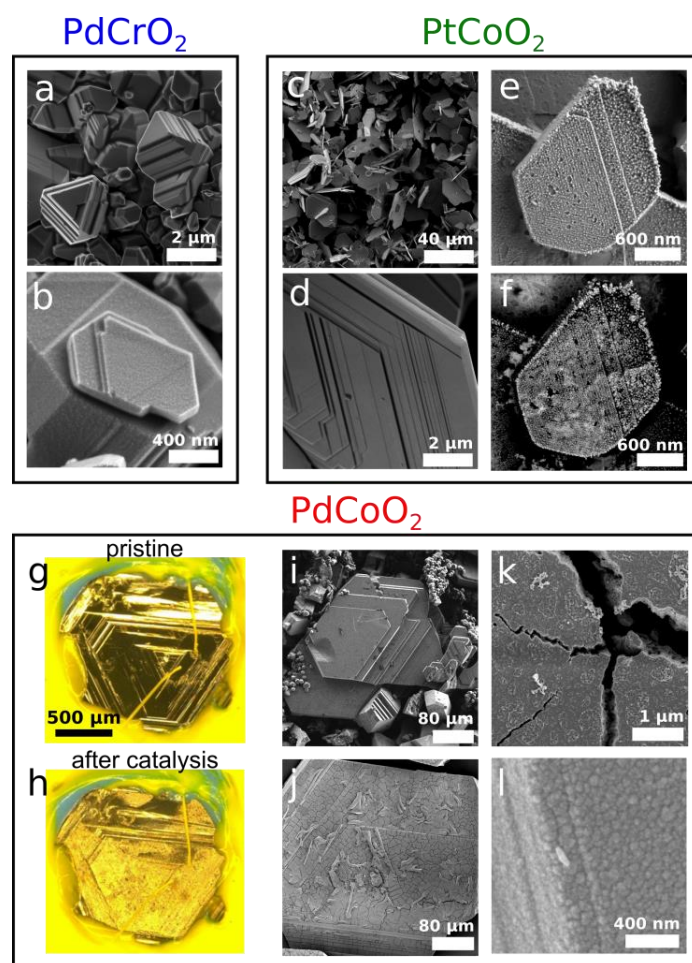
Figure 2: Surface modifications on the delafossites before and after electrocatalytic HER in 1M H_2SO_4. a: $PdCrO_2$ crystals as-synthesized. b: Enlarged image after cycling. c-d: As-synthesized $PtCoO_2$ crystals. e-f: PtCoO2 after cycling. The BSE detector image (f) highlights the heavy element nature of the capping layer, containing mostly Pt. g-h: Optical microscope images of a large $PdCoO_2$ crystal before and after catalysis, embedded in yellow sealing. i: SEM image of a large $PdCoO_2$ crystal embedded in a carbon paste electrode prior to cycling. j: $PdCoO_2$ surface modification after cycling showing the Pd rich capping layer. k: Zoom into the cracked surface structure. l: Magnification of the rough nanostructure on the surface.

To further investigate the surface modification, X-ray photoelectron spectroscopy (XPS) was used to measure the valence state of the respective components of all three materials before and after catalysis, as shown in Fig 3. A detailed discussion including survey spectra (Fig. S7) and peak lists (Tables ST2-5) can be found in the SI section 8. In brief, the main elemental lines of all pristine delafossites correspond well to the literature values. In the oxygen spectra (Fig. 3 c, f and i), an O 1s signal at 531-532 eV is

attributed to surface adsorbed oxygen. After catalysis, the amplitude of the delafossite M-O interaction peak at 529 eV is slightly lowered relative to the surface O 1s peak in $PdCrO_2$ (Fig. 3c), suggesting somewhat decreasing binding of Pd and Cr to O at the surface. For $PdCoO_2$ (Fig. 3 d-f) and $PtCoO_2$ (Fig. 3 g-i), the Co as well as the M-O 1s signals completely disappear after catalysis, with slightly slower kinetics for $PtCoO_2$ (see Fig. S8), underlining the formation of a Pd(0) or Pt(0) layer on the surface during catalysis, in agreement with the ICP measurements on Co dissolution. Summarizing these results, we can conclude that $PdCrO_2$ remains largely unchanged over the cycling experiments, while $PtCoO_2$ and $PdCoO_2$ gradually lose Co and are eventually reduced, forming a metallic capping layer of the respective noble metal.
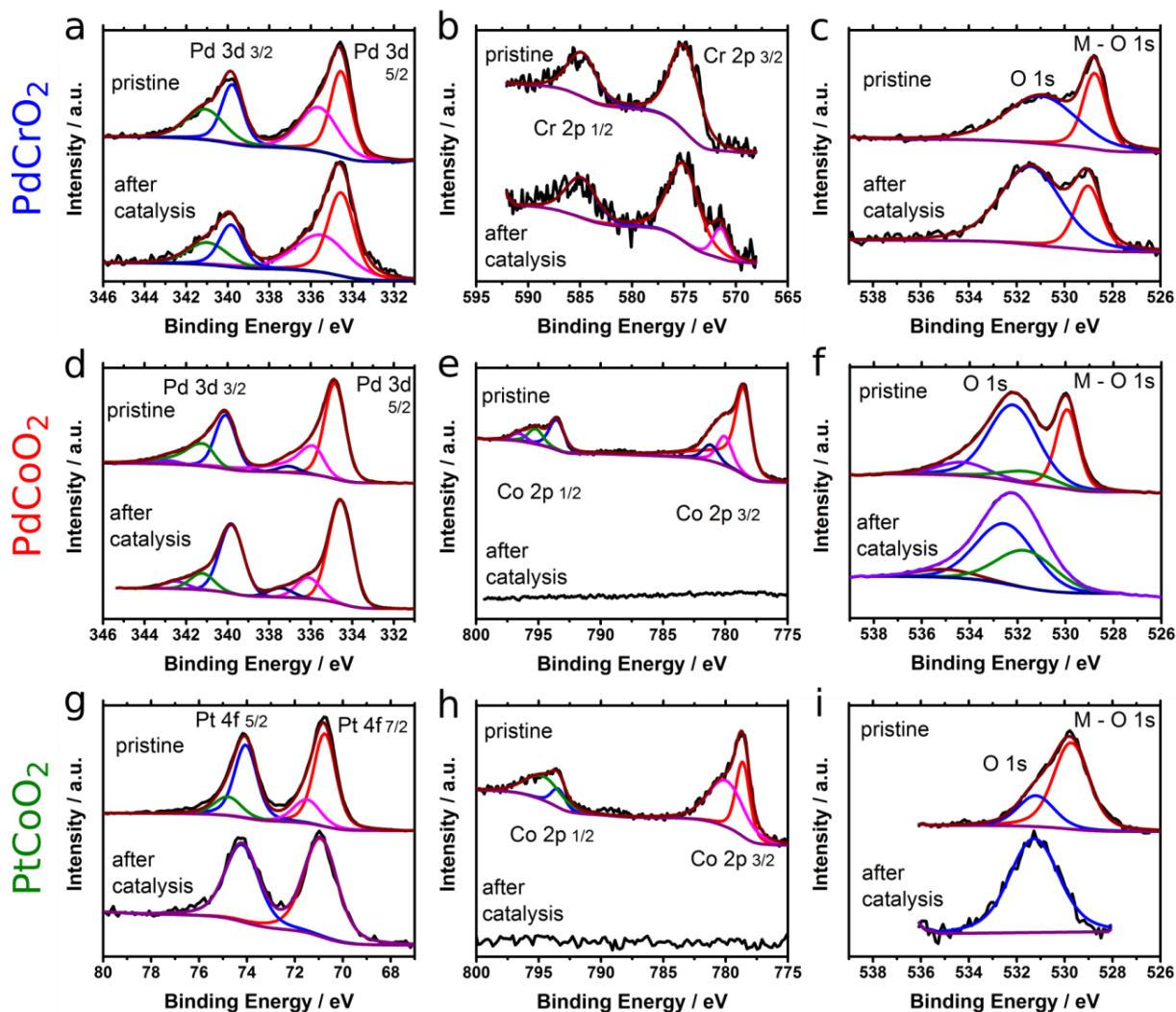
Figure 3: XPS spectra of $PdCrO_2$ (a-c), $PdCoO_2$ (d-f) and $PtCoO_2$ (g-i) before (top trace) and after (bottom trace) catalytic cycling in 1M H_2SO_4. While the surface of $PdCrO_2$ remains almost unchanged, the surface of $PdCoO_2$ is transformed into Pd with traces of oxygen adsorbed to the surface. For $PtCoO_2$, the behavior is similar and a Pt rich surface is obtained after longer aging. A peak list including all signals and their areas as well as the survey and additional spectra are shown in the SI section 8 (Fig. S7-8, Table ST 2-5).

Capping structure and strain analysis. Having identified the nature of the surface corrosion process as the reductive formation of a Pd rich capping layer on $PdCoO_2$, we turn to the question as to why this process leads to the observed exceptionally high activity towards HER. To this end, we first used scanning transmission electron microscopy (STEM) to characterize the structure and elemental

12

composition of the pre- and post-catalysis samples at high spatial resolution. STEM lamellae were prepared from a PdCoO$_2$ single crystal after short (5 min) and long (hours) chronoamperometric aging at -100 mV vs. RHE, which both lead to the formation of a capping layer with increasing thickness (see Fig. 2 c-e and S6). A cross section lamella of a 5 min aged single crystal contains both the capping layer and the underlying material, as shown in Fig. 4 (see SI section 6 for experimental details and Fig. S 6 for a lamella prepared after hours of aging). The Pd capping layer is ca. 30 nm thick and consists of Pd nanocrystals of 2-10 nm size (Fig. 4 a-d). Elemental analysis of the capping layer by EDS spectrum imaging [57] shows that the cap consists primarily of Pd (Fig. 4 e), while the Co concentration is below the detection limit (< 2%). O is only observed at the surface of the Pd capping layer. The concentration profiles are summarized in the right display element of Fig. 4 f. As shown in Fig. 4 a, the Pd *fcc* capping layer grows directly on the PdCoO$_2$ surface, in direct contact to the electrolyte. There is a sharp transition between the PdCoO$_2$ crystal and the Pd cap (Fig. 4 b). The atomic resolution STEM-high angle annular dark field (HAADF) image of PdCoO$_2$ (Fig. 4 c) is overlaid by the crystal structure along the [11-20] zone axis. We observe a preferred orientation of the cap on the PdCoO$_2$ substrate, suggesting quasi-epitaxial growth of the Pd (111) in the c-direction of the bulk PdCoO$_2$ (normal to the hexagonal Pd sublattice). Within the cap structure, twin variants of Pd nanocrystals are observed (Fig. 4 d and S9). Fast Fourier Transformations (FFT) of the respective cap (Pd *fcc*) and bulk (PdCoO$_2$) regions reveal only a few degrees tilt between Pd (111) and PdCoO$_2$ (0003), as shown in Fig. S9 (a and b). This lends further evidence that the capping layer grows via leaching of Co and O from the bulk material, while the hexagonal Pd lattice in PdCoO$_2$ evolves into an *fcc* Pd lattice with minimal structural reorganization, as illustrated in Fig. 4 g. To derive the lattice parameter of the Pd nanocrystals, STEM micrographs were calibrated using the lattice parameters of PdCoO$_2$ from XRD measurements. Compared to the sharp reflections of PdCoO$_2$, Pd reflections are broader along the radial and azimuthal axes, corresponding to a broader range of strain and rotation among Pd nanocrystals. Analysis of all Pd {111} reflections evidence

13

a homogeneous lattice parameter of 3.98 Å on average, which proves that the Pd *fcc* capping layer shows isotropic tensile strain, even for both twin variants (Fig. S9 c). Further comparison shows a slightly smaller lattice parameter at the top 5 nm of the cap than the bottom part (Fig. S9 e-g), suggesting partial strain relaxation towards the surface, especially for the Pd(111) planes that are parallel to the PdCoO$_2$ surface (Fig. S8, d-g). This is expected for quasi-epitaxial growth and partial strain release due to cracks. Nevertheless, the lattice parameters close to the surface are still larger than those of bulk Pd crystals (3.89 Å) [58] or the ones reported for Pd nanoparticles with similar size (approx. 10 nm) that show no lattice dilatation (see also Fig. S10).[59] Only below 3 nm, a comparable lattice parameter has been reported for pure Pd nanoparticles deposited on carbon. [60] A lattice constant of 3.98 Å in the capping layer corresponds to Pd nearest neighbour distances of 2.815 Å in the Pd *fcc* structure, which is very close to 2.83 Å in the Pd sublattice of PdCoO$_2$ and significantly differs from unstrained Pd (2.75 Å). This further underlines the relevance of lattice strain in the substrate material, PdCoO$_2$, which is transduced to the capping layer.
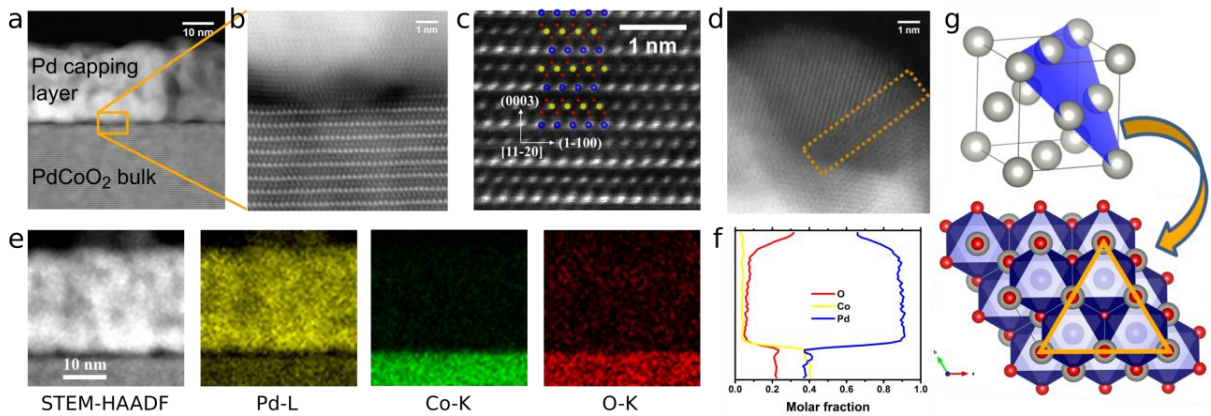
Figure 4: STEM analysis of the Pd capping layer on PdCoO$_2$. a: STEM-HAADF micrograph of PdCoO$_2$ after 5min aging at η = 100 mV in 1M H$_2$SO$_4$, showing the bulk material and the Pd rich capping layer. b: PdCoO$_2$ atomic structure (Pd: blue, Co: yellow, O: red). c: Pd *fcc* nanocrystals in the overlayer containing twinned grain boundaries (marked in orange). d: STEM-HAADF image and respective STEM-EDS elemental maps based on the Pd-L line (blue), the Co-K line (yellow) and O-K line (red) and a line profile of

their molar fractions (right element). e: Illustration of the Pd *fcc* structure with the (111) plane corresponding to the hexagonal Pd sublayers in $PdCoO_2$, which act as a growth template for Pd *fcc*.

The observations made on $PdCoO_2$ in Fig. 4 agree with ICP measurements of dissolved Co in the electrolyte and the XPS data (Fig. 3) but further suggest that the continuous dissolution of Co and O creates a significantly strained Pd-rich capping layer, where the strain is transmitted by the pseudomorphic growth of Pd(111) on the hexagonal Pd sublattice in $PdCoO_2$.

Pd nanoparticle reference measurements. Since the particle size and density of surface states of Pd nanocrystals in the capping layer (2-10 nm) differs from that of bulk Pd, which can affect the catalytic activity,[59, 61] we studied the electrochemical activity of Pd nanoparticles of comparable size (1 − 10 nm, *Sciventions*) to gauge the effect of the particle morphology and strain on the catalytic activity (see Fig. S10-11). Rietveld refined XRD measurements of the dried reference nanoparticles revealed an average lattice constant of 3.90(2) Å (see Fig. S10), which fits reported values for bulk Pd (3.89 Å) and Pd nanostructures of 8-10 nm size.[59] The lattice constant of the nanoparticles is thus 2% smaller than for the nanocrystals at the bottom of the Pd capping layer (3.98 Å). Since a comparable surface coverage and active surface area is difficult to achieve, the catalytic properties of both bulk Pd and the nanoparticles are best characterized by their Tafel slope, which is only sensitive to the underlying catalytic process and independent of the actual effective surface area.[42] Both the nanoparticles and the bulk Pd show a similar Tafel slope of ~105 mV/dec (Fig. S11 and S2), which is consistent with the Pd literature value of 103 mV/dec [49] and relates the surface catalytic process to a rate limiting Volmer (discharge) reaction. This value is much larger than the values found for surface modified $PdCoO_2$ in Fig. 1 and S2 (38 to 30 mV/dec), which suggests a rate limiting Volmer-Heyrovsky or -Tafel mechanism (38 and 30mV/dec, respectively). [42, 62] The intrinsic catalytic mechanism of the strained Pd capping layer is thus different from pure Pd, regardless of particle size or morphology.

Discussion. To rationalize the observed tensile strain-induced activity increase in $PdCoO_2$, we first consider the effect of strain as expected from classical d-band theory, which predicts a correlation between the position of the metal d-band center with the HER activity.[53] The relative energies of the metal d-band and the antibonding hydrogen σ^*-orbital directly determine their overlap and, hence, bonding strength of the H-adsorbate to the metal surface, ΔG_H.[63] Following Sabatier's principle, the catalyst – substrate interaction should be neither too strong nor too weak such that both adsorption of the substrate and desorption of the product is facile. Hence, ΔG_H is used as the most relevant descriptor of the intrinsic activity for HER, given by a turnover frequency or j_0, resulting in a volcano plot, with optimal catalyst – substrate interactions at the top of the volcano.[42, 64] Tensile lattice strain in Pd tends to flatten out the d-bands while upshifting the band center towards the Fermi level, leading to stronger overlap with the hydrogen σ^*-orbital and, thus, stronger metal—H bonds.[12, 65] In fact, growth of a pseudomorphic Pd layer on a single crystalline substrate with a larger lattice constant has been shown to increase ΔG_H and thus move tensile strained Pd away from the top of the volcano while decreasing the exchange current density. [13, 53] Interestingly, we observe the opposite trend, enhancing both j_0 and reducing the Tafel slope. The observed change in Tafel slope by a factor of almost 3 with respect to bulk Pd suggests a more fundamental change in the materials surface properties to be at play. Indeed, tensile strain positively affects the hydrogen adsorption capacity of Pd and has been described to modify the potential of hydrogen adsorption in Pd. [53, 66, 67, 68] On the other hand, the different lattice parameters between hydrogen poor α-Pd and the hydrogen rich β-phase (sharp transition and discontinuous lattice parameter transition from 3.89 to 4.02 Å) kinetically hinder a phase transformation. [69, 70, 71] Since our expanded Pd *fcc* lattice intrinsically shows stable lattice parameters (as probed by TEM after prolonged ex situ sample storage) close to those of β-PdH_x (3.98 Å and 4.02 Å, respectively), [71, 72] incorporation of

hydrogen is expected to be more facile.[66] This conjecture rationalizes the corresponding findings on the Tafel slopes, which indeed show β-PdH$_x$-like behavior (30-38 mV/dec Tafel slope). [51, 62] To investigate the possible *operando* formation of a hydride phase, faster cyclic voltammetry measurements (25 mV/sec and 100 mV/sec) were recorded after 1000 cycles (Fig. S 12). With increasing scan rate, a stronger capacitive contribution is observed. It is most prominent for PdCoO$_2$, as evidenced by the separation of the forward and backward scans around the open circuit potential (OCP), and the OCP shifts to more cathodic potentials for this material (Fig. S12 b, 100mV/s scans). This indicates, in accordance with the impedance data presented in Fig. S3, that the capping layer is active for hydrogen adsorption - a well-known phenomenon in Pd metal that forms interstitial hydrides (PdH$_x$). [48, 50, 51] Since the sorption effects are very fast (~1 s), the transition to β-PdH$_x$ can occur almost immediately once a strained Pd capping layer has been formed under reductive conditions.

In summary, we have investigated the delafossite oxides PdCrO$_2$, PdCoO$_2$, and PtCoO$_2$ for HER activity in acidic media for the first time. In their pristine form these materials outperform most reported electrocatalysts with respect to their overpotentials required for 10 mA/cm$^2_{geo}$ (71(15) mV for PdCrO$_2$, 54(12) mV for PdCoO$_2$, 82(3) mV for PtCoO$_2$ in the first cycles). The very high activity for HER originates from a superior intrinsic surface activity, translating into exchange current densities on the order of mA/cm^2 (initially 1.9(8) mA/cm^2 for PdCrO$_2$, 2.0(3) mA/cm^2 for PdCoO$_2$, 0.57(12) mA/cm^2 for PtCoO$_2$), which are orders of magnitude higher than most HER catalysts besides Pt. This property is especially beneficial for HER at small overpotentials, where the effect of activity increase by the Tafel slope does not yet come into play. While PdCrO$_2$ is relatively stable under acid HER conditions, the surfaces of PtCoO$_2$ and especially PdCoO$_2$ corrode over time *via* the reductive dissolution of Co and O at the surface near region. The resulting Pd or Pt enriched capping layers show significantly enhanced activities compared to the bulk materials: j_0 increases by a factor of 2.5 and 3.5 for PdCoO$_2$ and PtCoO$_2$, while the Tafel slopes decrease from 76(13) to 38(3) mV/dec and from 65(3) to 50(2) mV/dec, respectively.

In the case of PdCoO$_2$, the tensile strain, which is present in the noble metal sublattice of all these delafossites, is translated to the Pd *fcc* capping layer, which grows directly on the underlying bulk material. This strain increases the hydrogen adsorption energy as predicted by d-band theory and lowers the energetic barrier for the formation of a β-PdH$_x$ phase, which otherwise requires a significant lattice expansion (+3.3%). This phase transformation entails a change in HER mechanism, shifting the surface catalytic process away from the rate limiting Volmer-reaction found in Pd towards the more efficient Volmer-Tafel or Volmer-Heyrovsky mechanism. The resulting material has an overpotential of 12(3) mV for 10 mA/cm$^2_{geo}$ only, hence outperforming even bulk Pt.

The herein presented strain engineering points towards a more general design principle for the rational activity enhancement in electrocatalysts with inherently strained metal sublattices. It further suggests that phase transformations, stabilized by strain, may be key players in determining both metal—substrate interactions and the intrinsic catalytic activity, and as such, strain-induced phase changes may complement classical d-band theory as a model to predict catalytic performance.

Acknowledgements

Data availability

The data supporting the plots within this paper and other findings of this study are available from the corresponding author upon reasonable request.

Author contributions

F.P., D.W., F.H. and B.V.L conceived the project and the contributing measurements. The materials were synthesized by D.W., L.D. and R.E. All sample preparation and electrochemical measurements were done by F.P. The SECM data was analyzed and discussed by E.A.L and F.P. G.R. and F.P. analyzed the XPS data. S.Z. performed the STEM experiments including the data analysis and presentation. F.P. created all other graphs. F.P. and B.V.L wrote the manuscript. All authors including C.S. and A.F.M. contributed to the discussion of the measurements, the data interpretation and the manuscript discussion.

Conflict of interest

The authors declare no conflict of interest.

Literature

1.   Lewis NS, Nocera DG. Powering the planet: Chemical challenges in solar energy utilization. *Proceedings of the National Academy of Sciences* 2006, **103**(43)**:** 15729-15735.

2.   Lewis NS. Toward Cost-Effective Solar Energy Use. *Science* 2007, **315**(5813)**:** 798-801.

3.   Podjaski F, Kröger J, Lotsch BV. Toward an Aqueous Solar Battery: Direct Electrochemical Storage of Solar Energy in Carbon Nitrides. *Advanced Materials* 2018, **30**(9)**:** 1705477.

4.   Yu MZ, McCulloch WD, Huang ZJ, Trang BB, Lu J, Amine K*, et al.* Solar-powered electrochemical energy storage: an alternative to solar fuels. *Journal of Materials Chemistry A* 2016, **4**(8)**:** 2766-2782.

5.   Gülzow E. Alkaline fuel cells: a critical view. *Journal of Power Sources* 1996, **61**(1)**:** 99-104.

6.   Tobias R, Nhan NH, Detre T, Robert S, Peter S. Electrocatalytic Oxygen Evolution Reaction in Acidic Environments – Reaction Mechanisms and Catalysts. *Advanced Energy Materials* 2017, **7**(1)**:** 1601275.

7.   Carmo M, Fritz DL, Mergel J, Stolten D. A comprehensive review on PEM water electrolysis. *International Journal of Hydrogen Energy* 2013, **38**(12)**:** 4901-4934.

8.   Vesborg PCK, Jaramillo TF. Addressing the terawatt challenge: scalability in the supply of chemical elements for renewable energy. *RSC Advances* 2012, **2**(21)**:** 7933-7947.

9.   *Electrocatalysis in Fuel Cells*. Springer: London, 2013.

10.   Papageorgopoulos DC, Keijzer M, Veldhuis JBJ, de Bruijn FA. CO tolerance of Pd-rich platinum palladium carbon-supported electrocatalysts - Proton exchange membrane fuel cell applications. *Journal of the Electrochemical Society* 2002, **149**(11)**:** A1400-A1404.

11.   Mavrikakis M, Hammer B, Nørskov JK. Effect of Strain on the Reactivity of Metal Surfaces. *Physical Review Letters* 1998, **81**(13)**:** 2819-2822.

12.   Kibler LA, El-Aziz AM, Hoyer R, Kolb DM. Tuning Reaction Rates by Lateral Strain in a Palladium Monolayer. *Angewandte Chemie International Edition* 2005, **44**(14)**:** 2080-2084.

13.   Greeley J, Jaramillo TF, Bonde J, Chorkendorff I, Nørskov JK. Computational high-throughput screening of electrocatalytic materials for hydrogen evolution. *Nature Materials* 2006, **5:** 909.

14.   Strasser P, Koh S, Anniyev T, Greeley J, More K, Yu C*, et al.* Lattice-strain control of the activity in dealloyed core–shell fuel cell catalysts. *Nature Chemistry* 2010, **2:** 454.

15.   Du M, Cui L, Cao Y, Bard AJ. Mechanoelectrochemical Catalysis of the Effect of Elastic Strain on a Platinum Nanofilm for the ORR Exerted by a Shape Memory Alloy Substrate. *Journal of the American Chemical Society* 2015, **137**(23)**:** 7397-7403.

16.   Putungan DB, Lin S-H, Kuo J-L. A first-principles examination of conducting monolayer 1T'-MX2 (M = Mo, W; X = S, Se, Te): promising catalysts for hydrogen evolution reaction and its enhancement by strain. *Physical Chemistry Chemical Physics* 2015, **17**(33)**:** 21702-21708.

17.   Escudero-Escribano M, Malacrida P, Hansen MH, Vej-Hansen UG, Velázquez-Palenzuela A, Tripkovic V*, et al.* Tuning the activity of Pt alloy electrocatalysts by means of the lanthanide contraction. *Science* 2016, **352**(6281)**:** 73-76.

18. Wang H, Xu S, Tsai C, Li Y, Liu C, Zhao J*, et al.* Direct and continuous strain control of catalysts with tunable battery electrode materials. *Science* 2016, **354**(6315)**:** 1031-1036.

19. Luo M, Guo S. Strain-controlled electrocatalysis on multimetallic nanomaterials. *Nature Reviews Materials* 2017, **2:** 17059.

20. Shannon RD, Rogers DB, Prewitt CT. Chemistry of Noble Metal Oxides. I. Syntheses and Properties of ABO2 Delafossite Compounds. *Inorg Chem* 1971, **10**(4)**:** 713.

21. Prewitt CT, Shannon RD, Rogers DB. Chemistry of Noble Metal Oxides. II. Crystal Structures of PtCoO2, PdCoO2, CuFeO2, and AgFeO2. *Inorg Chem* 1971, **10**(4)**:** 719-723.

22. Rogers DB, Shannon RD, Prewitt CT, Gillson JL. Chemistry of Noble Metal Oxides. III. Electrical Transport Properties and Crystal Chemistry of ABO2 Compounds with Delafossite Structure. *Inorg Chem* 1971, **10**(4)**:** 723-&.

23. Mackenzie AP. The properties of ultrapure delafossite metals. *Reports on Progress in Physics* 2017, **80**(3)**:** 032501.

24. Daou R, Frésard R, Eyert V, Hébert S, Maignan A. Unconventional aspects of electronic transport in delafossite oxides. *Science and Technology of Advanced Materials* 2017, **18**(1)**:** 919-938.

25. Ong KP, Singh DJ, Wu P. Unusual Transport and Strongly Anisotropic Thermopower in PtCoO2 and PdCoO2. *Physical Review Letters* 2010, **104**(17)**:** 176601.

26. Moll PJW, Kushwaha P, Nandi N, Schmidt B, Mackenzie AP. Evidence for hydrodynamic electron flow in PdCoO2. *Science* 2016, **351**(6277)**:** 1061-1064.

27. Carcia PF, Shannon RD, Bierstedt PE, Flippen RB. O2 Electrocatalysis on Thin-Film Metallic Oxide Electrodes with the Delafossite Structure. *Journal of the Electrochemical Society* 1980, **127**(9)**:** 1974-1978.

28. Hinogami R, Toyoda K, Aizawa M, Kawasaki T, Gyoten H. Copper Delafossite Anode for Water Electrolysis. *Ecs Transactions* 2013, **58**(2)**:** 27-31.

29. Hinogami R, Toyoda K, Aizawa M, Yoshii S, Kawasaki T, Gyoten H. Active copper delafossite anode for oxygen evolution reaction. *Electrochemistry Communications* 2013, **35:** 142-145.

30. Toyoda K, Hinogami R, Miyata N, Aizawa M. Calculated Descriptors of Catalytic Activity for Water Electrolysis Anode: Application to Delafossite Oxides. *The Journal of Physical Chemistry C* 2015, **119**(12)**:** 6495-6501.

31. Gu J, Yan Y, Krizan JW, Gibson QD, Detweiler ZM, Cava RJ*, et al.* p-Type CuRhO2 as a Self-Healing Photoelectrode for Water Reduction under Visible Light. *Journal of the American Chemical Society* 2014, **136**(3)**:** 830-833.

32. Prévot MS, Jeanbourquin XA, Bourée WS, Abdi F, Friedrich D, van de Krol R*, et al.* Evaluating Charge Carrier Transport and Surface States in CuFeO2 Photocathodes. *Chemistry of Materials* 2017, **29**(11)**:** 4952-4962.

33. Varga A, Samu GF, Janáky C. Rapid synthesis of interconnected CuCrO2 nanostructures: A promising electrode material for photoelectrochemical fuel generation. *Electrochimica Acta* 2018, **272:** 22-32.

34. Ahmed J, Mao Y. Delafossite CuAlO2 Nanoparticles with Electrocatalytic Activity toward Oxygen and Hydrogen Evolution Reactions. *Nanomaterials for Sustainable Energy*, vol. 1213. American Chemical Society, 2015, pp 57-72.

35. Díaz-García AK, Lana-Villarreal T, Gómez R. Sol–gel copper chromium delafossite thin films as stable oxide photocathodes for water splitting. *Journal of Materials Chemistry A* 2015, **3**(39)**:** 19683-19687.

36. Park JE, Hu Y, Krizan JW, Gibson QD, Tayvah UT, Selloni A*, et al.* Stable Hydrogen Evolution from an AgRhO2 Photocathode under Visible Light. *Chemistry of Materials* 2018, **30**(8)**:** 2574-2582.

37. Oswald H-R, Kuhn P, Reller A. Bimetallic phases from reduction of delafossite-type oxides in hydrogen. *Solid State Ionics* 1989, **32-33:** 528-536.

38. Duncan H, Lasia A. Separation of hydrogen adsorption and absorption on Pd thin films. *Electrochimica Acta* 2008, **53**(23)**:** 6845-6850.

39. Tanaka M, Hasegawa M, Takei H. Crystal growth of PdCoO2, PtCoO2 and their solid-solution with delafossite structure. *Journal of Crystal Growth* 1997, **173**(3)**:** 440-445.

40. Takatsu H, Yonezawa S, Mouri S, Nakatsuji S, Tanaka K, Maeno Y. Roles of High-Frequency Optical Phonons in the Physical Properties of the Conductive Delafossite PdCoO2. *Journal of the Physical Society of Japan* 2007, **76**(10)**:** 104701.

41. Kikugawa N, Goswami P, Kiswandhi A, Choi ES, Graf D, Baumbach RE*, et al.* Interplanar coupling-dependent magnetoresistivity in high-purity layered metals. *Nature Communications* 2016, **7:** 10903.

42. Morales-Guio CG, Stern L-A, Hu X. Nanostructured hydrotreating catalysts for electrochemical hydrogen evolution. *Chemical Society Reviews* 2014, **43**(18)**:** 6555-6569.

43. McCrory CCL, Jung S, Ferrer IM, Chatman SM, Peters JC, Jaramillo TF. Benchmarking Hydrogen Evolving Reaction and Oxygen Evolving Reaction Electrocatalysts for Solar Water Splitting Devices. *Journal of the American Chemical Society* 2015, **137**(13)**:** 4347-4357.

44. Cherevko S, Geiger S, Kasian O, Kulyk N, Grote J-P, Savan A*, et al.* Oxygen and hydrogen evolution reactions on Ru, RuO2, Ir, and IrO2 thin film electrodes in acidic and alkaline electrolytes: A comparative study on activity and stability. *Catalysis Today* 2016, **262:** 170-180.

45. Awaludin Z, Safuan M, Okajima T, Ohsaka T. Investigating the physical and electrochemical effects of cathodic polarization treatment on TaOx. *Journal of Materials Chemistry A* 2015, **3**(32)**:** 16791-16800.

46. Mario C, C. TA, Sergio T. Thermally prepared Ti/RhOx electrodes: II H2 evolution in acid solution. *Hemijska industrija* 2002, **56**(6).

47. Shinagawa T, Garcia-Esparza AT, Takanabe K. Insight on Tafel slopes from a microkinetic analysis of aqueous electrocatalysis for energy conversion. *Scientific Reports* 2015, **5:** 13801.

48. Maoka T, Enyo M. Overpotential decay transients and the reaction mechanism on the Pd-H2 electrode. *Surface Technology* 1979, **8**(5)**:** 441-450.

49. Pentland N, Bockris JO, Sheldon E. Hydrogen Evolution Reaction on Copper, Gold, Molybdenum, Palladium, Rhodium, and Iron - Mechanism and Measurement Technique under High Purity Conditions. *Journal of the Electrochemical Society* 1957, **104**(3)**:** 182-194.

50. Searson PC. Hydrogen evolution and entry in palladium at high current density. *Acta Metallurgica et Materialia* 1991, **39**(11)**:** 2519-2525.

51. Elam M, Conway BE. Sorption Behavior of the Overpotential-Deposited H Species in the Cathodic H 2 Evolution Reaction at Pd and Pt-Pd Electroplated Composite Electrodes. *Journal of The Electrochemical Society* 1988, **135**(7)**:** 1678-1685.

52.   Jana R, Bhim A, Bothra P, Pati SK, Peter SC. Electrochemical Dealloying of PdCu3 Nanoparticles to Achieve Pt-like Activity for the Hydrogen Evolution Reaction. *ChemSusChem* 2016, **9**(20)**:** 2922-2927.

53.   Greeley J, Nørskov JK, Kibler LA, El-Aziz AM, Kolb DM. Hydrogen Evolution Over Bimetallic Systems: Understanding the Trends. *ChemPhysChem* 2006, **7**(5)**:** 1032-1035.

54.   Lin D, Lasia A. Electrochemical impedance study of the kinetics of hydrogen evolution at a rough palladium electrode in acidic solution. *Journal of Electroanalytical Chemistry* 2017, **785:** 190-195.

55.   Hollemann AF, Wiberg N. *Lehrbuch der Anorganischen Chemie*, 102 edn. Walter de Gruyter: Berlin, 2007.

56.   Wagner S, Uchida H, Burlaka V, Vlach M, Vlcek M, Lukac F*, et al.* Achieving coherent phase transition in palladium–hydrogen thin films. *Scripta Materialia* 2011, **64**(10)**:** 978-981.

57.   Zhang S, Scheu C. Evaluation of EELS spectrum imaging data by spectral components and factors from multivariate analysis. *Microscopy* 2018, **67**(suppl_1)**:** i133-i141.

58.   Arblaster JW. Crystallographic Properties of Palladium Assessment of properties from absolute zero to the melting point. *Platin Met Rev* 2012, **56**(3)**:** 181-189.

59.   Kuo C-H, Lamontagne LK, Brodsky CN, Chou L-Y, Zhuang J, Sneed BT*, et al.* The Effect of Lattice Strain on the Catalytic Properties of Pd Nanocrystals. *ChemSusChem* 2013, **6**(10)**:** 1993-2000.

60.   Kuhrt C, Anton R. On the origin of a lattice expansion in palladium and Pd⬜Au vapour deposits on various substrates. *Thin Solid Films* 1991, **198**(1)**:** 301-315.

61.   Teranishi T, Miyake M. Size Control of Palladium Nanoparticles and Their Crystal Structures. *Chemistry of Materials* 1998, **10**(2)**:** 594-600.

62.   Dafft EG, Bohnenkamp K, Engell HJ. Investigations of the Electrochemical Reduction of Hydrogen Ions on Palladium Electrodes. *Zeitschrift für Physikalische Chemie*; 1977. p. 33.

63.   Hammer B, Norskov JK. Why gold is the noblest of all the metals. *Nature* 1995, **376:** 238.

64.   Nilsson A, Pettersson LGM, Hammer B, Bligaard T, Christensen CH, Nørskov JK. The electronic structure effect in heterogeneous catalysis. *Catalysis Letters* 2005, **100**(3)**:** 111-114.

65. Gorzkowski MT, Lewera A. Probing the Limits of d-Band Center Theory: Electronic and Electrocatalytic Properties of Pd-Shell–Pt-Core Nanoparticles. *The Journal of Physical Chemistry C* 2015, **119**(32)**:** 18389-18395.

66. Hakamada M, Nakano H, Furukawa T, Takahashi M, Mabuchi M. Hydrogen Storage Properties of Nanoporous Palladium Fabricated by Dealloying. *The Journal of Physical Chemistry C* 2010, **114**(2)**:** 868-873.

67. Zhou H-B, Jin S, Zhang Y, Lu G-H, Liu F. Anisotropic Strain Enhanced Hydrogen Solubility in bcc Metals: The Independence on the Sign of Strain. *Physical Review Letters* 2012, **109**(13)**:** 135502.

68. Yang Y, Kumar KS. Elastic strain effects on the catalytic response of Pt and Pd thin films deposited on Pd–Zr metallic glass. *Journal of Materials Research* 2017, **32**(14)**:** 2690-2699.

69. Wagner S, Pundt A. Quasi-thermodynamic model on hydride formation in palladium–hydrogen thin films: Impact of elastic and microstructural constraints. *International Journal of Hydrogen Energy* 2016, **41**(4)**:** 2727-2738.

70. Baldi A, Narayan TC, Koh AL, Dionne JA. In situ detection of hydrogen-induced phase transitions in individual palladium nanocrystals. *Nature Materials* 2014, **13:** 1143.

71. Ulvestad A, Welland MJ, Collins SSE, Harder R, Maxey E, Wingert J*, et al.* Avalanching strain dynamics during the hydriding phase transformation in individual palladium nanoparticles. *Nature Communications* 2015, **6:** 10092.

72. Akiba H, Kofu M, Kobayashi H, Kitagawa H, Ikeda K, Otomo T*, et al.* Nanometer-Size Effect on Hydrogen Sites in Palladium Lattice. *Journal of the American Chemical Society* 2016, **138**(32)**:** 10238-10243.

Experimental Methods

Synthesis of $PdCrO_2$, $PdCoO_2$ and $PtCoO_2$

The synthesis of $PdCrO_2$ is based on a method described in literature. [1] First, a $LiCrO_2$-precursor was prepared from Li_2CO_3 (Acros 99+%) and Cr_2O_3 (Fisher Scientific, extra pure) at 1100 °C. The obtained homogeneous grey powder (2 eq.) was subsequently ground together with metallic Pd (1 eq., Alfa Aesar 99.95%) powder and $PdCl_2$ (1 eq., Alfa Aesar 99.9%). Then, the mixture was heated for 24 hours at 800 °C under argon atmosphere. For removal of the LiCl side phase, the powder was washed twice with H_2O and once with ethanol and dried at 60 °C.

The synthesis of micrometer sized $PdCoO_2$, which was used for the electrochemical measurements in the main text, is based on a literature procedure. [2] In brief, well mixed stoichiometric powder of $PdCl_2$ (1 eq., Alfa Aesar 99.9%) and CoO (2 eq., Alfa Aesar 99.995%) were heated to 1000°C in an evacuated quartz ampoule to obtain $PdCoO_2$. $CoCl_2$ was removed by dissolving in water or in hot ethanol.
The obtained $PdCoO_2$ crystals were subsequently used as seed crystals to increase the size in a second or third step.

The synthesis of up to millimeter sized $PdCoO_2$ is based on a modified literature procedure. [3] A mixture of 194 mg $PdCl_2$ (1 eq., Alfa Aesar) and 164 mg CoO (2.2 eq., Alfa Aesar) were ground, pelletized and reacted in a corundum crucible in an evacuated quartz ampoule. The reactants were heated to 700 °C with 3 °C/min, held at T_{max} for 40 h and cooled with 3 °C/min to room temperature. 10 % excess CoO were necessary to balance the losses due to a reaction with the crucible wall to the purple spinel $CoAl_2O_4$. After washing the product with ethanol to remove $CoCl_2$, the reaction yielded metallic crystalline platelets.

For the growth of larger, flat crystals of up to 1 mm, some seed crystals were added to the mixture. The addition of 10-20 mg $TeCl_4$ somewhat inhibited growth along the plane, yielding higher, bulkier crystals with a reduced aspect ratio.

$PtCoO_2$ crystals were synthesized following a similar route. [4] Well mixed stoichiometric powder of $PtCl_2$ (1 eq., Alfa Aesar 99.9%) and CoO (2 eq., Alfa Aesar 99.995%) were heated up to 700°C or 800°C in a evacuated quartz tube to obtain small $PtCoO_2$ crystals. The by-product $CoCl_2$ can be removed by leaching with water or hot ethanol. Unlike in the case of $PdCoO_2$, using seed crystals did not lead to millimeter sized crystals.

Sample and electrode preparation

Electrochemical measurements were performed in 1M H_2SO_4 (pH=0) using a Ag/AgCl reference electrode (RE) with saturated KCl (+0.197V vs. NHE) and a Pt wire or large area Pt plate (>10cm²) as counter electrode (CE). The delafossite working electrodes (WE) were prepared in two different ways. For $PdCoO_2$ only, large single crystals were glued with Ag paste to a fluorine doped tin oxide (FTO) substrate which was contacted to a Cu cable. The contacts were sealed by Scotch-Weld DP410 epoxy. Remnants of the Ag paste around the crystals were covered by nail polish, which was tested to be inert beforehand. In all other cases, the microcrystals were too small to be connected directly and thus measured on carbon paste electrodes. For this purpose, 1.5(1) mg of the respective material was deposited on the surface of the electrode area and pressed gently by carbon paper to ensure a stable adhesion. The carbon paste electrodes consist of a Teflon block with a 0.2cm² area filled by carbon paste (each 2.5 g graphite was mixed with 0.9 ml paraffin oil) that form a conductive and flexible but inactive substrate for electrochemical investigations. The mass loading was determined by a Quartz crystal microbalance.

Electrochemical measurements

The electrocatalytic measurements were performed in a home-made, closed glass reactor or beaker. The electrolyte was purged with > 99% pure H_2 for at least 20 min prior to every measurement through a porous glass frit to remove dissolved oxygen and to saturate the solution with H_2 in order to provide a well-defined redox-potential that is consistent with long term working conditions. The RHE potential for the respective electrolytes was measured under the same conditions using a Pt wire as WE and re-evaluated during the cycling process to avoid fluctuations of the RE in the mV region. For Faradaic efficiency measurements, the sealed reactor was purged with Argon prior to the measurement until no hydrogen or oxygen was found in the head space (see *Product Analysis*). The headspace was then sampled by a gas chromatograph (see *Product Analysis*). The respective results were referenced to measurements where two platinum wires were used as WE and CE. All measurements were recorded using an Ivium CompactStat potentiostat and the IviumSoft software. In order to correct for the series resistance to construct the Tafel plots, impedance measurement were recorded close to RHE (overpotential of 10 mV, current density usually ~1 mA/cm², 10 mV AC amplitude) and the series resistance was extracted by fitting to a Randles circuit in the high frequency region. All values obtained before the respective Tafel measurement cycles were very similar, so the average value of every sample resistance was used. To account for the IR-drop, the overpotential with respect to the calibration point with two Pt wires was corrected by subtracting *I*R* (current times series resistance). The Tafel slope was extracted from the linear region above 1 mA/cm² using the data from both the forward and the backward scan to exclude for possible surface capacitance effects. In all cases from cycle 10 on, the forward and backward scans were overlaid, so that capacitive contributions can be excluded.

The values and errors provided are averages and their respective error originating from different samples which were measured in the same way. At least three measurements were performed for the data shown in the main text, after qualitative tests made beforehand.

Scanning electrochemical microscopy (SECM)

Scanning electrochemical microscopy measurements were performed with a SECM M470 from Biologic, which was controlled by the Biologic M470 software. $PdCoO_2$ microcrystals were washed in concentrated HNO_3 before the measurements to remove any possible Pd rich surface layer that enhances catalytic activity. Subsequently, the sample was glued to an inactive Au coated substrate by Ag paste, which was sealed by nail polish. This way, the sample potential could be controlled by contacting the Au covered substrate. The sample and substrates were places in a Teflon cell equipped with a Ag/AgCl RE and a Pt wire as CE. The electrolyte employed contained 10 mM H_2SO_4 and 20 mM Na_2SO_4 exposed to air. Before the measurements, the feedback electrode was polished to ensure a clean Pt tip and pre-cleaned by applying +0.5V vs. Ag/AgCl until the current stabilized.

Scanning electron microscopy (SEM) and focused ion beam (FIB)

Scanning electron microscopy measurements were performed with a Merlin SEM from Zeiss at an accelerating voltage of 1.5 kV. For TEM lamella preparation and imaging, a Zeiss Crossbeam 1540 EsB FIB was used.

Product analysis

The dissolved and gaseous products of the electrochemical cycling were analyzed by means of inductively coupled plasma optical emission spectroscopy (ICP-OES) to analyze the composition of the liquid phase as well as by gas chromatography (GC) for the reactor head space. The product distribution in the head space of the glass reactors was analyzed by a S+H Trace GC Ultra, which is equipped with a thermal conductivity detector (TCD). The GC was calibrated for Faradaic efficiency measurements with a platinum wire within the same reactor.

TEM Characterization

Scanning transmission electron microscopy (STEM) was performed on Titan Themis microscope operated at 300 kV acceleration voltage. The aberration correction on the probe-forming lenses enables the focus of the electron probe down to ~1 Å size, at 24 mrad convergence semiangle. STEM images were recorded using the high angle annular dark field (HAADF) detector with collection semiangles between 73 and 352 mrad. Energy dispersive X-ray spectroscopy (EDS) spectrum images were recorded using a windowless, four quadrant silicon-drift detector (Super-X) with a solid angle of > 0.7 sr. Multivariate analysis on the EDS spectrum image data was performed to reduce the noise. [5] Then, the elemental concentrations were quantified using the Cliff-Lorimer formula.

To reach the highest precision for the determination of lattice constants in the Pd cap layer, the instrument was calibrated *in-situ*. The interplanar spacing was calibrated according to $PdCoO_2$ (0,0,0,12) and (1,0,-1,-1) interplanar spacings, using the lattice parameters from powder XRD and literature values. Both interplanar spacings yielded comparable results (0.35% relative difference). The following results were analyzed and plotted using the powder XRD calibration shown in Fig. S1.

X-ray Photoelectron Spectroscopy (XPS)

XPS analysis was performed with a Thermo VG Thetaprobe 300 system using monochromatic incident Al K_α radiation (hv = 1486.68 eV; spot size 400 µm; base pressure $<10^{-7}$ Pa; average detection angle of 53° with respect to the sample surface). Spectral decomposition of the as-measured spectra was performed by subtraction of a Shirley-type inelastic background over the concerned binding energy (BE) range for each spectral region, and subsequent, constrained, linear-least-squares fitting with one or more symmetric (mixed Gaussian–Lorentzian) peak components (while taking the same Gaussian–Lorentzian fraction and full width at half-maximum (FWHM) for each component in the fitted spectrum). A flood gun was used to reduce the effect of surface charging. This may lead to small measurement errors up to

1 eV. To eliminate small systematic deviations, the binding energy of adventitious carbon was set to 283.8 eV. All other peaks were referenced to literature taking into account all element lines. [6]

Literature

1.   Shannon RD, Rogers DB, Prewitt CT. Chemistry of Noble Metal Oxides. I. Syntheses and Properties of ABO2 Delafossite Compounds. *Inorg Chem* 1971, **10**(4)**:** 713-&.

2.   Kikugawa N, Goswami P, Kiswandhi A, Choi ES, Graf D, Baumbach RE*, et al.* Interplanar coupling-dependent magnetoresistivity in high-purity layered metals. *Nature Communications* 2016, **7:** 10903.

3.   Takatsu H, Yonezawa S, Mouri S, Nakatsuji S, Tanaka K, Maeno Y. Roles of High-Frequency Optical Phonons in the Physical Properties of the Conductive Delafossite PdCoO2. *Journal of the Physical Society of Japan* 2007, **76**(10)**:** 104701.

4.   Tanaka M, Hasegawa M, Takei H. Crystal growth of PdCoO2, PtCoO2 and their solid-solution with delafossite structure. *Journal of Crystal Growth* 1997, **173**(3)**:** 440-445.

5.   Zhang S, Scheu C. Evaluation of EELS spectrum imaging data by spectral components and factors from multivariate analysis. *Microscopy* 2018, **67**(suppl_1)**:** i133-i141.

6.   Moulder JF, Stickle WF, Sobol PE, Bomen KD. *Handbook of X-ray Photoelectron Spectroscopy*. Perkin-Elmer Corporation: Eden Prairie, Minnesota, USA, 1992.

7.   von Zeppelin F, Haluška M, Hirscher M. Thermal desorption spectroscopy as a quantitative tool to determine the hydrogen content in solids. *Thermochimica Acta* 2003, **404**(1)**:** 251-258.

4.2 New Insights into the Optoelectronic Properties of Photoconductive Pyrene-based COFs

Covalent organic frameworks are a very versatile class of organic based materials. Their large and ordered micro- or mesoporosity ranging up to pore sizes of 4.7 nm and specific surface areas of 4000 m^2/g for 2D and 3D structures. [119, 148] As such, the bulk equivalents essentially the surface, allowing for a rich and efficient surface active chemistry, as highlighted in Section 2.3.3. The chemical variability and hence, tunability of the building blocks in principle allows to rationally design the optoelectronic properties of these often semiconducting materials. As such, they are a promising playground for bottom-up organic based catalyst design, which has been pioneered by the group of Prof. Lotsch. [120] Although many COFs have an optical gap, their description as semiconductors often lacks further evidence and appears questionable since they show rather insulating behavior in the bulk. The extraction of their photophysical and (photo)transport properties by means of photoelectrochemistry is thus very challenging and the profound explanation of their photocatalytic activities remains often limited to calculations or assumptions based on structural abstractions. Although the hydrogen evolution in a family of COFs can be compared and trends can be related to structure-property-relationships like changes in light harvesting ability or thermodynamic driving forces, [121] the conclusions based on HER rates only may actually overlook hidden bottle-neck contributions, since it describes a convolution of many factors. As such, trends may actually be very different if other co-catalytic systems are added to drive the HER. [29]

The product formation rate combines many factors, as described in equation 2.2. To better understand the respective contributions, such as driving forces due to band positions and photocurrents describing the charge transfer properties, photoelectrochemical investigations should not be omitted to experimentally confirm assumptions or theoretical predictions of structure-property-activity relationships.

For this purpose, we studied a family of pyrene-based COFs (A-TE(**X**PY-COFs), which are among the first COFs to be reported active for photocatalytic sacrificial hydrogen evolution. For catalytic reactions using sacrificial electron sources, it often is questionable if the interaction with the sacrificial agent itself is not a rate limiting step, affecting the overall activity stronger than the thermodynamic driving force for electrons after exciton dissociation. Opposite to the azine based N_x-COF family, [121], these pyrene based sys-

tems have a rather electron rich backbone, which can be tuned to stabilize the formation of a radial cation. It thus can be assumed that photo-excited electrons react with protons first, while the stabilized radical cation subsequently reacts with the sacrificial electron donor for these types of COFs. As such, their activity should be much less dependent on the reaction with the donor and the process of pure photocatalytic hydrogen evolution is even better to be compared with PEC, which does not require or use donors.

Some of the COFs in this family, namely the A-TE((**B**,**N**)PY-COFs, can be grown directly on transparent conductive oxides. As such, their photoelectrochemical properties can be accessed more easily, since the low bulk conductivity can be compensated by forming very thin layers, focusing rather on intrinsic optoelectronic properties.

My contribution to this publication lies in the investigation of these photoelectrochemical properties. Since all three COFs in this family have a similar band gap, a comparable light induced charge carrier generation can be assumed. The HER rate seems thus to be related to the charge transfer and surface reaction efficiency. Photocurrent measurements on the A-TE((**B**,**N**)PY-COFs revealed a sub-second photoresponse time, highlighting a fast charge equilibration process under illumination and thus the applicability for opto-electronic devices. The measured photocurrents reflect the trends observed in the HER rate measured on these COFs. As such, it can be deduced that also the charge transfer properties are intrinsically comparable and depend on the surface catalytic process. The efficiency of this process itself depends on two factors – the coupling to the co-catalyst and the intrinsic driving force acting on the catalyst, which depends on the band positions. Since the HER activity of all COFs was studied with photodeposited Pt, a similar charge transfer on the cocatalysts can be assumed. It is thus crucial to determine the band positions of the COFs.

Often, Mott-Schottky-measurements are used to estimate the flat band potentials. These capacitive measurements rely on an accurate description of different capacitive contributions, which is difficult to ensure. As such, the reproducibility and validity of these measurements turned out to be questionable. A more intrinsic approach to estimate the band positions relies on potential dependent photocurrent measurements. The photocurrent is expected to cease if the CB of the semiconductor aligns with the RHE. This technique was now applied to COFs for the first time. Since the OCP itself is not very stable in COFs, we performed CV measurements in hydrogen saturated electrolytes while chopping the light. At a given potential, the photocurrents disappeared and changed their sign, which

can be attributed to a mechanism change from HER to the hydrogen oxidation reaction. The validity of this approach was confirmed by pH-dependent measurements, since the band positions shift with the pH due to Fermi level alignment of the semiconductor and the electrolyte. [42,45]. By these findings, the band positions of the A-TE(**B**,**N**)PY-COFs could be measured experimentally, while validating theoretical calculations and proving their pH dependence.

More details about the work can be found in the following publication by Stegbauer *et al., Adv. Energy Mater.* **2018**, *8*, 1703278. Title: "Tailor-made Photoconductive Pyrene-based Covalent Organic Frameworks for Visible-Light Driven Hydrogen Generation" and in the Supplementary Information in the Appendix, Section A.2.

Tailor-Made Photoconductive Pyrene-Based Covalent Organic Frameworks for Visible-Light Driven Hydrogen Generation

*Linus Stegbauer, Sebastian Zech, Gökcen Savasci, Tanmay Banerjee, Filip Podjaski, Katharina Schwinghammer, Christian Ochsenfeld, and Bettina V. Lotsch**

Covalent organic frameworks (COFs) have emerged as a new class of crystalline porous polymers displaying molecular tunability combined with structural definition. Here, a series of three conjugated, photoactive azine-linked COFs based on pyrene building blocks which differ in the number of nitrogen atoms in the peripheral aromatic units is presented. The structure of the COFs is analyzed by combined experimental and computational physisorption as well as quantum-chemical calculations, which suggest a slipped-stacked arrangement of the 2D layers. Photocurrents of up to 6 µA cm^{-2} with subsecond photoresponse times are measured on thin film samples for the first time. While all COFs are capable of producing hydrogen from water, their efficiency increases significantly with decreasing number of nitrogen atoms. The trending activities are rationalized by photoelectrochemical measurements and quantum-chemical calculations which suggest an increase in the thermodynamic driving force with decreasing nitrogen content to be the origin of the observed differences in hydrogen evolution activities.

1. Introduction

Covalent organic frameworks (COFs) constitute an emerging class of 2D and 3D porous polymers[1] combining molecular

Dr. L. Stegbauer, G. Savasci, Dr. T. Banerjee, F. Podjaski,
Dr. K. Schwinghammer, Prof. C. Ochsenfeld, Prof. B. V. Lotsch
Max Planck Institute for Solid State Research
Heisenbergstr. 1, 70569 Stuttgart, Germany
E-mail: b.lotsch@fkf.mpg.de
Dr. L Stegbauer, S. Zech, G. Savasci, K. Schwinghammer,
Prof. C. Ochsenfeld, Prof. B. V. Lotsch
Department of Chemistry
University of Munich (LMU)
Butenandtstr. 5-13, 81377 München, Germany
Dr. L Stegbauer, Prof. B. V. Lotsch
Nanosystems Initiative Munich (NIM) & Center for Nanoscience
Schellingstr. 4, 80799 München, Germany
F. Podjaski
Ecole Polytechnique Féderale de Lausanne
Station 12, CH-1015 Lausanne, Switzerland

tunability, supramolecular functionality and structural definition. COFs are formed by reversible condensation reactions under thermodynamic control, giving rise to precisely tunable framework topologies with adjustable pore dimensions.[2] The semiconducting properties inherent to COFs, comparable to carbon nitrides[3] and metal-organic frameworks (MOFs),[4] make them interesting candidates for applications in optoelectronics where ordered charge percolation pathways are key,[5,6] including photovoltaics,[7,8] photocurrent generation,[9] and visible-light driven photocatalysis.[10–12] COFs based on pyrene building units show local photoconductivity,[13] and their fluorescent backbone has been used for chemosensing by means of analyte selective fluorescence quenching.[14] In addition, pyrene's extended π-system offers a unique basis for visible-light absorption as demonstrated by pyrene-derived dyes such as pyranine.[15] Here, we present three completely planar pyrene-COFs extended by alkynes for the first time which are modulated by peripheral heteroaromatic building units. As suggested in our previous work, a planar COF backbone, resulting in an extended π-system, favorable interlayer interactions through π–π-stacking and smaller bandgaps, may play a key role in enhancing photocatalytic activity.[10] As a result, we propose to extend both the planarity and the π-system[11] by integrating alkyne moieties into the building blocks.

2. Results and Discussion

Three tetra-alkyne 1,3,6,8-tetraethinylpyrene building blocks – 1,3,6,8-tetrakis(4-ethynylbenzaldehyde)-pyrene (TE**B**PY), 1,3,6,8-tetrakis(6-ethynylnicotinaldehyde)-pyrene (TE**N**PY), and 1,3,6,8-tetrakis(2-ethynylpyrimidin-5-carbaldehyde)pyrene (TE**P**PY) (see the Supporting Information for experimental details and spectra) were designed in order to show an increasing nitrogen content in their peripheral aromatic units, entailing an increase in their electron withdrawing character. Each TEXPY monomer (X = B(enzaldehyde), N(icotinaldehyde), P(yrimidine-5-carbaldehyde) was reacted with hydrazine hydrate (120 °C, 3 d, see the Supporting Information for details) in an acetic acid catalyzed polycondensation in different aromatic solvent mixtures to yield an azine (A) connected COF as red powder (see Figure S1,
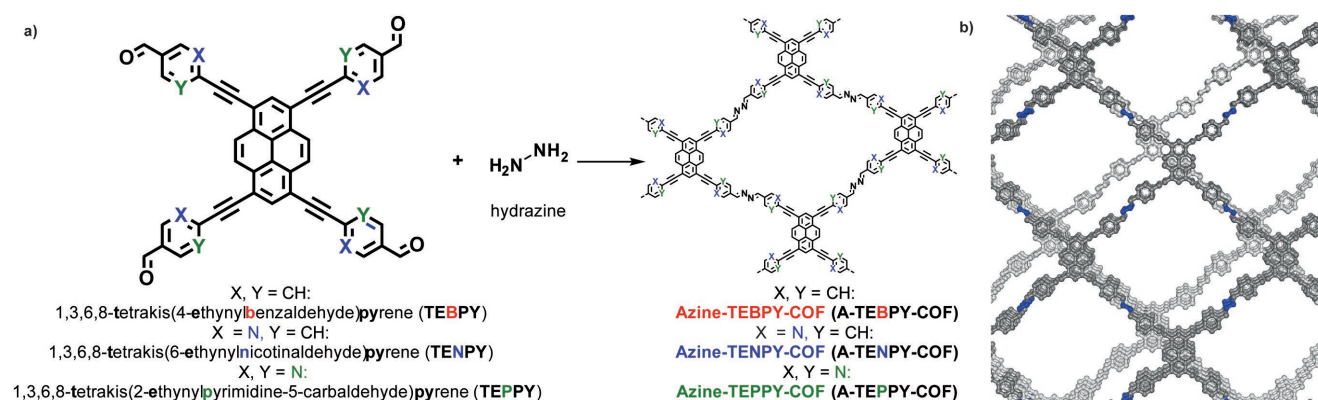
Figure 1. a) Synthesis of azine-linked COFs by the acetic acid catalyzed condensation reaction between the pyrene-based aldehyde linkers and hydrazine. b) Ball-and-stick model of the shifted AA' arrangement of A-TE**B**PY-COF. All COFs in this series adopt similar stackings.

Supporting Information): A-TE**B**PY-COF, A-TE**N**PY-COF, and A-TE**P**PY-COF (**Figure 1**, see the Supporting Information for details and solvent screening).

Compared to the corresponding aldehydes, the A-TEXPY-COFs lack the characteristic aldehyde C—H and C=O vibrations (see Figure S7, Supporting Information) in their FT-IR spectra and show the appearance of a C=N[16] band at 1620 cm^{-1} (see Figure S8, Supporting Information). The CC triple bond vibration at 2200 cm^{-1} suggests that the alkyne moiety in A-TEXPY-COFs is preserved (Figure S9, Supporting Information).

The local structures of the A-TEXPY-COFs were further confirmed by ^{13}C cross-polarization magic angle-spinning (CP-MAS) solid-state NMR spectroscopy. The disappearance of the characteristic aldehyde carbonyl ^{13}C resonance located at ≈190 ppm in the precursor aldehydes is observed, along with the appearance of the azine C=N signal at ≈160 ppm (see the Supporting Information for details, see highlighted regions in blue color in Figures S8–S11, and S12 for ^{1}H, Supporting Information), thereby attesting the conversion of the precursors into the respective COFs. Further characterization by scanning and transmission electron miscroscopy (SEM, TEM resp.) shows the platelet like structure of the COF agglomerates (see Figures S48 and S49, Supporting Information). X-ray photoelectron spectroscopy (XPS) is also consistent with the formation of the framework (see Figures S50–S55, Supporting Information).

2.1. Layer Stacking and Pore Size Distribution

Powder X-ray diffraction (PXRD) reveals only moderate crystallinity for A-TE**B**PY and A-TE**N**PY-COF (see Figures S2–S6, Supporting Information) with reflections at $2\theta = 4°$ and $8°$ (see **Figure 2**a). Both a fully eclipsed AA-type stacking (space group $P2/m$, see Figure 2c,d), which is often employed as an idealized structure model for 2D COFs, and a layer offset of 1.6 Å as proposed for other COFs[17,18] would be in agreement with the experimental PXRD (Figure 2a).[17] In contrast, AB stacking can be discarded on account of a significant mismatch in intensities of the PXRD (Figure 2a).[19]

Argon sorption isotherms at 87 K reveal the porous nature of all A-TEXPY-COFs with Brunauer-Emmett-Teller (BET) surface areas of 681 m^2 g^{-1} for A-TE**B**PY-COF, 470 m^2 g^{-1} for

A-TE**N**PY-COF, and 920 m^2 g^{-1} for A-TE**P**PY-COF. Interestingly, all compounds show type I isotherms characteristic of microporous materials (see Figure S14 (Supporting Information), and **Figure 3**a), while idealized AA or shifted (sh) 1.6 Å stacking would give rise to the formation of mesoporous pore windows of 2–2.2 nm in diameter, i.e., in the mesopore range. The observed type I isotherm may thus point to the presence of a larger layer offset or a mixture of different stacking modes, which apparently cannot be distinguished by PXRD, but may be revealed through closer inspection of the sorption isotherms and pore size distributions (PSDs). To this end, we compare two different stacking modes—a layer offset of 1.6 Å (1.6 Å-sh-AA') and a layer offset of 6.5 Å (6.5 Å-sh-AA')—based on their simulated, quenched solid density functional theory (QSDFT)-derived PSDs (Figure 3). The larger layer was exemplarily chosen based on the single-crystal X-ray structure of the related molecular building block LH$_4$[20] (4-[2-[3,6,8-*tris*[2-(4-carboxyphenyl)-ethynyl]-pyren-1-yl]ethynyl]-benzoic acid, containing dimethylformamide (DMF) molecules, which are omitted in Figure 2b for clarity), and used to model the A-TE**B**PY-COF crystal structure by introducing a 6.5 Å shift between adjacent layers which were stacked in a zigzag-type pattern (see Figure 2e,f; and Figures S3 and S4, Supporting Information).[17] Similarly large offsets have been found for other COFs such as the polyimide (PI) COFs previously.[21] Note that similar relative intensity distributions of the eclipsed AA and the offset 1.6 Å and 6.5 Å-sh-AA' stacking modes in the simulated PXRD patterns, along with the line broadening suggest that the different offset models cannot be distinguished experimentally by PXRD (Figure 1a).

The experimental PSDs, evaluated by QSDFT (cylindrical pores, carbon), exhibit a maximum at 1.2 nm for A-TE**B**PY-COF, at 1.3 nm for A-TE**P**PY-COF, and at 1.4 nm for A-TE**N**PY-COF (see Figure 3c; and Figure S14, Supporting Information). High-resolution TEM (HRTEM) micrographs show lattice fringes at 1.7 nm for A-TE**N**PY-COF, in line with the expected pore size (see Figure S49, Supporting Information). Simulations[5,22] were then performed based on the simulated sorption isotherms to extract the theoretical PSD. Here, the calculated PSD of the 6.5 Å-sh-AA' stacked structure shows the best agreement with the experimental isotherm (Figure 3c, regions marked by blue color, see the Supporting Information for details), while the

**ADVANCED
SCIENCE NEWS**

www.advancedsciencenews.com

**ADVANCED
ENERGY
MATERIALS**

www.advenergymat.de
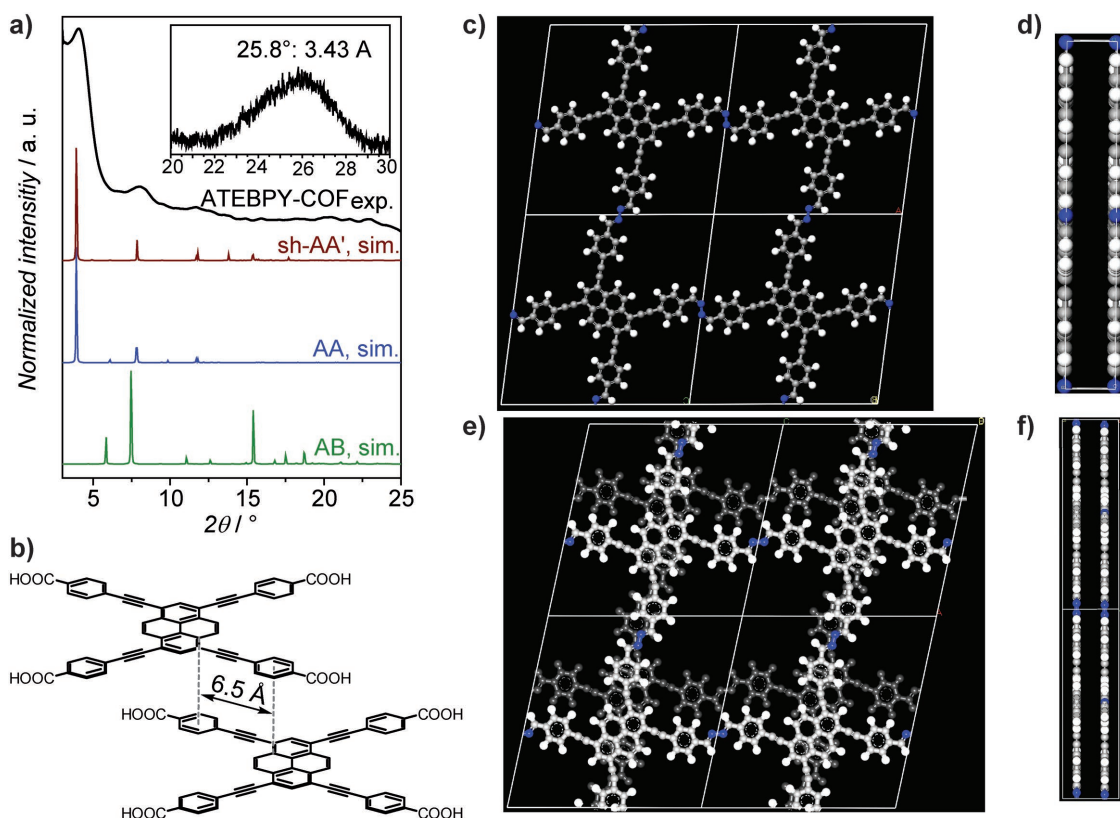
Figure 2. Characterization of A-TE**B**PY-COF by PXRD. a) PXRD suggests a shifted AA' or AA layer stacking. The inset shows the stacking reflection corresponding to 3.43 Å. b) Shifted stacking of pyrene units in LH₄ DMF solvate, extracted from the single-crystal X-ray structure;[20] c,d) AA stacking of A-TE**B**PY-COF (gray: carbon, white: hydrogen, blue: nitrogen) e,f) hypothetical 6.5 Å shifted-AA' stacking of A-TE**B**PY-COF (background layer in dark grey for better visibility) Note: d,f) have not the same scale.

1.6 Å-sh-AA′ stacking mode might account for the mesoporous pore volume at 2 nm (see Figure 3c regions marked by yellow color).

Next, the layer stacking modes were investigated by quantum-chemical calculations by evaluating potential energy curves of A-TE**B**PY-COF hexagon dimers (see Figures S28–S32 and Tables S4 and S5, Supporting Information) on the M06/def2-SVP level of theory.[23] With a calculated layer distance of 3.40 and 3.41 Å, respectively, the resulting potential energy curves for the dimer model of both the 1.6 and 6.5 Å shifted structures are close to the experimentally observed stacking distance of 3.43 Å (see Figure 2a, inset; and Figures S29, S31, and S33, Supporting Information). In contrast, the potential energy curve for the eclipsed AA stacking mode shows a minimum at 3.69 Å, while the AB stacking mode is found to have its minimum at an unrealistically short distance of 3.00 Å (for other shifts see the Supporting Information for details).

In addition, we scanned the layer offset at a fixed stacking distance of 3.42 Å, extracted from the crystal structure of the molecular model compound LH₄ which is in close agreement to the distance observed by PXRD of A-TE**B**PY-COF, starting from the AA stacking mode toward and beyond the layer offset of the 6.5 Å-sh-AA′ conformation. For our dimer model we find a pronounced thermodynamic minimum for the layer offset at 1.6 Å shifted from AA (see Table S5 and Figure S33 for details, Supporting Information), in line with literature.[17]

2.2. Photoluminescence Measurements

Since the above results are inconclusive regarding the type of layer offset, we carried out photoluminesce (PL) measurements to obtain further insights into both structural and optical aspects of the COFs. PL measurements of the three materials reveal a weak, broad, and structureless excimer emission band around 670–700 nm (see Figure S17b, Supporting Information). According to literature reports, COFs with nonplanar tetra(phenyl)pyrene type linkers have a stacking distance of about 3.9 to 4.33 Å.[14,24] In contrast, the all-planar linkers of the A-TE**X**PY-COFs lead to a significantly smaller stacking distance of about 3.43 Å (vide supra), hence enabling formation of excimers (see Figure S17b, Supporting Information). The TE**X**PY linkers in the COF thus not only result in an extended conjugation *in-plane*, but also enable electronic interactions *out-of-plane* in the form of excimers, i.e., between the COF layers, resulting in a highly redshifted emission around 670–700 nm. Note that this is the lowest energy emission ever observed in pyrene-based COFs.[13,14,24,25]

From the photoluminescence results, a 6.5 Å shift between adjacent layers seems unlikely (see Section SH, Supporting Information): While pyrene sandwich excimers could well form by a small conformational rearrangement, i.e., a small horizontal slip, upon photoexcitation in the 1.6 Å shifted-AA′ stacked system,[26] this is unlikely for large layer offsets such as

ADVANCED
SCIENCE NEWS
www.advancedsciencenews.com

ADVANCED
ENERGY
MATERIALS
www.advenergymat.de
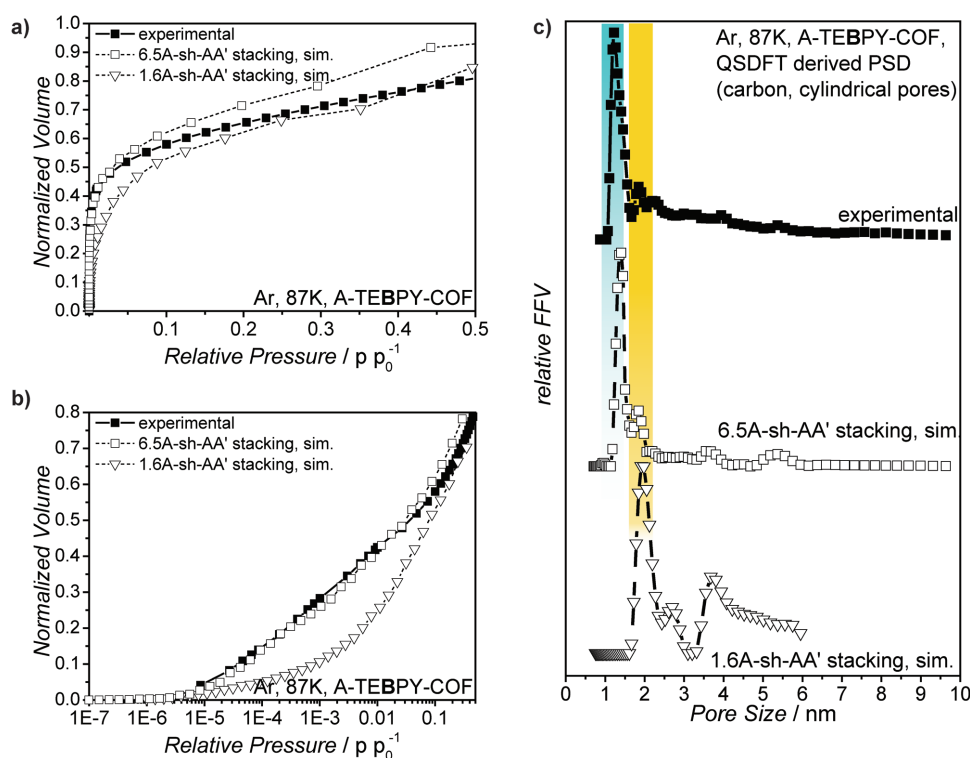
Figure 3. a) Ar isotherms at 87 K of A-TE**B**PY-COF, experimental (filled squares) and theoretical for 6.5Å-sh-AA' (empty square) and 1.6Å-sh-AA'stacking (empty triangle), with normalized volumes; b) logarithmic representation (relative pressure < 0.5 $p\,p_0^{-1}$) of experimental and simulated isotherms revealing microporous behavior of the experimental isotherm. c) QSDFT-derived pore size distributions of experimental and simulated Ar isotherms (carbon, cylindrical pores).

in the 6.5 Å shifted-AA' stacked system. Although in principle, a partially overlapped excimer could also be possible in the 6.5 Å-sh-AA' arrangement of the pyrene chromophores,[27] both the PL measurements and the quantum-chemical calculations point toward smaller layer offsets represented by the 1.6 Å-sh-AA', with admixtures of larger layer offsets as revealed by PSD simulations.

2.3. Optical Properties and Photo(electro)chemistry

The diffuse reflectance UV–vis spectra of the A-TEXPY-COFs exhibit an absorption edge around 600 nm (the spike at 340 nm is due to a change of the light source), with the absorption tail extending well beyond 800 nm (**Figure 4**a). We estimate an optical bandgap of 1.94 eV for A-TE**B**PY-COF, 1.92 eV for A-TE**N**PY-COF, and 1.91 eV for A-TE**P**PY-COF, based on the Tauc plot (see Figure S19, Supporting Information). Thus, the small optical bandgaps allow for the absorption of a significant portion of the solar spectrum.

A-TEXPY-COFs represent an excellent model platform for photocatalysis experiments, since compared to the previously described azine COF series[11] the relative activities of the all-planar A-TEXPY-COFs will be dominated by their composition and electronic properties, rather than by their geometrical structures.

We thus studied light-induced hydrogen evolution by suspending the COF in phosphate buffer at pH 7.0. The mixture was

irradiated with simulated sunlight (AM 1.5 G, 100 mW cm^{-2}) in the presence of in situ photodeposited platinum nanoparticles as cocatalyst for reducing the overpotential of hydrogen evolution, using 10 vol% triethanolamine (TEOA) as sacrificial electron donor (see the Supporting Information for details).[28] Figure 4c shows a plot of the amount of hydrogen produced during a test period of 22 h for all samples (Figure 4b). All A-TEXPY-COFs steadily produce hydrogen under these conditions for at least 24 h. While A-TE**B**PY-COF produces hydrogen at the rate of 98 µmol h^{-1} g^{-1}, A-TE**N**PY-COF with 22 µmol h^{-1} g^{-1} falls short by a factor of 4. A-TE**P**PY-COF with the highest nitrogen content produced only 6 µmol h^{-1} g^{-1} hydrogen (Figure 4c). Analysis after 4 h under photocatalysis conditions revealed that A-TE**B**PY-COF shows a considerable decline in crystallinity (see Figure S20, Supporting Information) but intact local order (see Figure S21 for ^{13}C ssNMR, Supporting Information).

These trends were confirmed by photocurrent density measurements in 1 M H$_2$SO$_4$ as shown in Figure 4c,d. A-TE**N**PY and A-TE**B**PY-COFs were grown directly on fluorine-doped tin oxide (FTO) (see the Supporting Information for details) and illuminated with chopped, simulated sunlight. The current density of the A-TE**B**PY-COF (6 µA cm^{-2}) at reversible hydrogen electrode (RHE) potential is approximately four times higher than the one of A-TE**N**PY-COF (1.5 µA cm^{-2}) without any cocatalyst and sacrificial donor (Figure 4c; see also Figure S24 for data in sodium phosphate buffer, Supporting Information). Chronoamperometry under visible-light irradiation at the RHE

ADVANCED
SCIENCE NEWS
www.advancedsciencenews.com

**ADVANCED
ENERGY
MATERIALS**
www.advenergymat.de
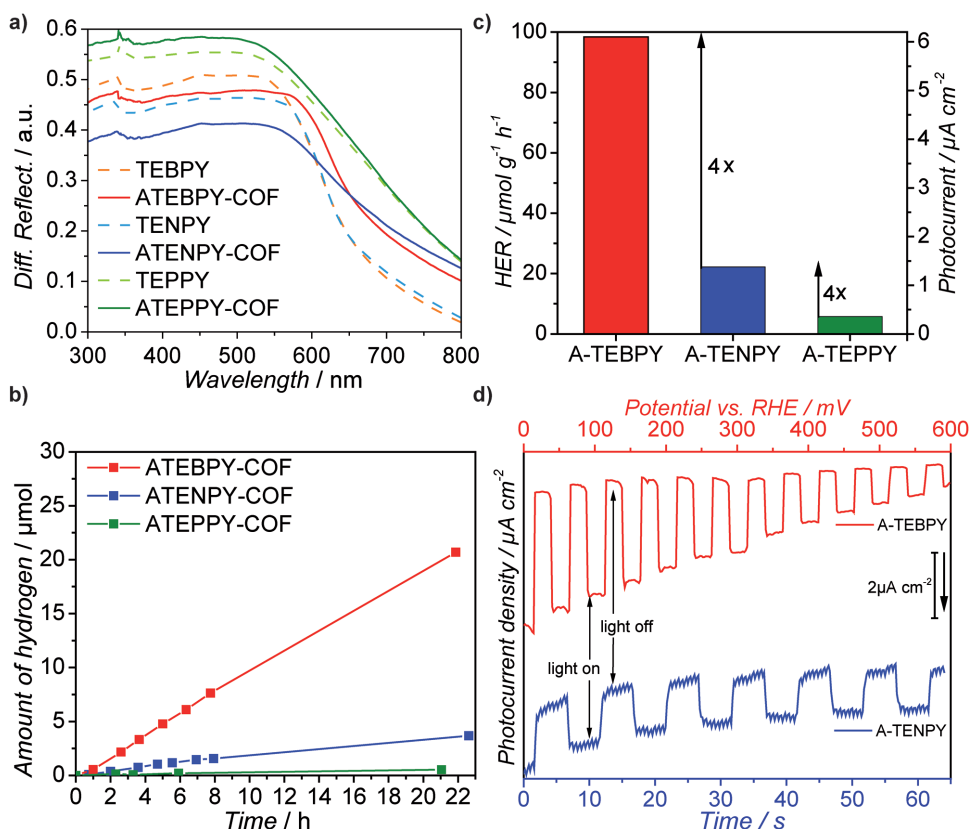
Figure 4. Optical properties of A-TEXPY-COFs, photocatalytic hydrogen evolution and photoelectrochemical characterization: a) UV–vis diffuse reflectance spectra of A-TEXPY-COFs (red, blue, green; solid lines) and their corresponding starting materials (light red, light blue, light green; dotted lines). b) Time course of photocatalytic hydrogen evolution from a 10 vol% aqueous TEOA suspension by the Pt-modified A-TEXPY-COFs under AM 1.5 G illumination. c) Comparison of the hydrogen evolution rates and photocurrents of A-TEXPY-COFs exhibiting a fourfold enhancement with decreasing nitrogen content in the peripheral aromatic unit of the system. Photocurrent densities were measured for A-TE(**B,N**)PY COFs@FTO under AM 1.5 G illumination at RHE potential in 1 M H_2SO_4. The photocurrents are attributed to photoelectrochemical hydrogen evolution. d) Cyclic voltammetry (top, red) and chronoamperometry (bottom, blue) measurements of the COF electrodes under chopped light. Both COFs show very fast photoresponses (<1 s).

potential (A-TE**N**PY, Figure 4d bottom) shows the subsecond photoresponse time.

The photoresponse occurs and saturates almost instantaneously (<1 s), while the photocurrents remain stable over the measurement time, being only limited by material detachment. This is demonstrated for COFs in aqueous solution for the first time. The photoresponse at bandgap illumination as well as the stability of the photocurrents support the notion of COFs as organic semiconductors. We note that our photocurrent is at least an order of magnitude higher than other so far measured photocurrents of COFs in a nonaqueous setting.[7,9,29] Cyclic voltammetry under visible-light irradiation (A-TE**B**PY-COF, Figure 4d top) shows the decrease of the photocurrents when applying a positive potential versus RHE. The anodic photoresponse occurs reproducibly over a wide range (up to 600 mV for A-TE**N**PY and 800 mV for A-TE**B**PY, see Figure S23, Supporting Information) of anodic potentials versus RHE.

The decreasing photocurrent arises from a decreasing thermodynamic driving force as the valence band (VB) and conduction band (CB) levels are shifted downward with applied positive bias. This dependence was used to estimate the position of the CB in the excited state (CB_{ex}) versus RHE in 1 M phosphate buffer

and 1 M H_2SO_4 (see Figures S22 and S23, Supporting Information). A disappearing cathodic photocurrent indicates the alignment of the CB_{ex} of the COF with RHE. This is directly followed by an appearing anodic photocurrent probably arising from the oxidation of adsorbed hydrogen. Within different electrolytes this observation follows a Nernstian dependence indicating the validity of this technique (see Figures S25 and S26, Supporting Information):[30] With a change of the electrolyte phosphate buffer (pH = 7) to H_2SO_4 (pH = 0) all energy levels drop significantly, following the chemical potential of the electrolyte (pH). The energetic positions of the conduction band in the excited state measured by this technique are shown in **Figure 5**a. VB levels are extrapolated by subtraction of the optical bandgap of the corresponding system.

VB and CB_{ex} energies derived by quantum-chemical calculations on PBE0-D3/def2-TZVP (see the Supporting Information for details) level of theory show a reasonable match with the photoelectrochemically derived energy levels (see Figure 5a orange lines). The brightest vertical excitations (see Tables S6–S9, and also Figures S39–S44, Supporting Information) show strong participation of the highest occupied molecular orbital (HOMO)→lowest unoccupied molecular orbital (LUMO)

**ADVANCED
SCIENCE NEWS**
www.advancedsciencenews.com

**ADVANCED
ENERGY
MATERIALS**
www.advenergymat.de
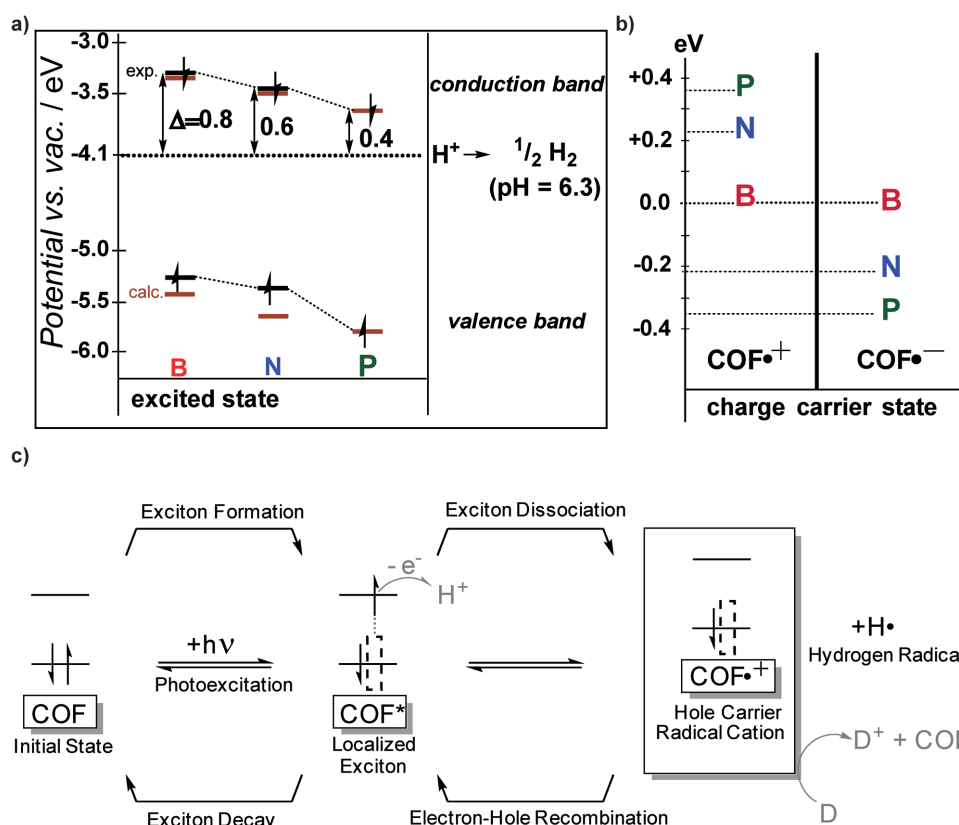
Figure 5. VB and CB alignments of the A-TEXPY-COF systems: a) Energy scheme visualizing the expected occupation and energy levels of valence and conduction band levels in the excited state of A-TE**B**PY, A-TE**N**PY and A-TE**P**PY-COF; black lines indicate measured data obtained by photoelectrochemistry, orange lines calculated data (PBE0-D3/def2-TZVP//PBE0-D3/def2-SVP). b) Comparison of vertical radical cation and radical anion stabilization energies relative to the A-TE**B**PY COF system.; c) Proposed photoinduced reaction leading to the hydrogen radical and radical cation which is subsequently quenched by the sacrificial donor (D).

transition ($\approx$60% for all three COFs) and are very close to the experimental values ($\approx$2.10, 2.10, and 2.11 eV compared to exp. 1.94, 1.92, and 1.91 eV for B, N, and P, respectively).

Therefore, we assign the VB$\rightarrow$VB$_{ex}$,CB$_{ex}$ (HOMO$\rightarrow$ HOMO$_{ex}$,LUMO$_{ex}$) transition as crucial for photocatalysis. Electronic difference densities of this transition indicate no significant variations between the three A-TEXPY systems (see the Supporting Information). We therefore conclude that the absolute levels of the CB$_{ex}$ are the main criteria to distinguish between the hydrogen evolution activity of those three COFs, which is in agreement with the electrochemical measurements: Excited electrons in the CB of A-TE**B**PY-COF have an increased thermodynamic driving force[31] for hydrogen evolution compared to A-TE**N**PY-COF and A-TE**P**PY-COF (0.8 eV against 0.5 and 0.4 eV, respectively, see Figure 5a).[32] The computed energy levels of the CB were derived by addition of the lowest, and also brightest, vertical excitation energy to the HOMO. They match very well with the experimental ones (see Figure 5a, orange and black lines). Note that kinetic factors may play a crucial role in photocatalysis as well, but are much harder to describe by both experiment and theory. To investigate possible intermediate species during photocatalysis, we have devised a general photoexcitation scheme for the three COFs (see Figures S46 and S47, Supporting Information):[11,31] After

excitation the exciton can either be quenched oxidatively or reductively, i.e., it can follow a radical cation or a radical anion pathway. Quantum-chemical calculations clearly show that for A-TE**B**PY-COF the proposed radical cation species is favored by 0.2 eV versus A-TE**N**PY-COF and 0.4 eV versus A-TE**P**PY-COF, respectively (see Figure 5b left side; and Tables S10 and S11 and Figure S45, Supporting Information). The relative stability of the radical cation follows the same trend as the hydrogen evolution efficiencies—the less nitrogen in the COF, the better stabilized is the radical cation. Subsequently, this cation would be quenched by the sacrificial donor by electron donation, which closes the catalytic cycle. It is therefore conceivable that due to the increasingly electron-rich nature of the A-TEXPY-COFs along the series X = P $\rightarrow$ N $\rightarrow$ B, a radical cation pathway may operate in the photocatalytic hydrogen evolution (Figure 5c), in contrast to the N$_x$-COF series, which likely involves the formation of a radical anion.[11]

Taken together, the planarity of the A-TEXPY-COFs and the extended in-plane conjugation, combined with the excimer formation in the axial direction as confirmed by the PL measurements sets the stage for the observed hydrogen evolution activity of the A-TEXPY-COF series. Trends in the hydrogen evolution reaction (HER) can be rationalized by gradual changes in the thermodynamic driving force for HER and

are consistent with a radical cation pathway, which however requires additional experimental confirmation in future studies.

3. Conclusion

In conclusion, three all-planar and conjugated azine-linked COFs were successfully synthesized by condensation of the three novel aldehyde linkers TE**B**PY, TE**N**PY, and TE**P**PY with hydrazine. A comprehensive study based on PXRD, theoretical calculations, simulations of the pore size distribution, and photoluminescence measurements suggests the presence of stacking polytypes characterized by the prevalence of small layer offsets (<2 Å) complemented with additional larger layer offsets giving rise to microporosity. Photocatalysis experiments show significant hydrogen evolution rates for these rather electron rich systems where A-TE**B**PY-COF with the lowest nitrogen content and, hence, most developed donor properties, shows the highest hydrogen evolution rate. The observed trend in the photocatalytic activities is in line with an increasing thermodynamic driving force for hydrogen reduction with decreasing nitrogen content, as suggested by photocurrent measurements and quantum-chemical calculations. Subsecond photoresponse times of the COFs grown directly on FTO open up new perspectives for the potential use of these materials in optoelectronic devices. This is supported by quantum-chemical calculations indicate that the stability of the radical cation increases with decreasing nitrogen content, suggestive of an oxidative quenching mechanism. The present results further suppose that switching from p-type[33] to n-type character of the COFs may be feasible by rational design of their molecular building blocks.

Supporting Information

Supporting Information is available from the Wiley Online Library or from the author.

Conflict of Interest

The authors declare no conflict of interest.

[1] a) G. Lin, H. Ding, R. Chen, Z. Peng, B. Wang, C. Wang, *J. Am. Chem. Soc.* **2017**, *139*, 8705; b) G. Lin, H. Ding, D. Yuan, B. Wang, C. Wang, *J. Am. Chem. Soc.* **2016**, *138*, 3302.

[2] A. P. Côté, A. I. Benin, N. W. Ockwig, M. O'Keeffe, A. J. Matzger, O. M. Yaghi, *Science* **2005**, *310*, 1166.

[3] a) J. Fu, J. Yu, C. Jiang, B. Cheng, *Adv. Energy Mater.* **2018**, *8*, 1701503; b) R. Shi, Z. Li, H. Yu, L. Shang, C. Zhou, G. I. N. Waterhouse, L.-Z. Wu, T. Zhang, *ChemSusChem* **2017**, *10*, 4650; c) H. Yu, R. Shi, Y. Zhao, T. Bian, Y. Zhao, C. Zhou, G. I. N. Waterhouse, L.-Z. Wu, C.-H. Tung, T. Zhang, *Adv. Mater.* **2017**, *29*, 1605148; d) H. Zhao, X. Ding, B. Zhang, Y. Li, C. Wang, *Sol. Photocatal. Energy Convers.* **2017**, *62*, 602.

[4] a) T. Song, L. Zhang, P. Zhang, J. Zeng, T. Wang, A. Ali, H. Zeng, *J. Mater. Chem. A* **2017**, *5*, 6013; b) T. Song, P. Zhang, J. Zeng, T. Wang, A. Ali, H. Zeng, *Int. J. Hydrogen Energy* **2017**, *42*, 26605; c) H. Liu, Y. Zhao, Z. Zhang, N. Nijem, Y. J. Chabal, X. Peng, H. Zeng, J. Li, *Chem. – Asian J.* **2013**, *8*, 778; d) H. Liu, Y. Zhao, Z. Zhang, N. Nijem, Y. J. Chabal, H. Zeng, J. Li, *Adv. Funct. Mater.* **2011**, *21*, 4754.

[5] X. Feng, L. Chen, Y. Honsho, O. Saengsawang, L. Liu, L. Wang, A. Saeki, S. Irle, S. Seki, Y. Dong, D. Jiang, *Adv. Mater.* **2012**, *24*, 3026.

[6] S. Wan, F. Gándara, A. Asano, H. Furukawa, A. Saeki, S. K. Dey, L. Liao, M. W. Ambrogio, Y. Y. Botros, X. Duan, S. Seki, J. F. Stoddart, O. M. Yaghi, *Chem. Mater.* **2011**, *23*, 4094.

[7] M. Dogru, M. Handloser, F. Auras, T. Kunz, D. Medina, A. Hartschuh, P. Knochel, T. Bein, *Angew. Chem., Int. Ed.* **2013**, *52*, 2920.

[8] J. Guo, Y. Xu, S. Jin, L. Chen, T. Kaji, Y. Honsho, M. A. Addicoat, J. Kim, A. Saeki, H. Ihee, S. Seki, S. Irle, M. Hiramoto, J. Gao, D. Jiang, *Nat. Commun.* **2013**, *4*, 2736.

[9] S. Wan, J. Guo, J. Kim, H. Ihee, D. Jiang, *Angew. Chem., Int. Ed.* **2009**, *48*, 5439.

[10] L. Stegbauer, K. Schwinghammer, B. V. Lotsch, *Chem. Sci.* **2014**, *5*, 2789.

[11] V. S. Vyas, F. Haase, L. Stegbauer, G. Savasci, F. Podjaski, C. Ochsenfeld, B. V. Lotsch, *Nat. Commun.* **2015**, *6*, 8508.

[12] J. Thote, H. B. Aiyappa, A. Deshpande, D. Díaz Díaz, S. Kurungot, R. Banerjee, *Chem. – Eur. J.* **2014**, *20*, 15961.

[13] S. Wan, J. Guo, J. Kim, H. Ihee, D. Jiang, *Angew. Chem., Int. Ed.* **2008**, *47*, 8826.

[14] S. Dalapati, S. Jin, J. Gao, Y. Xu, A. Nagai, D. Jiang, *J. Am. Chem. Soc.* **2013**, *135*, 17310.

[15] O. F. Mohammed, J. Dreyer, B.-Z. Magnes, E. Pines, E. T. J. Nibbering, *ChemPhysChem* **2005**, *6*, 625.

[16] L. D. Frederickson, *Anal. Chem.* **1964**, *36*, 1349.

[17] B. T. Koo, W. R. Dichtel, P. Clancy, *J. Mater. Chem.* **2012**, *22*, 17460.

[18] a) X. Chen, M. Addicoat, S. Irle, A. Nagai, D. Jiang, *J. Am. Chem. Soc.* **2012**, *135*, 546; b) B. T. Koo, P. G. Berard, P. Clancy, *J. Chem. Theory Comput.* **2015**, *11*, 1172; c) J. Gao, D. Jiang, *Chem. Commun.* **2016**, *52*, 1498; d) F. Haase, K. Gottschling, L. Stegbauer, L. S. Germann, R. Gutzler, V. Duppel, V. S. Vyas, K. Kern, R. E. Dinnebier, B. V. Lotsch, *Mater. Chem. Front.* **2017**, *1*, 1354;

e) A. Sharma, A. Malani, N. V. Medhekar, R. Babarao, *CrystEngComm* **2017**, *19*, 6950.

[19] B. Lukose, A. Kuc, T. Heine, *Chem. – Eur. J.* **2011**, *17*, 2388.

[20] O. V. Gutov, W. Bury, D. A. Gomez-Gualdron, V. Krungleviciute, D. Fairen-Jimenez, J. E. Mondloch, A. A. Sarjeant, S. S. Al-Juaid, R. Q. Snurr, J. T. Hupp, T. Yildirim, O. K. Farha, *Chem. – Eur. J.* **2014**, *20*, 12389.

[21] Q. Fang, Z. Zhuang, S. Gu, R. B. Kaspar, J. Zheng, J. Wang, S. Qiu, Y. Yan, *Nat. Commun.* **2014**, *5*, 4503.

[22] T. C. Wang, W. Bury, D. A. Gómez-Gualdrón, N. A. Vermeulen, J. E. Mondloch, P. Deria, K. Zhang, P. Z. Moghadam, A. A. Sarjeant, R. Q. Snurr, J. F. Stoddart, J. T. Hupp, O. K. Farha, *J. Am. Chem. Soc.* **2015**, *137*, 3585.

[23] a) Y. Zhao, D. G. Truhlar, *Theor. Chem. Acc.* **2008**, *120*, 215; b) F. Weigend, R. Ahlrichs, *Phys. Chem. Chem. Phys.* **2005**, *7*, 3297.

[24] X. Chen, N. Huang, J. Gao, H. Xu, F. Xu, D. Jiang, *Chem. Commun.* **2014**, *50*, 6161.

[25] a) W. Leng, Y. Peng, J. Zhang, H. Lu, X. Feng, R. Ge, B. Dong, B. Wang, X. Hu, Y. Gao, *Chem. Eur. J.* **2016**, *22*, 9087; b) J. W. Crowe, L. A. Baldwin, P. L. McGrier, *J. Am. Chem. Soc.* **2016**, *138*, 10120.

[26] A. T. Haedler, H. Misslitz, C. Buehlmeyer, R. Q. Albuquerque, A. Köhler, H.-W. Schmidt, *ChemPhysChem* **2013**, *14*, 1818.

[27] a) F. M. Winnik, N. Tamai, J. Yonezawa, Y. Nishimura, I. Yamazaki, *J. Phys. Chem.* **1992**, *96*, 1967; b) Y. Tsujii, T. Itoh, T. Fukuda, T. Miyamoto, S. Ito, M. Yamamoto, *Langmuir* **1992**, *8*, 936; c) T. Wang, N. Zhang, K. Zhang, J. Dai, W. Bai, R. Bai, *Chem. Commun.* **2016**, *52*, 9679.

[28] a) D. J. Martin, K. Qiu, S. A. Shevlin, A. D. Handoko, X. Chen, Z. Guo, J. Tang, *Angew. Chem., Int. Ed.* **2014**, *53*, 9240; b) S. Yang, Y. Gong, J. Zhang, L. Zhan, L. Ma, Z. Fang, R. Vajtai, X. Wang, P. M. Ajayan, *Adv. Mater.* **2013**, *25*, 2452.

[29] M. Calik, F. Auras, L. M. Salonen, K. Bader, I. Grill, M. Handloser, D. D. Medina, M. Dogru, F. Löbermann, D. Trauner, A. Hartschuh, T. Bein, *J. Am. Chem. Soc.* **2014**, *136*, 17802.

[30] Z. Chen, H. N. Dinh, E. Miller, *Photoelectrochemical Water Splitting: Standards, Experimental Methods, and Protocols*, Springer, New York **2013**.

[31] P. Guiglion, E. Berardo, C. Butchosa, M. C. C. Wobbe, M. A. Zwijnenburg, *J. Phys.: Condens. Matter* **2016**, *28*, 74001.

[32] a) A. Kudo, Y. Miseki, *Chem. Soc. Rev.* **2009**, *38*, 253; b) H. Kisch, *Angew. Chem., Int. Ed.* **2013**, *52*, 812.

[33] T. M. Figueira-Duarte, K. Müllen, *Chem. Rev.* **2011**, *111*, 7260.

4.3 Direct Solar Energy Storage for New Aqueous Solar Batteries

Apart from solar or other regeneratively produced fuels, the importance of batteries remains unquestioned for the decentralized storage and supply of electrical energy. Nevertheless, battery manufacturing and large scale electrical energy storage remain important issues due to high system costs, the limited abundance of Co and Li used for electrode materials, and due to the flammability and volatility of Li battery electrolytes. Nowadays, major research efforts are being put into the development of integrated solar batteries of photocapacitors. In this setting, however, a major cost factor and technical inconvenience arises from different components being responsible for light harvesting and electrochemical energy storage.

Back in 1976, Hodes *et. al.* proposed photoabsorbers to be used simultaneously as charge generation and storage moieties. [71] Helmut Tributsch and coworkers subsequently described this concept based on photo-intercalation in p-type inorganic semiconductors. [35] Nevertheless, this job-sharing device architecture appeared less efficient than separated charge storage, partially due to structural and functional changes induced by the incorporation of alkali metal ions into the photoabsorber. [72] Consequently, this approach ceased to be investigated in the following decades, possibly also by a missing global awareness about global pollution and the coming developments in solar energy generation on a large scale. Nowadays, the fluctuations in renewable energy supply regularly overcome local power consumption, urging society for new technologies. As such, reports of inorganic solar battery materials with a dual functionality appeared very recently, in parallel to our work. [73–76]

In 2017, our group has shown that the storage of solar energy in NCN-PHI is possible, overcoming the solar day-and night cycle. [30] The HER, which is most often studied on CN_x for immediate photocatalytic reactions, could be delayed and triggered by the addition of a co-catalyst, akin to natural photosynthesis, where energy is stored in NADPH and subsequently used to generate higher value organic materials from CO_2 in the dark. After having shown that a radical anion state on this material actually can also be triggered electrically, investigations into its applicability for direct solar batteries were started. In the work presented herein, we could show for the first time that the NCN-PHI can be used to extract also electrical energy after illumination, even after a significant delay time.

This work therefore opens up new perspective for the use of CN_x and related systems as both light absorbers and charge storage materials for the design of earth-abundant single-component solar battery systems.

After having optimized the deposition on a transparent conductive oxide, the discharge behavior was studied after illumination in the presence of a donor, which simulates a redox shuttle for a full battery. It was found that a trade-off between substrate-induced discharge and kinetic barriers has to be considered. While increasing the illumination time, a gradual increase in potential and extracted charge could be measured. This evidenced a non-linearly increasing density of states in the conduction band of the material. To further study the charge storage process itself, CVs were recorded in different aqueous electrolytes and within different potential windows. A linear relationship between scanrate and charge storage was observed, highlighting a pseudocapative mechanism (i.e., rather than a pure double layer capacitance). Variations of the electrolyte cation enabling the charge stabilization effect have proven that its size has to fit the material's structural pores. By electrical charge and discharge curves, the possibility of external purely electrical energy storage in this battery anode material was proven in parallel. Other attractive features of this system, such as a light induced increase in conductivity, were shown by impedance measurements and DC measurements on NCN-PHI sandwiched between two electrodes, i.e. in an ion-blocking configuration. These findings significantly affect the direct solar battery anode kinetics, while the presence of oxygen appears to discharge the material by inducing parasitic reactions, primarily electron transfer to O_2 to form the $O_2^{-\cdot}$ radical.

These findings are explained in more depth in the following publication by Podjaski *et al.*, *Adv. Mat.* **2018**, *30*, 1705477. Title: "Toward an Aqueous Solar Battery: Direct Electrochemical Storage of Solar Energy in Carbon Nitrides" (©Wiley-VCH, reprinted with the permission of the journal) and in the Supplementary Information in the Appendix, Section A.3.

Toward an Aqueous Solar Battery: Direct Electrochemical Storage of Solar Energy in Carbon Nitrides

Filip Podjaski, Julia Kröger, and Bettina. V. Lotsch*

Graphitic carbon nitrides have emerged as an earth-abundant family of polymeric materials for solar energy conversion. Herein, a 2D cyanamide-functionalized polyheptazine imide (NCN-PHI) is reported, which for the first time enables the synergistic coupling of two key functions of energy conversion within one single material: light harvesting and electrical energy storage. Photo-electrochemical measurements in aqueous electrolytes reveal the underlying mechanism of this "solar battery" material: the charge storage in NCN-PHI is based on the photoreduction of the carbon nitride backbone and charge compensation is realized by adsorption of alkali metal ions within the NCN-PHI layers and at the solution interface. The photoreduced carbon nitride can thus be described as a battery anode operating as a pseudocapacitor, which can store light-induced charge in the form of long-lived, "trapped" electrons for hours. Importantly, the potential window of this process is not limited by the water reduction reaction due to the high intrinsic overpotential of carbon nitrides for hydrogen evolution, potentially enabling new applications for aqueous batteries. Thus, the feasibility of light-induced electrical energy storage and release on demand by a one-component light-charged battery anode is demonstrated, which provides a sustainable solution to overcome the intermittency of solar radiation.

In the quest to reduce global warming and our reliance on fossil fuels, renewable energy has become a key technology driver and a major socioeconomic growth factor.[1] To circumvent the fluctuation and storage issues renewables are facing, different solutions are at hand, all of which however suffer from certain

F. Podjaski, J. Kröger
Max Planck Institute for Solid State Research
Heisenbergstraße 1, 70569 Stuttgart, Germany
F. Podjaski
Ecole Polytechnique Fédérale de Lausanne
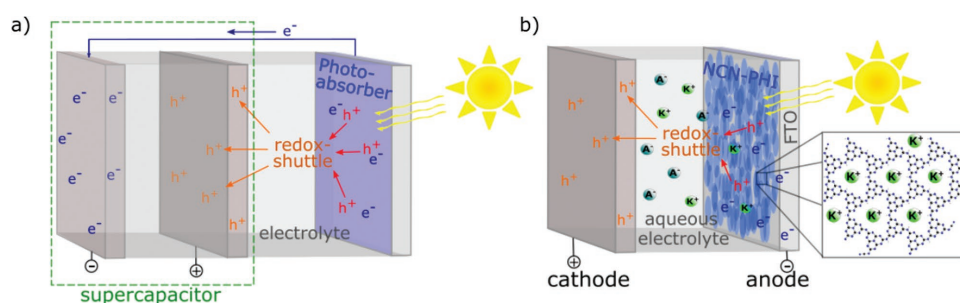Station 12, 1015 Lausanne, Switzerland
J. Kröger, Prof. B. V. Lotsch
Department of Chemistry
University of Munich (LMU)
Butenandtstraße 5-13, 81377 München, Germany
E-mail: b.lotsch@fkf.mpg.de
Prof. B. V. Lotsch
Nanosystems Initiative Munich (NIM)
Schellingstraße 4, 80799 München, Germany
Prof. B. V. Lotsch
Center for Nanoscience
Schellingstraße 4, 80799 München, Germany

The ORCID identification number(s) for the author(s) of this article can be found under https://doi.org/10.1002/adma.201705477.

disadvantages. Solar energy produced by photovoltaic devices is typically stored decentralized in batteries, requiring decoupling of energy conversion and storage, which is both a major loss and cost factor. At the same time, batteries suffer from low power densities that pose problems to the versatility of batteries, especially regarding their use in mobile applications. This can in part be overcome by electrochemical capacitors, which are promising alternatives for high power applications on short time scales; these devices however still suffer from low energy densities. In principle, fuels provide a natural solution to bridge the "storage gap" as they can store high amounts of energy per mass in chemical bonds. Consequently, research efforts are being put into the production of solar fuels such as hydrogen or methane by means of photocatalysis. However, their implementation shifts the energy supply problem to the requirement of a viable infrastructure based on those alternative energy carriers, which is currently nonexistent on a large scale.

One desirable solution would thus be the on-site storage of solar energy light where it is produced—i.e., in the light absorber—in the form of readily usable electrical energy rather than chemical bonds. This would require the seamless combination of the elementary steps of light harvesting, charge carrier separation, and their storage to retrieve them as electrical energy on demand, ideally in one single, earth-abundant material.

Here, we report on a material that is able to harvest, store, and release solar energy in the form of electrical energy. The material is a 2D cyanamide (NCN^-)-functionalized polyheptazine imide (NCN-PHI),[2,3] which upon light excitation and extraction of photogenerated holes accumulates electrons in the form of stable π-radicals. Notably, these radicals can be visually discerned by their blue color. We have previously shown that such "trapped" electrons can be collected in the dark after a time delay of several hours by addition of a cocatalyst, which produces hydrogen on demand.[3] It is thus possible to decouple the absorption of solar energy from the catalytic step in the dark, thus mimicking the separation of light and dark reactions in natural photosynthesis.

We now take this concept one step further and propose a solar battery half-cell, which enables the absorption of light, and the storage of photoinduced electrons and their release in the form of electrical energy in one single carbon nitride material.

ADVANCED
SCIENCE NEWS
www.advancedsciencenews.com

ADVANCED
MATERIALS
www.advmat.de

Figure 1. a) Concept of a traditional solar battery or solar photocapacitor. Photogenerated electrons and holes created in a photoabsorber are transported via an external circuit and a redox shuttle to an electrochemical storage device. The implementation shown here corresponds to that of a photo-supercapacitor. b) Proposed monolithic solar battery based on NCN-PHI. Photoabsorption and electron storage occurs within the same material. Holes are extracted to a counterelectrode via the electrolyte by a redox shuttle (or charge selective contact).

While the concept of a solar battery may be primarily associated with bulk electrodes, we emphasize the continuous transition from battery to pseudocapacitor materials with decreasing particle size and increasing surface area.[4] Our material solution provides several advantages over existing solar-powered electrochemical energy storage systems, the so-called "solar batteries."[5,6] These are integrated multicomponent solutions featuring different types of inorganic materials (**Figure 1**).[7] All approaches used to date are integrated devices based on photo-elements that charge either supercapacitors or redox batteries.[5,8] This is also the case for other de facto "two-electrode" redox-based solar batteries where the photoabsorber forms a composite with one electrode by nanostructuring.[9] In our one-component system, the external charging circuit becomes redundant, thus reducing the complexity of the device significantly. The conceptual difference between the traditional solution and the realization of a photoabsorber with a charge storage ability proposed here is schematically shown in Figure 1a,b. Although photo-supercapacitors integrate a solar cell with a supercapacitor (Figure 1a), the photogenerated electrons need to be shuttled from the photoabsorber to the capacitor-type counterelectrode for storage through external wiring. In contrast, the proposed monolithic system is based on a photoanode that simultaneously absorbs light and locally stores photogenerated electrons in one single material (Figure 1b). The holes are extracted to a counterelectrode via some sort of redox shuttle in both cases.

In the following, we will concentrate on the dual light harvesting and charge storage/release functionality of NCN-PHI operating as the solar battery anode. Band gap irradiation (2.76 eV; see Figure S1.3 in the Supporting Information) of exfoliated NCN-PHI nanosheets deposited on fluorine doped tin oxide (FTO) substrate triggers the formation of electron–hole pairs, which subsequently have to be separated spatially.[2,3,10] This is usually achieved via a redox shuttle in a full solar battery, which however puts limitations to the overall cell kinetics. In order to mimic a cathode that swiftly takes up the holes, we therefore extract them chemically by a sacrificial electron donor, as previously described.[3,11] To this end, we add aqueous 4-methylbenzyl alcohol (4-MBA) as a reducing agent that acts both as a highly efficient and selective hole quencher,[11] thus allowing us to concentrate on the photoanode half-cell in the following.

In the first part, we evaluate key properties of the NCN-PHI solar battery anode—open-circuit potential (OCP), charge storage capacity, and the stability of the stored charges, i.e., the storage time. We then analyze the microscopic processes and limitations underlying the observed photo-electrochemical performance.

When the NCN-PHI photoelectrodes are illuminated with AM1.5 G solar radiation in O_2-free 1 M Na-based phosphate buffer solution (pH 7) in the presence of 4-MBA, the photocharge or OCP rises up to −800 mV vs Ag/AgCl (−600 mV vs NHE, +2.45 V vs Li) (see Figure 4a).[3] We can thus roughly distinguish between this charged, blue state and a ground or decayed state with an OCP around −200 mV vs Ag/AgCl. This photovoltage in the charged state represents the average potential of the highest energy levels occupied by the electrons, thus defining the half-cell voltage of this solar battery anode.

Next, we analyze the capacity of the photoanode by determining its charge storage properties. The resulting (solar) battery properties of our NCN-PHI photoelectrodes are summarized in **Figure 2**.

In order to estimate the maximum charge that can be extracted from the solar battery anode, we varied the discharge currents after 1 min of 1 sun illumination (AM1.5 G) in 1 M phosphate buffer and 5×10^{-3} M 4-MBA in order to find optimized charge extraction currents (see Figure 2a and Figure S2.1 in the Supporting Information). Current densities between 10 and 100 mA g^{-1} balance losses due to slow self-discharge at low currents (1 mA g^{-1}, red shaded) and high intrinsic resistive losses due to limited conductivity at high discharge currents (1 A g^{-1}, gray shaded). The optimum was found at 100 mA g^{-1} and was used for all further measurements.

To investigate the evolution of the stored charge and its stability, we increased the illumination time stepwise and measured the respective discharge curves shown in Figure 2b. Increasing illumination and thus charging times lead to an increase in charge storage up to 43.7 C g^{-1} (12.1 mA h g^{-1}) after 100 min of illumination. Longer illumination times above 12 h affect the electrode stability (as discussed in Sections S2.2 and S2.3 in the Supporting Information). Assuming an average mass of 231(2) g mol^{-1} per NCN-functionalized heptazine unit, 43.7 C g^{-1} correspond to one electron being stored on every 9th to 10th heptazine moiety. The average mass is obtained by assuming a cyanamide functionalization at every second heptazine, 0.58 potassium ions per functionalized heptazine units and deprotonated NH bridges, resulting in an overall neutral molecule (see Section S1 in the Supporting

**ADVANCED
SCIENCE NEWS**

www.advancedsciencenews.com

**ADVANCED
MATERIALS**

www.advmat.de
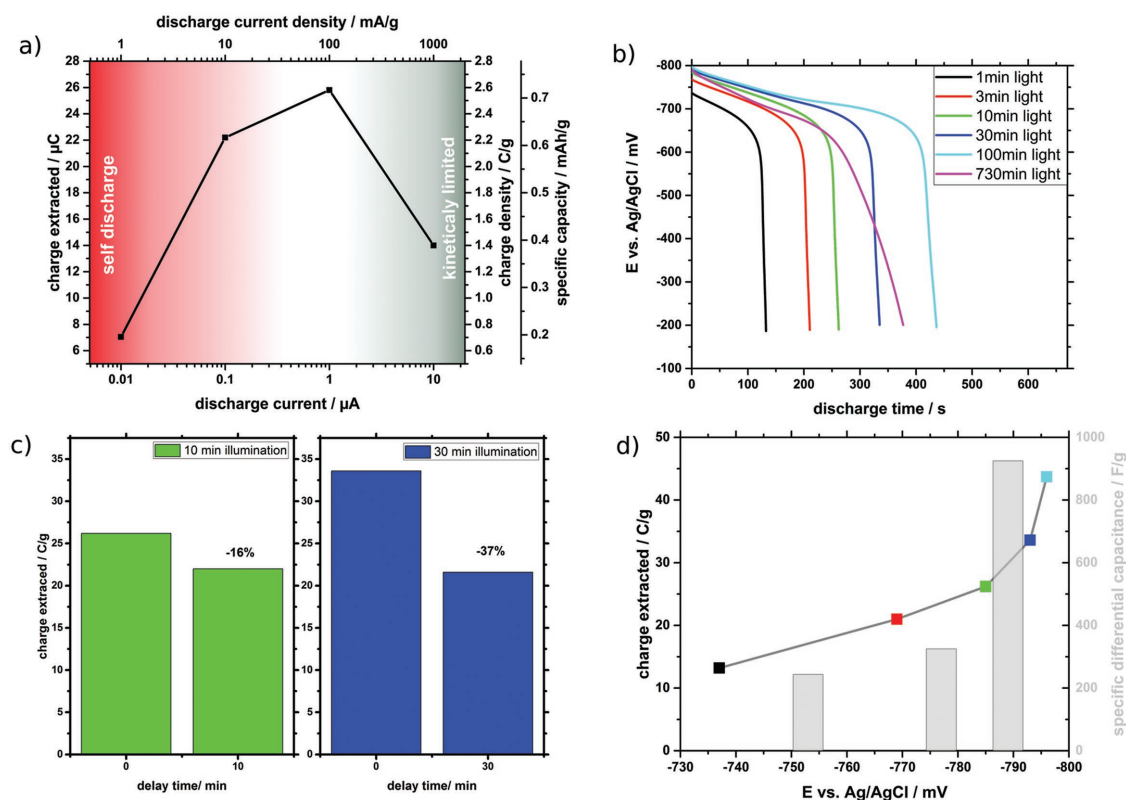
Figure 2. NCN-PHI solar battery half-cell characteristics summarizing the discharge properties of electrodes with 10 µg NCN-PHI, phosphate buffer, and 5×10^{-3} M 4-MBA. a) Evaluation of the total extracted charge after 1 min of illumination as a function of the discharge current densities varying from 1 mA g^{-1} to 1 A g^{-1} (raw data; Figure S2.1, Supporting Information). b) Discharge profiles at 100 mA g^{-1} showing increased charge storage after increasing illumination times. c) Comparison of the extracted charge after 10 min illumination and direct (0 min) or 10 min delayed discharge (left) as well as 30 min illumination and direct as well as 30 min delayed discharge (right). Raw data for delayed discharge, see Figure S2.2 in the Supporting Information. d) Extracted charge from (b) as a function of the corresponding electrode potential before the discharge and evaluation of the charge density (differential capacitance) resulting from the charge difference between the respectively attained voltage values.

Information). Note that the conjugation length of the imide-bridged polymer, which varies with the synthesis conditions, influences the amount of negative charge that can be trapped on the heptazine rings as well as its delocalization across the polymer backbone and, hence, its capacity profile. The fact that the extractable charge increases nonlinearly with illumination time (partly due to losses via the substrate as discussed further below; see Figure 4b and Section S2.2 in the Supporting Information) is beneficial to charge a solar battery continuously. This situation is in contrast to solar supercapacitors that attain their capacity limit within minutes and comparable to other solar batteries that are charged by a photoelement.[12]

To investigate for how long and efficiently this stored charge can be used after the illumination has stopped, we delayed the discharge after 10 and 30 min of illumination by 10 and 30 min, respectively, as shown in Figure 2c. Delaying the discharge by 10 min leads to a slightly decreased capacity of only 16%, while in the 30 min case, 37% are lost. This charge decay is related to Faradaic charge transfer from the partially uncovered FTO substrate to the electrolyte (see Section S2.2 in the Supporting Information).

The increased charge storage in the NCN-PHI correlates with the electrode potential, which becomes more negative with irradiation time, as shown in Figure 2d. The variable electrode potential and the amount of charge stored at each respective potential reflect the distribution of energy levels that are accessible to the photoinduced electrons, and is therefore an indirect measure of the electronic density of state (DOS), which formally translates into a differential capacitance. An analysis of the differential charge extracted after reaching the respective potentials thus allows us to estimate a differential capacitance ($C = Q/V$ or dQ/dV) in the respective potential windows. Note that due to the Faradaic losses the differential capacitance values we extract are likely underestimated. Increasing the illumination time from 10 to 30 min leads to a voltage difference of 8 mV (-785 to -793 mV vs Ag/AgCl) and a difference in extracted charge of 7.4 C g^{-1}. From this, a specific differential capacitance of 925 F g^{-1} can be extracted at an average intermediate potential of 789 mV, which is higher than, e.g., 379.9 F g^{-1} obtained from g-C3N4@graphene oxide at similar current densities of 250 mA g^{-1}.[13] Following the trend shown in Figure 2d, we expect even higher specific capacities if the photovoltage is increased even more, thus again highlighting the promise of NCN-PHI as a high-capacity solar battery photoanode. Note, however, that an evaluation of the differential capacitance after longer illumination times was hindered by electrode stability issues that could lead to an overestimation of the capacitance.

**ADVANCED
SCIENCE NEWS**

www.advancedsciencenews.com

**ADVANCED
MATERIALS**

www.advmat.de

The long stability of the NCN-PHI discharge potential above −700 mV vs Ag/AgCl is due to the high DOS in this voltage region. Opposite to the fast voltage decay observed in common photocapacitors, which do not have a built-in storage option in the absorber and use separated capacitors,[8,14] this high DOS and capacitance in our material is a key property for a stable operation potential of a solar battery. For illumination times of only 1 min, the capacity of 13.2 C g^{-1} for our NCN-PHI photoanode is comparable to photocapacitors based on carbon nanotubes (CNT) with a capacitance of 17.5 C g^{-1}.[14] However, such CNT devices must be discharged within 2 min immediately after illumination due to fast self-discharge, a drawback that is circumvented by the long-term storage capacity of our material (see Figure S2.8 in the Supporting Information). As the potentials for electron storage are mostly more negative than −700 mV vs Ag/AgCl in phosphate buffer and even below −800 mV in KCl (corresponding to −100 and −200 mV vs RHE at pH7), the long-term stability of the charge storage on NCN-PHI is remarkable. Note that since NCN-PHI is unable to evolve hydrogen without the presence of a cocatalyst (see Section S2.2 in the Supporting Information: Decay via hydrogen evolution by NCN-PHI), this high overpotential for the hydrogen evolution reaction (HER) is thus a beneficial factor to increase the potential window of a solar battery anode operating in water.

An interesting aspect in terms of charge storage properties is the question whether NCN-PHI can also be charged purely electrically, i.e., by application of a negative bias and without the presence of a sacrificial donor in the dark. We therefore cycled NCN-PHI electrodes electrically in the dark in 1 M phosphate buffer to investigate the battery charging and discharging properties at 100 mA g^{-1} as shown in **Figure 3**. We find that reversible electrical charging and discharging is indeed possible. The charge required to reach a potential of −800 mV vs Ag/AgCl is slightly higher than the charge that can be extracted subsequently which is attributed to partial charge transfer to the electrolyte from uncovered substrate parts (see Section S2.2 in the Supporting Information). The specific charge extracted on the discharge (45–60 C g^{-1}, Figure 3b) is

in good agreement with measurements after light charging up to almost −800 mV vs Ag/AgCl (see Figure 2d) although the electrical measurement underestimates the full capacity. While a complete charging of the electrode material is possible by sunlight in the presence of a donor, purely electrical charging is limited by slow kinetics and low conductivity of the NCN-PHI films, giving rise to a potential drop across the material. It therefore does not allow charging the electrode homogenously in a short period of time and thus underestimates the capacity of the whole material.

This point is further discussed later in the text. Figure 3a,b shows a decrease in capacity with increasing cycle number, which is attributed to a lack in mechanical stability of the sample (see discussion in Section S2.3 in the Supporting Information). To decouple the mechanical stability from the charge–discharge stability, we assume that the charge extracted at the discharge correlates with the mechanical stability (i.e., the leftover material), while the evolution of the ratio between charge stored and charge extracted (Coulombic efficiency) provides a good measure for the electronic charge–discharge stability. As visible in the inset of Figure 3b, the evolution of this Coulombic efficiency quickly approaches a constant value of 75%–80% with increasing cycle number, indicating continuously good electronic stability of the NCN-PHI nanosheets after some initial charging cycles that activate the material. This highlights that the lifetime limitations are most probably purely mechanical, i.e., limited by adhesion. The observed Coulombic efficiencies are even above the value of 45% observed in melon-type carbon nitride (dark) battery anodes.[15]

For a better understanding of the microscopic processes that both enable and limit solar and electrical energy storage in NCN-PHI, further photo-electrochemical experiments have been performed. First, we address the accessible OCP under different conditions. If the NCN-PHI electrodes are illuminated without a dedicated donor in pure water or phosphate buffer, an OCP of −170 and −570 mV vs Ag/AgCl, respectively, is observed, which is caused by the presence of some photoelectrons in the conduction band (see **Figure 4**a, pink and
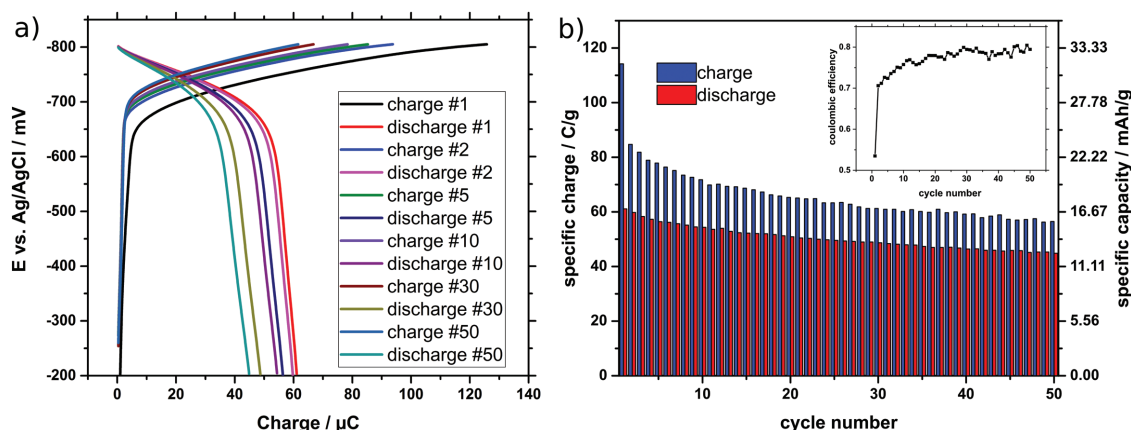
Figure 3. Cyclic electrical charging and discharging profiles (50 cycles) with 100 mA g^{-1} between −200 and −800 mV vs Ag/AgCl in phosphate buffer. a) Selected profiles of the 1st, 2nd, 5th, 10th, 30th, and 50th charging and discharging cycles. The relatively slow voltage increase above −700 mV vs Ag/AgCl underlines the increased capacitance in that region. b) Evolution of the charge stored and extracted during 50 cycles. While the overall charge stored and extracted decreases with increasing cycle number, the Coulombic efficiency (inset) approaches a constant value of ≈80%, indicating a good electronic stability.

ADVANCED
SCIENCE NEWS
www.advancedsciencenews.com

ADVANCED
MATERIALS
www.advmat.de
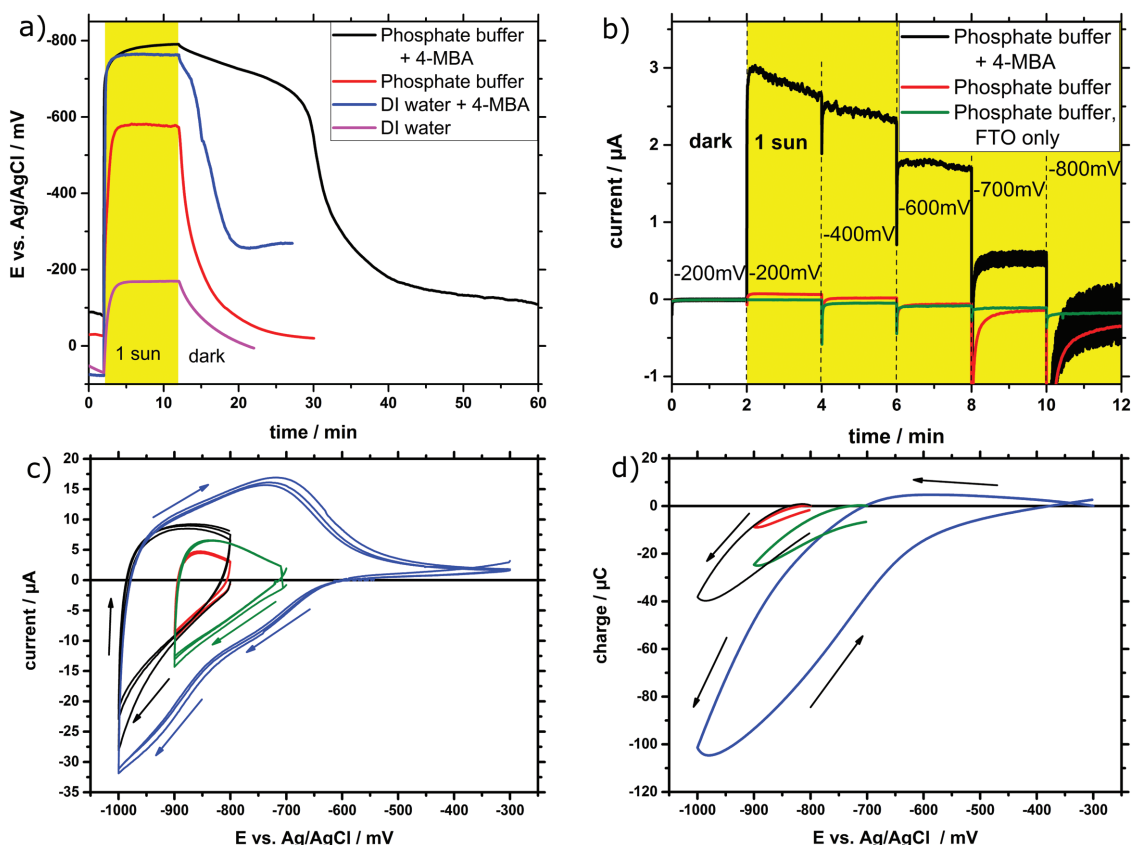
Figure 4. (Photo)electrochemical measurements on NCN-PHI electrodes. a) OCP measurements before, during, and after 10 min of 1 sun illumination, showing the potential and the stability of stored photoelectrons depending on the electrolyte and donor. b) (Dis)charging currents at different potentials under illumination in the presence of a donor and without, providing a measure of electron generation and self-discharge currents under illumination. c) CV scans at 50 mV s^{-1} in the dark in 1 M KCl for different potential windows, highlighting the voltage-dependent charge storage ability of NCN-PHI electrodes. d) Charge stored in and withdrawn from the electrode during the respective scans in (c).

red curves). These OCP values can thus be attributed to the electron quasi-Fermi-level under 1 sun illumination and is due to a balance between charge generation and recombination. The higher OCP in the phosphate buffer case is attributed to a small capacitive stabilization of the photoelectrons that will be discussed in more detail below. When the donor 4-MBA is added, the OCP value is again −800 mV vs Ag/AgCl, thus 200 mV more negative than in the case with only phosphate buffer (blue and black curves, respectively): since now the holes are quenched and electrons can accumulate, they reach more negative states. Furthermore, the charging process continues if both donor and phosphate buffer are present, which leads to a gradual increase in the OCP (see difference between black and blue curves) as well as a more stable electrode potential after illumination, i.e., a delayed decrease in potential after the light is switched off. This phenomenon points again to a capacitive storage of electrons in the potential window more negative than −600 mV vs Ag/AgCl, as discussed further below.

To investigate the amount of charges per second that are effectively generated and stored in NCN-PHI upon illumination, i.e., the electron generation currents, we measured the photocurrents at different potentials vs Ag/AgCl applied to the NCN-PHI@FTO electrodes in the presence and absence of a

donor (see Figure 4b). A negative current corresponds to electron injection through the FTO substrate into the NCN-PHI or into the electrolyte, while a positive current is a measure for photoelectrons withdrawn from the material (i.e., the desired process). Without any illumination, an applied voltage of −200 mV vs Ag/AgCl corresponds to dark OCP conditions and no current flow is observed for all cases. Under illumination and in the presence of a donor, the application of a bias of +600 mV (i.e., a working potential at −200 mV vs Ag/AgCl) creates an extraction driving force with respect to the electrons being present in the conduction band (CB) and leads immediately to a positive charge extraction current. It is an order of magnitude higher than without 4-MBA (Figure 4b, black curve vs red/green curves). This highlights the importance of an efficient hole extraction to charge the electrode efficiently and to stabilize the charges in low voltage states. With an increasing negative voltage that is applied as indicated in Figure 4b, the driving force for hole extraction decreases and so does the current until the applied voltage is −800 mV vs Ag/AgCl (see black curve). The small positive current, even without a dedicated donor (red curve), highlights that a kinetically hindered oxidation of the phosphate buffer or water is possible, which is consistent with the valence band lying well below the required potentials for these reactions.[11,16] In other words, water can

**ADVANCED
SCIENCE NEWS**

www.advancedsciencenews.com

**ADVANCED
MATERIALS**

www.advmat.de

also act as a donor for NCN-PHI, but is less efficient than 4-MBA.

Without donor, we already observe a negative current at −600 mV vs Ag/AgCl, arising from electron injection into the conduction band of the material as the applied potential is more negative than the OCP under illumination. In the same voltage region (< −600 mV), the FTO substrate shows a small negative current due to redox reactions with the electrolyte (water reduction or phosphate reduction).[17] From this we can deduce that the charging currents for NCN-PHI electrodes in this potential range are limited by self-discharge involving electrons being injected back through the substrate into the electrolyte. Although this process is orders of magnitude smaller compared to the charging currents with a donor present, it nevertheless presents a loss channel explaining the discrepancy between the direct and delayed discharging processes shown in Figure 2c (see discussion in Section S2.2 in the Supporting Information). Hence, a complete coverage of the substrate with NCN-PHI is crucial to achieve a stable OCP after illumination, which remains to be optimized.

To further study the role of ions for the energy storage process and its kinetics, we cycled the electrodes electrochemically in the dark. Figure 4c shows the current–voltage (CV) measurements of NCN-PHI@FTO electrodes in 1 M KCl in different potential windows. KCl was chosen instead of phosphate buffer due to the better electrochemical stability of the electrolyte (no reaction with phosphates possible) and the improved cycling stability of the electrodes (Figures S2.5 and S2.6, Supporting Information; similar data for measurements in phosphate buffer are shown and discussed in Figure S2.13 in the Supporting Information). The blue curve (−300 to −1000 mV vs Ag/AgCl) shows that a significant current flows into the electrode starting from −600 mV vs Ag/AgCl, first with a flatter slope, then with an increasing slope from −800 mV onward. The shape of the curves suggests that (i) the charge transfer is capacitive in nature and (ii) the charge uptake by the NCN-PHI electrode, and, hence, also the charge extracted from NCN-PHI, is dependent on the absolute potential window. This further proves different capacitive regimes for electron uptake, corresponding to a potential-dependent DOS in the conduction band that is increasing with negative potential, in agreement with Figure 2d. The presence of kinetic limitations of this charge storage and release process are best visible in the blue scan in Figure 4c,d and in the data shown in Figure S2.13 (Supporting Information). It requires a whole scan back to −300 mV and forward to −600 mV to release all the charges stored in the conduction band below −600 mV vs Ag/AgCl before a refilling of the NCN-PHI at more negative potentials starts again (Figure 4c,d, blue curve vs other curves). This behavior puts a limit to the discharge kinetics, indicating that a fast discharge is not able to extract all the electrons in the CB, as previously observed in Figure 2a and the galvanostatic charge and discharge experiments in Figure 3. Possible causes for this effect are an increase in electronic conductivity if the CB is gradually filled, similar to TiO_2,[18] which is discussed in the following text, or a kinetically limited pseudocapacitance that enhances charge transport and stabilizes the negative charge on the material by the in-diffusion and adsorption of alkali metal ions, i.e., a diffusion-limited mass transport process, or both. In fact, scan-rate-dependent measurements in the region between −700 and −900 mV vs Ag/AgCl (see Figures S2.9–S2.11 in the Supporting Information) show linearly increasing positive peak currents that follow pseudocapacitive behavior rather than a double-layer capacitance that should follow a square root dependency.[19] This is an indirect proof of the stabilization of the negative charge (i.e., "trapped electrons") by alkali metal ion adsorption. This screening of the negative charge is also the reason for the observed increased OCP without donor in the case of phosphate buffer vs pure water (Figure 4a, red vs pink curve). Control CV experiments without alkali metal ions present in the solution have been performed with 1 M tetrabutylammonium chloride (TBA-Cl) and did not show any positive currents (Figure S2.12 in the Supporting Information and other control experiments in Figures S2.9–S2.11(Supporting Information)), indicating that TBA cations are unable to support charge storage in this material. This clearly highlights the importance of an appropriate cation size (or more specifically, its hydrodynamic or equivalent Stokes radius) in order to penetrate the structural pores of NCN-PHI (3.8(4) Å) and thus to stabilize the electron storage by a pseudocapacitive process.[20] Solvated TBA ions (4.95 Å) seem to be too large to penetrate the pores, while Na+ (1.84 Å) and K+ (1.25 Å) both fit inside the pores, thus enabling pseudocapacitive charge stabilization.[21]

To further investigate the influence of illumination on the role of the counter ions as well as the mobility of charge carriers in NCN-PHI electrodes, we performed impedance measurements in the ground state voltage region (−24 mV vs Ag/AgCl) and in the charged or "activated" region (−850 mV vs Ag/AgCl), in KCl, again due to a more pronounced capacitive response, see **Figure 5**a,b. The data are fitted by an equivalent circuit diagram, which can be deduced from generalized equivalent circuits,[22] see the inset in Figure 5a. It accounts for series resistance losses in both, the electrode contact and the electrolyte, and includes a constant phase element accounting for double-layer capacitance Q_{DL} in parallel to a charge transfer resistance as well as a constant phase element accounting for pseudocapacitance Q_P in parallel to a resistive element R_C, accounting for the materials' conductivity. The measurement under illumination (blue curve) shows a significantly lower charge transfer resistance (i.e., better conductivity) with respect to the one measured in the dark (black curve). The appearance of an additional semicircle at higher frequencies is due to changes in the respective capacitive and conductive parameters (see Table S2.14 in the Supporting Information and discussion). The dominant contribution to the capacitance shifts from double-layer capacitance (5.9 F g⁻¹, black curve, dark measurement) to pseudocapacitance (blue curve, illuminated) and becomes as high as 191 F g⁻¹. The increasing value with respect to CV measurements beforehand (Figures S2.9–S2.11, Supporting Information) is due to more homogeneous charging as discussed above and in the graph, and is approaching the differential capacitance values extracted from the measurements under illumination in Figure 2d.

The apparent increase in conductivity that is observed in the blue state can be due to either increased electronic or ionic conductivity in the (light) charged state in an aqueous environment. To distinguish between both effects, the purely light-dependent conductivity was determined by sandwiching NCN-PHI between

**ADVANCED
SCIENCE NEWS**

www.advancedsciencenews.com

**ADVANCED
MATERIALS**

www.advmat.de
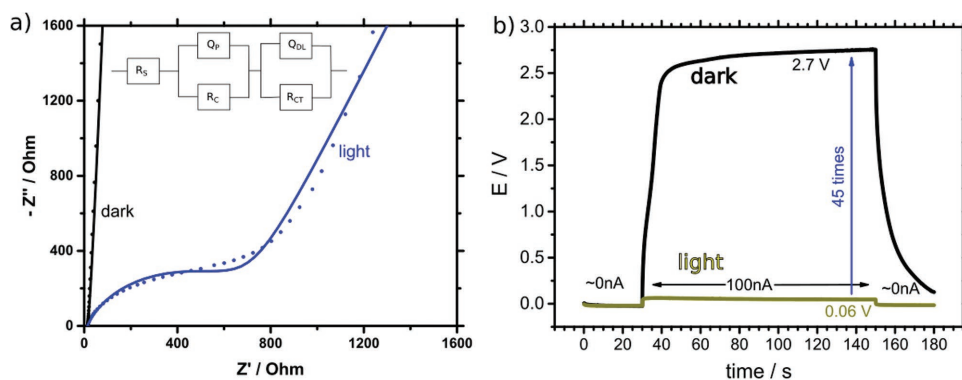
Figure 5. Conductivity of NCN-PHI nanosheets on FTO. a) Impedance measurements in oxygen-free 1 M KCl + 5 × 10^{-3} M 4-MBA in the yellow ground state (black curve: measurement and fit) and in the light induced, blue state (blue curve) which shows a significantly lower charge transfer resistance. Insets: Equivalent circuit diagram used to fit the data. b) Galvanostatic two-point resistivity measurements on an FTO–NCN-PHI–FTO electrode sandwich measured in air. The voltage drop due to resistance in the dark is 45 times higher than in the illuminated case (beige).

two FTO electrodes and measuring their DC conductivity galvanostatically in air. Since FTO is conductive only for electrons and blocking to ions, the measured equilibrium potential corresponds to the electronic conductivity of NCN-PHI alone. The measurement results are shown in Figure 5b. After an equilibration period of 30 s at 0 nA, a current of 100 nA has been forced through the sandwich for 120 s. Afterwards, the current was set back to 0 nA. During the whole process, the voltage drop over the sample was recorded. Comparing the measurement in complete darkness to the one where the sample was illuminated (≈7 sun) during the 120 s period of current flow, a resistance reduction of NCN-PHI by a factor of 45 is observed (27 MΩ in the dark compared to 600 kΩ under illumination). This indicates that light-induced electrons in the conduction band—even without the presence of a hole quencher—enhance the conductivity of the material significantly. It furthermore rationalizes why NCN-PHI photoelectrodes can be used more efficiently when charged by light rather than purely electronically, which is due to a decrease in resistive losses as further discussed in Section S4 in the Supporting Information. While locally increased photoconductivity in melon-type carbon nitrides has been observed several times by means of impedance measurements and photocurrents,[23] this represents the first direct evidence for enhanced long-range DC conductivity in carbon nitrides under illumination, to the best of our knowledge.

Taken the above evidence together, the mechanism of the observed light-induced pseudocapacitive behavior of NCN-PHI can be traced back to the following microscopic origin:

(i) The unique ability of NCN-PHI—in contrast to other carbon nitrides—to "store" electrons upon photoreduction, likely assisted by the electron-poor character and 2D conjugation of the imide-bridged heptazine backbone, as well as an extremely efficient hole extraction by the sacrificial electron donor. The latter aspect is general and works for a range of sacrificial electron donors,[3] which ultimately should simplify the hole transfer to a cathode in the presence of an appropriate hole shuttle in an overall solar battery configuration.

(ii) Screening of the light-induced electrons by alkali ions via diffusion into and through the structural pores of NCN-PHI as well as the mobile alkali ions that are provided and

replenished through the electrolyte (see **Figure 6**). This interaction between the electrons that accumulate on the heptazine backbone and the cations that rearrange in the pores and in solution seems to be vital for high capacity and long-term electron storage, but at the same time limits the kinetics of the charge storage and release.

(iii) Light-induced increase in electronic conductivity of NCN-PHI. This feature is diagnostic of improved charge transport through the electrode under solar irradiation, which is likely due to the increased density of states accessible to the photoinduced electrons, see also Figure 6. An implication of this observation is that NCN-PHI shows improved charge storage and release when operated by light rather than when charged purely electrically.

The interplay between these processes is schematically summarized in Figure 6. The charge storage performance of the NCN-PHI electrode is currently limited by nonoptimized adhesion to the substrate for drop cast electrodes and the slow self-discharge processes occurring via the FTO substrate (e.g., reduction of the electrolyte), becoming significant at long delay times between light-induced charge storage and subsequent electrical extraction (see Figure 2b,c). Following the trend in Figure 2d, we expect even higher specific capacities if the photovoltage can be further increased, which would be equivalent on the microscopic level to a higher electron storage density than one in every 9th heptazine unit. In fact, if every heptazine unit would store one electron, a capacity of more than 100 mA h g^{-1} could be achieved and NCN-PHI would be compatible to actual carbon based supercapacitors operating only in the dark.[24] On the other hand, a more negative anode voltage, going hand in hand with such an increased charge storage, is contingent on decreasing the parasitic currents. Such loss channels can be reduced for example by optimizing the surface coverage of NCN-PHI and/or the choice of substrate, such that even higher OCPs are clearly realistic.

A noticeable feature of our solar battery half-cell is the fact that the electron storage occurs at very negative potentials, up to −850 mV vs Ag/AgCl (−240 mV vs RHE at pH7), enabling a large potential window when operated in water. Since the energy stored scales linearly with the capacitance C

ADVANCED
SCIENCE NEWS
www.advancedsciencenews.com

ADVANCED
MATERIALS
www.advmat.de
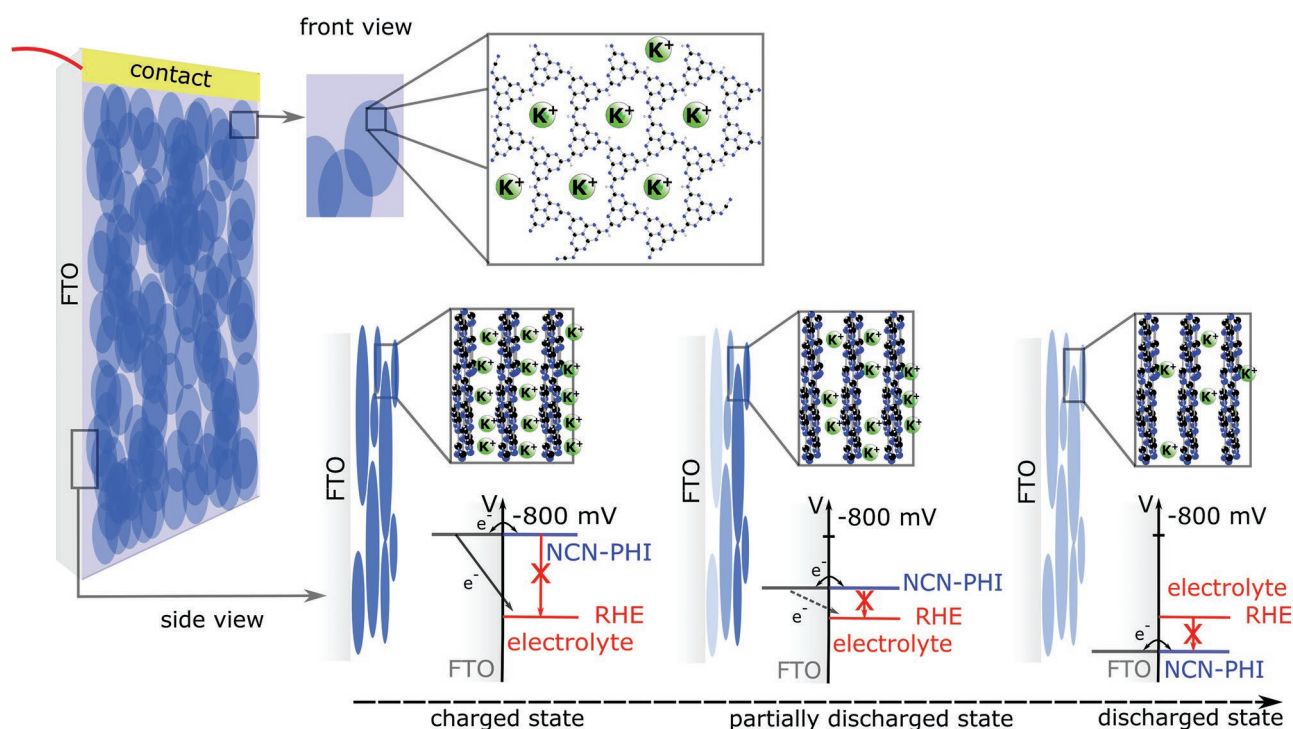
Figure 6. Schematics of a layered NCN-PHI photoelectrode, illustrating the role of alkali metal cations from the solution that can access the pores and stabilize the electronic charge on the NCN-PHI by pseudocapacitance. Note that the effectiveness of charge stabilization is thus a diffusion-limited process that is significantly influenced by the structure (pore size and alignment) and morphology (surface area) of the carbon nitride. Since discharging starts from the inner parts of the NCN-PHI film which are in close contact to the substrate (shown in light blue color), the morphology-limited percolation of charge carriers affects the material's conductivity at high current densities. The evolution from a charged to a discharged state is illustrated in the bottom part, showing the potential measured at the FTO surface, possible charge transfer paths between FTO, NCN-PHI and the electrolyte, as well as the role of alkali metal ions from the electrolyte that enables pseudocapacitive screening of the trapped electrons.

and quadratically with the potential difference V between the anode and the cathode via $E = 1/2 \, CV^2$, the high overpotential of NCN-PHI for HER (Section S2.2, Supporting Information) pushes the fundamental limits of the energy that can be stored in aqueous batteries without parasitic water reduction occurring.

The amount of energy that could be extracted from a full battery depends on the energy levels of both the stored electrons and holes. With the conduction band lying approximately at −800 mV vs Ag/AgCl,[3] the material's large band gap of 2.76 eV allows for a reasonable tradeoff between visible light absorption and a high cell voltage.[25] For an estimation of the potential of a full battery we assume a system comparable to the one published by Wu and co-workers where an aqueous Li–I electrolyte is used in a solar flow battery with a Pt electrode as cathode.[26] The valence band holes (+1.9 V vs Ag/AgCl) would be stored in the electrolyte using the I^-/I_3^- redox couple at +330 mV vs Ag/AgCl.[27] The overall potential of a full battery would thus be around 1.13 V. Combining this potential with the capacity of 43.7 C g^{-1} (12.1 mA h g^{-1}) (Figure 2), a corresponding energy density of 49.4 J g^{-1} (13.7 Wh kg^{-1}) and a power density of 0.11 kW kg^{-1} (assuming the anode to be rate limiting) at discharge currents of 100 mA g^{-1} as used in Figure 2 with a discharge rate corresponding to 8.6 C would be realistic. Note that this is a very conservative estimate since the valence band of NCN-PHI is very positive, thus allowing for redox shuttles and cathodes with far more positive potentials. In addition, the

oxygen evolution reaction, which would be a limiting reaction in an aqueous environment, has higher overpotentials than the hydrogen evolution reaction, thus likely allowing for even higher cell voltages.

In summary, we have shown that NCN-PHI, an earth-abundant and cheap material with an easy and scalable synthesis from organic precursors, can be used as a solar battery anode by the combination of two key optoelectronic properties—light absorption and electrical energy storage—within the very same material. To the best of our knowledge, this is the first example of such a dual functionality that is essential to reduce the complexity and applicability of solar batteries or solar-powered electrochemical energy storage systems. At the same time, this material allows for on-site or decentralized storage of renewable energies in the form of electricity and, hence, to bypass solar fuel production. The capacity and stability of charge storage is contingent on the pseudocapacitive incorporation of alkali metal ions into the porous 2D-NCN-PHI network. Since the material has a high intrinsic overpotential for water reduction, it shows an increased potential window for operating in an aqueous environment, thus promising significantly higher energy densities than in existing aqueous batteries. The capacity of NCN-PHI has been shown to be potential dependent and its conductivity is increased by illumination. Nevertheless, the low conductivity of NCN-PHI in its uncharged state limits its applicability to thin films with high power densities or thick films with higher charge retention abilities (i.e., higher

energy density if used as battery anode), at the expense of power density. Therefore, morphology engineering will be key to overcome charge percolation issues in this system. Finally, in order to create a full aqueous solar battery, a technically convenient solution for hole transport to a battery cathode remains to be found.

While we have focused here on the potential of NCN-PHI as a solar battery anode, the light-induced charge storage capability and conductivity enhancement observed in NCN-PHI are intriguing features for a number of other light-driven devices, ranging from organic-based electrochromic materials to photodriven resistive switches and photodetectors. Studies along these lines are ongoing in our lab. Taken together, the findings reported herein may present a key step toward an economy based not only on renewable energy, but also on renewable materials to build and power its infrastructure.

Supporting Information

Supporting Information is available from the Wiley Online Library or from the author.

Conflict of Interest

The authors declare no conflict of interest.

[1] a) N. S. Lewis, D. G. Nocera, *Proc. Natl. Acad. Sci. USA* **2006**, *103*, 15729; b) M. Z. Jacobson, *Energy Environ. Sci.* **2009**, *2*, 148; c) M. Z. Jacobson, M. A. Delucchi, *Sci. Am.* **2009**, *301*, 58; d) M. Z. Jacobson, M. A. Delucchi, *Energy Policy* **2011**, *39*, 1154; e) M. A. Delucchi, M. Z. Jacobson, *Energy Policy* **2011**, *39*, 1170.

[2] V. W. H. Lau, I. Moudrakovski, T. Botari, S. Weinberger, M. B. Mesch, V. Duppel, J. Senker, V. Blum, B. V. Lotsch, *Nat. Commun.* **2016**, *7*, 12165.

[3] V. W. Lau, D. Klose, H. Kasap, F. Podjaski, M. C. Pignié, E. Reisner, G. Jeschke, B. V. Lotsch, *Angew. Chem. Int. Ed. Engl.* **2017**, *56*, 510.

[4] a) P. Balaya, A. J. Bhattacharyya, J. Jamnik, Yu. F. Zhukovskii, E. A. Kotomin, J. Maier, *J. Power Sources* **2006**, *159*, 171; b) J. Maier, *Chem. Mater.* **2014**, *26*, 348; c) B. E. Conway, *J. Electrochem. Soc.* **1991**, *138*, 1539.

[5] M. Z. Yu, W. D. McCulloch, Z. J. Huang, B. B. Trang, J. Lu, K. Amine, Y. Y. Wu, *J. Mat. Chem. A* **2016**, *4*, 2766.

[6] H. G. Wei, D. P. Cui, J. H. Ma, L. I. Chu, X. O. Zhao, H. X. Song, H. Liu, T. Liu, N. Wang, Z. Guo, *J. Mat. Chem. A* **2017**, *5*, 1873.

[7] a) A. Takshi, T. Tevi, F. Rahimi, in *Next Generation Technologies for Solar Energy Conversion VI*, Vol. *9562*, (Eds: O. V. Sulima, G. Conibeer), SPIE, San diego **2015**, http://dx.doi.org/10.1117/12.2187671; b) Y. Sun, X. Yan, *Solar RRL* **2017**, *1*, 1700002.

[8] C. H. Ng, H. N. Lim, S. Hayase, I. Harrison, A. Pandikumar, N. M. Huang, *J. Power Sources* **2015**, *296*, 169.

[9] A. Hauch, A. Georg, U. O. Krasovec, B. Orel, *J. Electrochem. Soc.* **2002**, *149*, A1208.

[10] H. Xu, J. Yan, X. J. She, L. Xu, J. X. Xia, Y. G. Xu, Y. H. Song, L. Y. Huang, H. M. Li, *Nanoscale* **2014**, *6*, 1406.

[11] H. Kasap, C. A. Caputo, B. C. M. Martindale, R. Godin, V. W. H. Lau, B. V. Lotsch, J. R. Durrant, E. Reisner, *J. Am. Chem. Soc.* **2016**, *138*, 9183.

[12] J. T. Xu, Y. H. Chen, L. M. Dai, *Nat. Commun.* **2015**, *6*, 8103.

[13] Y. B. Ding, Y. H. Tang, L. M. Yang, Y. X. Zeng, J. L. Yuan, T. Liu, S. Q. Zhang, C. B. Liu, S. L. Luo, *J. Mater. Chem. A* **2016**, *4*, 14307.

[14] G. Wee, T. Salim, Y. M. Lam, S. G. Mhaisalkar, M. Srinivasan, *Energy Environ. Sci.* **2011**, *4*, 413.

[15] Y. T. Gong, M. M. Li, Y. Wang, *ChemSusChem* **2015**, *8*, 931.

[16] X. C. Wang, K. Maeda, A. Thomas, K. Takanabe, G. Xin, J. M. Carlsson, K. Domen, M. Antonietti, *Nat. Mater.* **2009**, *8*, 76.

[17] W. M. Haynes, *CRC Handbook of Chemistry and Physics*, CRC Press, Florida **2014**.

[18] a) A. C. Fisher, L. M. Peter, E. A. Ponomarev, A. B. Walker, K. G. U. Wijayantha, *J. Phys. Chem. B* **2000**, *104*, 949; b) F. Fabregat-Santiago, G. Garcia-Belmonte, J. Bisquert, A. Zaban, P. Salvador, *J. Phys. Chem. B* **2002**, *106*, 334.

[19] a) V. Augustyn, J. Come, M. A. Lowe, J. W. Kim, P. L. Taberna, S. H. Tolbert, H. D. Abruna, P. Simon, B. Dunn, *Nat. Mater.* **2013**, *12*, 518; b) H. Angerstein-Kozlowska, J. Klinger, B. E. Conway, *J. Electroanal. Chem.* **1977**, *75*, 45.

[20] a) C. Largeot, C. Portet, J. Chmiola, P. L. Taberna, Y. Gogotsi, P. Simon, *J. Am. Chem. Soc.* **2008**, *130*, 2730; b) G. H. Lane, E. Jezek, *Electrochim. Acta* **2014**, *150*, 173.

[21] a) P. C. F. Pau, J. O. Berg, W. G. McMillan, *J. Phys. Chem.* **1990**, *94*, 2671; b) S. Sugiharto, T. M. Lewis, A. J. Moorhouse, P. R. Schofield, P. H. Barry, *Biophys. J.* **2008**, *95*, 4698.

[22] J. Jamnik, J. Maier, *Phys. Chem. Chem. Phys.* **2001**, *3*, 1668.

[23] a) R. K. Gupta, A. A. Al-Ghamdi, F. El-Tantawy, W. A. Farooq, F. Yakuphanoglu, *Mater. Lett.* **2014**, *134*, 149; b) J. H. Wang, C. Zhang, Y. F. Shen, Z. X. Zhou, J. C. Yu, Y. Li, W. Wei, S. Q. Liu, Y. J. Zhang, *J. Mater. Chem. A* **2015**, *3*, 5126; c) A. K. Diaz-Garcia, M. I. Diez-Garcia, T. Lana-Villarreal, R. Gomez, *Electrochim. Acta* **2016**, *219*, 453.

[24] B. Li, F. Dai, Q. F. Xiao, L. Yang, J. M. Shen, C. M. Zhang, M. Cai, *Energy Environ. Sci.* **2016**, *9*, 102.

[25] Y. Liu, N. Li, S. C. Wu, K. M. Liao, K. Zhu, J. Yi, H. S. Zhou, *Energy Environ. Sci.* **2015**, *8*, 2664.

[26] M. Z. Yu, W. D. McCulloch, D. R. Beauchamp, Z. J. Huang, X. D. Ren, Y. Y. Wu, *J. Am. Chem. Soc.* **2015**, *137*, 8332.

[27] P. Atkins, *Physical Chemistry*, 6th ed., W.H. Freeman and Company, New York **1997**.

5

Conclusion & Outlook

In this thesis, we investigated different materials and mechanisms that enable (photo)-electrochemical energy conversion and storage. Regarding electrocatalytic hydrogen evolution, the *operando* modified activities of delafossite oxides were investigated in detail and described by electrochemical methods, i.e. CV, EIS and SECM. The structural modifications on the material's surfaces, which appear to host the active sites, have been studied by SEM, XPS and TEM. As such, they provide new insights on the structure, growth and origin of the activity of a Pd cap layer growing on $PdCoO_2$ in acidic media. While tensile strain usually disfavors the intrinsic HER activity, i.e. j_0, we found that both, the apparent $j_{0,geo}$ and the Tafel slope were enhanced by *operando* electrodissolution. While the former appears to partially originate from an increasing active surface area, the Tafel parameters are most probably modified by a strain-facilitated and stabilized phase transformation towards β-PdH_x, which is expected to show Tafel slopes similar to Pt. The modification of both the intrinsic surface area and the Tafel parameters enables not only the use of Pd as very efficient alternative to Pt, but this material even outperforms bulk Pt through a decrease in the required overpotential η_{10} by a factor of 2. The approach of using inherently strained Pd sublattice in delafossites as template for the growth of strained Pd cap layers contributes to a better understanding of material properties, i.e. structure-property-activity relationships, while providing pathways how to design or tune them *operando*. As such, new design principles of how to rationally form strained structures and how to stabilize otherwise metastable materials or their phases are an important contribution to the field of electrocatalysis and beyond.

To gain more insights of the growth and nature of different cap layers, we plan to investigate also the cap layer evolution on $PtCoO_2$, $PdCrO_2$ and possibly other, new delafossite structures in more detail. Furthermore, a stepwise investigation on the surface structure and properties by means of EIS, TEM and secondary ion mass spectroscopy (SIMS) shall lead to a better understanding of the growth process and nature of the cap layer itself. Capacitive and sorption measurements are foreseen to provide insights into other material properties that might be altered by strain effects, while conductivity and susceptibility measurements on the cap structure shall yield a better understanding of its electronic properties, providing possibly direct evidence for the formation of β-PdH_x.

In publication 2, we investigated the PEC properties of pyrene based COFs, which are used as heterogeneous photocatalysts for the the HER. Due to their high chemical versatility, COFs are interesting model systems to design purely organic, molecular based photocatalysts bottom-up. To understand the origin of the observed HER activity, different intrinsic contributions have to be analyzed and compared. We focused on the dependence of the dark and photocurrents during CVs to monitor the charge transfer properties and to offer a new technique to measure band positions in COFs. By this, we could show that an estimation of the band positions in COFs can be extracted from the photocurrent onset potential for the first time, to the best of our knowledge. These results were backed by theoretical calculations and thus essentially enabled the correct description of the different contributions enabling the photocatalytic HER in the A-TEXPY-COFs. The methods and findings shown herein enable more detailed studies of different contributions to the HER in organic based materials, while confirming assumptions on band alignment with the electrolyte, which are typically not obvious *a priori*. As such, these photoelectrochemical measurements contribute to the understanding of optoelectronic properties in bottom-up designed organic based materials and beyond. In future experiments, it would be interesting to systematically study and compare different techniques for band position determination with organic based photocatalysts. This would also help to provide methodological recommendations for the extraction of parameters for different materials. Furthermore, consistent findings allow for determining more hidden fitting parameters, such as the amount of band bending (if present and coupled to Mott-Schottky-measurements by appropriate equivalent circuit diagrams). Additional measurements, such as the Hall-effect,

would reveal the charge carrier densities independently. Thus, access to the charge carrier mobility and the dielectric factors of these rather insulating materials could be obtained. Ultimately, a more complete description of physical parameters affecting photocatalytic properties would be possible. If this knowledge could then be related to specific building blocks and structural features, an even more rational bottom-up design of COFs would become possible by combining insights from both physics and chemistry.

In publication 3, we studied the origins of simultaneous light absorption and charge storage in the 2D CN_x NCN-PHI. PEC measurements were performed to study the material's applicability as photoelectrode while extracting associated energy levels and charge storage properties. Furthermore, the underlying charge storage process was found to be pseudocapacitive in nature. This turned out to be very favorable for direct solar battery applications, where the photoabsorber and a storage electrode are combined in one single material. To the best of our knowledge, this is the first time that such effects are reported for organic based materials. As such, this work significantly contributes to the establishment of an emerging field of research on direct solar batteries – i.e. materials that enable a job-sharing between light absorption and energy storage. Besides highlighting the conceptual benefits of such an approach that combines the absorber and storage functionality in one material, we also point out the applicability of the system under aqueous conditions. Since the stable electron storage occurs more negative than RHE, it appears interesting to use this material also in a purely electrical aqueous battery where the potential energy window can be increased by NCN-PHI on the anode side. In fact, the pseudocapacitive effect was evidenced with alternative earth abundant alkali metal ions besides Li, such as Na or K being present in the electrolyte, offering unprecedented flexibilities. Since NCN-PHI can be synthesized in a cheap and easy way, relying on abundant raw materials only, it might become a very relevant material solution for sustainable renewable energy storage applications.

Besides further studies of the material charge storage properties and its limits, which partially arise from a low conductivity that needs to be increased, similar materials should be investigated in future to gain insights on the structural conditions that give rise to such a dual functionality. Furthermore, full solar battery concepts based on a half-cell

like NCN-PHI have to be developed. For this purpose, different pathways can be followed. The most critical part arises from the necessity to localize positive charges on a counter-electrode, ideally an organic one to maintain the overall earth-abundant character of the system. Suitable redox shuttles might enable this localization, while charge recombination via the shuttles needs to be prevented. Solid state approaches using hole conductors in contact with NCN-PHI could fulfill the task more efficiently. Besides, tandem structures with other semiconductors could create a junction that separates charges at the interface. In these cases, the hole storage capacity of the cathode material would have to be adapted to the NCN-PHI anode and a trade-off between high driving force for charge separation and final cell voltage has to be addressed. Furthermore, the material could be combined to other bifunctional solar battery cathodes in a Z-scheme. In this case, both materials would absorb and store energy, while half of the charges would recombine. Last but not least, redox-flow-solutions for hole storage might be promising to separate positive charges in a mobile electrolyte, which itself acts as positive electrode upon discharge of the solar battery. The high versatility of these solutions makes further research even more appealing.

Overall, this thesis describes important insights into different fields of (photo)electro-chemical energy conversion and storage, which are all connected. It ranges from rational electrocatalyst design, where the activity is modified by structurally enabled sorption effects, over photocatalyst studies on COFs, where the activity is an interplay of light absorption, charge transfer to the electrochemical co-catalyst and the provided driving force, to multifunctional solar battery materials. In the latter, the charge storage or its potential dependent pseudocapacitive behavior is actually akin to the potential dependent *operando* formation of the β-PdH$_x$ phase in strained Pd structures under cathodic bias. As such, this work underlines the importance and benefits of multidisciplinary research, ranging from chemical synthesis over (photo)electrochemical characterization to its description by (mostly physical) models in various fields of energy conversion. Combining the strengths of all fields, knowledge about the nature of material properties can be gained in a more profound way. With the promotion of such interdisciplinary research, the scientific advancement and new solutions for global energy or pollution issues can hopefully be obtained even more efficiently in future.

A

Supporting Information of Articles

In this Appendix, the supporting information for the three articles presented in Chapter 4 is attached.

A.1 Supporting Information for Publication 1

Supporting Information for "Rational Strain Engineering in Delafossite Oxides for Highly Efficient Hydrogen Evolution Catalysis in Acidic Media"

Filip Podjaski[1,2], Daniel Weber[1,3], Siyuan Zhang[4], Leo Diehl[1,3], Roland Eger[1], Viola Duppel[1], Esther Alarcon-Llado[5], Gunther Richter[6], Frederik Haase[1,3], Anna Fontcuberta i Morral[2,7], Christina Scheu[4], Bettina V. Lotsch[1,3,8,9]

[1]Max-Planck-Institute for Solid State Research, Heisenbergstraße 1, 70569 Stuttgart, Germany. [2]Laboratory of Semiconductor Materials, Institute of Materials, Faculty of Engineering, Ecole Polytechnique Fédérale de Lausanne, Station 12, 1015 Lausanne, Switzerland. [3]Department of Chemistry, University of Munich (LMU), Butenandtstraße 5-13, 81377 München, Germany. [4]Max-Planck-Institut für Eisenforschung GmbH, Max-Planck-Straße 1, 40237 Düsseldorf, Germany. [5]AMOLF, Science Park 104, 1098 XG Amsterdam, The Netherlands. [6]Max-Planck-Institute for Intelligent Systems, Heisenbergstr. 3, 70569 Stuttgart, Germany. [7]Institute of Physics, Faculty of Basic Sciences, EPFL, 1015 Lausanne, Switzerland. [8]Nanosystems Initiative Munich (NIM), Schellingstraße 4, 80799 München, Germany. [9]Center for Nanoscience, Schellingstraße 4, 80799 München, Germany.

Table of Contents

1. Pre-electrocatalysis characterization: XRD
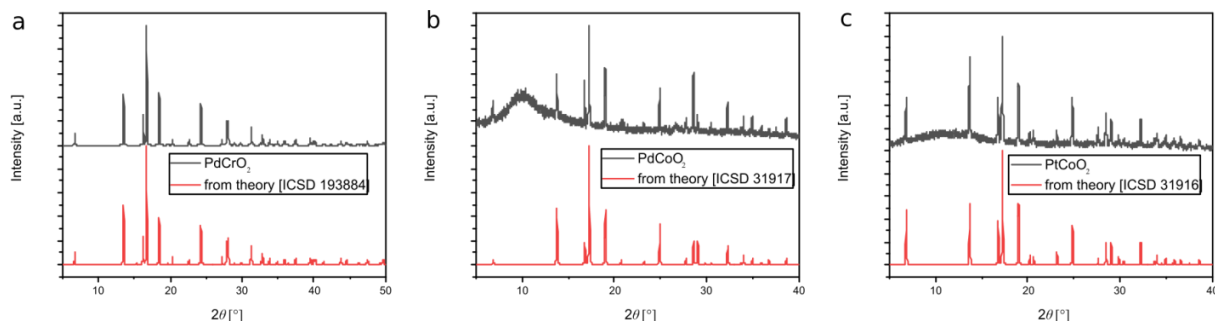
Figure S1: XRD patterns of $PdCrO_2$ (a), $PdCoO_2$ (b) and $PtCoO_2$ (b) before catalysis and reference,[1] using Mo K_α radiation.

Post-catalysis PXRD analysis did not show any differences compared to the results obtained on the as-synthesized material. This can be rationalized by the fact that PXRD as a bulk sensitive technique is insensitive to the small dissolution-induced changes at the surface. The hump at approx. 10° (b and c) is a measurement artifact.

2. Reference measurements: Bulk Pd and Pt vs. aged $PdCoO_2$
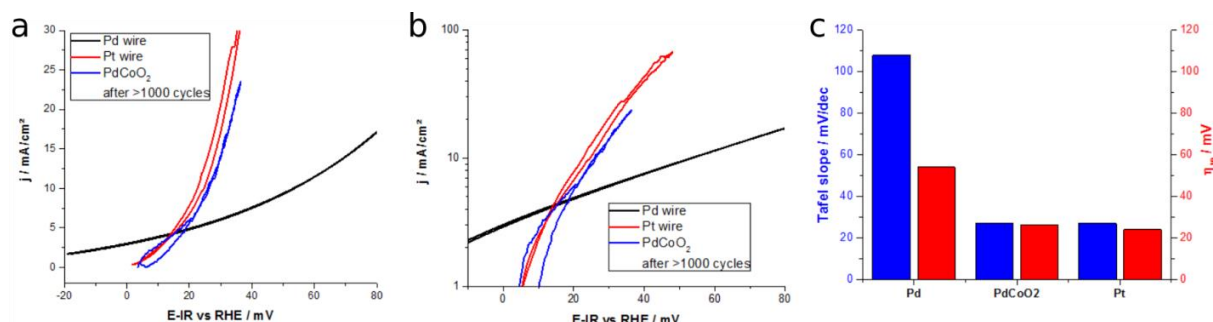
Figure S2: a: CV of a Pd wire, a Pt wire and a pre-cycled $PdCoO_2$ single crystal in hydrogen saturated 1M H_2SO_4 (Pt CE, sat. Ag/AgCl RE). b: Tafel plot of the data after IR-correction. c: Extracted Tafel slopes and overpotentials at 10 mA/cm²$_{geo}$ (η_{10}) for all three materials.

3. Impedance measurements
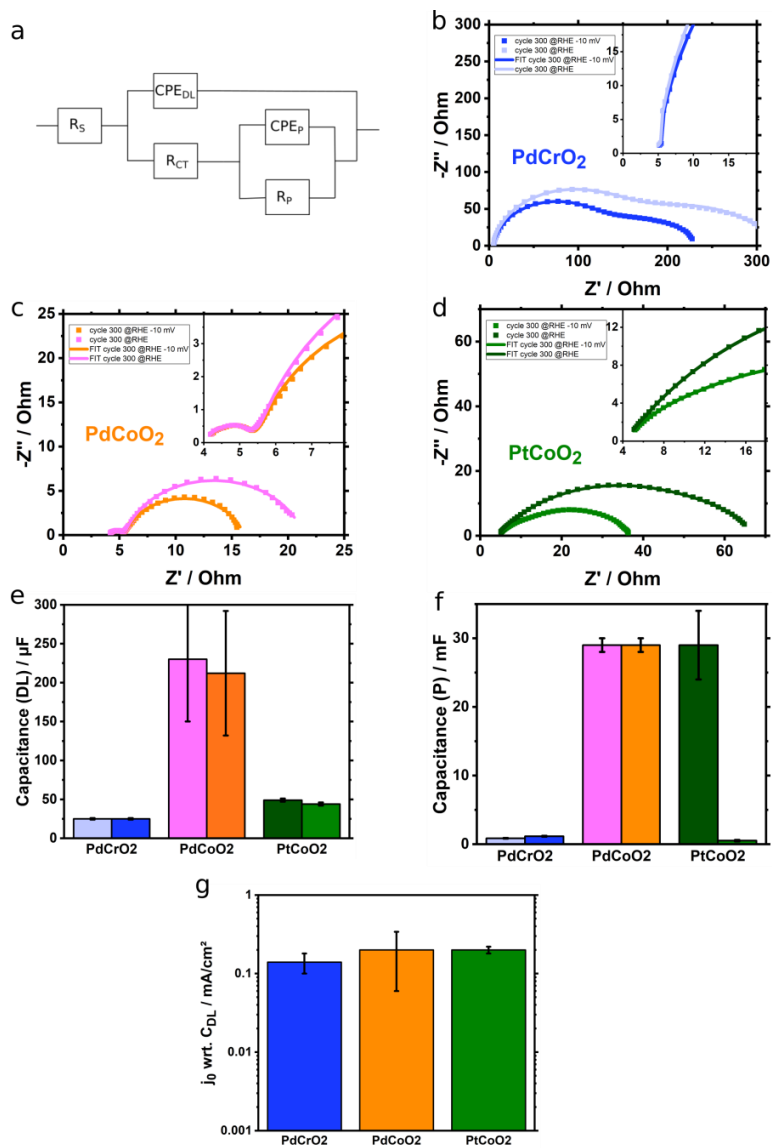
Figure S3: Impedance measurements during electrocatalytic cycling in hydrogen saturated 1M H_2SO_4. a: Equivalent circuit diagram for the separation of double layer capacitance (C_{DL}) and pseudocapacitance (C_P). b-d: Impedance spectra after 300 cycles, recorded at RHE and at a cathodic bias of -10 mV. e-f: C_{DL} and C_P extracted for all three materials. The left value is recoded at RHE, the right at RHE -10 mV, respectively. g: Exchange current densities normalized to the electrochemical surface area (ECSA) of bulk Pd or Pt for all measured samples after 300 cycles, evaluated at RHE -10 mV.

The extraction of the real electrochemical surface area for *operando* modified samples is difficult since a suitable reference accounting for all factors is missing. This applies especially to surface sensitive techniques based on sorption or monolayer metal deposition. Uncertainties arise from the modified incorporation of H_2 into the Pd (or Pt) lattice, an undefined surface termination and structure dependent monolayer coverages. [2, 3, 4, 5, 6, 7] Furthermore, surface deposition based methods would modify the surface termination and hence, its activity, thus hindering continuous studies. For this reason, we relied on impedance measurements.

Since the impedance measurements require significant recording time and the measurement process also modifies the surface structure, this data were recorded after 300 cycles, i.e. after a sufficient stabilization has occurred. After 1000 cycles, the extraction of C_{DL} itself resulted in error bars of similar size as the measurement data themselves.

The model presented in Fig. S3a was recently proposed by Lasia *et al.* to measure bulk surfaces that are also sorption active.[8] Compared to previous versions, it uses constant phase elements (CPE) instead of pure capacitances to account also for inhomogeneous surfaces. Compared to approaches based on Randles circuits, it leads to better fits and does not rely on any parameter fixation or suggestion.

The respective capacitances were extracted by the following formulas:

$$C_{DL} = Q_{DL}^{1/n_{DL}} (\frac{1}{R_S} + \frac{1}{R_{CT}})^{(1-1/n_{DL})}$$

$$C_P = Q_P^{1/n_P} (\frac{1}{R_S + R_{CT}} + \frac{1}{R_P})^{(1-1/n_P)}$$

with R_S being the series resistance (electrolyte, contacts, bulk), R_{CT} being the charge transfer resistance (accounting for double layer effects or the adsorption step) and R_P the pseudocapacitive resistance, which in case of a Faradaic reaction can also be described as hydrogen evolution resistance.[9] Q_x and n_x

denote the values and ideality factors of the respective CPEs. Since this approach takes also into account R_S for the extraction of C_{DL}, the capacitive values per surface area were extracted from a publication using this model. [9] For the Pd compounds, a reported specific capacitance of 50 µF/cm² was assumed. For Pt, a value of 25 µF/cm² was used to extract the ECSA from C_{DL}.[10]

To ensure the general validity of this approach, the impedance data were recorded at different potentials (RHE and RHE -10 mV). The increased stability of the high frequency contribution (described by the semicircle at low impedance values) at different potentials underlines the validity of this approach. C_P is rather insensitive to small changes in the applied potential for Pd, which is why the Pd based compounds give more stable values. The capacitive values extracted are not to be confused with the diameters of the semicircles (i.e. the respective resistances), which are sensitive to the charge transfer process and thus potential dependent.[8]

It should be noted that the C_{DL} response factors for the electrochemically modified materials reported herein may significantly differ from literature values reported for the bulk noble metal surfaces. As such, the error bars shown represent only the averaging error over different samples and no systematic deviation.

4. Scanning electrochemical Microscopy (SECM)
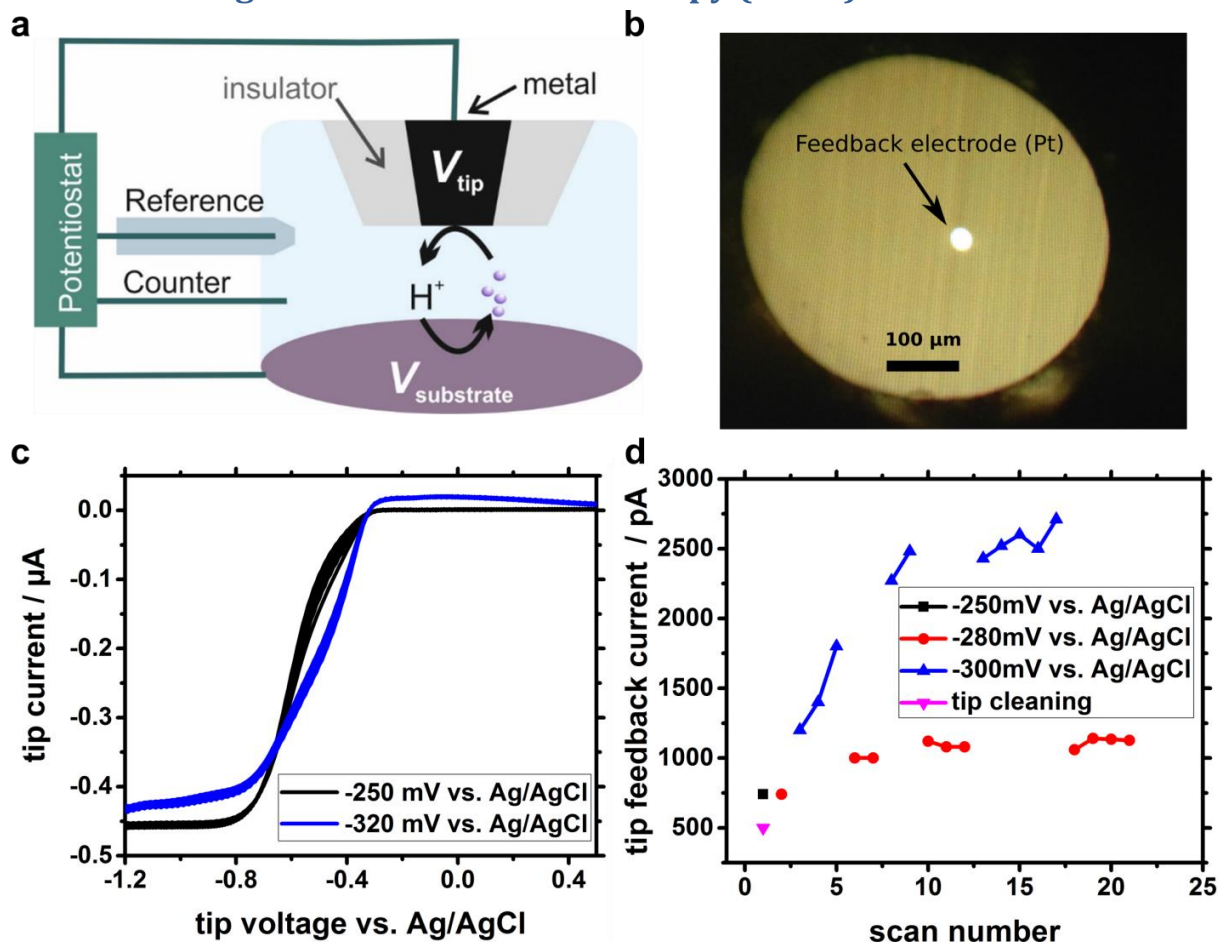
Figure S4: Scanning electrochemical microscopy (SECM) measurements on the surface of a $PdCoO_2$ single microcrystal in 10 mM H_2SO_4 and 20mM Na_2SO_4 exposed to air. a: Illustration of the working principle of a SECM probing the products dissolved in the electrolyte by driving the respective backwards reaction at the tip. b: Optical image of the polished SECM probing / feedback electrode with a 10μm Pt-core. c: Tip CV recorded at a sample potential of -250 mV (weak hydrogen evolution) and -320mV (stronger activity for HER). d: Evolution of the tip feedback current at +0.5 V vs. Ag/AgCl after stabilization while the $PdCO_2$ sample is kept at different potentials.

Due to the consumption of protons by the $PdCoO_2$ crystal at cathodic potentials, the diffusion limited tip current for HER, which competes with the crystals' HER, is decreased (c). An increased anodic current at more positive potentials indicates the hydrogen oxidation reaction (HOR) taking place. This competitive effect evidences an increasing hydrogen evolution at the $PdCoO_2$ sample.

While different potentials are applied to the electrode, the feedback current at +0.5V vs. Ag/AgCl is measured after 5 min of equilibration time (d), driving the HOR. The more negative the sample potential is, the more hydrogen is evolved, leading to an increased tip feedback. Increasing currents (both, as function of potential and time) highlight a temporally increasing hydrogen evolution at each potential, which may be due to an increased Faradaic efficiency, current density, or both.

5. Gas Chromatography for Hydrogen Detection
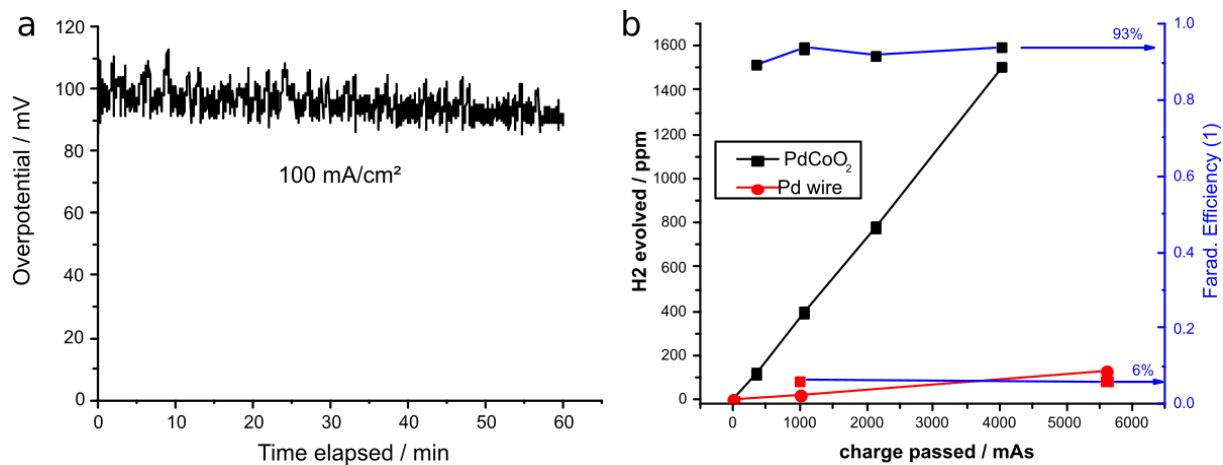
Figure S5: a: Chronopotentiometry at 100 mA/cm² used for gas evolution on a pre-aged large single crystal of $PdCoO_2$ in Ar-purged 1M H_2SO_4 and a Pt CE. The overpotential vs. RHE is not *IR*-corrected. b: Hydrogen gas evolution on $PdCoO_2$ in comparison to a bulk Pd wire and resulting Faradaic efficiency (ratio of hydrogen evolved to charge passed). The gas chromatograph has been calibrated for Faradaic efficiencies with two Pt wires beforehand. Dissolved hydrogen or hydrogen adsorbing to the material could not be taken into account.

6. FIB-preparation of the TEM lamella
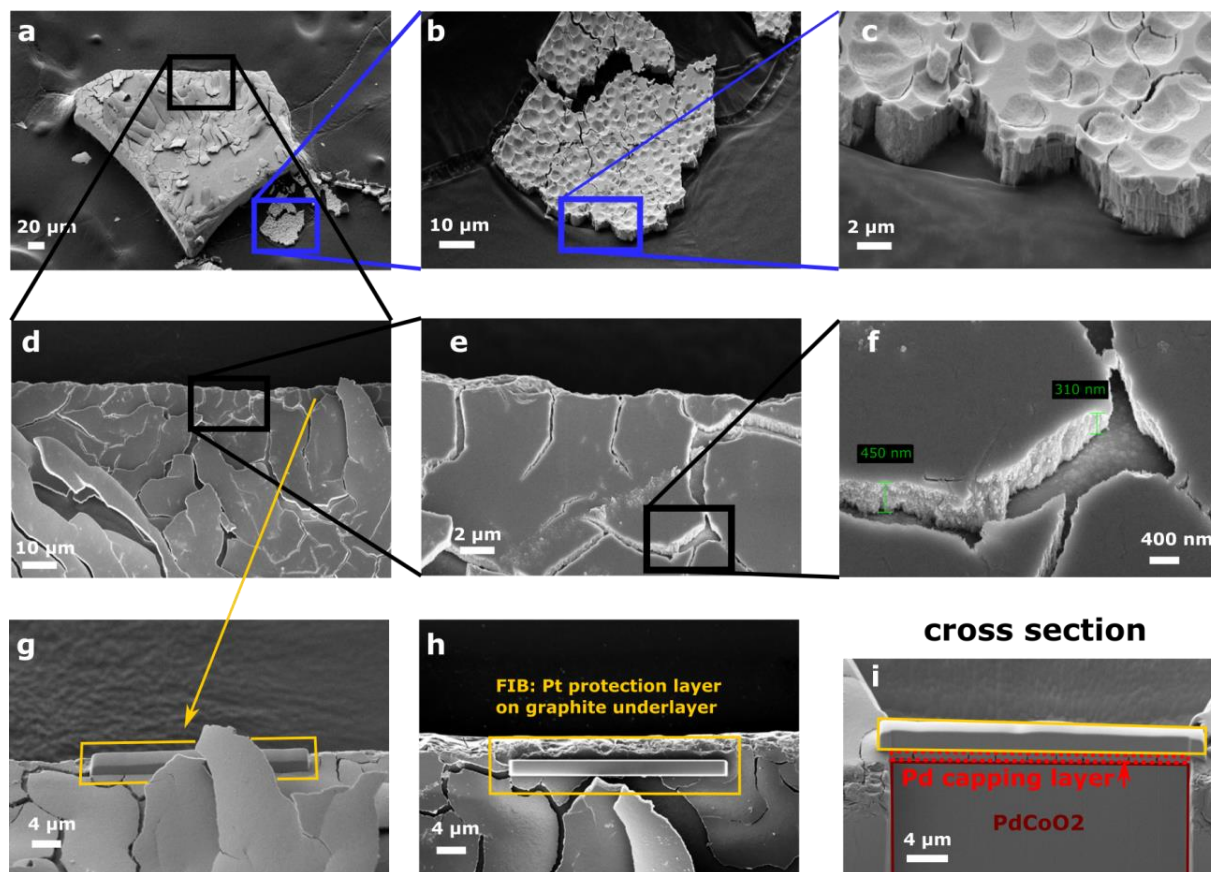
Figure S6 PdCoO$_2$ crystallite after four hours of chronoamperometric aging deposited on a FTO substrate while using an SCE reference electrode and a Pt counter electrode. The crystallite was pressed on a carbon support for SEM and FIB analysis. a: Overall surface of a particle with many thick Pd-rich slabs adhering to the underlying PdCoO$_2$. b and c: Zoom into a detached slab that was turned around, showing the back side in the interface between the PdCoO$_2$ and the Pd-rich capping. It is possible that this part detached due to mechanical stress. A bubble-like texture is visible with diameters of ~2 µm. The thickness of this capping part is 4-5 µm. d - f: Zoom into the capping layer region still attaching to the underlying PdCoO$_2$. While some parts are bent off (d), the adhering slabs show large cracks perpendicular to the surface that seem to grow continuously. The capping layer in this area seems to grow inhomogenously, probably due to different effective potentials and transmission line effects. In this region, the capping layer thickness ranges from 300 to 500 nm(f). g – h: Process of TEM lamella fabrication. After evaporating a thin layer of carbon (invisible), a Pt protection layer (yellow) deposited by the electron and Ga beam. h: Top view of the protection bar. The cross section (i) contains thus the Pt protection layer and the Pd-rich capping layer directly on the PdCoO$_2$ bulk material.

The TEM lamella, which was shown in Fig. 4 in the main text, was prepared with shorter aging times (100 mV overpotential, 5 min of chronoamperometry) with a Ag/AgCl RE and an Au CE. These changes were necessary to avoid any trace contaminations such as Hg due to the initial use of an SCE RE. The preparation of the lamella shown in Fig. 4 is analogous, but the capping layer formation is not well visible in the SEM yet.

7. ICP-OES analysis of the electrolyte after catalysis

Table ST1: amounts of dissolved elements found in the electrolyte after 1000 cycles with a sample loading of 1.5 mg on average; and mass amounts normalized to elemental abundance in 1.5 mg of electrode material. Note that for $PdCrO_2$, a fairly easy detachment of smaller particles was observed, which is possibly why Pd was found in the electrolyte, thus also carrying some Cr (most measurements showed no Cr at all).

	PdCrO2	PdCoO2	PtCoO2
Element	Dissolved amount in 80ml 1M H2SO4 / mg/l		
Pd	0.023(16)	-	-
Pt	-	-	-
Co	-	0.52(5)	0.009(2)
Cr	0.004(5)	-	-
	Dissolved amount wrt. element mass on electrode / %		
Pd	0.22(14)	-	-
Pt	-	-	-
Co	-	9.35(90)	0.24(3)
Cr	0.078(104)	-	-

8. XPS analysis

XPS survey spectra
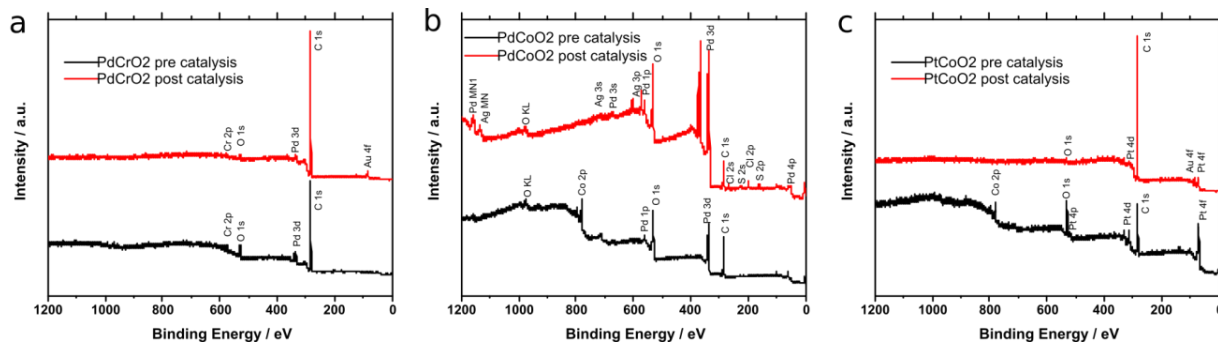
Figure S7 Survey spectra pre and post catalysis for the XPS data shown in Fig 3. in the main text. The Au signals stem from redeposition from the counter electrode while Ag and Cl are due to small leakage of the reference electrode. The signal is attributed to leftovers of the sulfuric acid that dried on the surface after electrochemistry.

XPS intermediate spectrum of PtCoO$_2$
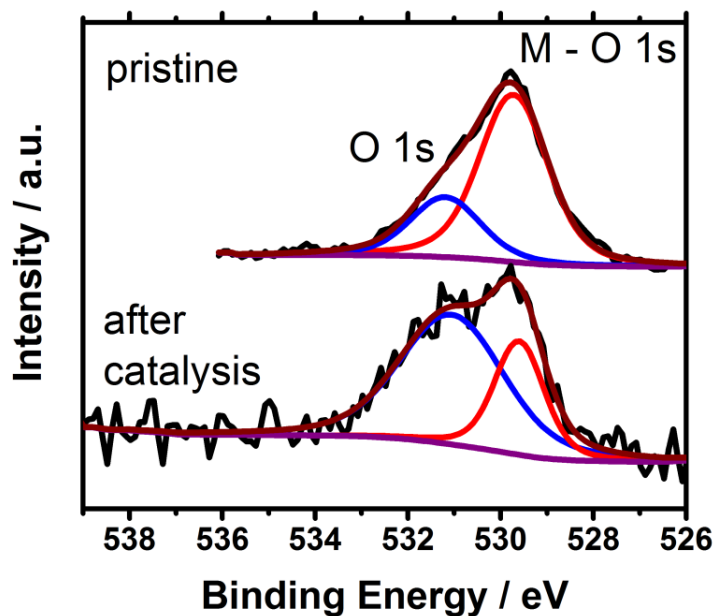
Figure S8 XPS spectrum of PtCoO$_2$ after 1000 cycles, corresponding to the data acquisition from Fig. 1. The interaction between the Pt 3p or Co and O 1s is slowly decreasing (red vs. blue line) but is still present, suggesting a yet incomplete (corrosive) formation of a thick enough Pt layer after 1000 cycles only. Aging the material longer (approx. 300% more charge passed)

S12

makes this interaction disappear (Fig. 3i). The growth of a capping layer thus occurs with slower kinetics for $PtCoO_2$ than in the case of $PdCoO_2$. The information depth of emitted X-rays is only a few (tens) of nm and larger than in the case of Co with respect to Pt, where the binding energies are higher (Fig. 3 h). It is thus well possible to detect a $M - O$ 1s interaction without seeing a Co signal near the surface due to different probing depths.

XPS Tables

Table ST2: XPS fitting data for $PdCrO_2$ pre and post catalysis as shown in Fig. 3 (a-c).

PdCrO2	Pd 3d 3/2 / eV (CPS*eV)			Pd 3d 5/2 / eV (CPS*eV)		
	high	mid	low	high	mid	low
pristine	-	341.1 (568)	339.8 (621)	-	335.6 (818)	334.6 (896)
post catalysis	-	341.0 (209)	339.8 (239)	-	335.5 (460)	334.6 (529)
	Cr 2p 1/2			Cr 2p 3/2		
	high	mid	low	high	mid	low
pristine	-	584.8 (545)	-	-	575.0 (1052)	-
post catalysis	-	584.9 (205)	-	-	575.0 (397)	-
	O 1s			M - O 1s		
	high	mid	low		mid	
pristine	-	531 (1326)	-		528.8 (717)	
post catalysis	-	531.4 (719)	-		529 (262)	

The satellite peak after catalysis, which appears at 572 eV, cannot be attributed to any element since other corresponding lines are missing. The values in brackets (blue) describe the peak area and can be compared within one sample only (pristine or post catalysis).

Table ST3: XPS fitting data for PdCoO$_2$ pre and post catalysis as shown in Fig. 3 (d-f).

PdCoO2	Pd 3d 3/2 / eV (CPS*eV)			Pd 3d 5/2 / eV (CPS*eV)		
	high	mid	low	high	mid	low
pristine	342.8 (324)	341.2 (3402)	340.1 (4949)	337.0 (580)	335.9 (4410)	334.8 (8784)
post catalysis	342.5 (2054)	341.2 (4477)	339.8 (18656)	337.5 (2502)	336.1 (5717)	334.6 (28123)
	Co 2p 1/2			Co 2p 3/2		
	high	mid	low	high	mid	low
pristine	796.6 (577)	795.2 (1151)	793.5 (2275)	781.2 (1226)	780.1 (2227)	778.5 (9139)
post catalysis	-	-	-	-	-	-
	O 1s			M - O 1s		
	high	mid	low		mid	
pristine	533.2 (2053)	531.1 (11759)	530.4 (1978)		528.8 (5547)	
post catalysis	534.3 (2239)	531.8 (17581)	530.9 (10880)		-	

Due to higher counting statistics an additional small satellite component can be fitted, which would be in line with PdO or Pd(OH)$_4$ species being present at the surface. It might also indicate the presence of Pd(I) in deeper sample regions. [11, 12]

Table ST4: XPS fitting data for PtCoO$_2$ pre and post catalysis as shown in Fig. 3 (g-i).

PtCoO2	Pt 4f 5/2 / eV (CPS*eV)			Pt 4f 7/2 / eV (CPS*eV)		
	high	mid	low	high	mid	low
pristine		74.8 (3276)	74.1 (1376)	-	71.5 (2579)	70.8 (1087)
post catalysis	-	74.2 (505)	-	-	70.9 (639)	-
	Co 2p 1/2			Co 2p 3/2		
	high	mid	low	high	mid	low
pristine	-	794.7 (930)	793.4 (282)	-	780 (1798)	778.6 (1130)
post catalysis	-	-	-	-	-	-
	O 1s			M - O 1s		
	high	mid	low		mid	
pristine		531.2 (1087)			529.7 (2974)	
post catalysis	-	531.3 (804)			-	

Table ST5: XPS fitting data for PtCoO$_2$ post catalysis (1000 cycles, Fig. S8), directly after recording Fig. 1 d.

PtCoO2	O 1s / eV (CPS*eV)			M - O 1s / eV (CPS*eV)		
	high	mid	low		mid	
pristine		531.2 (1087)			529.7 (2974)	
post catalysis		531.1 (384)			529.6 (162)	

XPS discussion

The spectra of the main elemental lines are shown in Fig. 3, the respective signal positions are listed in the Tables ST2-5. The first row in Fig. 3 represents $PdCrO_2$. The Pd 3d signals, consisting of Pd 3d 5/2 and 3/2 components at 335.6 and 341.1 eV, with one satellite each, (Fig. 3 a), correspond well to the literature values at 336 and 341 eV. [54] Within the experimental error, these values can be attributed to metallic Pd (335 and 340 eV) and PdO (336 and 341eV). [55, 56] The shift for the Pd peak at 341 eV is consistent with a formal oxidation state of Pd of +1.[57, 58] The binding energies remain practically unchanged before and after electrocatalytic aging. The same is observed for the Cr 2p 1/2 and 3/2 lines (584.8 and 575.0 eV), which remain unchanged and fit the reported values for Cr. In the oxygen spectra, the O 1s signal at 531 eV also remains at the same position, while the signal at 529 eV, marked in red and present also in all other pristine delafossite XPS spectra (Fig. 3c, f, i), can be attributed to the O 1s peak in Cr oxide or an interaction between Pd 3p and O 1s, both expected at 529.3 eV.[55, 56, 59] After catalysis, the amplitude of this M-O interaction peak is lowered with respect to the O 1s peak attributed to unbound oxygen, suggesting decreased binding of Pd and Cr to O. The overall composition of the surface remains largely intact during electrocatalytic cycling, while only the M-O interaction is slightly weakened. The survey spectra (Fig. S7) also show the deposition of inactive metal traces (e.g. Ag from the RE solution) on the surface. These may lead to altered charge transfer properties and hence, a slight decrease of activity over time. Additionally, adsorbed water might further increase the amplitude of the adsorbed O 1s species with respect to the M-O 1s signal.

For pristine $PdCoO_2$ (Fig. 3 d-f), the Pd 3d and O 1s spectra are similar to $PdCrO_2$ and in good agreement with the literature. After catalysis, the Pd 3d peak position are partially shifted by +0.3 eV, which corresponds to a more metallic surface. The Co 2p 1/2 and 3/2 signals in the pristine material (Fig. 3 d) fit reported values for $PdCoO_2$ and also for Pd-Co alloy HER catalysts. [55, 58, 60] The Co signal as well as the

additional peak in the O 1s states arising from oxidized Pd or Co completely disappears after catalysis,[61] thus underlining the formation of a Pd(0) layer on the surface during catalysis, in agreement with the ICP measurements on Co dissolution. It should further be noted that the formation of a Palladium hydride would result in only slight changes in the Pd 3d spectra, which are below the measurement error. {Teschner, 2005 #401}

$PtCoO_2$ (Fig. 3 g-i) represents an intermediate case between the two materials discussed above. The Pt 4f lines remain unchanged in position before and after catalysis, and both the Pt and Co signals are in line with reported values.[27] As in the case of the Pd compounds, the small differences in binding energies between the noble metal in the pristine delafossites and the pure metal are typically rationalized by the metallic character of the delafossite oxides and a decoupling of the A-site sublattice from the surrounding oxide sublattice.[24] Similar to the case of $PdCoO_2$, the Co 2p 3/2 and 1/2 lines at 794.7 and 780 eV vanish after catalysis (Fig. 3 h). Since the measurement depth is limited to less than 10 nm, XPS evidences reduction close to the surface. The metal – O 1s spectrum reveals a sustained interaction after 1000 cycles with decreasing intensity as observed in $PdCrO_2$ (Fig. S8). This corresponds to the observed slower dissolution of Co from $PtCoO_2$ compared to $PdCoO_2$, as evidenced by ICP-OES. Ultimately, the platinum-oxygen interaction disappears after approx. three times longer aging (Fig. 3 i) and eventually, only surface oxygen is detected, as in the case of $PdCoO_2$.

9. TEM analysis
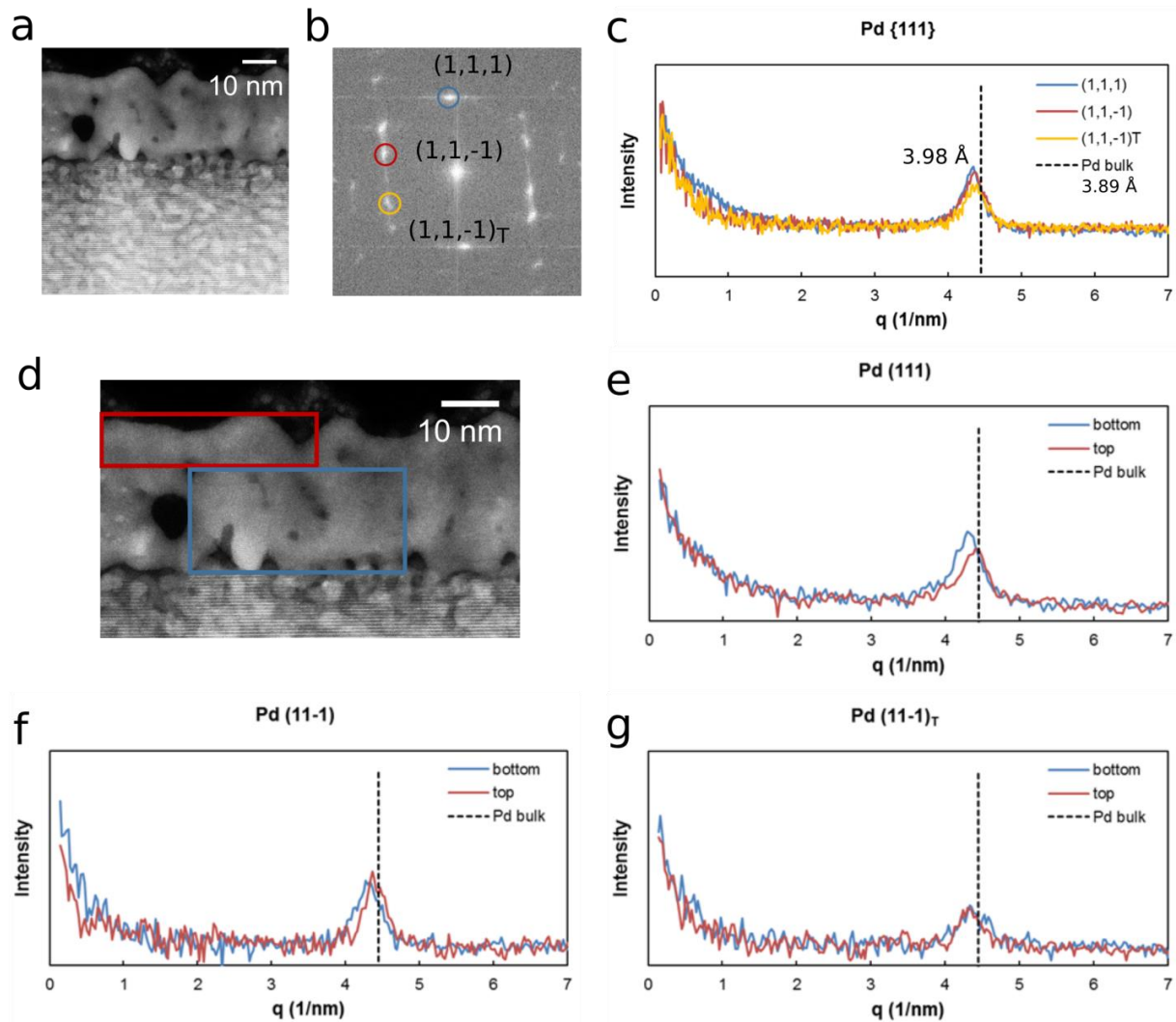
Figure S9: TEM analysis of the Pd capping layer on PdCoO$_2$. a: Image of the PdCoO$_2$ bulk and the Pd rich capping layer. b: FFT of the capping region as a whole. A slight misorientation (<4°) with respect to the c-direction of the bulk is visible (blue circle, (1,1,1) spot in FFT, which could also be caused by the FIB thinning process. The Pd *fcc* crystals are twinned, which is evidenced by the symmetry axis between the (1,1,-1) and (1,1,-1)$_T$ reflections. c: Radial intensity profile of the {111}-reflexes in the capping layer. An isotropic strain with an average value of 3.98 Å can be extracted. d: bulk-PdCoO$_2$-near (blue) and surface near (red) regions analyzed to evaluate the strain evolution across the Pd capping layer. e-g: Radial intensity profiles of the FFT of the eared marked in (d) for Pd (1,1,1), Pd (1,1,-1) and Pd (1,1,-1)$_T$.

10. Pd nanoparticles
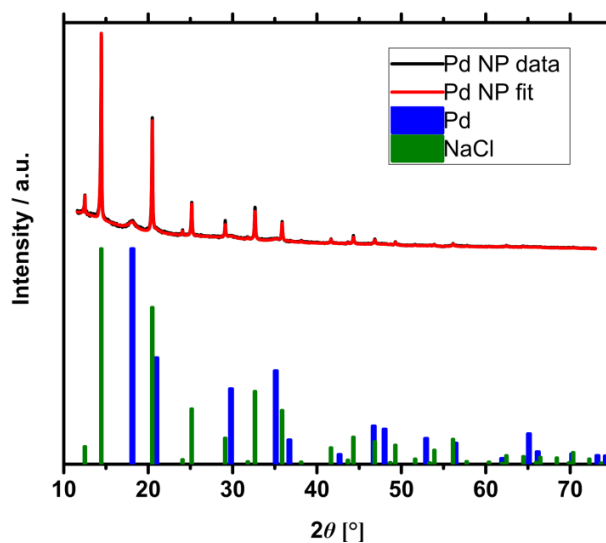
Figure S10: XRD patterns of Pd nanoparticles (*Sciventions*, 1-10nm, average size from fit: 4nm) , dispersed in a NaCl solution, recorded using Mo K_α radiation (black line) and the Rietveld refinement (red line, fit). Ratio of Pd/ NaCl: 10.69%/89.31%. The peaks for bulk Pd and NaCl are shown below in blue and green. The average lattice parameter extracted is estimated to 3.90(2) Å.
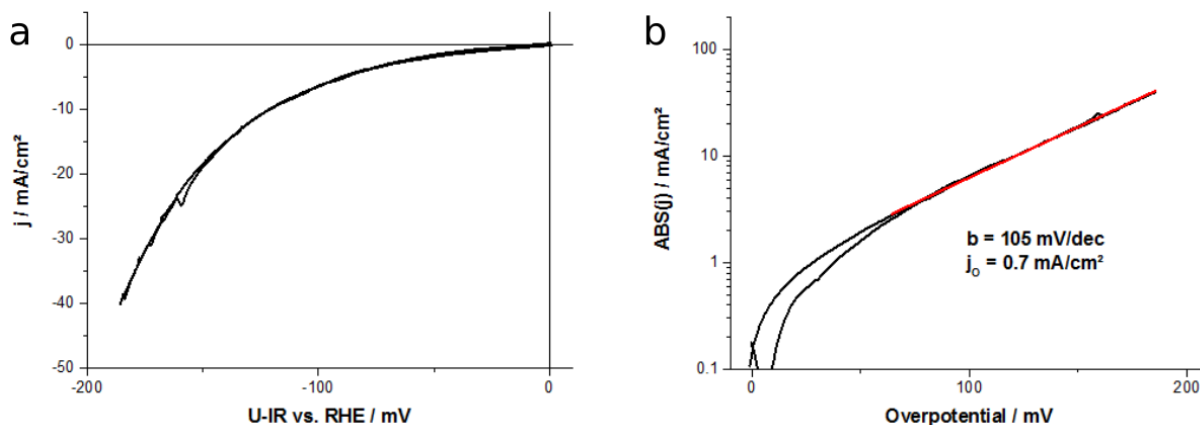
Figure S11: a: *IR*-drop corrected CV of 15µg Pd nanoparticles (1-10nm, 1.5 mg / ml stable suspension from *Sciventions*) deposited on a glassy carbon rod (0.07 cm²) after initial improvement and stabilization (100 CV cycles in the displayed range) in H_2-purged 1M H_2SO_4. b: Resulting Tafel plot and Tafel parameters.
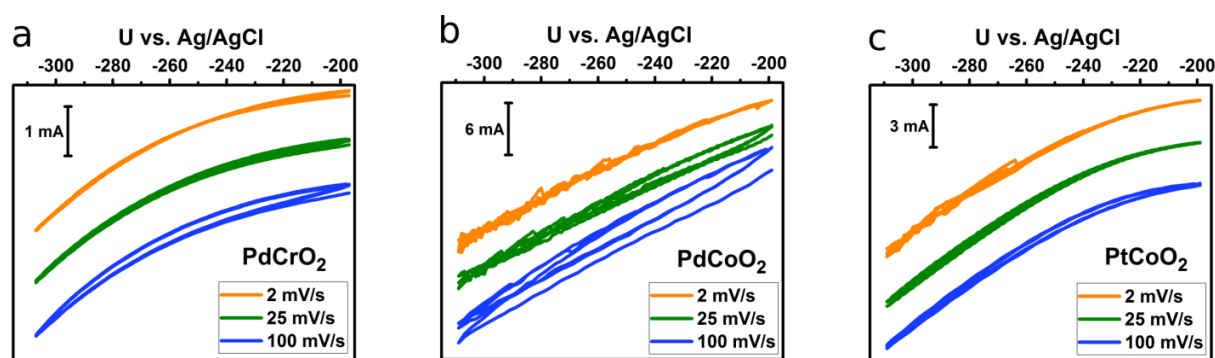
Figure S12: CVs of the delafossite oxide materials studied herein after 1000 cycles in 1M H_2SO_4 with increasing scan rates. a: PdCrO$_2$ showing a small capacitive effect at 100 mV/s. The three measurements were shifted by 1 mA each for better visibility. b: PdCoO$_2$ showing a capacitive effect from 25 mV/s on. After the first cycle, the sample is H_2-saturated and had no time to relax, which is why the OCP shifts to more negative values. The three measurements were shifted by 4 mA each for better visibility. a: PtCoO$_2$ showing a very small capacitive effect at 100 mV/s. The three measurements were shifted by 3 mA each for better visibility.

Literature

1.   Shannon RD, Rogers DB, Prewitt CT. Chemistry of Noble Metal Oxides. I. Syntheses and Properties of ABO2 Delafossite Compounds. *Inorg Chem* 1971, **10**(4)**:** 713-&.

2.   Pourbaix MJN, Van Muylde J, de Zoubov N. Electrochemical Properties of the Platinum Metals. *Platinum Metals Rev* 1959, **3**(3)**:** 100-106.

3.   Searson PC. Hydrogen evolution and entry in palladium at high current density. *Acta Metallurgica et Materialia* 1991, **39**(11)**:** 2519-2525.

4.   Rezaei M, Tabaian SH, Haghshenas DF. Electrochemical nucleation of palladium on graphene: A kinetic study with an emphasis on hydrogen co-reduction. *Electrochimica Acta* 2013, **87:** 381-387.

5.   Huang M, Henry JB, Fortgang P, Henig J, Plumeré N, Bandarenka AS. In depth analysis of complex interfacial processes: in situ electrochemical characterization of deposition of atomic layers of Cu, Pb and Te on Pd electrodes. *RSC Advances* 2012, **2**(29)**:** 10994-11006.

6.   Czerwiński A, Zamponi S, Marassi R. The influence of carbon monoxide on hydrogen absorption by thin films of palladium. *Journal of Electroanalytical Chemistry and Interfacial Electrochemistry* 1991, **304**(1)**:** 233-239.

7.   Henning S, Herranz J, Gasteiger HA. Bulk-Palladium and Palladium-on-Gold Electrocatalysts for the Oxidation of Hydrogen in Alkaline Electrolyte. *Journal of the Electrochemical Society* 2015, **162**(1)**:** F178-F189.

8.   Lin D, Lasia A. Electrochemical impedance study of the kinetics of hydrogen evolution at a rough palladium electrode in acidic solution. *Journal of Electroanalytical Chemistry* 2017, **785:** 190-195.

9.   Gabrielli C, Grand PP, Lasia A, Perrot H. Investigation of Hydrogen Adsorption and Absorption in Palladium Thin Films: III. Impedance Spectroscopy. *Journal of The Electrochemical Society* 2004, **151**(11)**:** A1943-A1949.

10.   Bai L, Harrington DA, Conway BE. Behavior of overpotential—deposited species in Faradaic reactions—II. ac Impedance measurements on H2 evolution kinetics at activated and unactivated Pt cathodes. *Electrochimica Acta* 1987, **32**(12)**:** 1713-1731.

11.   Rahul R, Singh RK, Bera B, Devivaraprasad R, Neergat M. The role of surface oxygenated-species and adsorbed hydrogen in the oxygen reduction reaction (ORR) mechanism and product selectivity on Pd-based catalysts in acid media. *Physical Chemistry Chemical Physics* 2015, **17**(23)**:** 15146-15155.

12.   Moulder JF, Stickle WF, Sobol PE, Bomen KD. *Handbook of X-ray Photoelectron Spectroscopy*. Perkin-Elmer Corporation: Eden Prairie, Minnesota, USA, 1992.

A.2   Supporting Information for Publication 2

ADVANCED ENERGY MATERIALS

Supporting Information

Tailor-Made Photoconductive Pyrene-Based Covalent Organic Frameworks for Visible-Light Driven Hydrogen Generation

Linus Stegbauer, Sebastian Zech, Gökcen Savasci, Tanmay Banerjee, Filip Podjaski, Katharina Schwinghammer, Christian Ochsenfeld, and Bettina V. Lotsch*

Supporting Information

Tailor-made Photoconductive Pyrene Based Covalent Organic Frameworks for Visible-Light Driven Hydrogen Generation.

Linus Stegbauer[1,2,3], Sebastian Zech[1,2], Gökcen Savasci[1,2], Tanmay Banerjee,[1] Filip Podjaski,[1,4] Katharina Schwinghammer[1,2], Christian Ochsenfeld[1,2] and Bettina V. Lotsch[1,2,3]*

[1]*Max Planck Institute for Solid State Research Heisenbergstr. 1, 70569 Stuttgart, Germany*
[2]*Department of Chemistry, University of Munich (LMU), Butenandtstr. 5-13, 81377 München, Germany*
[3]*Nanosystems Initiative Munich (NIM) & Center for Nanoscience, Schellingstr. 4, 80799 München, Germany*
[4]*Ecole Polytechnique Féderale de Lausanne, Station 12, CH-1015 Lausanne, Switzerland*

A. Materials and Methods

The solvents dichloromethane, chloroform, *n*-hexane and ethyl acetate were purified by distillation on a rotary evaporator prior to use. Ethanol was dried using activated molecular sieve (3 Å, SIGMA ALDRICH). All other commercially available chemicals and solvents used in this work are listed in Table S1, including their sources of supply and purity grade.

Moisture- and air-sensitive reactions were conducted under dry argon (MESSER, purity grade 4.8) in standard SCHLENK glassware or BIOTAGE microwave vials capped with common NS14 rubber septa. Standard syringe techniques were applied to transfer the reagents. Vacuum ($>10^{-3}$ mbar) was provided by a VACUUBRAND RZ6 rotary vane pump. Unless otherwise stated, solvents and solutions were degassed by purging with dry argon under vigorous stirring for at least 15 min.

Analytical **thin-layer chromatography** was performed on MERCK silica gel 60 aluminum sheets containing manganese-activated zinc silicate. Substances were identified by irradiation of UV-light (254 nm) after separation. **Preparative column chromatography** was carried out using MERCK silica gel 60 with a particle size distribution of 15–40 µm. Before elution of products, the columns were pre-treated with a mixture of 0.5 % triethylamine in *n*-hexane during the packing procedure.

EI-Mass spectrometry was performed on a JOEL JMS-700 MStation equipped with a double-focusing sector field detector. Samples were deposited on a platinum filament and heated from 20°C to 1600°C at a rate of 120°/min. **ESI-Mass analysis** was achieved on a THERMO Finnigan LTQ FT Ultra using a THERMO Ion Max ion source with a spray-capillary voltage of 4 kV. **MALDI** analysis was obtained on a BRUKER Daltonics Autoflex II TOF mass spectrometer. Samples were co-crystallized with either sinapinic acid or anthracene and ionized by a nitrogen laser operating at 337 nm. All listed mass values refer to the most abundant isotopic species.

Table S1 Overview of chemicals used in this work.

Compound	Purity	Supplier
4-Bromobenzaldehyde	98 %	ACROS ORGANICS
6-Bromonicotinaldehyde	95 %	SIGMA ALDRICH
Bromine	≥ 99 %	RIEDEL DE HAËN
Celite powder (particle size <0.1 mm)	p. a.	MERCK
Copper iodide	98 %	SIGMA ALDRICH
Dimethylacetamide (anhydrous)	99.5 %	ACROS ORGANICS
Dimethylformamide	99 %	ALFA AESAR
Dioxane (anhydrous)	99.5 %	ACROS ORGANICS
Diphenyl ether	99 %	ACROS ORGANICS
Hydrazine hydrate	≥ 99 %	MERCK
Mesitylene	99 %	ACROS ORGANICS
Pyrene	98 %	MERCK
Sodium sulfate	99 %	GRÜSSING
Tetrahydrofuran (anhydrous, inhibitor-free)	≥ 99.9 %	SIGMA ALDRICH

Tetrakis(triphenylphosphine)palladium(0)	99 %	SIGMA ALDRICH
Tetra-*n*-butylammonium fluoride	98 %	SIGMA ALDRICH
Triethylamine	≥ 99 %	SIGMA ALDRICH
Trimethylsilylacetylene	98 %	SIGMA ALDRICH

NMR spectra in solution were recorded on BRUKER Avance and JOEL Eclipse devices operating at 270 MHz or 400 MHz in deuterated solvents at room temperature, unless otherwise stated. The chemical shifts (δ) for ^{1}H- and ^{13}C nuclei refer to tetramethylsilane as an internal standard. Splitting patterns are indicated as *s* (singlet), *d* (doublet), *t* (triplet), *q* (quartet), *m* (multiplet) and *br* (broad).

Solid-state MAS NMR spectra were recorded at ambient temperature on a BRUKER Avance 500 solid-state NMR spectrometer, operating at LARMOR frequencies of 500.2 MHz, 125.8 MHz and 50.7 MHz for ^{1}H-, ^{13}C- and ^{15}N-nuclei, respectively. The sample was contained in a 4 mm zirconium(IV) oxide rotor (BRUKER), which was mounted in a standard double resonance probe at a MAS frequency of 10 kHz. The ^{1}H and ^{13}C chemical shifts were referenced relative to tetramethylsilane. The ^{1}H-^{13}C cross-polarization (CP) MAS spectra were recorded at a spinning speed of 10 kHz using a ramped-amplitude (RAMP) CP pulse on ^{1}H, centered on the n = +1 Hartmann-Hahn condition, with a nutation frequency v_{nut} of 55 kHz (^{15}N) and 40 kHz (^{13}C). During a contact time of 7 ms the ^{1}H radio frequency field was linearly varied about 20%.

UV/Vis data was collected on a JASCO V650 double-beam spectrophotometer equipped with a photomultiplier tube detector. Solid samples were loaded into a special designed holder and pressed against a quartz disc at the edge of the integrating sphere. Data was processed with JASCO's proprietary software Spectra Manager II.

IR-spectra were recorded on a JASCO FT/IR-4100 spectrometer equipped with a diamond ATR unit in a range of 600 cm^{-1}–4000 cm^{-1}. Data was background corrected and processed with JASCO's proprietary software Spectra Manager II.

Argon sorption measurements were performed at 87 K with a QUANTACHROME Autosorb iQ instrument. Samples of 20 mg were preheated in vacuum at 120 °C for 12 h. For BET calculations pressure ranges were chosen according to the implemented micropore BET assistant. For BET calculations pressure ranges of the Ar isotherms were chosen with the help of the BET Assistant in the ASiQwin software. In accordance with the ISO recommendations multipoint BET tags equal to or below the maximum in V(1 - P/P$_0$) were chosen. Pore-size distributions were determined using the calculation model for Ar at 87 K on carbon (cylindrical pores, QSDFT/NLDFT equilibrium model) of the ASiQwin software (v3.01) from Quantachrome.

The **pore size distribution** was calculated from argon adsorption isotherms by non-local density functional theory (NLDFT) using the "*Ar-carbon cylindrical pores at 87 K*" kernel (applicable pore diameters 3.5 Å–1000 Å) for argon data as implemented in the AUTOSORB data reduction software.

Microwave reactions were conducted in a BIOTAGE Initiator Classic instrument in sealed pressure vials under magnetic stirring. Reaction mixtures were rapidly cooled after completed heating *via* nitrogen gas flow.

Steady-State and Time-Resolved Emission data were collected at room temperature using an Edinburgh FLS980 spectrometer. For steady-state emission, samples were excited using light output from a housed 450 W Xe lamp passed through a single grating (1800 l/mm, 250 nm blaze) Czerny-Turner monochromator and finally a bandwidth slit. Emission from the sample was passed through a double grating (1200 l/mm, 500 nm blaze) Czerny-Turner monochromator (appropriate bandwidth) and finally detected by a peltier-cooled Hamamatsu R928P photomultiplier tube.

The dynamics of emission decay were monitored by using the FLS980's time-correlated single-photon counting capability (1024 channels; 5, 20 or 50 ns window) with data collection for 10000 counts (5000 counts for weakly emitting samples). Excitation was provided by an Edinburgh EPL-375 picosecond pulsed laser diode (375 $\pm$ 6 nm, pulse width - 68 ps) and a cooled microchannel plate photomultipler tube (MCP-PMT) was used as the detector. Kinetics were fit with a single exponential function by using Edinburgh software package, when required.

Emission quantum yields were acquired using an integrating sphere incorporated into a spectrofluorometer (FLS980, Edinburgh Instruments). The samples were placed in the sphere and a movable mirror was used for direct or indirect excitation, making it possible to measure absolute emission quantum efficiency following the De Mello method.[1] No bandpass filters were used during quantum yield measurements. For the very weakly emitting solid samples, a 3 OD neutral density filter was used on the emission arm when measuring the scattering. This allows the emission slits to be opened further for the emission spectrum to be accurately measured without detector saturation.

Relative fluorescence quantum yields (ϕ_f) were estimated using equation S1 by using the integrated emission intensity of a water dispersion of A-TEBPY-COF ($\phi_f = 0.002$ in water at RT) as a reference:

$$\phi_f = \phi_f' \, (I_{sample}/I_{ref})(A_{ref}/A_{sample})(\eta^2_{sample}/\eta^2_{ref}) \qquad \text{Eq. S1}$$

where ϕ_f' is the absolute quantum yield for A-TEBPY-COF in water (0.002); I_{sample} and I_{ref} are the integrated emission intensities of the sample and the reference; A_{sample} and A_{ref} are the absorbances of the water dispersion of the sample and the reference, respectively, at the excitation wavelength; and η_{sample} and η_{ref} are the respective refractive indices.

Photocatalytic hydrogen evolution experiments were performed in a double-walled glass reactor kept at a constant temperature (25 °C) by water cooling. The samples (10 mg) were suspended in water (9 mL) and dispersed in an ultrasonic bath for 30 min. The sacrificial electron donor triethanolamine (1 mL, ALFA AESAR) and aqueous hydrogen hexachloroplatinate(IV) solution (6 µL of 8 wt% in H_2O, SIGMA ALDRICH, ≈ 2.2 wt% Pt) as precursor for the *in situ* formation of the platinum co-catalyst was added. The flask was evacuated and purged with argon to remove any dissolved gases. The suspension was top-irradiated through a quartz window with a xenon lamp (NEWPORT, 300 W) equipped with an AM 1.5 G filter

(100 mW cm^{-1}). In the course of the experiment, the headspace of the reactor was periodically sampled and the components were quantified by a THERMO SCIENTIFIC TRACE Ultra gas chromatograph equipped with a thermal conductivity detector, using argon as the carrier gas.

Powder X-ray diffraction experiments were carried out on a STOE Stadi P transmission diffractometer in DEBYE-SCHERRER geometry using Cu-Kα_1-radiation (λ = 1.54051 Å) and a Ge(111) monochromator. The samples were grinded in a mortar and loaded into a glass capillary.

Compound names are those generated by the "*convert structure to name*" algorithm implemented in the PERKIN ELMER ChemBioDraw Ultra 13.0 software.

Quantum-Chemical Calculations. Structures for all investigated compounds were optimized at the PBE0-D3/def2-SVP level of theory.[2–6] Structures for stacked conformations were obtained by stacking optimized monolayered compounds without further optimization steps Molecular orbital energies and resulting Kohn-Sham band gaps were extracted from single point calculations on the same level of theory. Vertical radical cation and radical anion stabilization energies were calculated as differences in total energies with respect to the total energy of the neutral species. Double differences in vertical stabilization energies were reported with respect to the ATEBPY-COF hexagon.

Potential energy curves for stacked conformations were obtained by calculating single point energies for dimers of the ATEBPY-COF hexagon on M06/def2-SVP level of theory.[6,7] Dimers were modeled by stacking two optimized hexagons and varying stacking distances in 0.1 Å steps first and in 0.01 Å steps in z-direction after localizing the minimum next.

Geometry optimizations were performed using the Turbomole program package (TURBOMOLE V7.0 2015, a development of University of Karlsruhe and Forschungszentrum Karlsruhe GmbH, 1989-2007, TURBOMOLE GmbH, since 2007; available from http://www.turbomole.com), all other quantum chemical calculations using the FermiONs++ program package.[8]

B. Synthetic Procedures

Scheme S1. Three-step synthesis of starting material 1,3,6,8-tetraethynylpyrene (**13**). Reagents and conditions: *i)* Br$_2$, PhNO$_2$, 120 °C, 4 h; *ii)* TMS-acetylene, Pd(PPh$_3$)$_4$, CuI, NEt$_3$/toluene, 80 °C, 20 h; *iii)* K$_2$CO$_3$, MeOH, rt, 24 h.

1,3,6,8-Tetrabromopyrene

1,3,6,8-Tetrabromopyrene.
C$_{16}$H$_6$Br$_4$, MW = 517.84 g mol^{-1}.

According to ref.[9] To a solution of pyrene (2.02 g, 10.0 mmol, 1 eq) in nitrobenzene (20 mL) was slowly added bromine (2.26 mL, 44.0 mmol, 4.4 eq) over a period of 1 h with the aid of a syringe pump. The resulting slurry was kept at 120 °C for 4 h and then allowed to cool to room temperature. The precipitate was collected, washed with copious amounts of ethanol and dried in a desiccator to yield the desired compound (4.83 g, 9.32 mmol, 93.2 %) as an off-white solid.

MS (DEI+, LR)**:**Calculated for C$_{16}$H$_6$Br$_4$: 517.7 m/z found: 517.5 m/z [M]$^+$

1,3,6,8-Tetrakis[(trimethylsilyl)ethynyl]pyrene

1,3,6,8-Tetrakis[(trimethylsilyl)ethynyl]pyrene.
$C_{36}H_{42}Si_4$, MW = 587.07 g mol^{-1}.

According to ref.[10],[11] A degassed suspension of 1,3,6,8-tetrabromopyrene (518 mg, 1.00 mmol, 1 eq) in a mixture of toluene (4 mL) and triethylamine (12 mL) was charged with tetrakis(triphenylphosphine)palladium(0) (173 mg, 150 µmol, 0.15 eq) and copper(I)iodide (57.1 mg, 300 µmol, 0.3 eq) and was heated to 50 °C. Subsequently, (trimethylsilyl)acetylene (793 µL, 5.50 mmol, 5.5 eq) was added dropwise through a rubber septum and the yellow reaction mixture was kept at 80 °C overnight under inert atmosphere. After dilution with dichloromethane (48 mL), the dark orange suspension was filtrated through celite powder, washed with saturated ammonium chloride solution, 0.1 M hydrochloric acid as well as brine (50 mL, respectively) and was evaporated to dryness. Purification of the orange-red residue by flash column chromatography (cyclohexane/toluene, 20:1) provided the desired compound (481 mg, 0.819 mmol, 81.9 %) as a bright orange solid.

^{1}H-NMR (CDCl$_3$, 270 MHz)**:** δ = 8.59 (s, 4H), 8.30 (s, 2H), 0.37 (s, 36H) ppm. **^{13}C{^{1}H}-NMR** (CDCl$_3$, 68 MHz)**:** δ = 134.6, 132.1, 127.1, 122.8, 118.7, 102.9, 102.0, 0.2 ppm. **MS** (DEI+, LR)**:** Calculated for C$_{36}$H$_{42}$Si$_4$: 586.2 m/z found: 586.3 m/z [M]$^+$

1,3,6,8-Tetraethynylpyrene
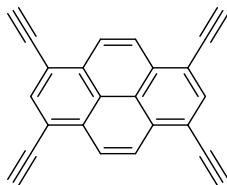
1,3,6,8-Tetraethynylpyrene.
$C_{24}H_{10}$, MW = 298.34 g mol^{-1}.

Potassium carbonate (1.11 g, 8.00 mmol, 8 eq) was added to a suspension of 1,3,6,8-tetrakis[(trimethylsilyl)ethynyl]pyrene (587 mg, 1.00 mmol, 1 eq) in methanol (58 mL). The mixture was vigorously stirred at room temperature for 24 h, then poured into water (290 mL) and deep-freezed overnight. After thawing at room temperature, the fine precipitate was collected by filtration and rinsed neutral with water. The residual filter cake was washed with a small amount of ice-cold methanol and dried in a desiccator to afford the desired compound (293 mg, 0.982 mmol, 98.2 %) as a yellow solid.

1H-NMR (THF-d$_8$, 400 MHz, 50 °C)**:**δ = 8.68 (s, 4H), 8.35 (s, 2H), 4.27 (s, 4H) ppm. **13C{1H}-NMR** (THF-d$_8$, 101 MHz, 50 °C)**:** δ = 135.3, 133.0, 127.5, 124.2, 118.9, 86.1, 81.5 ppm. **MS** (DEI+, LR)**:** Calculated for C$_{24}$H$_{10}$: 298.1 m/z found: 298.2 m/z [M]$^+$

1,3,6,8-Tetrakis(4-ethynylbenzaldehyde)pyrene
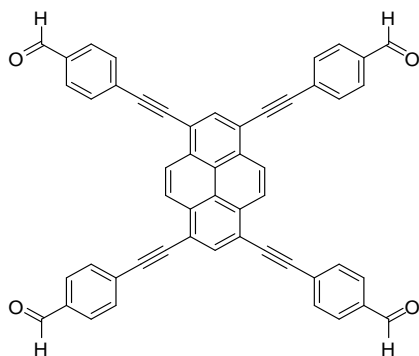
1,3,6,8-Tetrakis(4-ethynylbenzaldehyde)pyrene. (TEBPY)
$C_{52}H_{26}O_4$, MW = 714.78 g mol^{-1}.

A degassed solution of 4-bromobenzaldehyde (793 mg, 4.20 mmol, 6 eq) in a mixture of tetrahydrofuran (14 mL) and triethylamine (14 mL) was charged with tetrakis(triphenylphosphine)palladium(0) (8.1 mg, 7.0 µmol, 0.01 eq) and copper(I) iodide (2.7 mg, 14 µmol, 0.02 eq) and stirred at room temperature until all solids dissolved. 1,3,6,8-tetraethynylpyrene (209 mg, 0.700 mmol, 1 eq) was added and the resulting orange suspension was kept at 70 °C for 24 h under inert atmosphere. After addition of pyridine (2 mL) and stirring for 5 min at room temperature, the red fine precipitate was collected *via* filtration and successively washed with pyridine, tetrahydrofuran, acetone as well as dichloromethane to give TE**B**PY (428 mg, 0.599 mmol, 85.5 %) as a fine red powder.

MS (DEI+, HR)**:** Calculated for $C_{52}H_{26}O_4$: 714.1831 m/z found: 714.1860 m/z [M]$^+$

IR (FT, ATR)**:** $\tilde{\nu}$ = 2820 (*v*CHO), 2725 (*v*CHO), 2198 (*v*C≡C), 1700 (*v*C=O), 1598 (*v*C=C, ar), 1559, 1507, 1470, 1413, 1382, 1302, 1285, 1208, 1163, 1101, 1012, 888, 820 (*δ*CH, oop), 777, 713 cm^{-1}

1,3,6,8-Tetrakis(6-ethynylnicotinaldehyde)pyrene
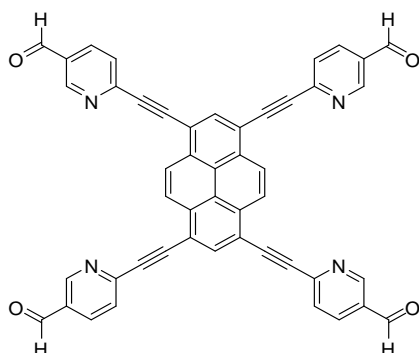
1,3,6,8-Tetrakis(6-ethynylnicotinaldehyde)pyrene.
$C_{48}H_{22}N_4O_4$, MW = 718.73 g mol^{-1}.

A degassed solution of 6-bromo-3-pyridinecarboxaldehyde (822 mg, 4.20 mmol, 6 eq) in a mixture of tetrahydrofuran (14 mL) and triethylamine (14 mL) was charged with tetrakis(triphenylphosphine)palladium(0) (8.1 mg, 7.0 µmol, 0.01 eq) and copper(I) iodide (2.7 mg, 14 µmol, 0.02 eq) and stirred at room temperature until all solids dissolved. 1,3,6,8-tetraethynylpyrene (209 mg, 0.700 mmol, 1 eq) was added and the resulting orange suspension was kept at 70 °C for 24 h under inert atmosphere. After addition of pyridine (2 mL) and stirring for 5 min at room temperature, the red fine precipitate was collected *via* filtration and successively washed with pyridine, tetrahydrofuran, acetone as well as dichloromethane to give TENPY (336 mg, 0.467 mmol, 66.8 %) as a fine red powder.

MS (DEI+, HR)**:** Calculated for $C_{48}H_{22}N_4O_4$: 718.1641 m/z found: 718.1642 m/z [M]$^+$

IR (FT, ATR)**:** $\tilde{\nu}$ **=** 2831 (*v*CHO), 2728 (*v*CHO), 2200 (*v*C≡C), 1696 (*v*C=O), 1583 (*v*C=C, ar), 1552, 1496, 1476, 1403, 1355, 1282, 1247, 1190, 1159, 1118, 1018, 900, 831 (*δ*CH, oop), 782, 751, 713 cm^{-1}

1,3,6,8-Tetrakis(2-ethynylpyrimidine-5-carbaldehyde)pyrene
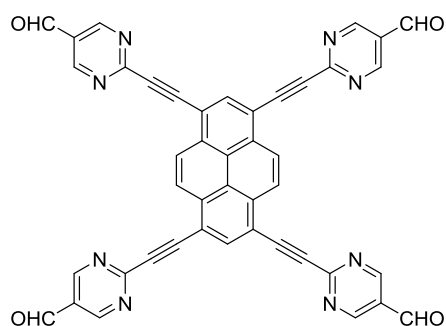
1,3,6,8-Tetrakis(2-ethynylpyrimidine-5-carbaldehyde)pyrene.
$C_{48}H_{22}N_4O_4$, MW = 722.68 g mol^{-1}.

A degassed solution of 2-chloropyrimidine-5-carboxaldehyde (220 mg, 1.38 mmol, 5.5 eq) in a mixture of tetrahydrofuran (5 mL) and triethylamine (5 mL) was charged with tetrakis(triphenylphosphine)palladium(0) (5.8 mg, 5.0 µmol, 0.02 eq) and copper(I) iodide (1.9 mg, 10 µmol, 0.04 eq) and stirred at room temperature until all solids dissolved. 1,3,6,8-tetraethynylpyrene (75 mg, 0.25 mmol, 1 eq) was added and the resulting orange suspension was kept at 70 °C for 24 h under inert atmosphere. After addition of pyridine (0.2 mL) and stirring for 5 min at room temperature, the red fine precipitate was collected *via* filtration and successively washed with pyridine, CH$_2$Cl$_2$, THF, Isopropanol, water, 1M HCl,water, dilute NaHCO$_3$, water, isopropanol and diethylether to give TE**P**PY (110 mg, 0.152 mmol, 60.9 %) as a fine brown powder.

MS (MALDI-TOF, Anthracene in acetone, LR)**:** Calculated for $C_{44}H_{18}N_8O_4$: 722.14 m/z found: 721.1 m/z [M-H]⁻ **IR** (FT, ATR)**:** $\tilde{v}$ **=** 2845 (*v*CHO), 2726 (*v*CHO), 2201 (*v*C≡C), 1657 (*v*C=O), 1592 (*v*C=C, ar), 1526, 1426, 1359, 1210, 1171, 1023, 902, 835 (*δ*CH, oop) cm^{-1}
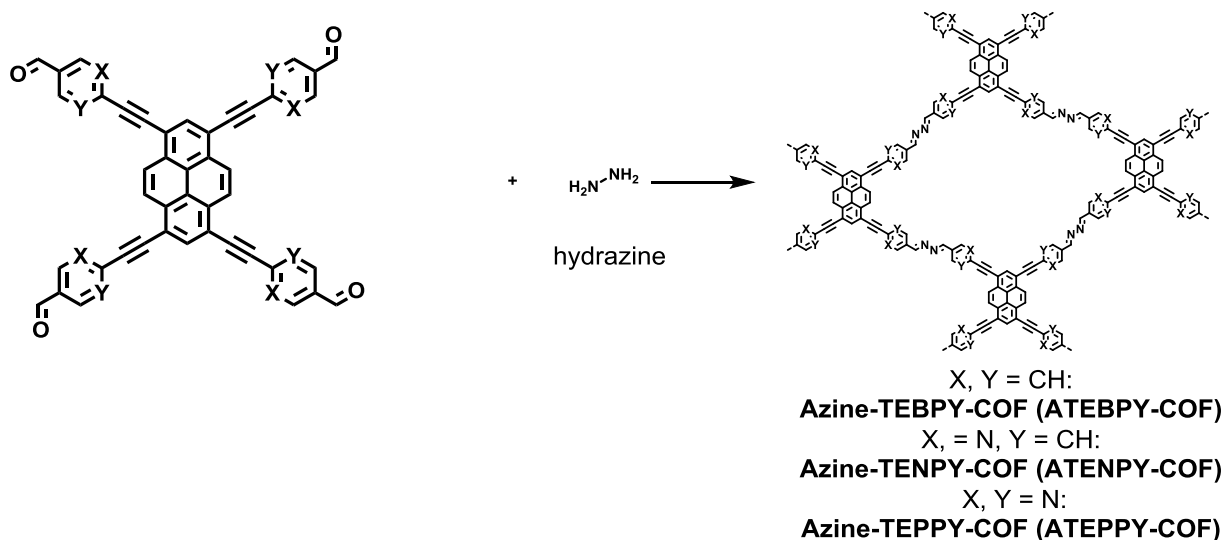
Scheme S2. Synthesis of A-TEXPY-COFs by acid catalyzed azine formation.

A-TEXPY COFs

A 2 mL BIOTAGE® microwave vial was charged with the respective starting material (TE**B**PY, TE**N**PY or TE**P**PY, 17.2 mg, 24.0 µmol, 1 eq), capped with a common NS14 rubber septum and flooded with argon by three pump/purge cycles. After addition of the solvent mixture, the resulting suspension was degassed by four pump/purge cycles under vigorous stirring. 6M aqueous acetic acid (0.1 mL, 0.6 mmol, 25 eq for TE**B**PY / 0.2 mL, 1.2 mmol, 50 eq. in case of TE**N**PY and 0.3 mL, 1.5 mmol, 75 eq in cas of TE**P**PY) was then added all at once, directly followed by addition of hydrazine hydrate (3.53 µL, 72.0 µmol, 3 eq). The vial was sealed and heated to 130 °C for 40 min under microwave irradiation. After cooling to room temperature, the vial was transferred to a muffle furnace, where it was slowly heated to 120 °C over a period of 2 h and maintained at this temperature for 72 h. After slow cooling, the fluffy red to brown precipitate was collected *via* suction filtration and thoroughly washed with dimethylformamide (3 × 2.5 mL), tetrahydrofuran (3 × 2.5 mL) and dichloromethane (3 × 2.5 mL). Subsequent drying *in vacuo* furnished A-TE**B**PY-COF, A-TE**N**PY-COF or A-TE**P**PY-COF as fluffy red to brown powders.

Best solvent mixtures for:

- A-TE**B**PY-COF, A-TE**N**PY-COF: *o*-dichlorobenzene/dimethylacetamide 1:2 v/v: 0.33/0.66 mL
- A-TE**P**P#Y-COF: *o*-dichlorobenzene/dimethylacetamide 1:1 v/v: 0.5/0.5 mL (75 eq. AcOH)

Analytical data for A-TE**B**PY-COF:

^{13}C{^{1}H}-NMR (MAS, 10 kHz)**:** δ = 159.8, 130.8, 125.8, 117.3, 95.4, 90.9 ppm.
IR (FT, ATR)**:** $\tilde{\nu}$ **=** 2193 (νC≡C), 1620 (νC=N), 1603 (νC=C, ar), 1509, 1407, 1300, 1209, 1171, 1104, 1015, 940, 892, 827 (δCH, oop), 716 cm^{-1}

Analytical data for A-TE**N**PY-COF:

¹³C{¹H}-NMR (MAS, 10 kHz)**:** δ = 159.6, 143.8, 127.4, 116.2, 94.8, 90.7 ppm.

IR (FT, ATR)**:** $\tilde{v}$ = 2200 (vC≡C), 1622 (vC=N), 1585 (vC=C, ar), 1551, 1496, 1471, 1373, 1314, 1278, 1250, 1125, 1021, 957, 893, 834 (δCH, oop), 754, 718 cm^{-1}

Analytical data for A-TE**P**PY-COF:

¹³C{¹H}-NMR (MAS, 10 kHz)**:** δ = 159.7, 142.6, 128.5, 117.3, 82.8, 81.8 ppm.

IR (FT, ATR)**:** $\tilde{v}$ = 2192 (vC≡C), 1658 (vC=N), 1594 (vC=C, ar), 1538, 1496, 1427, 1360, 1220, 1155, 890, 828 (δCH, oop) cm^{-1}
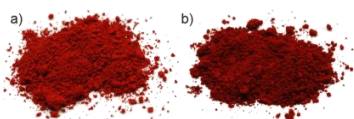
Figure S1. Photographs of COFs obtained from TE**B**PY (a) and TE**N**PY (b)
Photographs were taken with identical exposure parameters.

A-TEXPY COFs @ FTO (X = B, N)

A 25mL teflon liner in a conventional stainless-steel autoclave was charged with the respective starting material (TE**B**PY, TE**N**PY or TE**P**PY, 6.8 mg, 9.5 µmol, 1 eq) under a flow of nitrogen. A freshly cleaned FTO-coated glass substrate (Sigma Aldrich) was placed in a homemade, Π-shaped Teflon holder, 5 mm away from the bottom of the liner.[12] The FTO side of the substrate points towards the bottom of the liner. After addition of the solvent mixture (1:1 v/v 2.1/2.1 mL dioxane/*o*-dichlorobenzene), 6M aqueous acetic acid (25 µL, 0.15 mmol, 25 eq for TE**B**PY / 50 µL, 0.3 mmol, 50 eq. in case of TE**N**PY) was then added all at once, directly followed by addition of hydrazine hydrate (2.33 µL, 47.5 µmol, 5 eq). The auotclave was sealed and heated to 120 °C for 12 h in a pre-heated muffle furnace. The coated substrates were removed, washed with DMF and ethanol and dried in a steam of nitrogen. This procedure did not yield any coated substrates for ATEPPY-COF.

After an extensive solvent screening (see below), the best conditions in terms of maximizing the BET surface area were applied to the synthesis of the COFs.

Solvent screening results and BET surface area of the products obtained from the condensation reaction[†] between **TEBPY**, **TENPY** and **TEPPY** and hydrazine hydrate.

Solvent mixture[‡]		BET surface area [$m^2\,g^{-1}$]		
		TE**B**PY	TE**N**PY	TE**P**PY
anisole		470	—	—
dioxane		565	212[*]	—
dioxane/mesitylene	1:1	412	—	—
dioxane/mesitylene	1:2	313	—	—
diphenyl ether		566	201[*]	—
o-DCB		553	—	
o-DCB/anisole	1:1	565	212	
o-DCB/*n*-BuOH	19:1	405	—	
o-DCB/DMA	1:2	668/556[#]	410/470[*]	625[*]/720[§]
o-DCB/DMA	1:1	589	397	921[§]
o-DCB/DMA	2:1	515	—	—
o-DCB/dioxane	1:1	681	400[*]	—
o-DCB/*n*-BuOH	1:1	—	—	815[§]

[†] general conditions: Monomer (1 eq), 6M AcOH (25 eq), $N_2H_4 \cdot H_2O$ (3 eq),
  1 mL total solvent volume, 40 min at 130 °C (microwave), 72 h at 120 °C

[‡] stated ratios refer to parts per volume

[*] 50 eq instead of 25 eq were used

[§] 75 eq instead of 25 eq were used

[#] conventional oil bath synthesis

C. Powder X-ray diffraction and simulation

Molecular modeling of the COF was carried out using the Materials Studio (6.0) suite of programs by Accelrys.

The unit cell was defined by one TE**B**PY (A-TE**B**PY-COFs) molecule bonded via four azine linkages to hydrazine. The initial structure was geometry optimized using the MS Forcite molecular dynamics module (Universal force fields, Ewald summations), and the resulting distance between opposite formyl carbon atoms in the structure was used as the a and b lattice parameters (initially 16 and 18 Å) of the unit cell with $P2_1/m$ symmetry (c centered), taking into account the non-C_4 geometry of TE**B**PY and the shifted AA' stacking observed for LH_4 * DMF single crystals.[13] The crystal structure was geometry optimized using Forcite (resulting in $a = 25.1$ Å, $b = 6.7$ Å and $c = 25.2$ Å for A-TE**B**PY-COF). The AA structure with $P2/m$ symmetry and the AB structure ($P2_1/m$) were simulated accordingly.
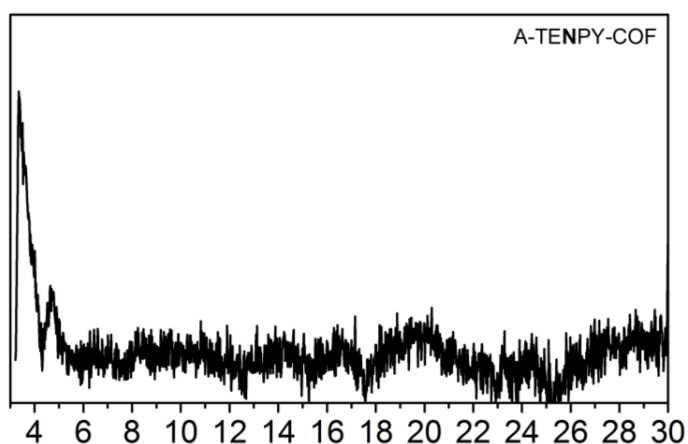
Figure S2. PXRD of A-TE**N**PY-COF confirming its crystallinity.
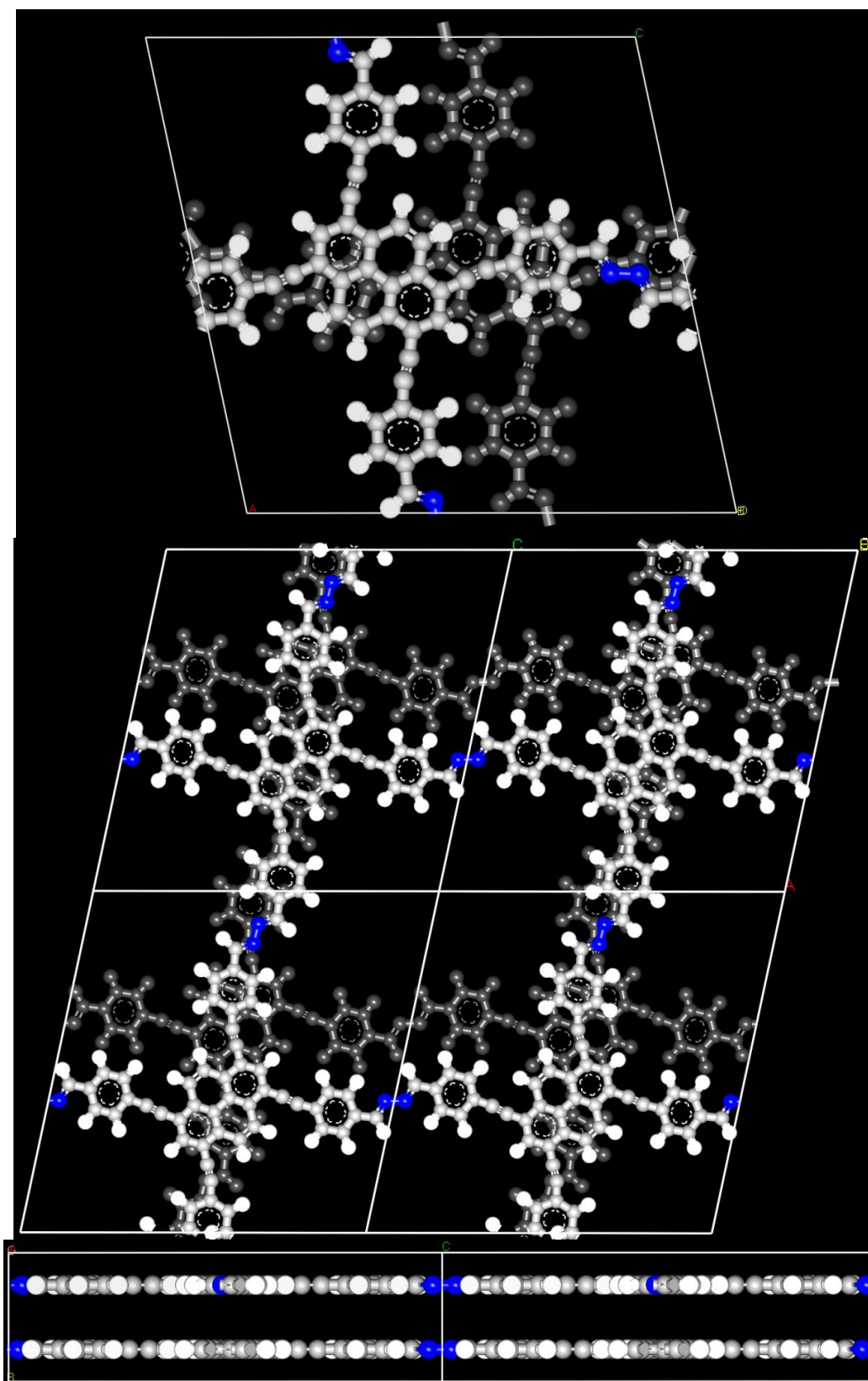
Figure S3. A-TEBPY-COF: Simulation of the unit cell content calculated in a shifted (sh)-AA' arrangement: View onto the *ab*-plane (top), view onto the *ab*-plane with four unit cells (middle) and view perpendicular to the *c*-axis (bottom).
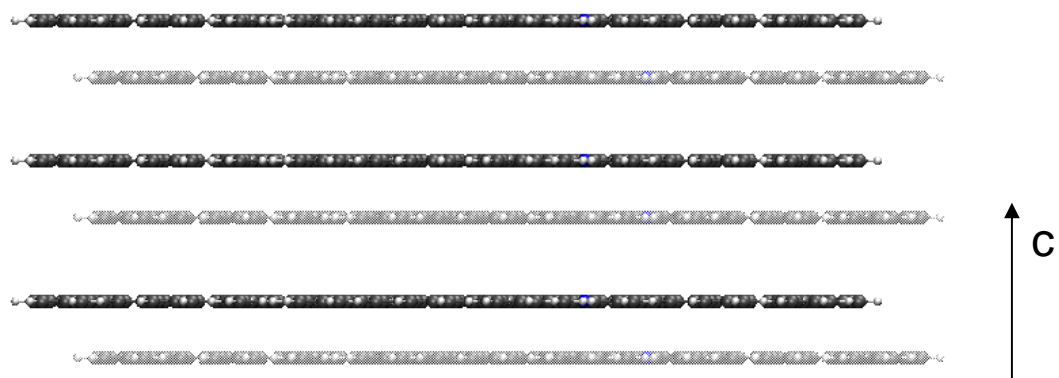
Figure S4. A-TEBPY-COF: Simulation of the unit cell content calculated in a sh-AA' arrangement: view perpendicular to the *c*-axis along three unit cells visualizing the zigzag-type pattern.
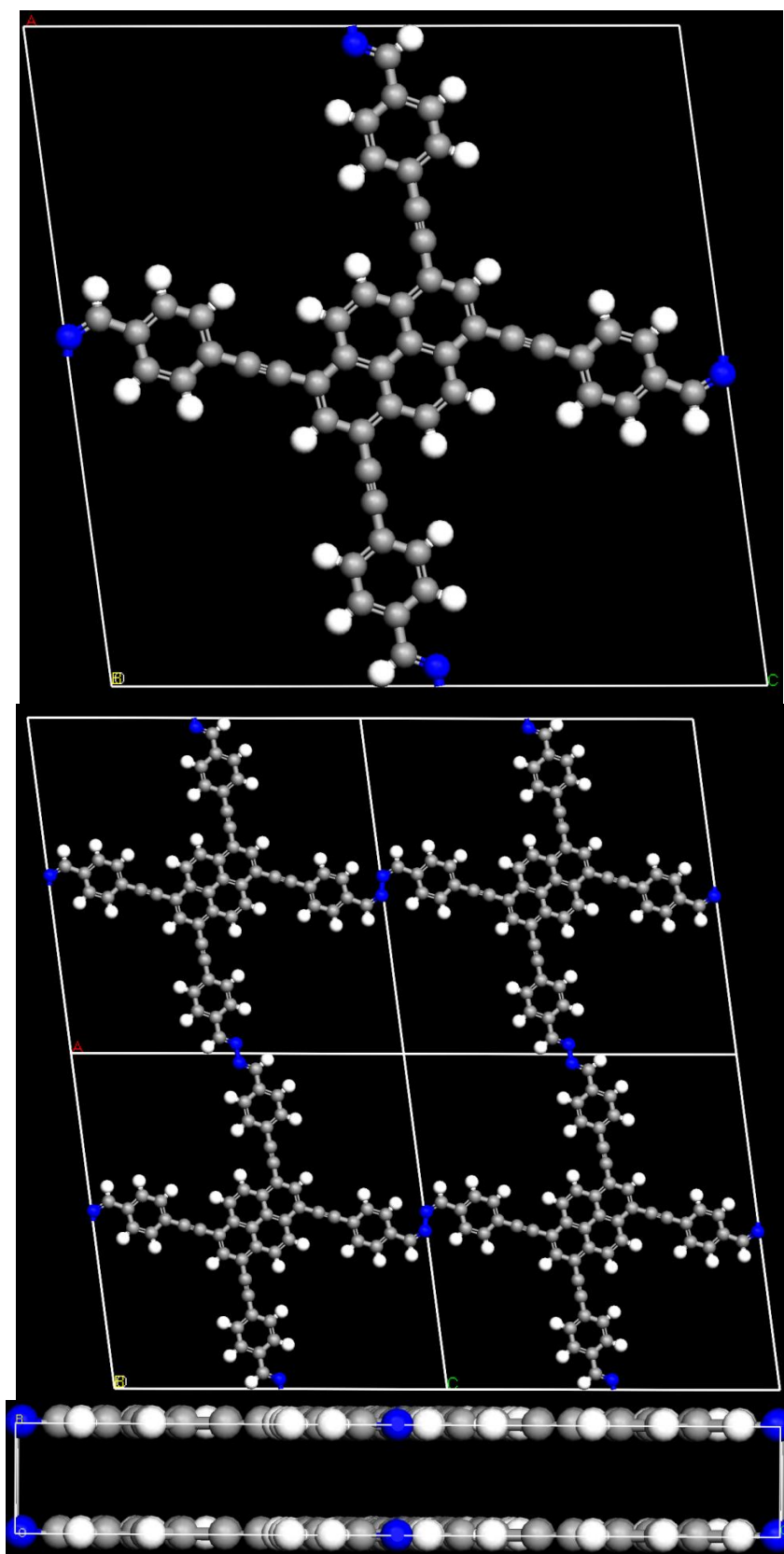
Figure S5. A-TEBPY-COF: Simulation of the unit cell content calculated in an eclipsed AA arrangement: View onto the *ac*-plane (top), view onto the *ab*-plane with four unit cells (middle) and view perpendicular to the *c*-axis (bottom).
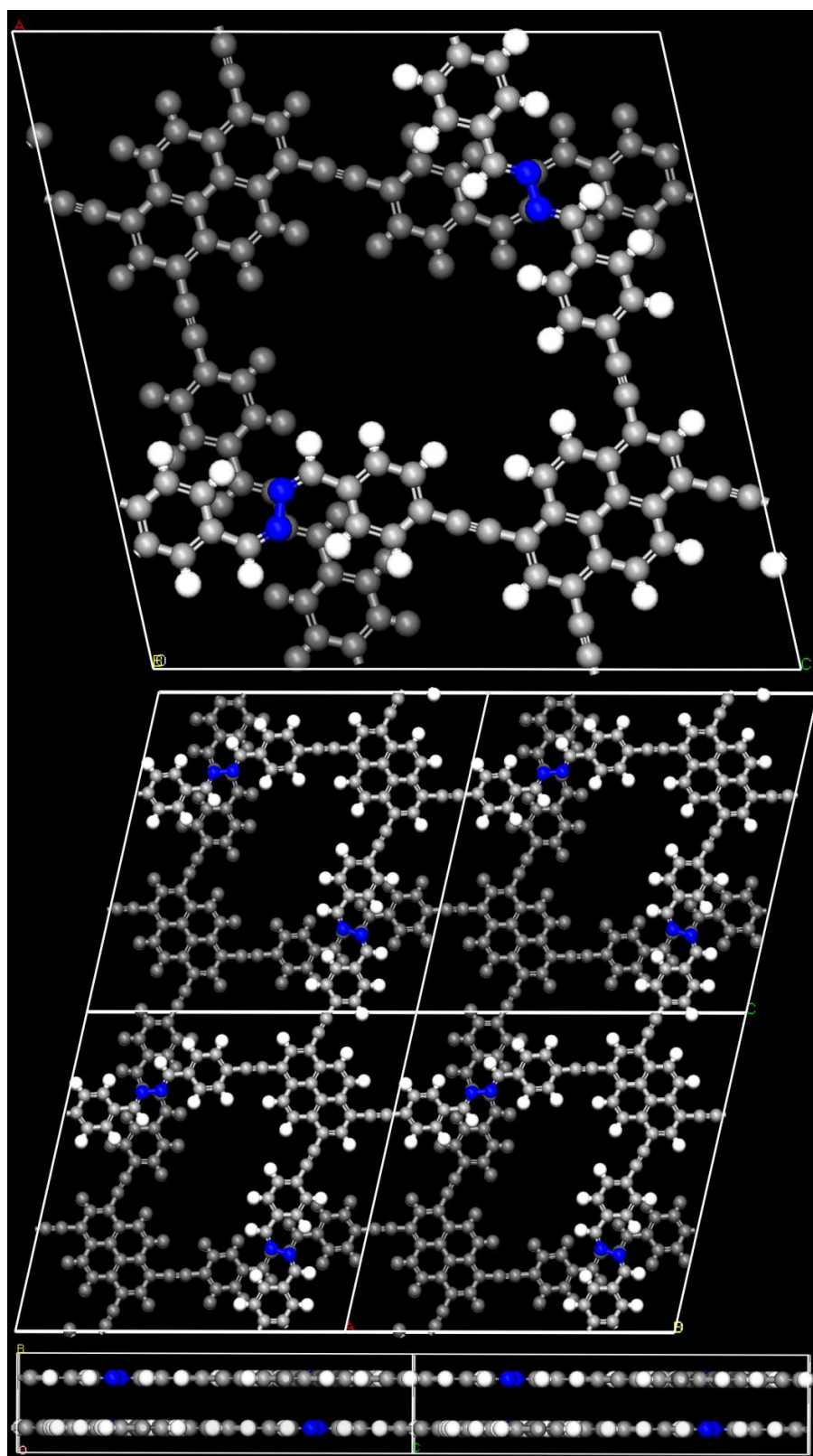
Figure S6. A-TE**B**PY-COF: Simulation of the unit cell content calculated in an AB arrangement, where the underlying layer is directly centered in the pore of the top layer: View onto the *ab*-plane (top), view onto the *ac*-plane with four unit cells (middle) and view perpendicular to the *c*-axis (bottom).

D.   FT-IR Spectra
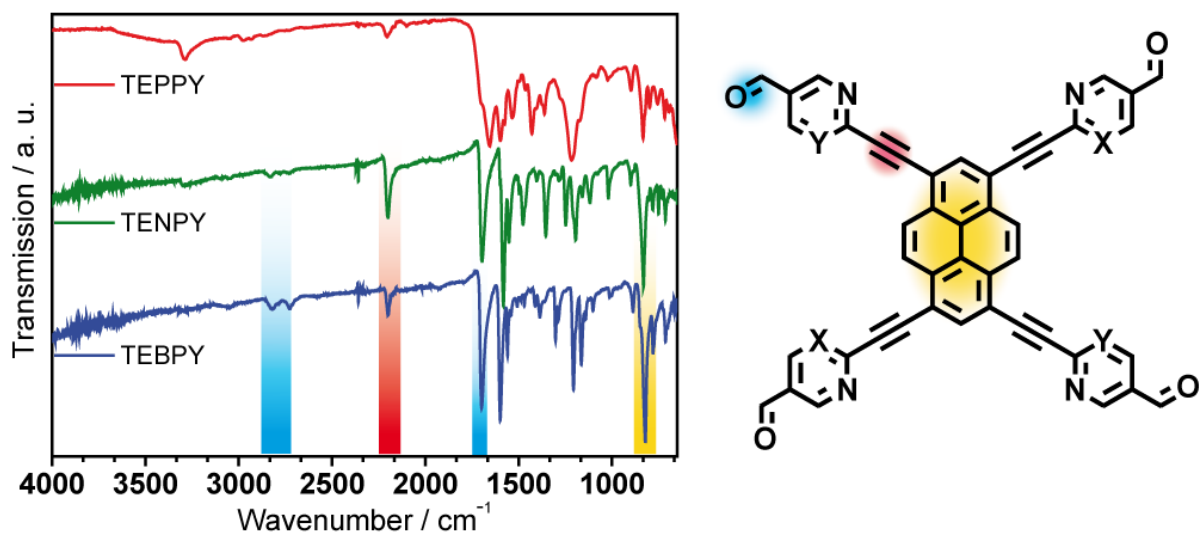
Figure S7. Stack plot showing the FT-IR spectra of TEXPY molecules. The band highlighted yellow at 821 cm^{-1} corresponds to the C-H out of plane stretching of pyrene.[14] The band highlighted blue at 2700 cm^{-1} corresponds to the Fermi double resonance of CHO, and the band highlighted in red corresponds to the CC triple bond stretch vibration.
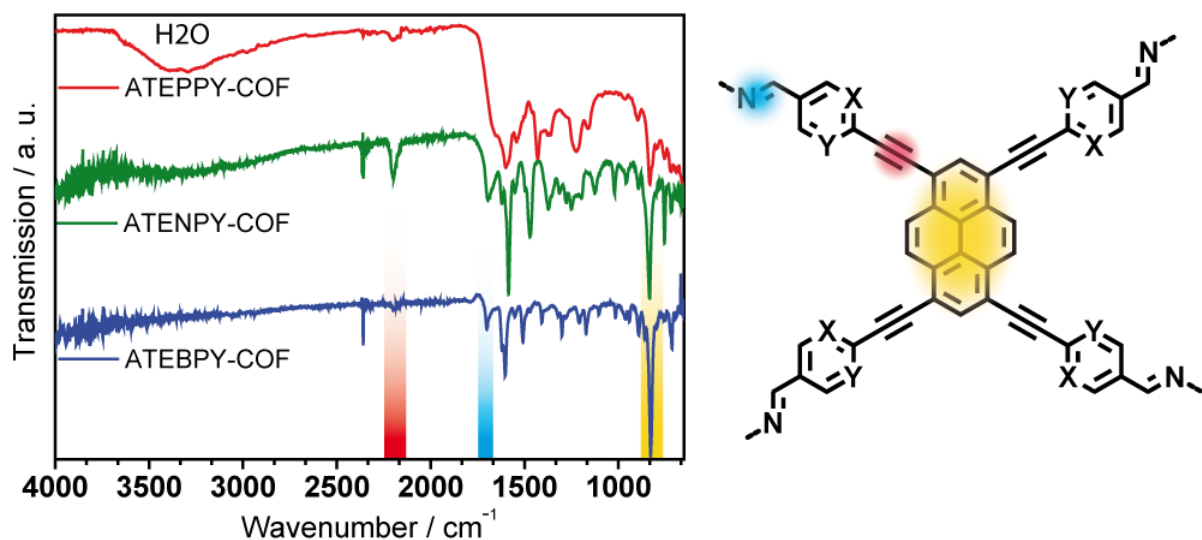
Figure S8. Stack plot showing the FT-IR spectra of A-TEXPY-COFs. The band highlighted yellow at 821 cm^{-1} corresponds to C-H out of plane stretching of pyrene.[14] The band highlighted blue at 1620 cm^{-1} corresponds to the C=N double bond, and the band highlighted in red corresponds to the CC triple bond stretch vibration.

E.   CP-MAS NMR Measurements

All molecular building blocks are hardly soluble in common organic solvents. Their identity has been proven by means of solid-state NMR (ssNMR, see below) and mass spectrometry (see section B). In all ^{13}C CP-MAS NMR spectra, asterisks indicate spinning side bands. The local molecular structure of the building blocks remains intact during COF formation, as evidenced by the largely unchanged chemical shifts of the peripheral phenyl rings and the internal alkyne (≈ 85-95 ppm) (ESI, see regions highlighted by red color in Figs. S9-12). By increasing the nitrogen content in the A-TEXPY-COF series, new downfield shifted peaks arise next to the aromatic region indicating the carbon atoms situated next to the nitrogen atom in the heterocycles (≈ 140 ppm) (see regions highlighted by green color in Figs. S9, 11-12).
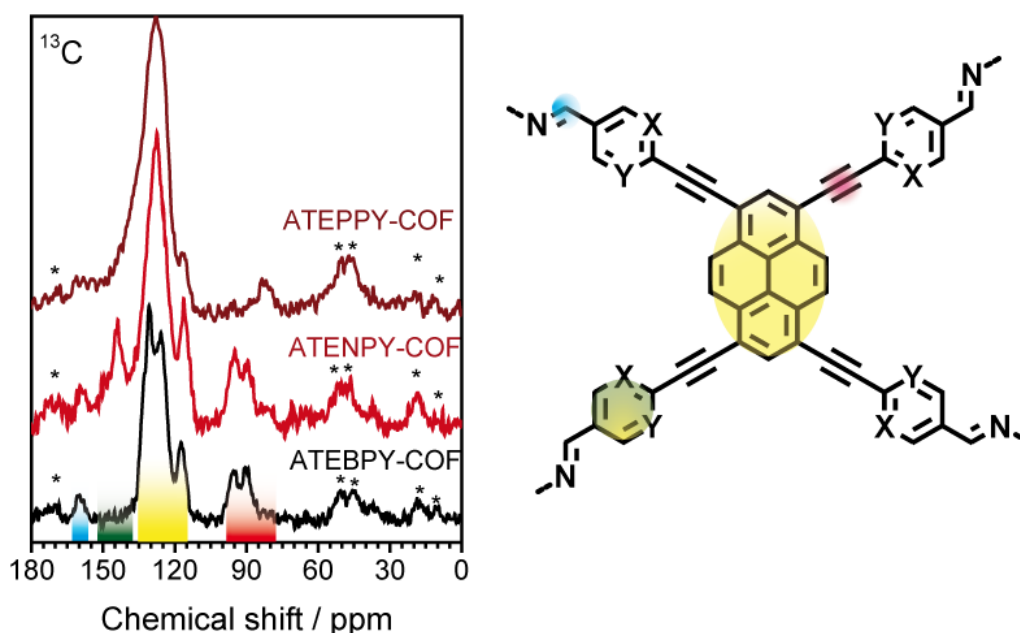
Figure S9. ssNMR characterization of A-TEXPY-COFs by ^{13}C CP-MAS NMR spectroscopy and assignment of spectral data. The change of the peripheral aromatic units from phenyl to pyridyl and pyrimidyl is accompanied with the appearance of new downfield shifted signals (region is marked by green color).
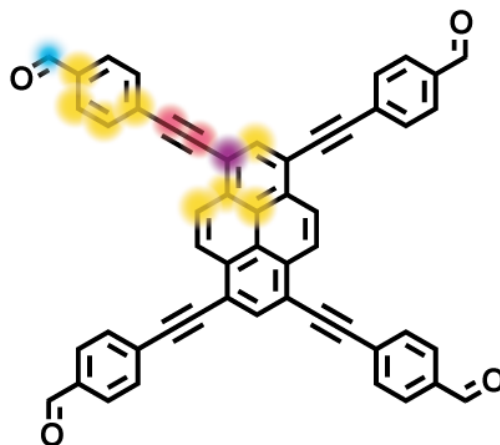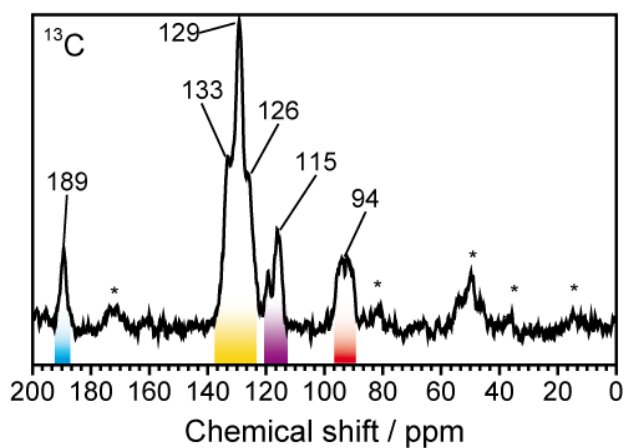
Figure S10. ^{13}C ssNMR of TE**B**PY linker. The peaks at 133 ppm correspond to the aromatic carbon atom next to the aldehyde group and the one at 126 ppm to the bay pyrene carbons.
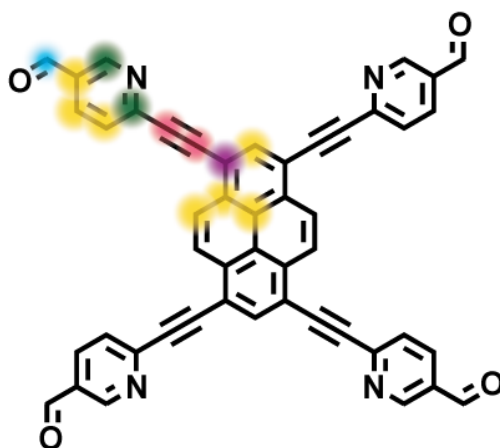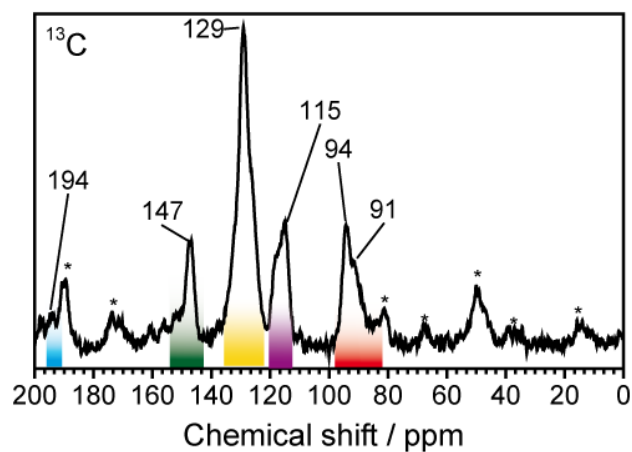
Figure S11. ^{13}C ssNMR of the TE**N**PY linker.
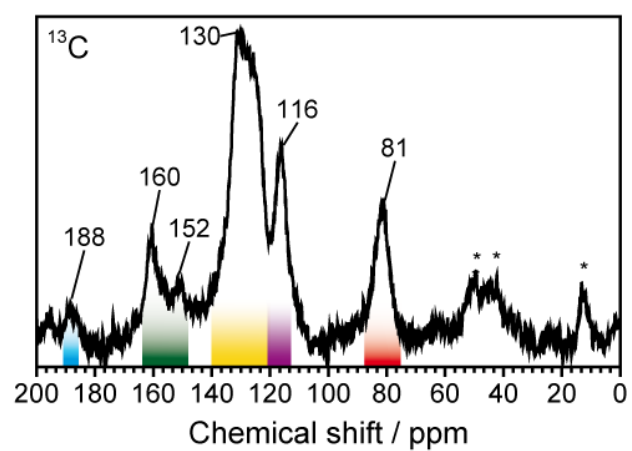
Figure S12. ^{13}C ssNMR of the TE**P**PY linker.

^{1}H solid-state MAS NMR spectroscopy of A-TEXPY-COFs shows the presence of aromatic protons through signals at 7.0 – 7.5 ppm. With increasing nitrogen content the peak of this singal shifts further downfield. The signal around 3.7 ppm corresponds to residual water in the pores, which is increasing in intensity in line with the increasing nitrogen content and accordingly increasing hydrophilicity of the COFs.
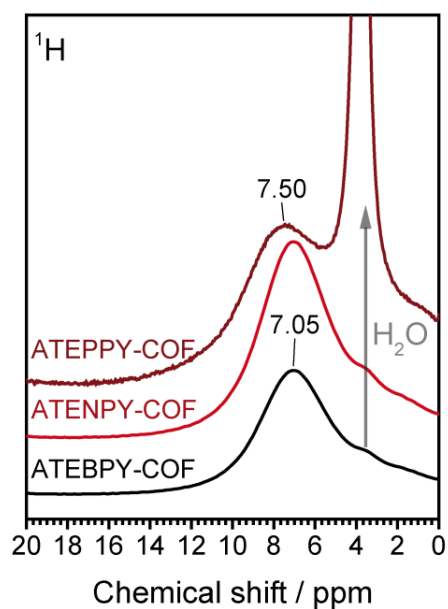
Figure S13. ssNMR characterization of A-TEXPY-COFs by ^{1}H MAS NMR spectroscopy. The change of the peripheral aromatic units from phenyl, to pyridyl and pyrimidyl is accompanied with a small downfield shift of the signal maximum at 7.05 ppm (A-TE**B**PY) to 7.50 ppm (A-TE**P**PY) and an increase of the residual water content in the pores (3.53 ppm).

F. Ar Sorption Measurements and Pore Size Distribution
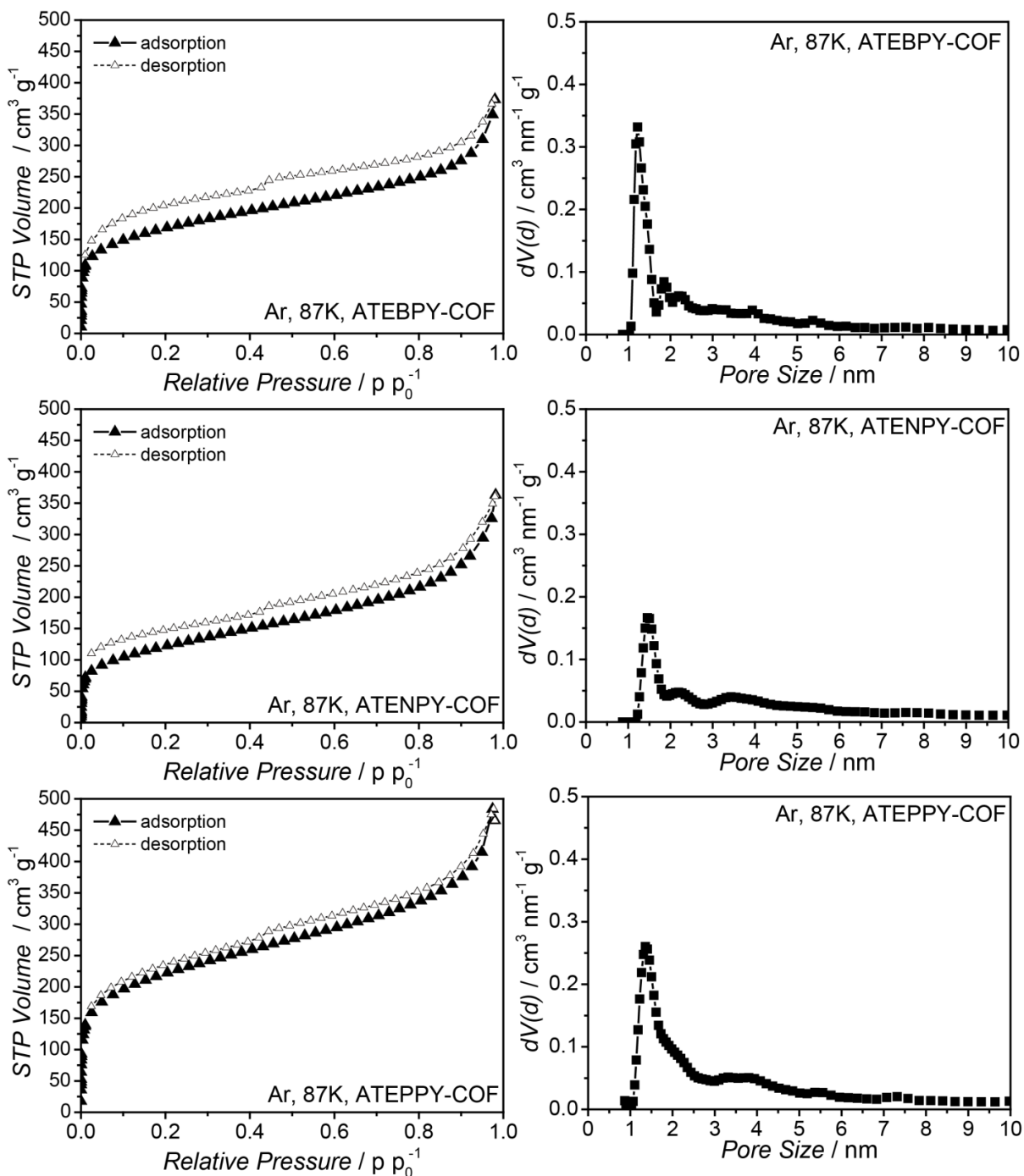
Figure S14. Argon physisorption isotherms at 87 K of A-TEXPY-COFs. The type I isotherm (adsorption: black triangles, desorption: white triangles) gives BET surface areas of 681 m^2 g^{-1} for A-TE**B**PY-COF, 470 m^2 g^{-1} for A-TE**N**PY-COF and 920 m^2 g^{-1} for A-TE**P**PY-COF, respectively. QSDFT (carbon, cylindrical pores) derived pore size distributions showing the formation of micropores in A-TEXPY-COFs with maxima between 1.2-1.4 nm, consistent with the predicted size based on the sh-AA'(6.5A) stacking structure model.

G. Ar Sorption and Pore Size Simulation
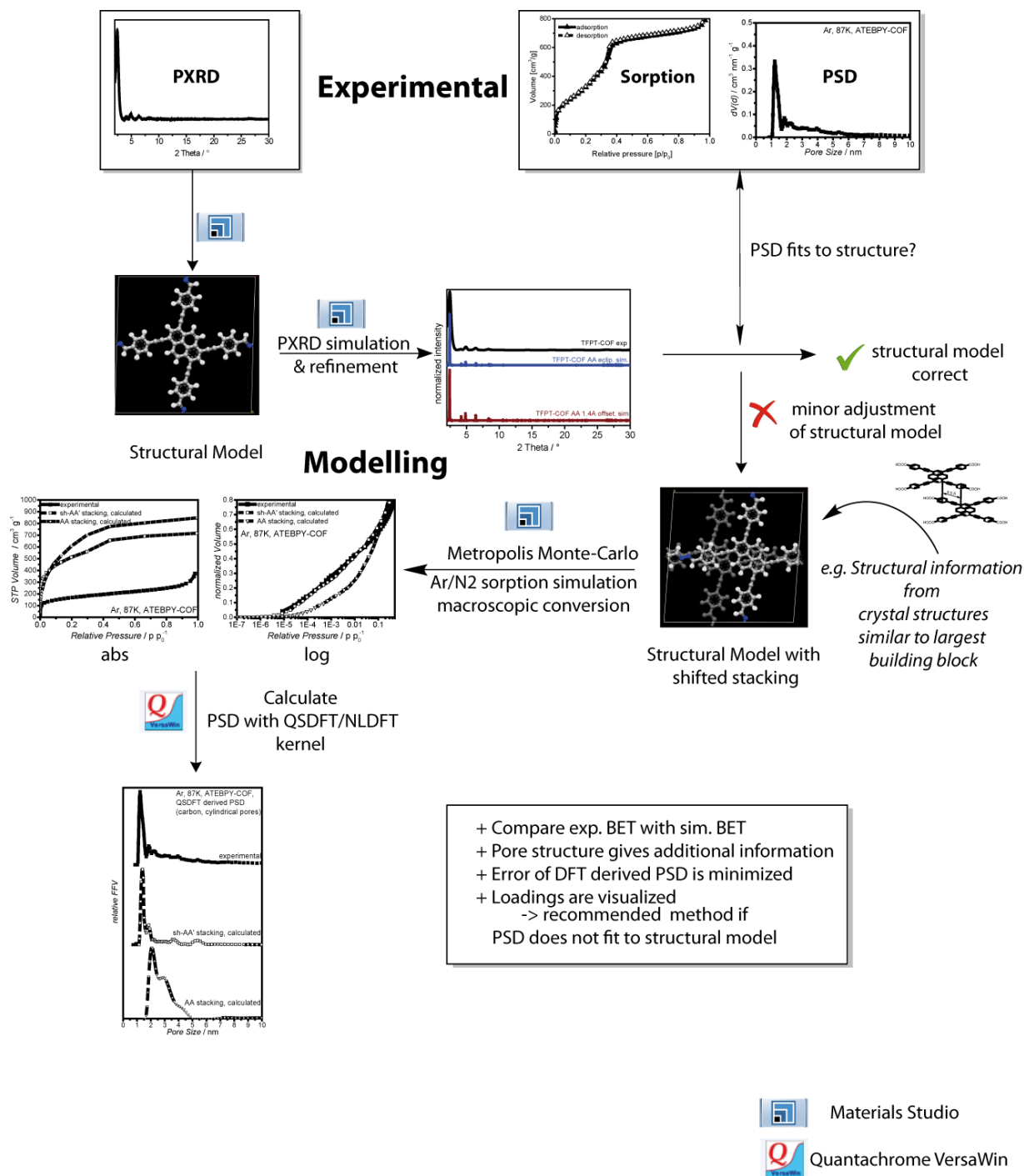
Figure S15. Flow chart to explain the structure model elucidation by pore size simulation as a complement to the structure elucidation based solely on PXRD.

Theoretical surface area calculations. Simulations of the adsorption isotherms were performed under the 'Sorption' module of Materials Studio. The Metropolis Monte Carlo method was utilized for calculation of the argon adsorption in the framework under 40 fugacity steps in a logarithmic scale (10^{-5} to 100 kPa); the Universal force field was selected for the energy calculation. All simulations included random insertion/deletion, translation, and rotation moves of molecules with equal probabilities. Atoms in COFs were fixed at their crystallographic positions. A LJ cutoff distance of 13 Å was used. The Ewald & Groups technique was used to compute the electrostatic interactions. All GCMC simulations included a 1,000,000-cycle equilibration period followed by a 10,000,000-cycle production run. The $2 \times 2 \times 2$ unit cell of A-TE**B**PY-COF were used for simulations of the Ar adsorption isotherms at 87 K. BET surface areas were determined from the calculated isotherms by the same method used for treating experimental data at the low relative pressure range of 0.005 to 0.05. With the simulated isotherms in our hand, the next step was the comparison of their extracted pore size distributions. As we applied the same QSDFT-based kernel to the simulated and experimental isotherms, potential kernel-related artifacts such as vague pore potentials apply to both.[15]

The calculated isotherms were imported into the Quantachrome Versawin(R) sorption software. Pore size distributions were then calculated by application of the QSDFT (carbon, cylindrical pores) kernel.

Comparison of the calculated PSD with the experimental PSD clearly shows that A-TE**B**PY-COF predominantly adopts the sh-AA' stacking model. We note that this procedure can be used to obtain stacking information from the PSD in cases where PXRD cannot distinguish between different stacking modes as is often the case with low quality XRD data.

Carefully considering the advantages and disadvantages of this method, extracting stacking information from the PSD is more applicable to less crystalline COFs suffering from low quality PXRDs as compared to the standard method of comparing the modelled and experimental PXRDs. The applicability of this method to other COFs will be clarified in future studies. We currently work on implementation of this method to gather more information on the pore structure of more crystalline COFs. We note that especially layer offsets in microporous COF systems can have a significant impact on the pore size distribution and, hence, properties of the materials.

We visualized the argon-accessible surface in a movie by 0.2 Å steps along the stacking axis (see attached movie).
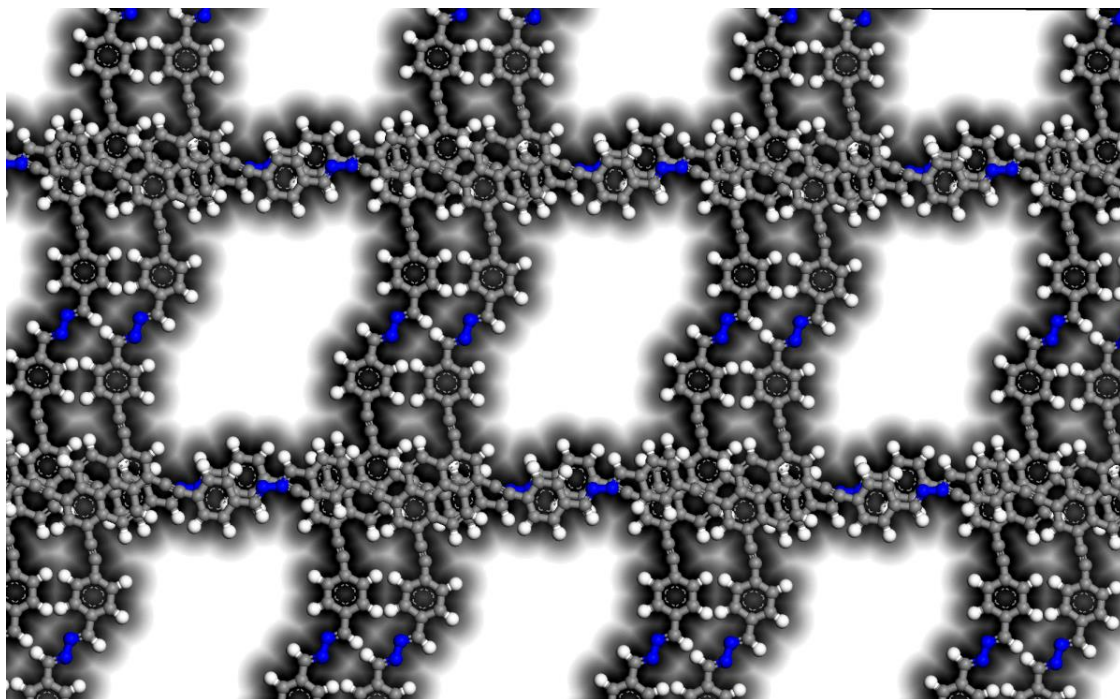
Figure S16. Accessible surface for sh-AA' layer stacking with a probe diameter of 3.6 Å (kinetic diameter of Ar) showing the formation of micropores (white color refers to a pore window with 18 Åx13 Å size).

H.   Photoluminescence measurements
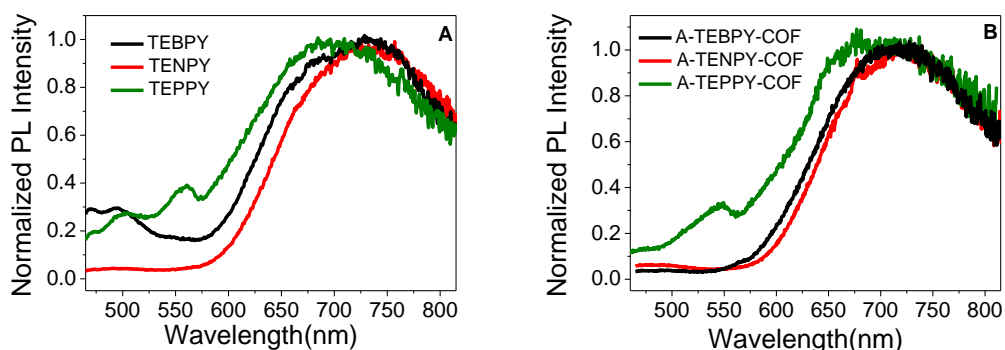
Figure S17. Normalized solid state emission spectrum of the pyrene based linkers (A) and the corresponding COFs (B) (λ_{exc}=400 nm).

Photophysical properties of the aldehyde linkers have been studied in degassed DMF and as solids (Figs. S17, Tables S2-3). In solution, structured monomer emission centered around 490-530 nm is seen for all the three linkers. The emission is red shifted by more than 50 nm as compared to molecular pyrene because of the ethynyl-phenyl units attached to the core. Quantum yields are found to be 73.01%, 57.48% and 28.36% for TEBPY, TENPY and TEPPY, respectively. For all the three compounds, the fluorescence decay profiles can be fitted with a single exponential curve, with fluorescence lifetimes around 2 ns (Table S3). As solids, however, the linkers show a broad structureless excimer emission band with λ_{max} around 700-730 nm.[16] The quantum yields of emission are at least two orders of magnitude less than those in solution. A small monomer emission feature around 500 nm can be seen for TEBPY only. Interestingly, the COF solids exhibit a similar weak, broad and structureless excimer emission band around 670-700 nm as that for the linkers when measured as solids.

Table S2: Emission properties of the linkers and the COFs at room temperature

Compound	Mode of measurement	λ_{max} (nm)	Φ_{PL}
TEBPY	DMF solution	496, 537	0.7301
	solid	730	0.0055
TENPY	DMF solution	496, 527	0.5748
	solid	730	0.0031
TEPPY	DMF solution	500, 531	0.2836
	solid	700	0.0025
A-TEBPY-COF	solid	720	0.0025
	dispersion in water	668	0.002
	TEOA + Pt precursor[a]	668	0.00029[b]
A-TENPY-COF	solid	720	0.0022
	dispersion in water	695	0.0013[b]
	TEOA + Pt precursor[a]	695	0.00023[b]
A-TEPPY-COF	solid	690	0.0007
	dispersion in water	695	0.000123[b]
	TEOA + Pt precursor[a]	695	< 0.00005[b]

All solutions have been degassed with argon before measurement. [a]Dispersion in water with TEOA and Pt precursor in respective amounts as during photocatalysis. [b]Obtained using dispersion of A-TEBPY-COF in water as the reference.

For all the three COFs, the quantum yield decreases when measured in photocatalytic conditions in the presence of the platinum precursor and the electron donor in water, vs. when measured just as dispersion in water (Table S2). Interestingly, the photoluminescence lifetimes, recorded under the same conditions using the time-correlated single-photon counting method (TCSPC), remain unperturbed (Figure S18). The quantum yield (Φ) and the excited state lifetime (τ) are related to the radiative (k_r) and the non-radiative rates (k_{nr}) in the following way –

$$\Phi = k_r/(k_r + k_{nr}) \qquad \text{Equation S2}$$

$$\tau = 1/(k_r + k_{nr}) \qquad \text{Equation S3}$$

Thus, unperturbed photoluminescence lifetimes along with the decreased absolute emission quantum efficiency of A-TEXPY-COFs implies a further slower radiative rate (with $k_{nr} \gg k_r$) in the presence of donor triethanolamine and platinum co-catalyst. It should be noted that the decrease in quantum yield of the COFs when measured as water dispersions vs. when measured as solids is most likely due to non-radiative deactivation of the excited state in H-bonding solvent water.

Because of their different degrees of crystallinity, and hence structural order, which can have possible influence on the measured parameters, it is unfortunately very difficult to extract a trend in the photophysical properties within the A-TEXPY-COF series.

Table S3: TCSPC lifetimes of the COF precursors in DMF at room temperature. All solutions have been degassed with argon before measurement.

| Compound	τ (ns)
TEBPY	1.93
TENPY	2.08
TEPPY	1.84
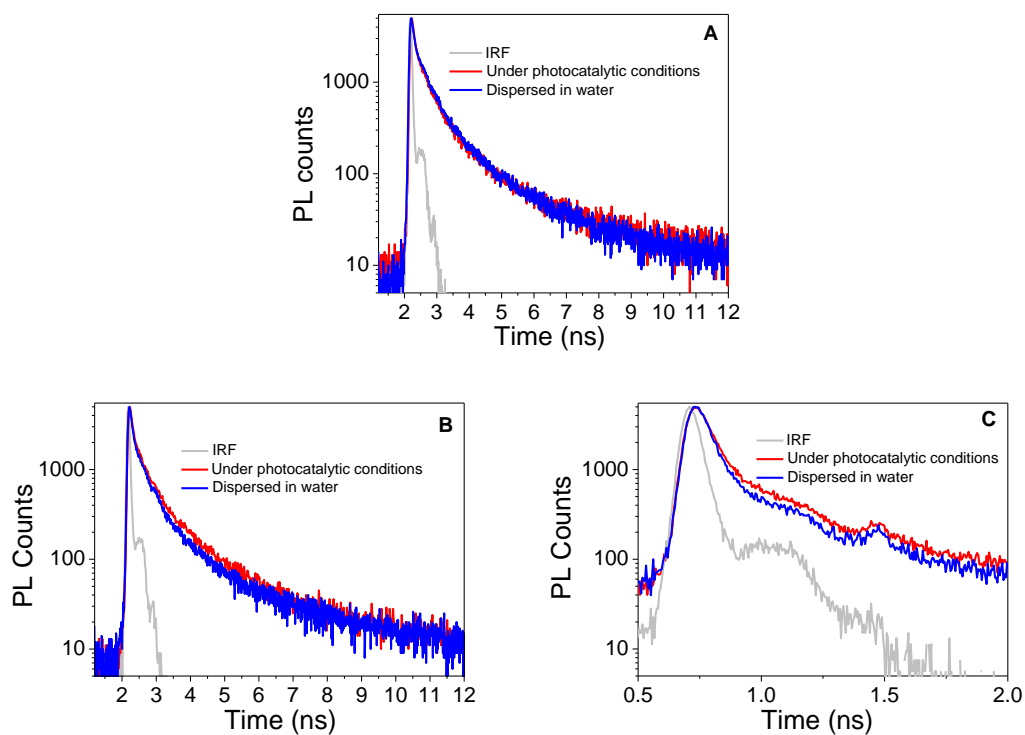
Figure S18. TCSPC decay traces of A-TEBPY-COF (A), A-TENPY-COF (B) and A-TEPPY-COF (C) in the presence and in the absence of triethanolamine donor and platinum precursor.
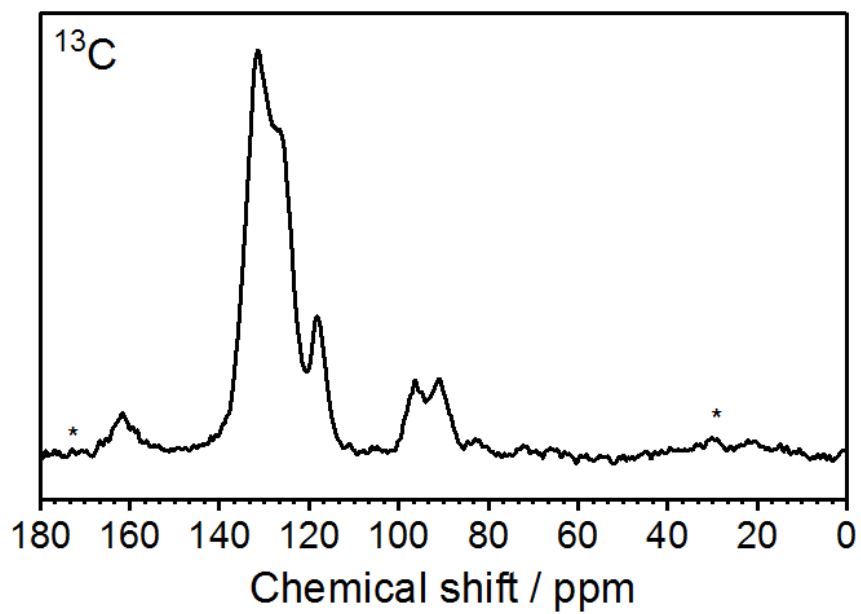
I. Tauc plots
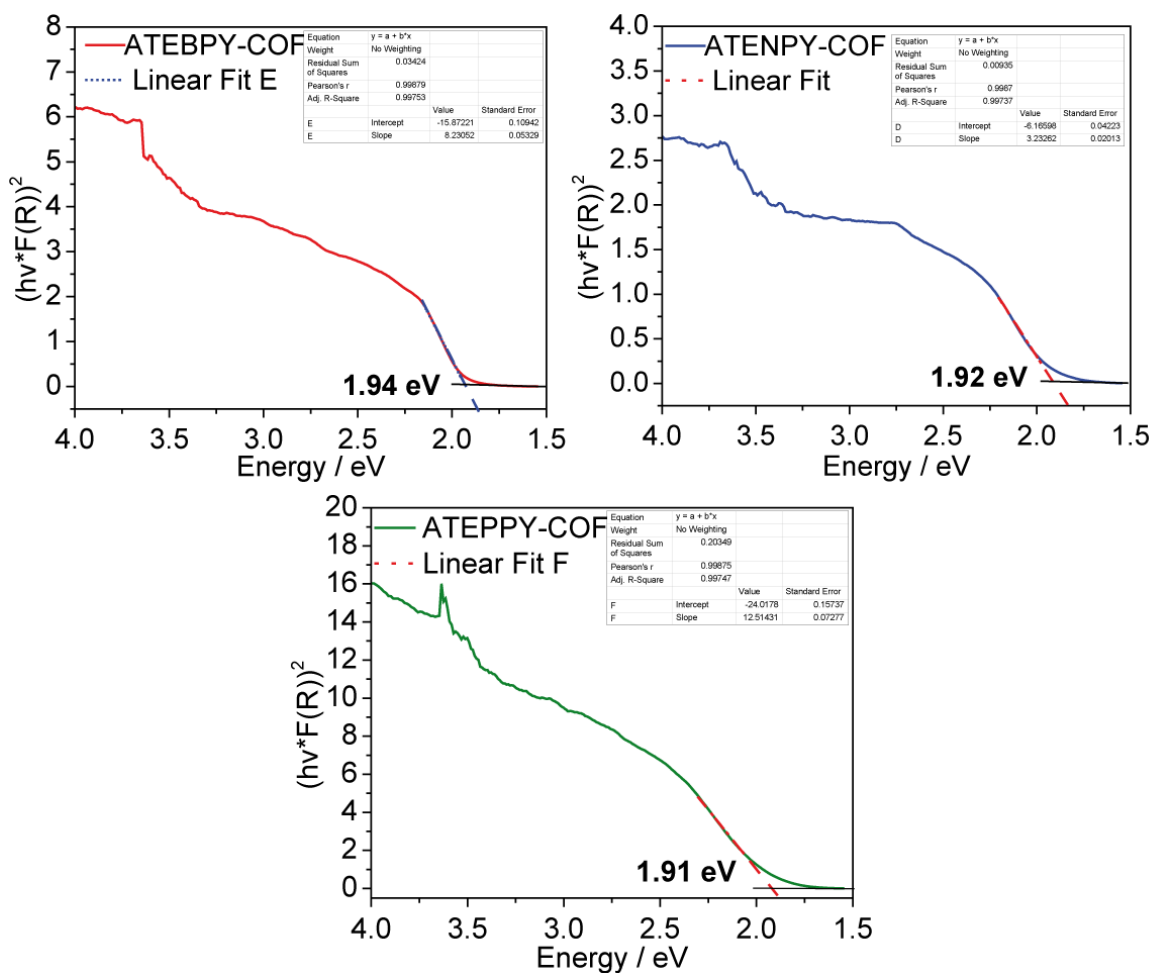
Figure S19. Tauc plots of A-TEXPY-COFs showing a slight decrease in bandgap with increasing nitrogen content. The Tauc plot was calculated for the direct-bandgap semiconductor model.[17]
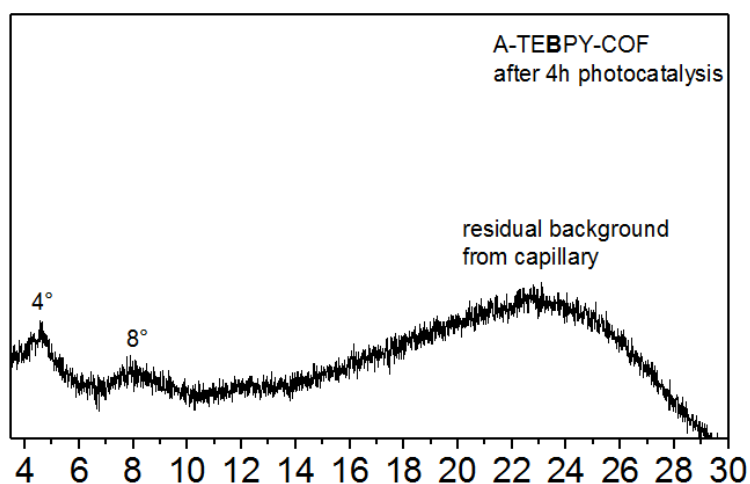
Figure S20. PXRD of A-TE**B**PY-COF after 4h. of constant irradiation in PBS/10vol% TEOA/ catalytic amounts of H_2PtCl_6.

Figure S21. ^{13}C ssNMR spectrum of A-TE**B**PY-COF after 4h. of constant irradiation in PBS/10vol% TEOA/ catalytic amounts of H_2PtCl_6.

J.   Photoelectrochemical measurements

Photoelectrochemical measurements were performed in 1M H_2SO_4 (pH=0) and 1M phosphate buffer (pH=6.3) using a Ag/AgCl reference electrode with saturated KCl (+0.197V vs. SHE) and a Pt wire as counter electrode. All sample substrates were contacted by a copper wire with Ag paste. The contact was sealed with 3M Scotch-Weld DP410 epoxy. The measurements were performed in a closed glass reactor equipped with a quartz window for illumination. The electrolyte was purged with >99% pure H_2 prior to every measurement through a porpous glass frit to remove dissolved oxygen and to saturate the solution with H_2 in order to provide a well-defined redox-potential consistent with long term working conditions. The RHE potential for the respective electrolytes was measured under the same conditions using a Pt wire as working electrode. Measurements were recorded using an IVIUM CompactStat postentiostat and the IviumSoft software.

Simulated sunlight was provided by a SCIENCETECH LightLine A4 solar simulator (class AAA) fitting the ASTM standard G138. The intensity was measured at the place of the sample by a calibrated THORLABS S310C thermal power meter and further confirmed by a calibrated OCEAN OPTICS USB4000 spectrometer.

The negative photocurrent onset potentials measured by this technique may be slightly shifted for all COFs from the true band alignment wrt RHE due to the COFs' surface adsorption energy of hydrogen, which can be positive or negative.[18] This effect is neglected in the further data evaluation because it is independent of the pH, most probably similar for the different COFs, and small (<0.1V).
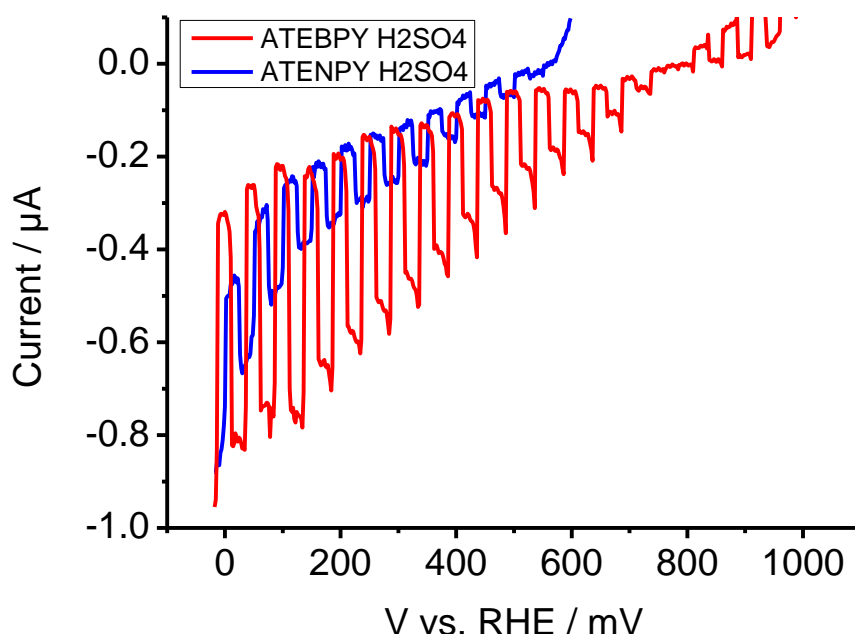
Figure S22. Cyclic voltametry of A-TE**X**PY-COF@FTO (X=B, N) under visible light in hydrogen saturated 1M H_2SO_4. The light is chopped every 5s. The scan rate is 5 mV/s.
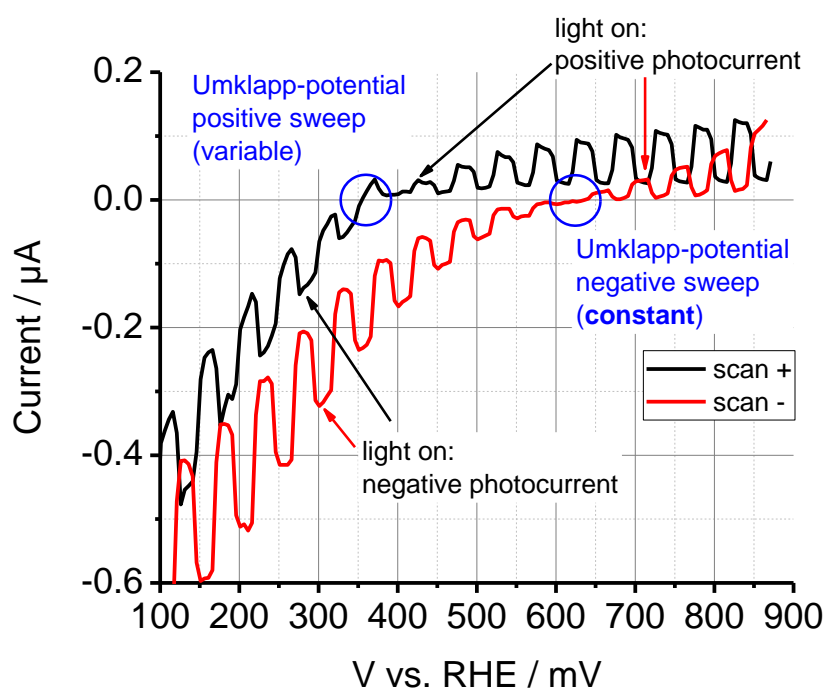
Figure S23. Chopped light cyclic voltammetry measurement (5 mV/s) for ATE**N**PY-COF@FTO in hydrogen saturated 1M phosphate buffer (pH=6.3) to estimate the alignment level. The light is chopped every 5s. At +630 mV vs. RHE, the LUMO aligns with the solution potential (RHE) and the (photo)current switches from cathodic to anodic.
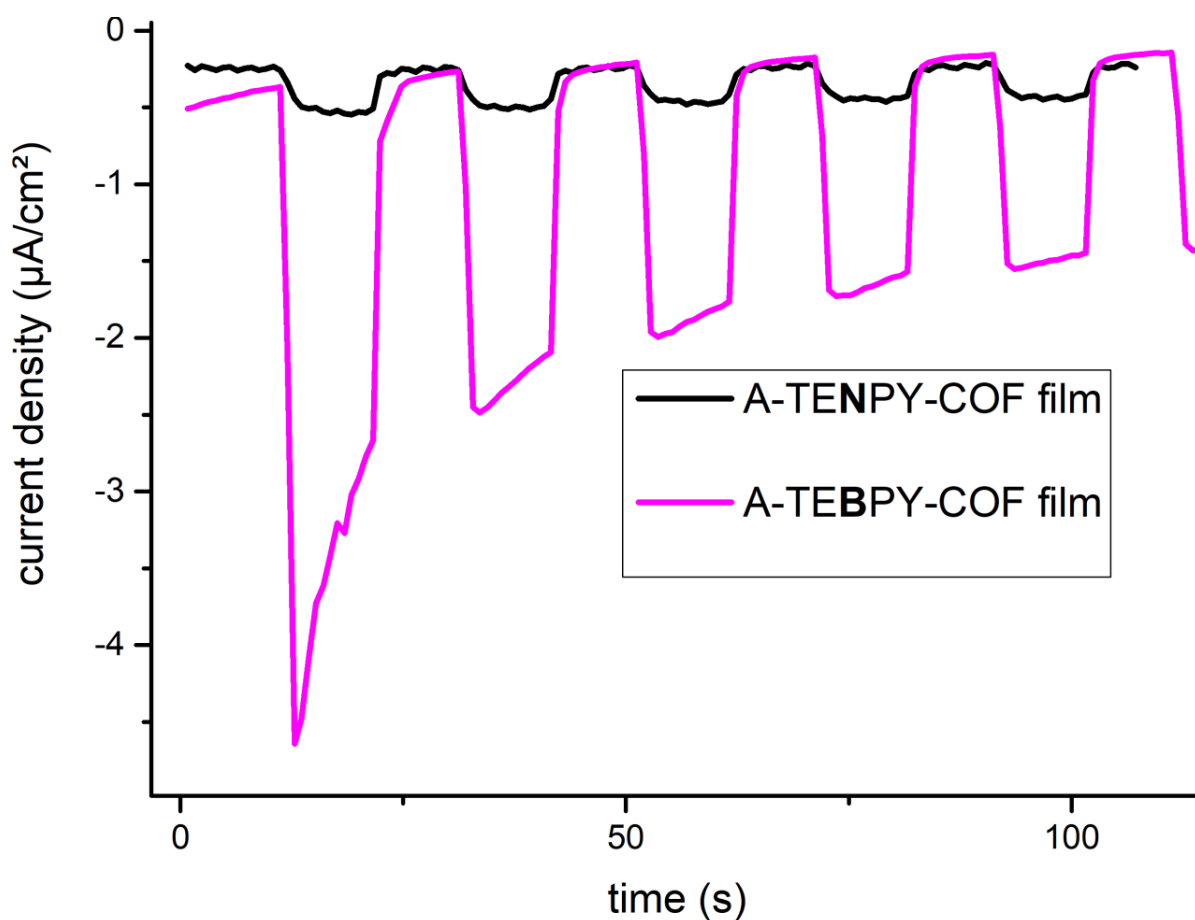
Figure S24. Chronoamperometry of A-TE**X**PY-COF@FTO (X=B, N) under visible light in hydrogen saturated 1M Na based phosphate buffer (pH 7) at RHE under chopped light. The initial transient behaviour leading to photocurrent decay is attributed to the loss of weakly adhering material, which could be clearly observed by an increasing transparency of the A-TE**B**PY-COF electrodes.
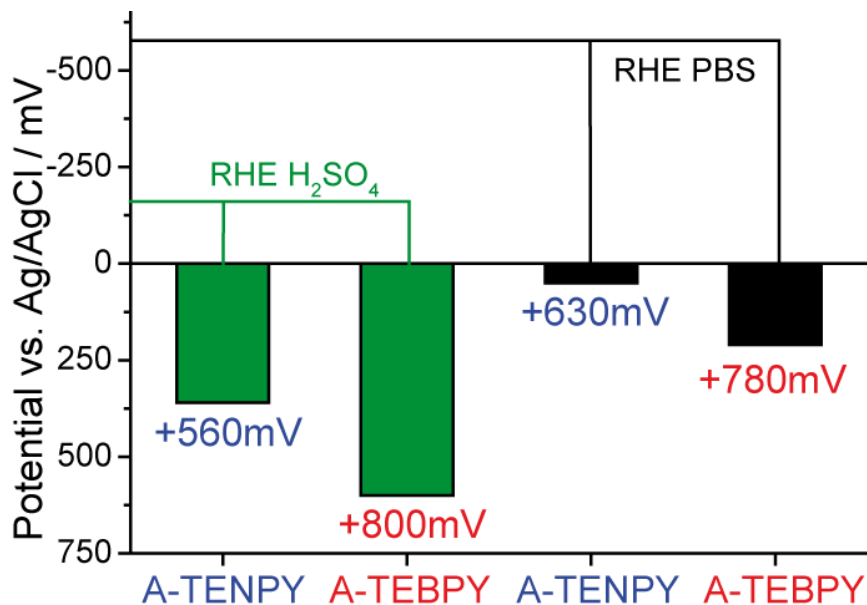
Figure S25. Average applied potentials vs. Ag/AgCl required to align the conduction band with the solution potential for the ATE(**B,N**)PY-COF@FTO in 1M H_2SO_4 (green) and 1M phosphate buffer (black). The four numbers given in the diagram refer to potentials above RHE of H_2SO_4 (two left) and RHE of phosphate buffer (two right). The alignment of the LUMO with respect to the electrolyte potential (RHE) follows a Nerstian dependence.
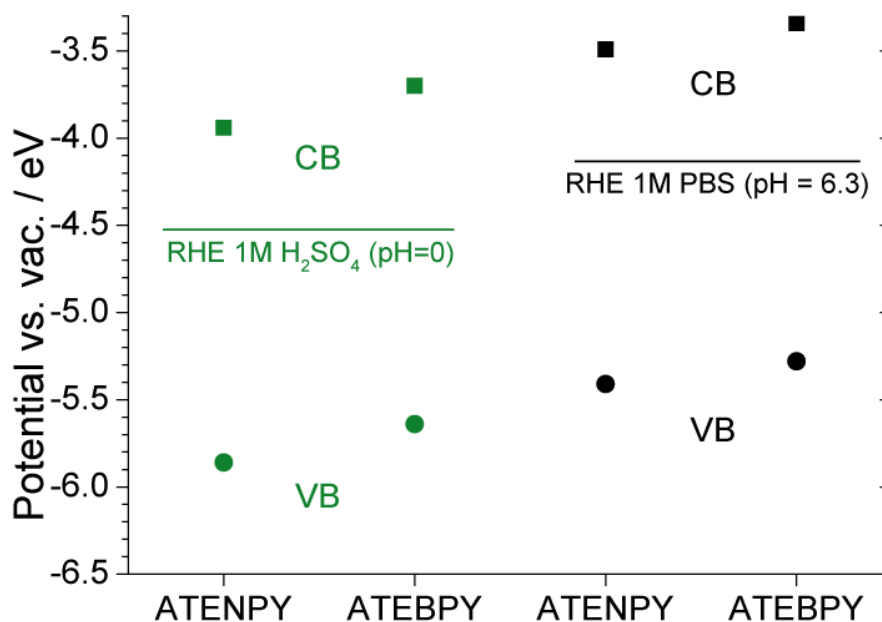
Figure S26. Conduction band (CB, LUMO) and valence band positions (VB, HOMO) of the ATE(**B,N**)PY COFs in 1M H_2SO_4 and 1M phosphate buffer vs. vacuum energy, extracted from photoelectrochemical measurements, and the optical band gaps showing the Nernstian, pH dependent band shifts and thus a significant absolute drop of the conduction band under acidic conditions.

S36

K.   Quantum-chemical Calculations
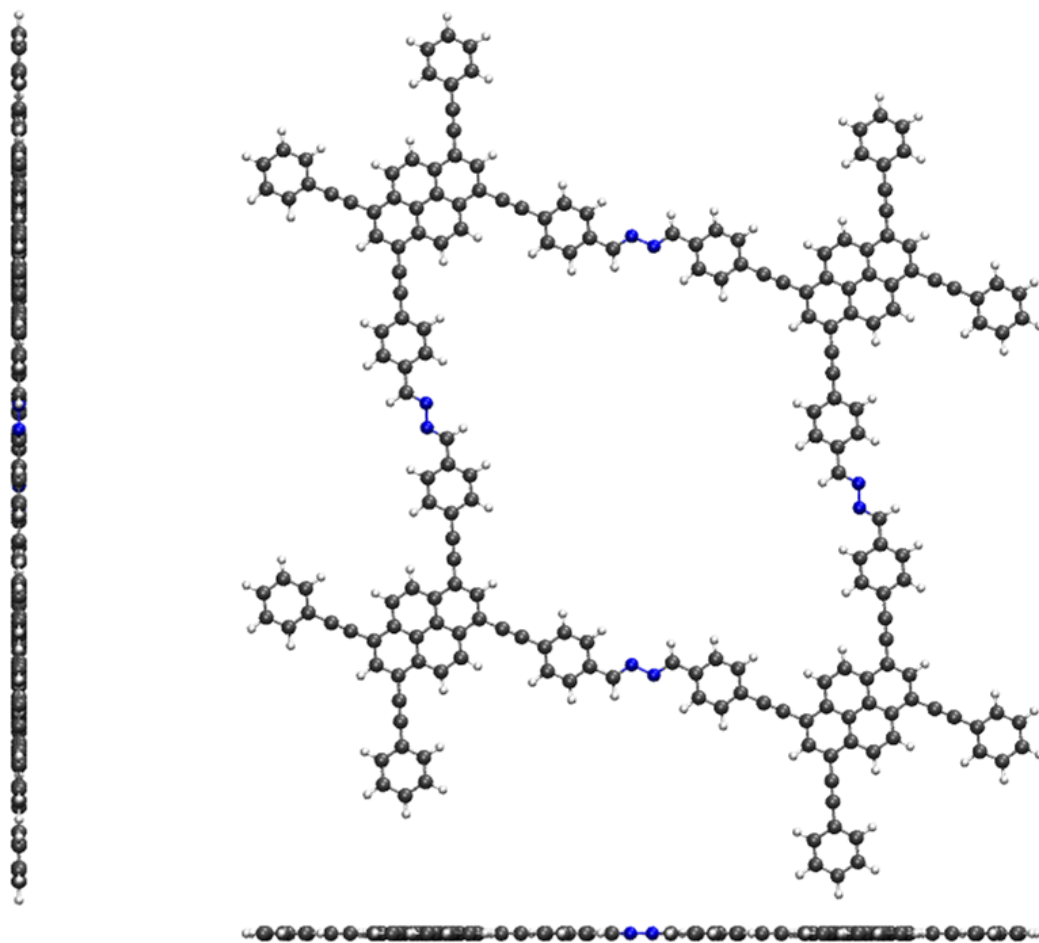
Figure S27. Optimized geometry of a single A-TE**B**PY-COF pore as a model for the framework, calculated at the **PBE0-D3/def2-SVP** level of theory. [2–6]
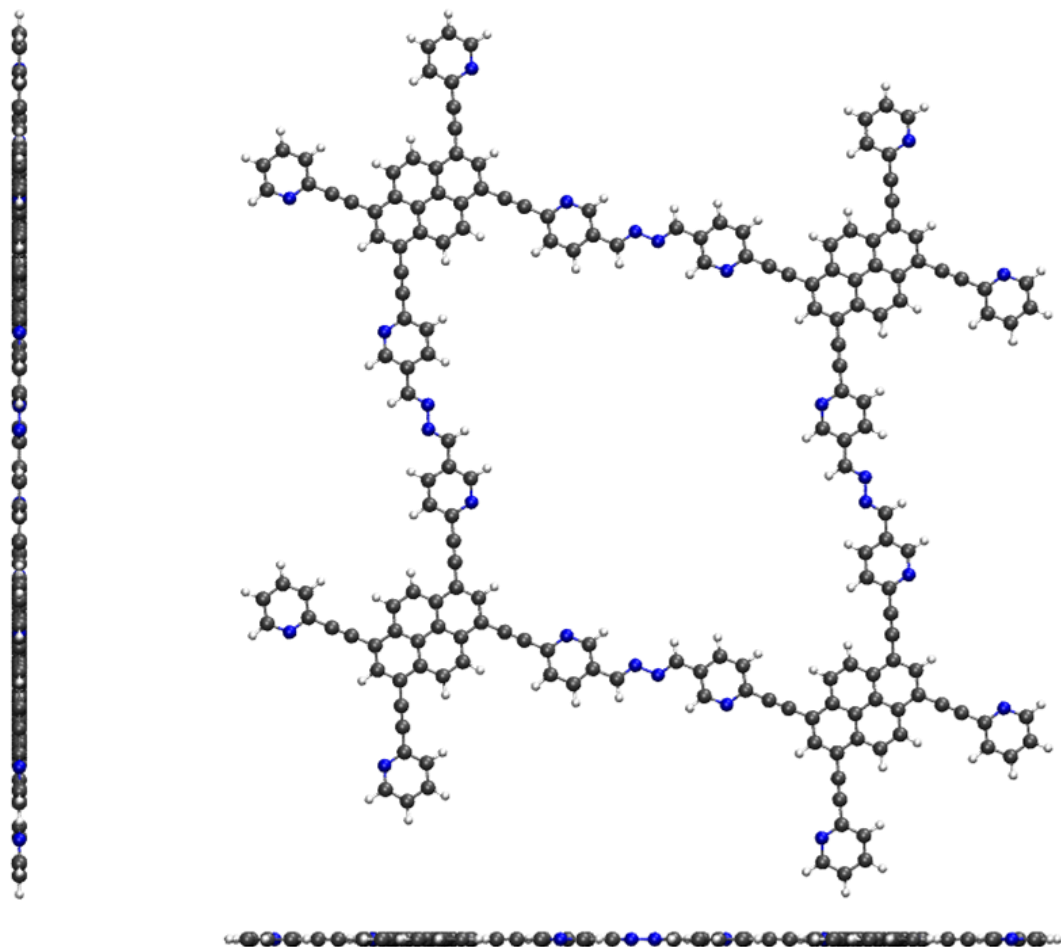
Figure S28. Optimized geometry of a single A-TE**N**PY-COF pore as a model for the framework, calculated at the **PBE0-D3/def2-SVP** level of theory.[2–6]
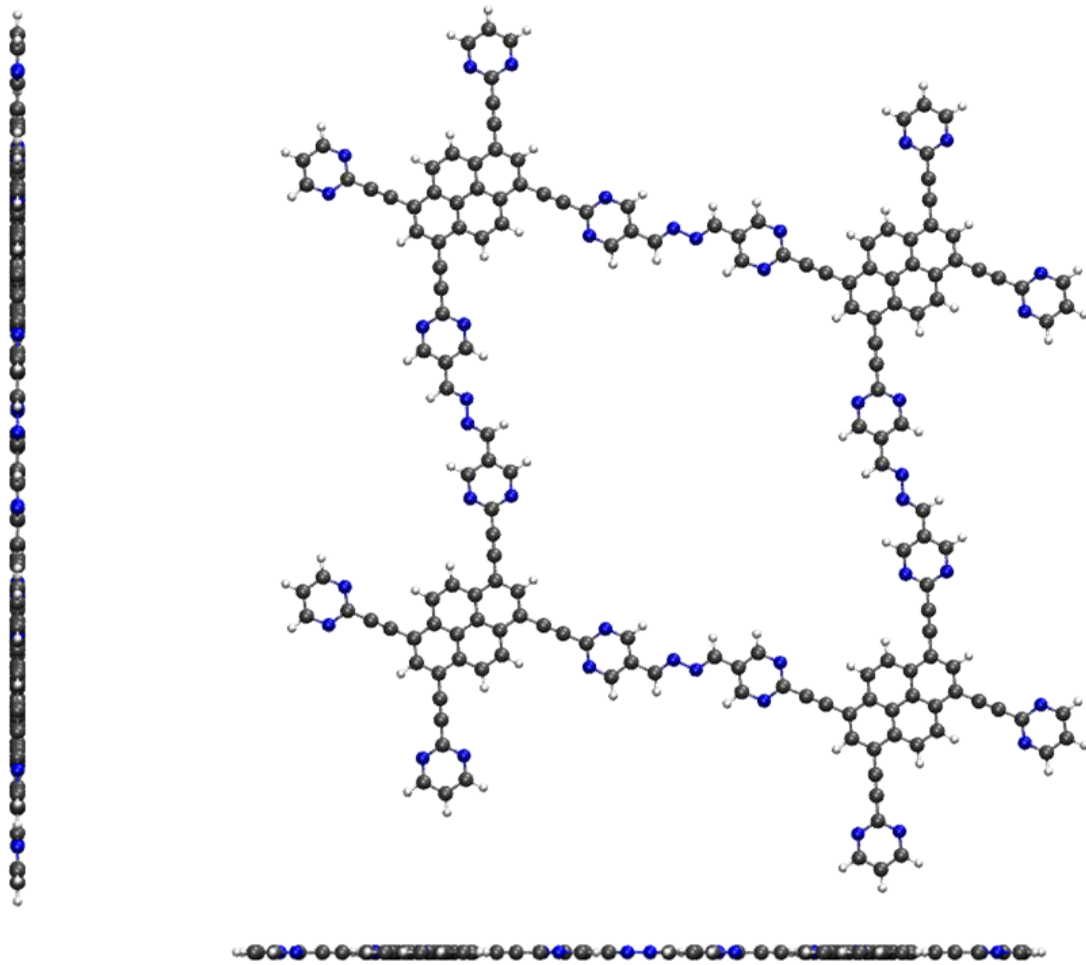
Figure S29. Optimized geometry of a single A-TE**P**PY-COF pore as a model for the framework, calculated at the **PBE0-D3/def2-SVP** level of theory.[2–6]
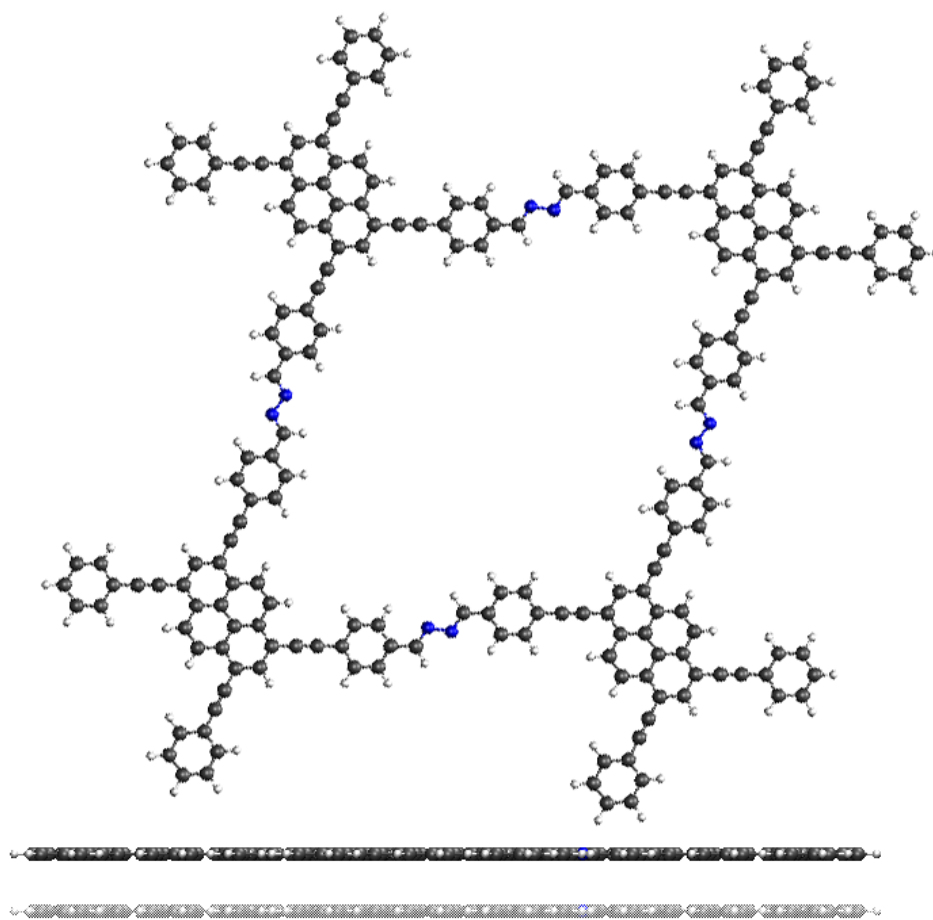
Figure S30. Geometry for the **AA** stacked conformation of the ATE**B**PY-COF pore dimer.
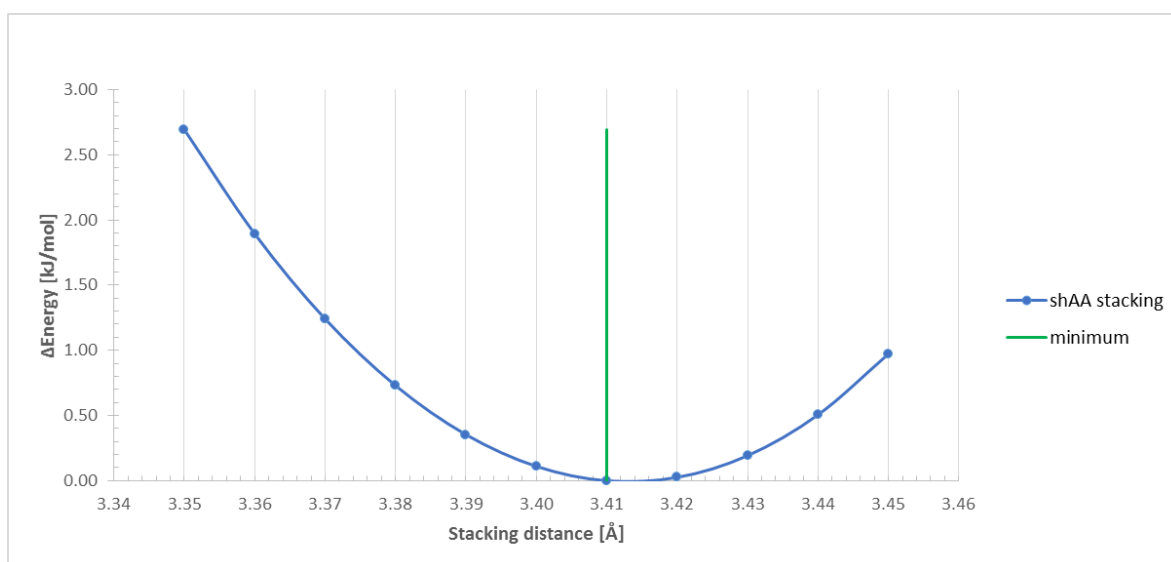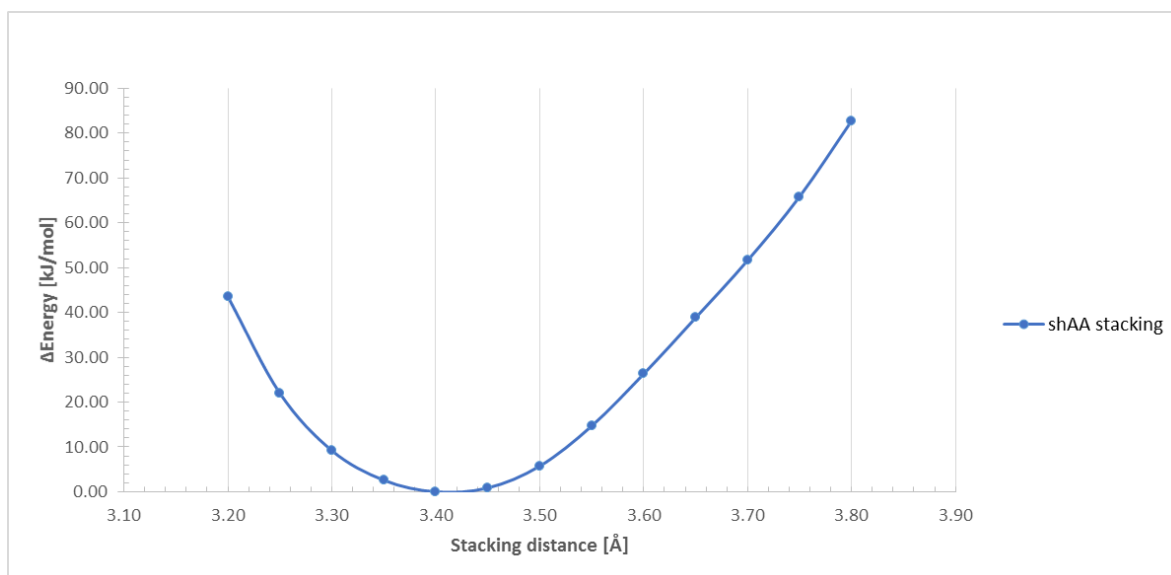View along z (top) and x (bottom).
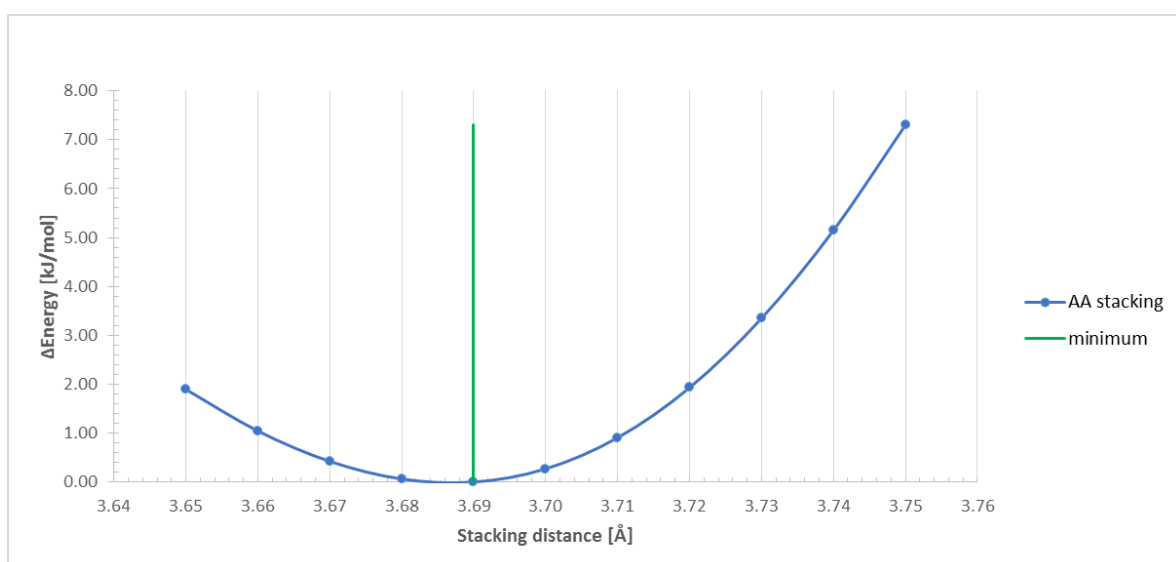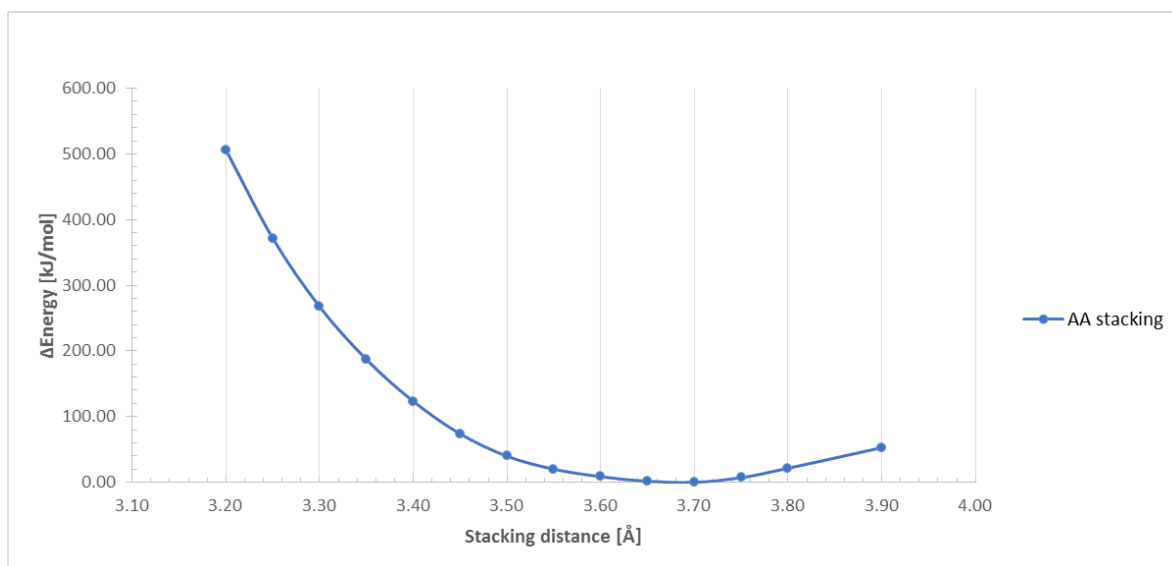
Figure S31. Potential energy curve for the AA stacking model of the A-TE**B**PY-COF pore dimer, relative to the found minimum at **3.69 Å**, marked in green. Energies obtained on **M06/def2-SVP** level of theory.[6,7]
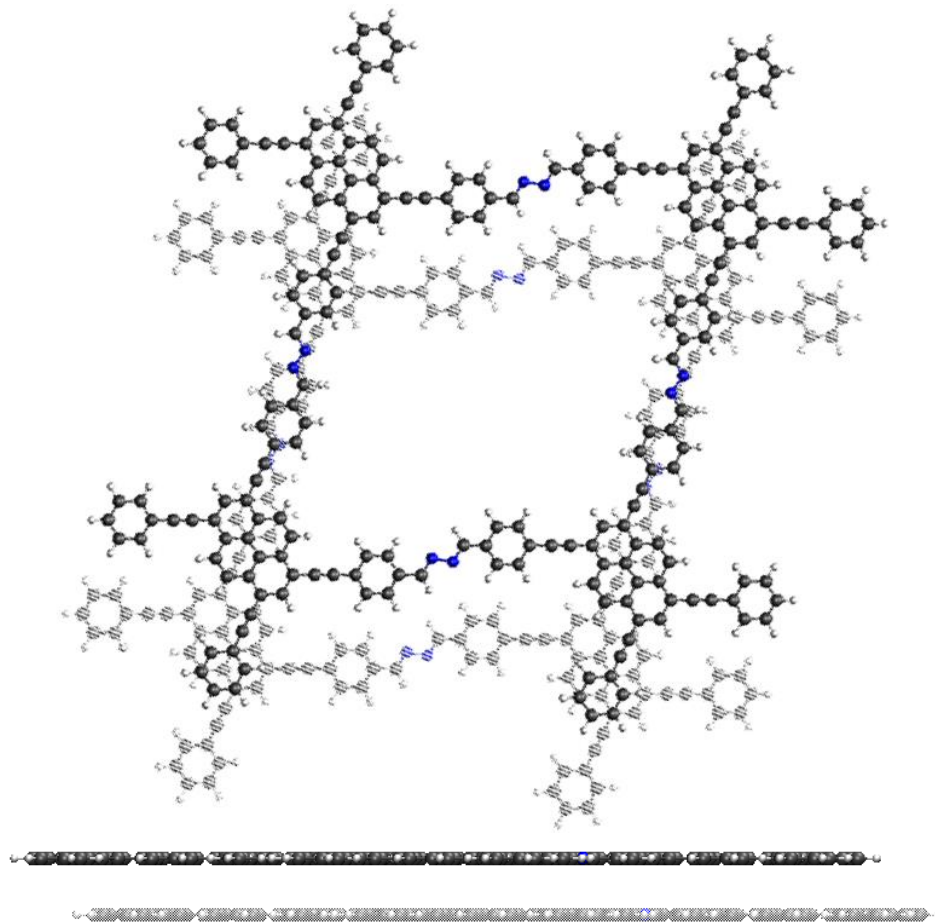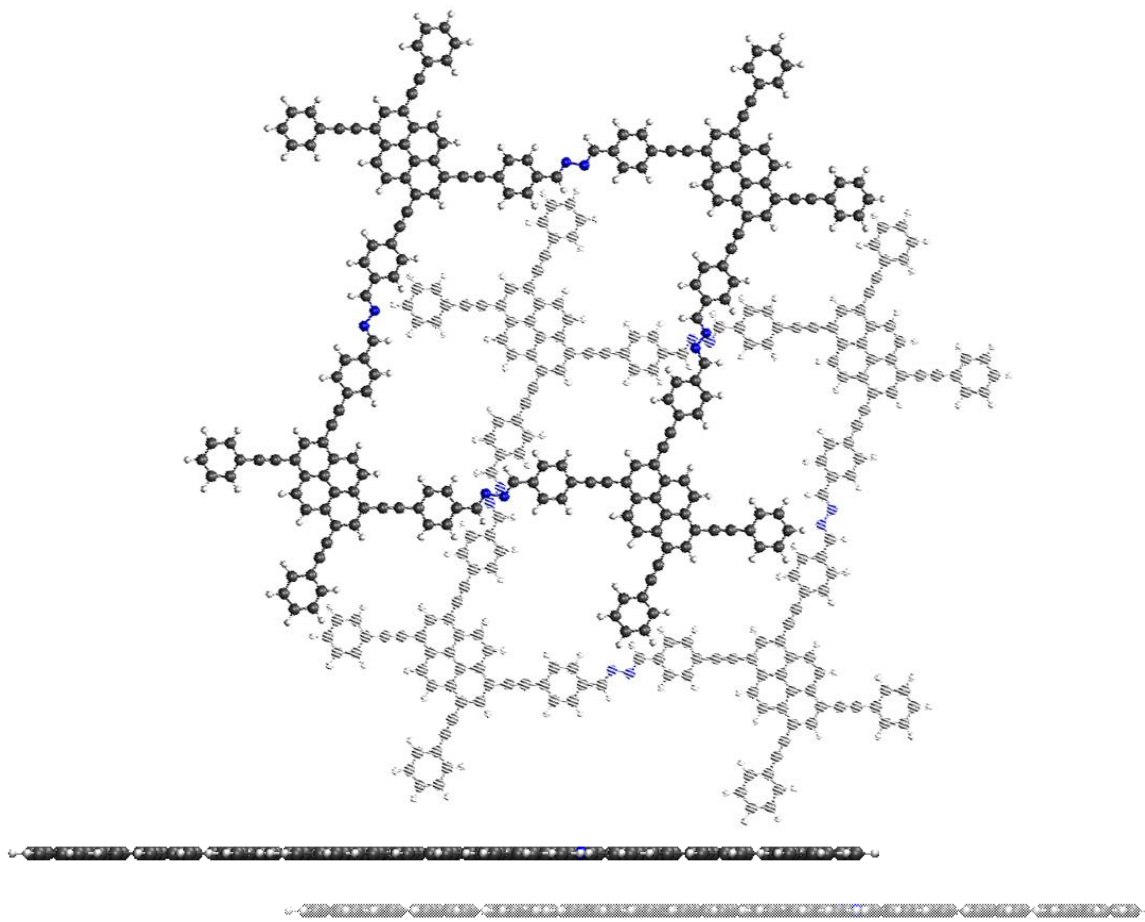
Figure S32. Geometry for the **6.5A-sh-AA'** stacked conformation of the A-TE**B**PY-COF pore dimer. View along z (top) and x (bottom).

Figure S33. Potential energy curve for the **6.5A-sh-AA'** stacked conformation of the A-TEBPY-COF pore dimer, relative to the found minimum at **3.41 Å**, marked in green. Energies obtained on **M06/def2-SVP** level of theory.[6,7]

Figure S34. Geometry for the **AB** stacked conformation of the A-TE**B**PY-COF pore dimer.
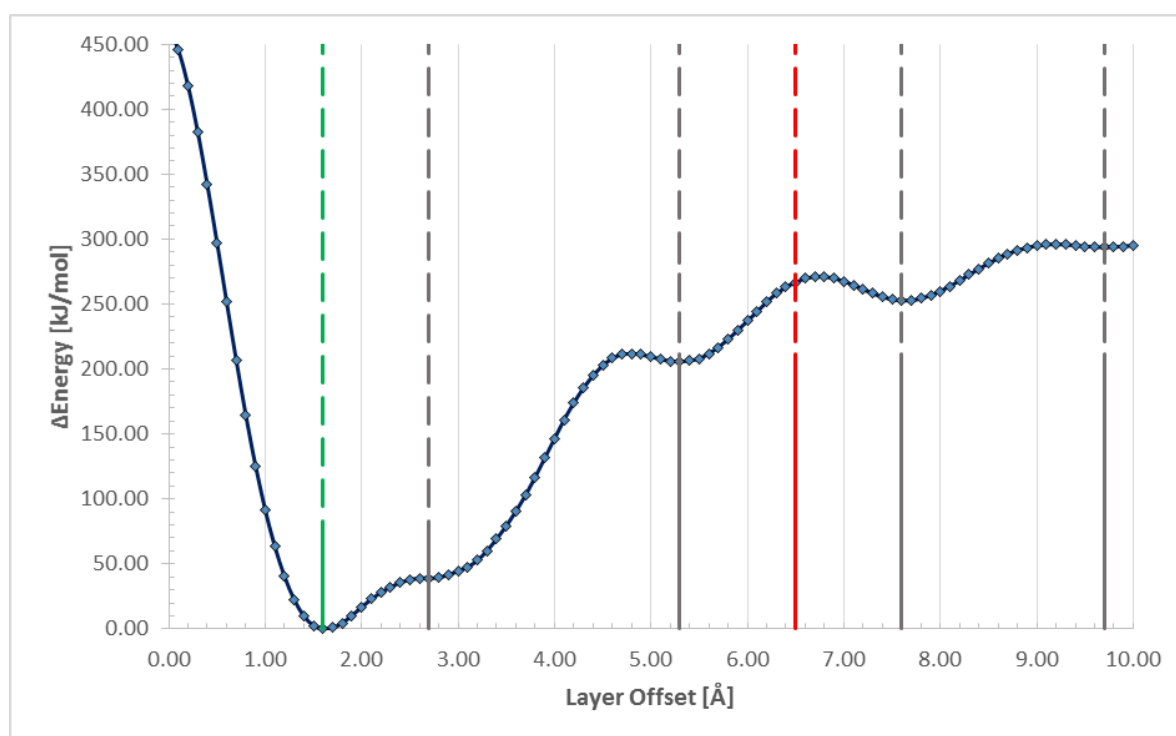
View along z (top) and x (bottom).
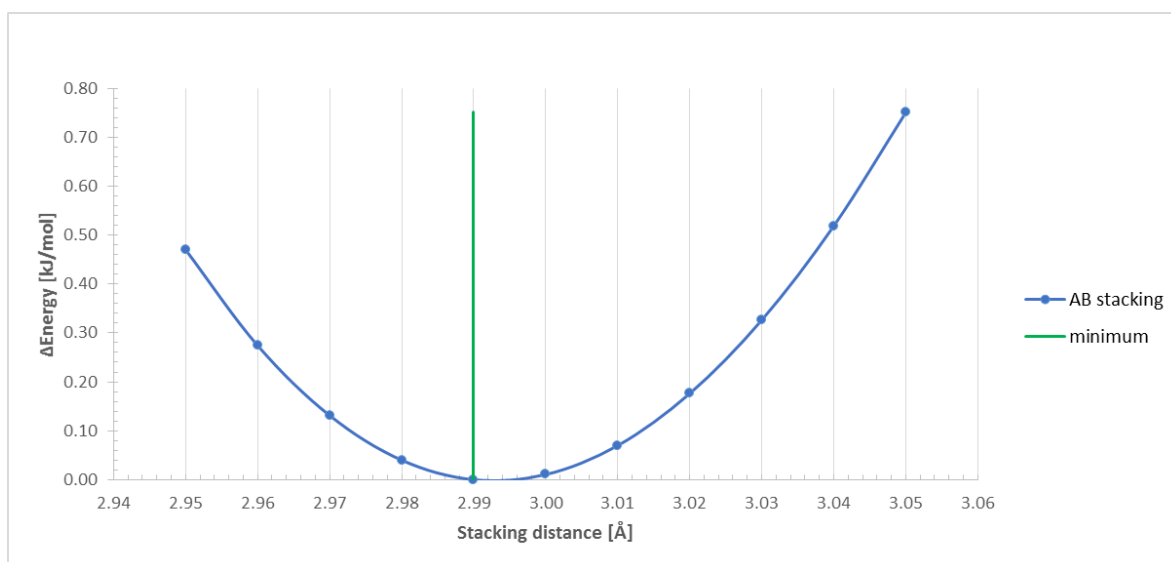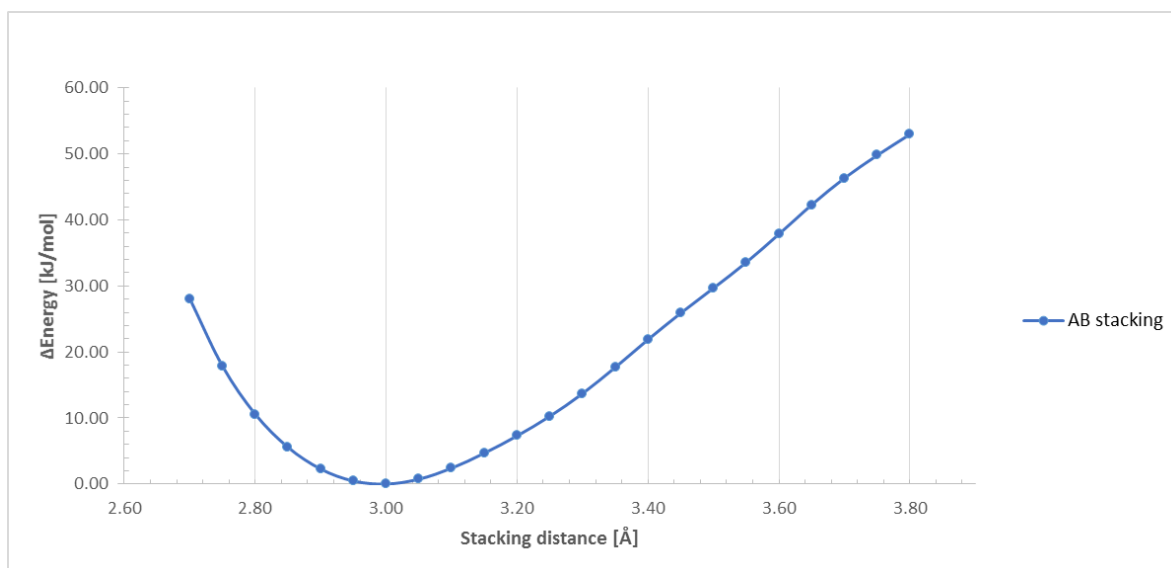
Figure S35. Potential energy curve for the **AB** stacked conformation of the ATE**B**PY-COF pore dimer, relative to the found minimum at **2.99** Å, marked in green. Energies obtained on **M06/def2-SVP** level of theory.[6,7]

Table S4. Summary of obtained minimum stacking distances for the ATE**B**PY-COF pore dimers.

Stacking Configuration	AA	shAA	AB
Minimum Stacking Distance [Å]	3.69	3.41	2.99

Table S5. Summary of obtained Interaction Energies for calculated minimum stacking distances for the ATE**B**PY-COF pore dimers calculated on **PBE0-D3/def2-SVP** level of theory.

Stacking Configuration	AA	6.5A-sh-AA'	AB
Interaction Energy [kcal/mol]	-108.1	-101.6	-34.3
Δ Interaction Energy [kcal/mol]	±0.0	+6.5	+73.8

Figure S36. Potential energy curve for the **layer offset scan** of the 6.5A-**sh-AA'** stacked conformation of the ATE**B**PY-COF pore dimer, relative to the found minimum at **1.60 Å**, marked in green. Energies obtained on **M06/def2-SVP** level of theory.[6,7]
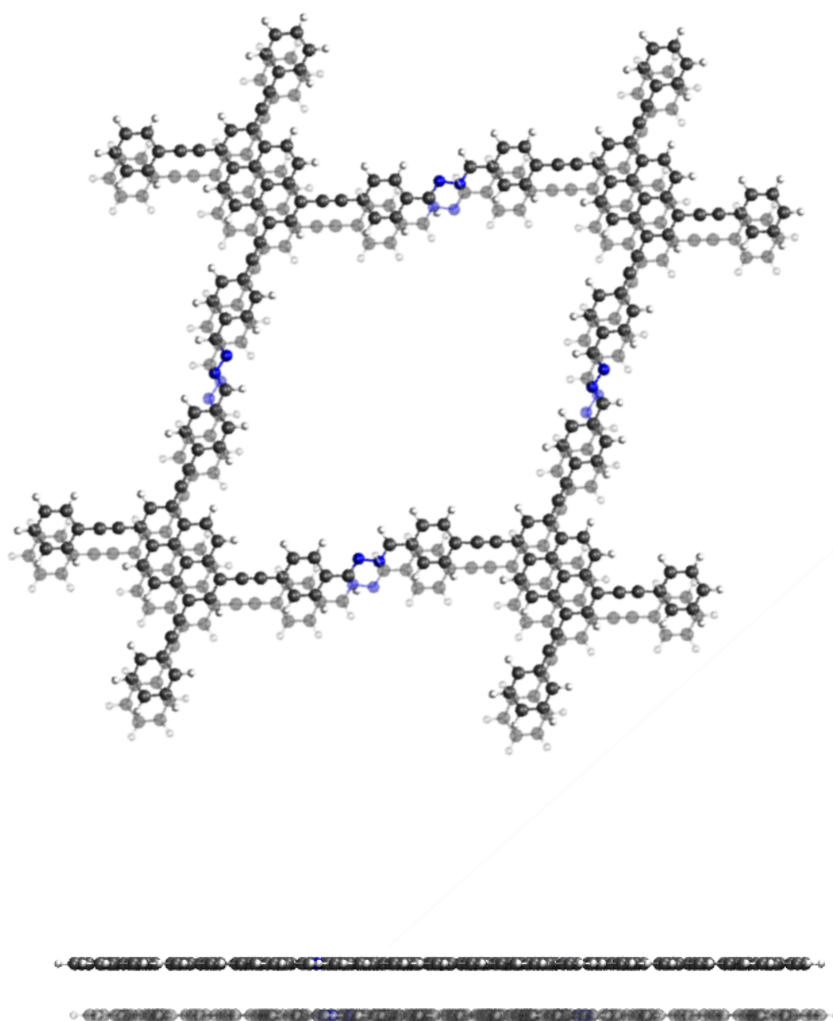
Figure S37. Geometry for the 1.6A-**sh-AA'** stacked polymorph of the A-TE**B**PY-COF pore dimer. View along z (top) and x (bottom).
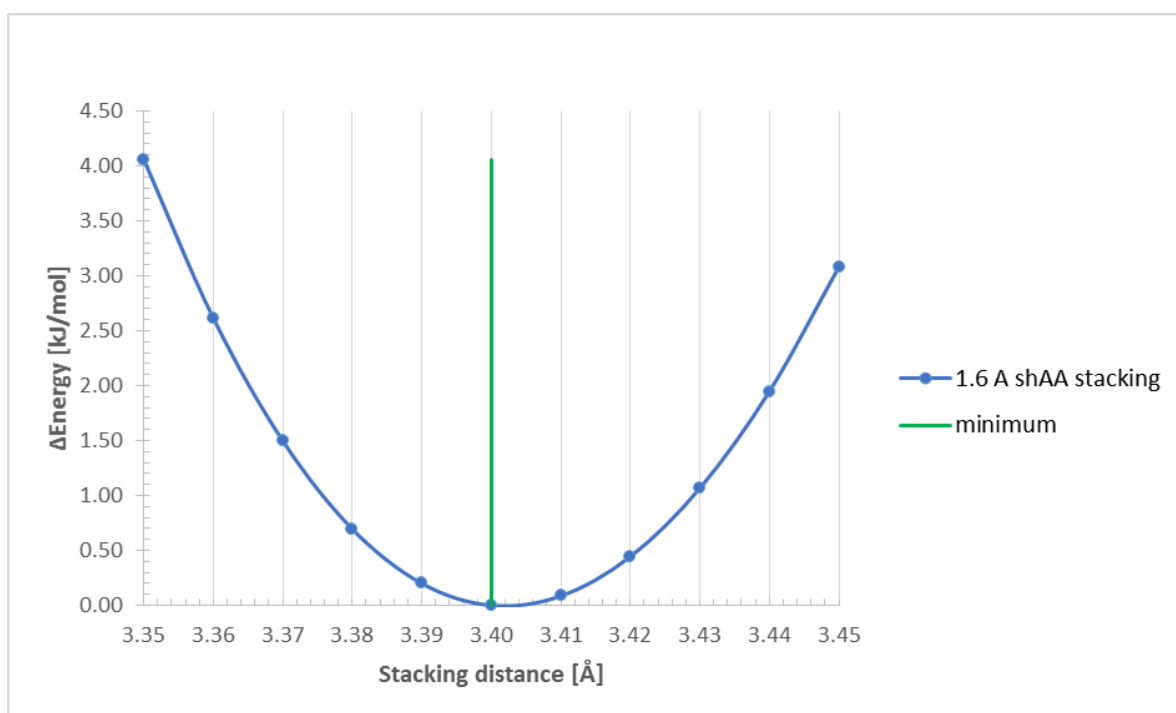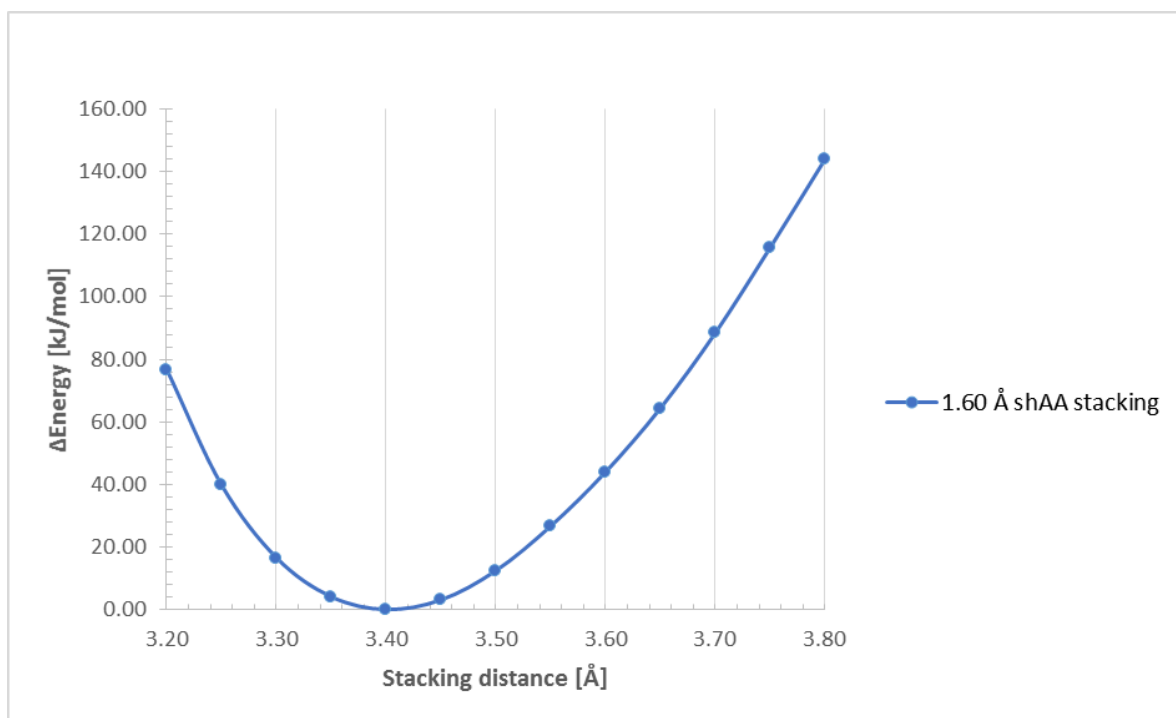
Figure S38. Potential energy curve for the **shAA(1.6A)** stacked conformation of the ATE**B**PY-COF pore dimer, relative to the found minimum at **3.40 Å**, marked in green. Energies obtained on **M06/def2-SVP** level of theory.[6,7]

Table S6. Kohn-Sham band gaps and energies of molecular orbitals for one ATE**X**PY-COF hexagon calculated on **PBE0-D3/def2-TZVP** level of theory.[2–6]

	A-TE**B**PY		A-TE**N**PY		A-TE**P**PY	
	Energy [H]	Energy [eV]	Energy [H]	Energy [eV]	Energy [H]	Energy [eV]
LUMO	-0.11038138	-3.00	-0.11846219	-3.22	-0.12374346	-3.37
HOMO	-0.20011831	-5.45	-0.20850443	-5.67	-0.21343113	-5.81
Band Gap	0.08973693	2.44	0.09004224	2.45	0.08968767	2.44

Table S7. Vertical excitation energies for a ATE**B**PY-**COF** pore calculated on
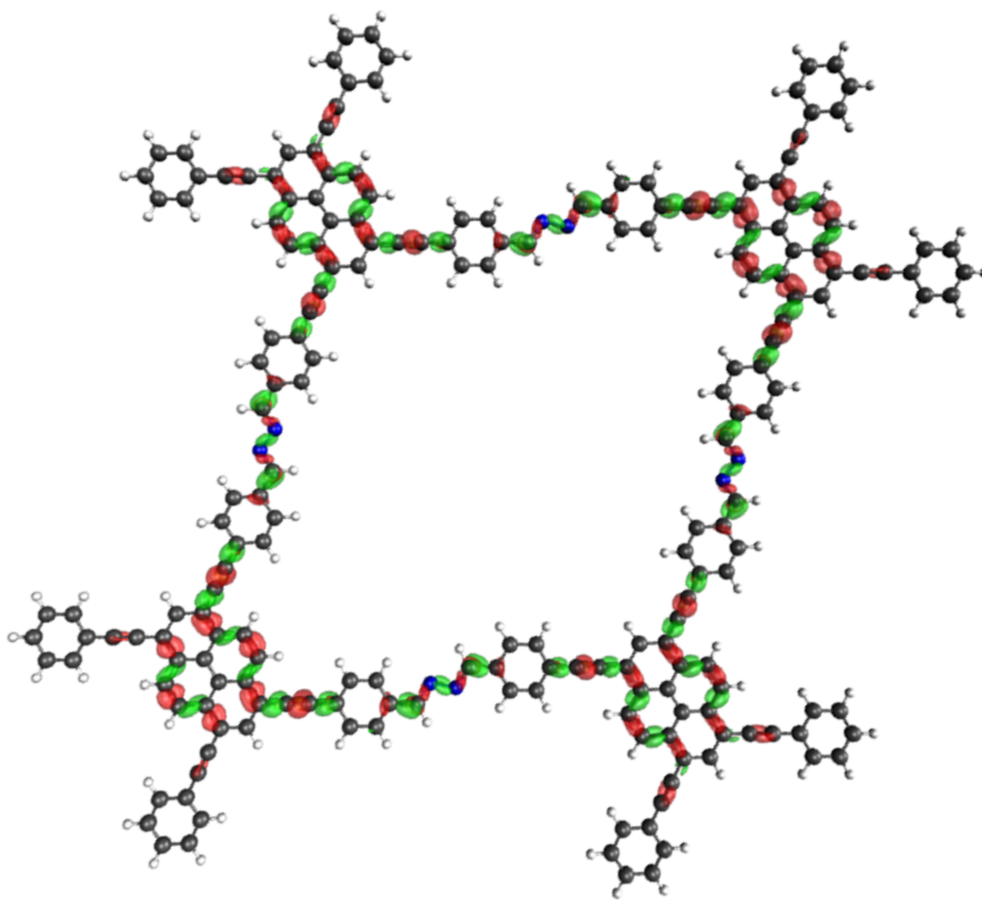**TD-PBE0/Def2-TZVP//PBE0-D3/def2-SVP** level of theory.

Excitation	Irrep	Excitation Energy [eV]	Oscillator Strength [km/mol]	Occupied Orbital		Virtual Orbital		|coeff.|^2*100 [%]
1	bu	2.10	5.642	HOMO	52bg	LUMO	53au	59.1
2	bu	2.29	0.000	HOMO-3	51bg	LUMO	53au	40.0
3	bu	2.37	2.031	HOMO-1	52au	LUMO+1	53bg	83.7
4	bu	2.38	0.504	HOMO	52bg	LUMO	53au	39.4
5	bu	2.40	0.790	HOMO-2	51au	LUMO+2	54bg	87.2
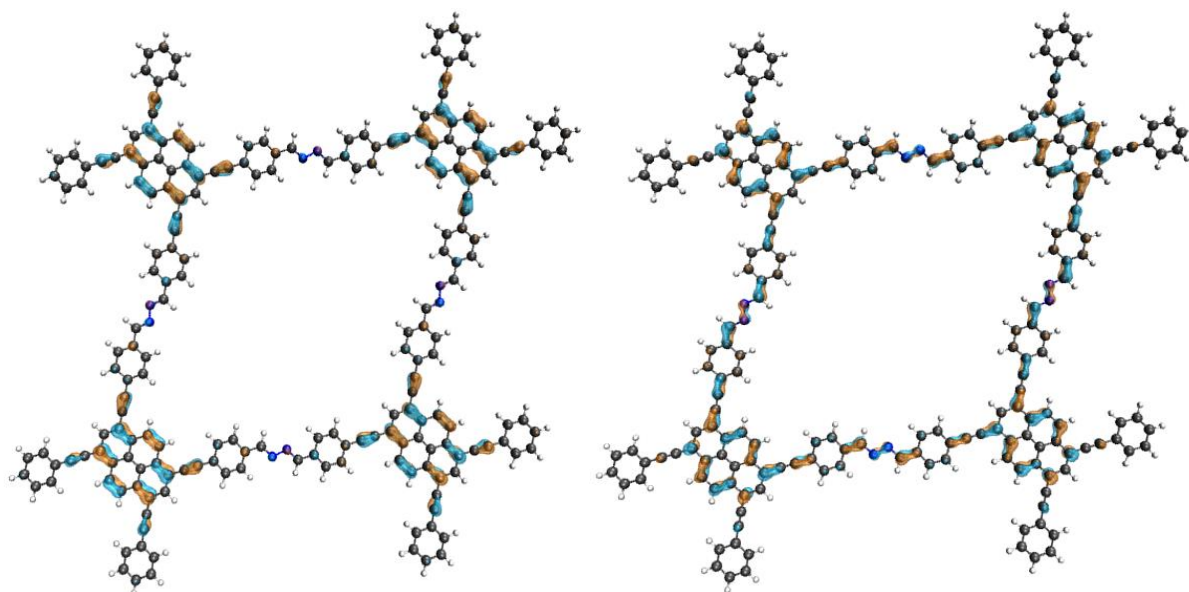
Figure S39. Visualization of the HOMO (left) and LUMO (right) for the A-TE**B**PY COF calculated on **PBE0-D3/def2-SVP** level of theory. [2–6]

Figure S40. Difference densities for the lowest excited state for A-TE**B**PY**-COF** pore, calculated on
TD-PBE0/Def2-SVP//PBE0-D3/Def2-SVP level of theory.

Table S8. Vertical excitation energies for ATE**N**PY**-COF** pore calculated on **TD-PBE0/def2-TZVP//PBE0-D3/def2-SVP** level of theory.

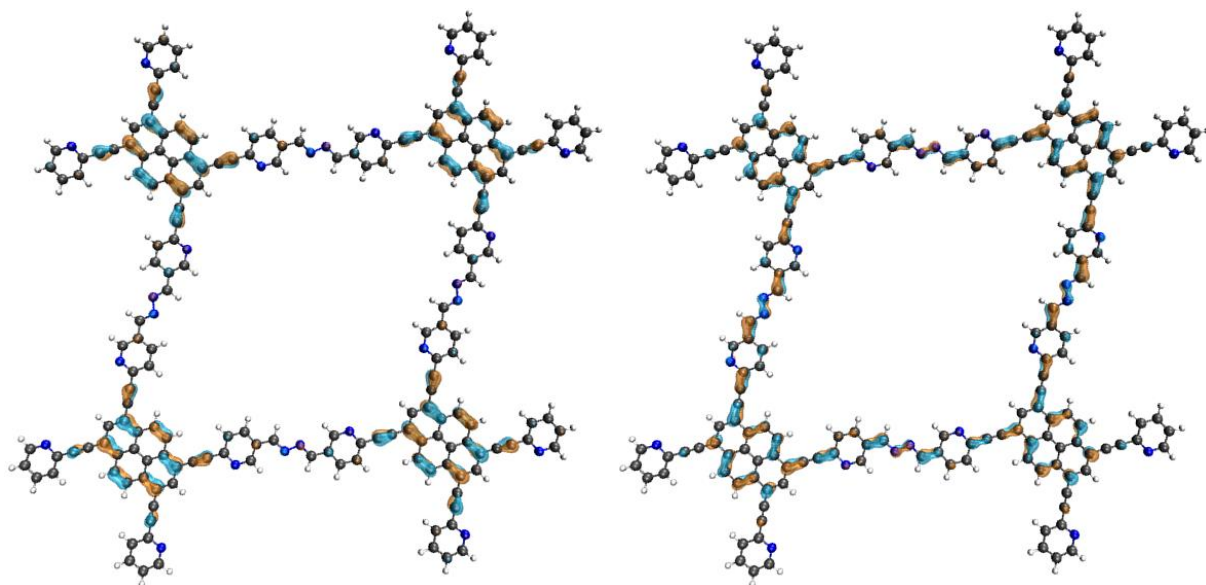| Excitation	Irrep	Excitation Energy [eV]	Oscillator Strength [km/mol]	Occupied Orbital		Virtual Orbital		|coeff.|^2 *100 [%]
1	bu	2.10	5.615	HOMO	52bg	LUMO	53au	58.8
2	bu	2.30	0.002	HOMO-3	51bg	LUMO	53au	43.2
3	bu	2.36	1.973	HOMO-1	52au	LUMO+1	53bg	78.2
4	bu	2.39	0.496	HOMO	52bg	LUMO	53au	39.2
5	bu	2.41	0.891	HOMO-2	51au	LUMO+2	54bg	82.5

Figure S41. Visualization of the HOMO (left) and LUMO (right) for the A-TE**N**PY-COF calculated on **PBE0-D3/def2-SVP** level of theory. [2–6]
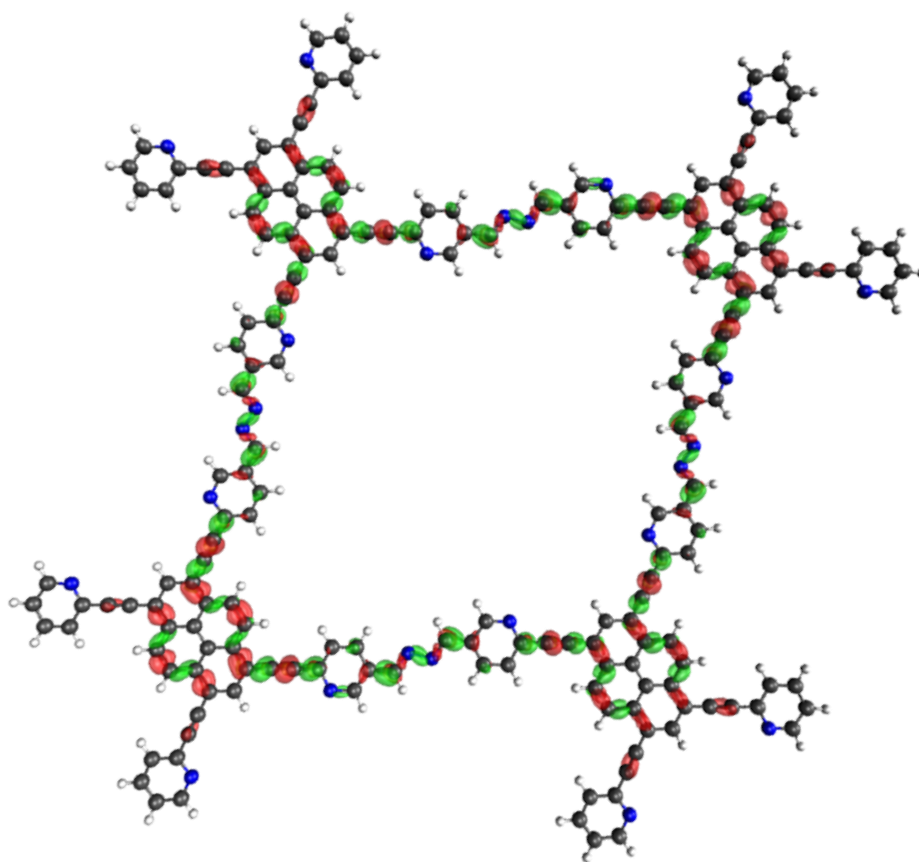
Figure S42. Difference densities for the lowest excited state for A-TE**N**PY-COF pore, calculated on
TD-PBE0/Def2-SVP//PBE0-D3/Def2-SVP level of theory.

Table S9. Vertical excitation energies for ATE**PPY-COF** pore calculated on
TD-PBE0/def2-TZVP//PBE0-D3/def2-SVP level of theory.

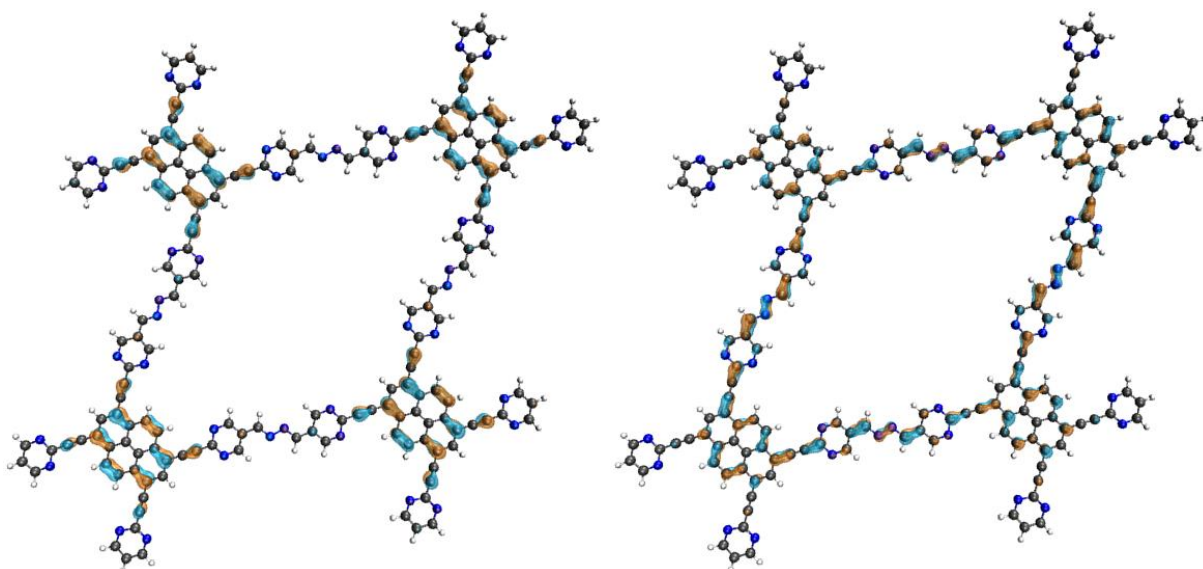| Excitation	Irrep	Excitation Energy [eV]	Oscillator Strength [km/mol]	Occupied Orbital		Virtual Orbital		|coeff.|^2 *100 [%]
1	bu	2.09	4.528	HOMO	52bg	LUMO	53au	59.2
2	bu	2.28	0.003	HOMO-3	51bg	LUMO	53au	48.5
3	bu	2.32	2.444	HOMO-1	52au	LUMO+1	53bg	77.4
4	bu	2.37	0.403	HOMO-1	52au	LUMO+2	54bg	43.4
5	bu	2.39	0.889	HOMO-2	51au	LUMO+2	54bg	79.3

Figure S43. Visualization of the HOMO (left) and LUMO (right) for the ATE**P**PY-COF calculated on **PBE0-D3/def2-SVP** level of theory. [2–6]

Figure S44. Difference densities for the lowest excited state for ATE**P**PY**-COF** pore, calculated on **TD-PBE0/Def2-SVP//PBE0-D3/Def2-SVP** level of theory.
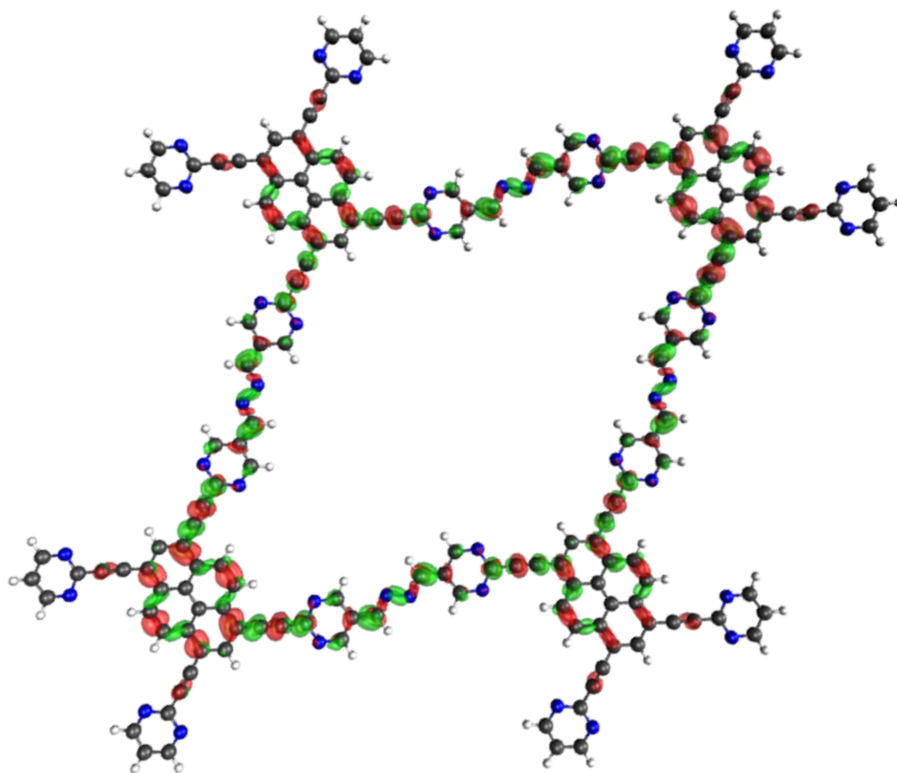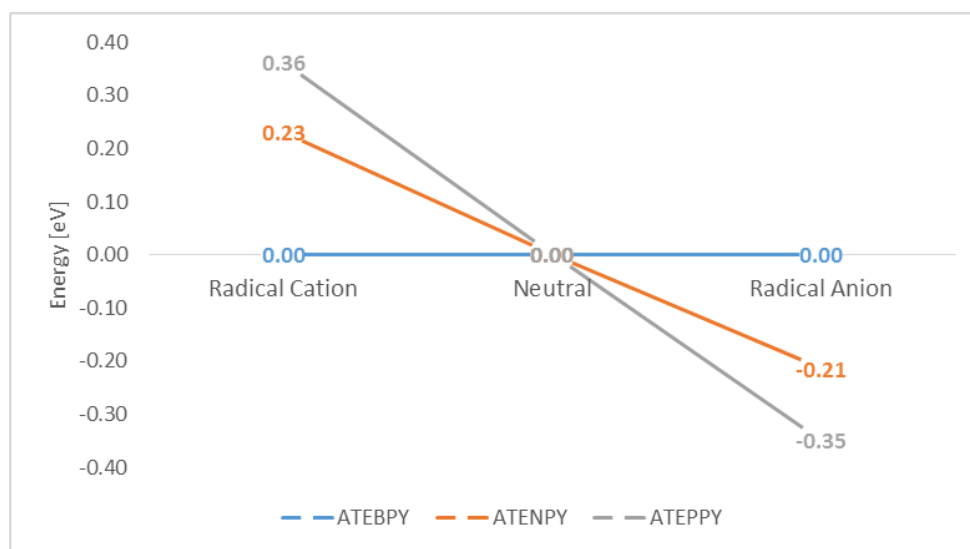
Table S10. Vertical radical cation stabilization energies for the ATE**X**PY-COF hexagons, calculated on **PBE0-D3/def2-SVP** level of theory.[2–6]

	Radical Cation Species				Neutral Species
	ΔVCSE [eV]	ΔVCSE [H]	VCSE [H]	Total Energy [H]	Total Energy [H]
ATE**B**PY	0.00	0.000000	0.214525	-8105.743005	-8105.957529
ATE**N**PY	0.23	0.008468	0.222992	-8361.835479	-8362.058472
ATE**P**PY	0.36	0.013290	0.227814	-8618.001462	-8618.229277

Table S11. Vertical radical anion stabilization energies for the ATE**X**PY-COF hexagons, calculated on **PBE0-D3/def2-SVP** level of theory.

	Radical Anion Species				Neutral Species
	ΔVASE [eV]	ΔVASE [H]	VASE [H]	Total Energy [H]	Total Energy [H]
ATE**B**PY	0.00	0.000000	-0.096051	-8106.053580	-8105.957529
ATE**N**PY	-0.21	-0.007873	-0.103924	-8362.162395	-8362.058472
ATE**P**PY	-0.35	-0.012821	-0.108871	-8618.338148	-8618.229277

Figure S45. Comparison of vertical radical cation and radical anion stabilization energies with respect to the ATE**B**PY-COF hexagon as the reference using values obtained on **PBE0-D3/def2-SVP** level of theory.[2–6]

L.   Mechanism and charge transfer pathways after photoexcitation of the COFs
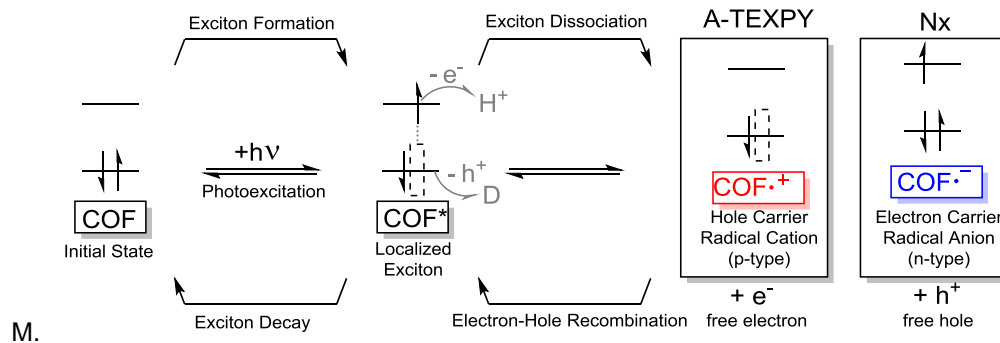
Figure S46. General scheme for possible pathways for the formation of a radical anion and a radical cation upon excitation of the COF and the formation of a localized exciton. Top pathway: Transfer of the excited electron to a proton (H⁺), resulting in a radical cation on the COF. Bottom pathway: Transfer of the hole to the sacrificial donor (D), resulting in a radical anion on the COF.

M.
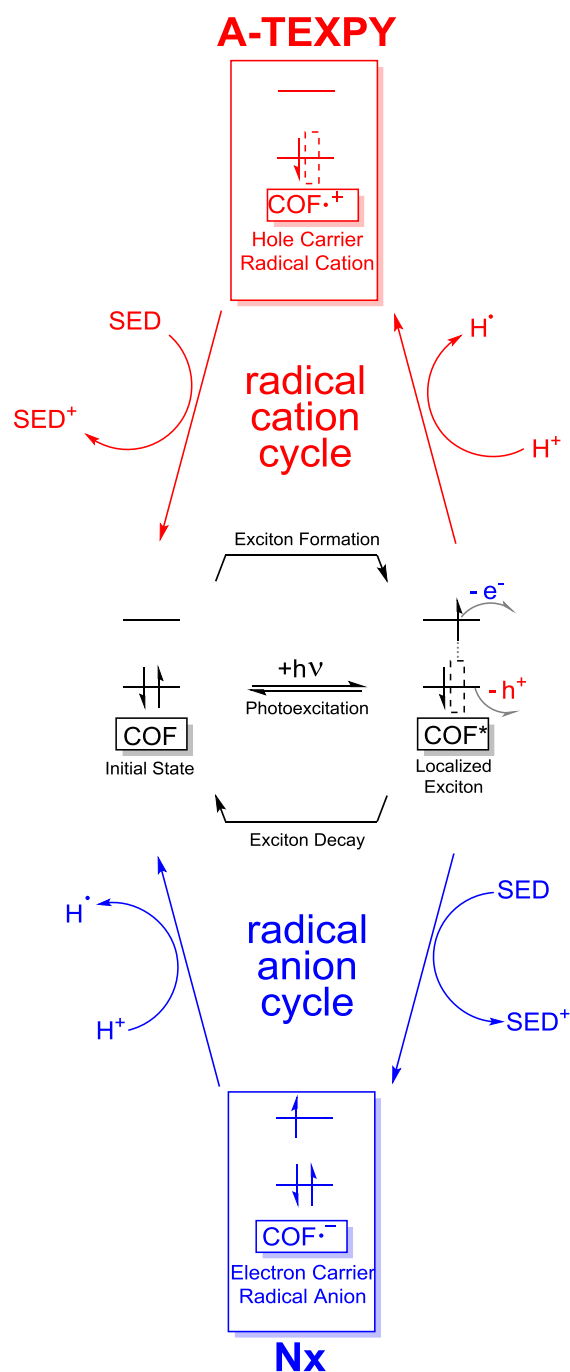
**Figure S47.** Comparison of the ATEXPY-COFs (this publication) with the Nx-COFs (Nat. Commun. 2015, 6, 8508) regarding the suggested catalytic cycles involving the formation of a radical cation and a radical anion, respectively, upon excitation of the COF and the formation of a localized exciton.

Top cycle (red): Oxidative quenching. Initial transfer of the excited electron to a proton (H^+), resulting in a radical cation on the COF. Subsequently, the radical cation of the COF gets quenched by reduction with the sacrificial electron-donor (SED, e.g. TEOA). This cycle is suggested to happen with ATEXPY-COFs.

Bottom cycle (blue): Reductive quenching. Initial transfer of the hole to the sacrificial electron donor (SED, e.g. TEOA), resulting in a radical anion on the COF. Subsequently, the radical anion is oxidized by a proton to produce a hydrogen radical. This is the n-type cycle suggested to happen with Nx-COFs..

N.   SEM and TEM of the COFs
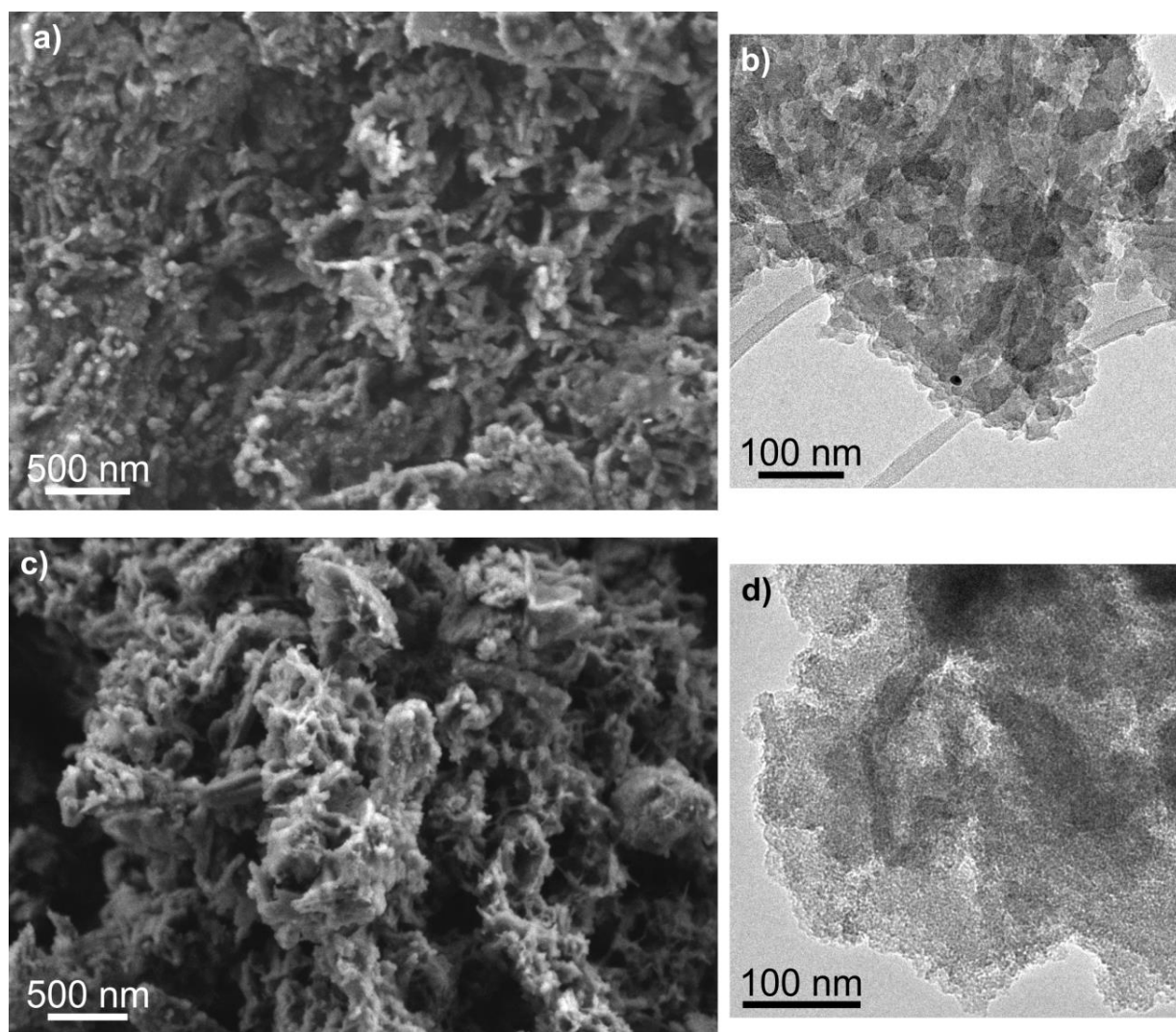
Figure S48. SEM (left) and TEM (right) micrographs of A-TE**B**PY (a,b) and A-TE**P**PY COF (c,d) showing multiflake agglomerates and sub-100nm platelets.
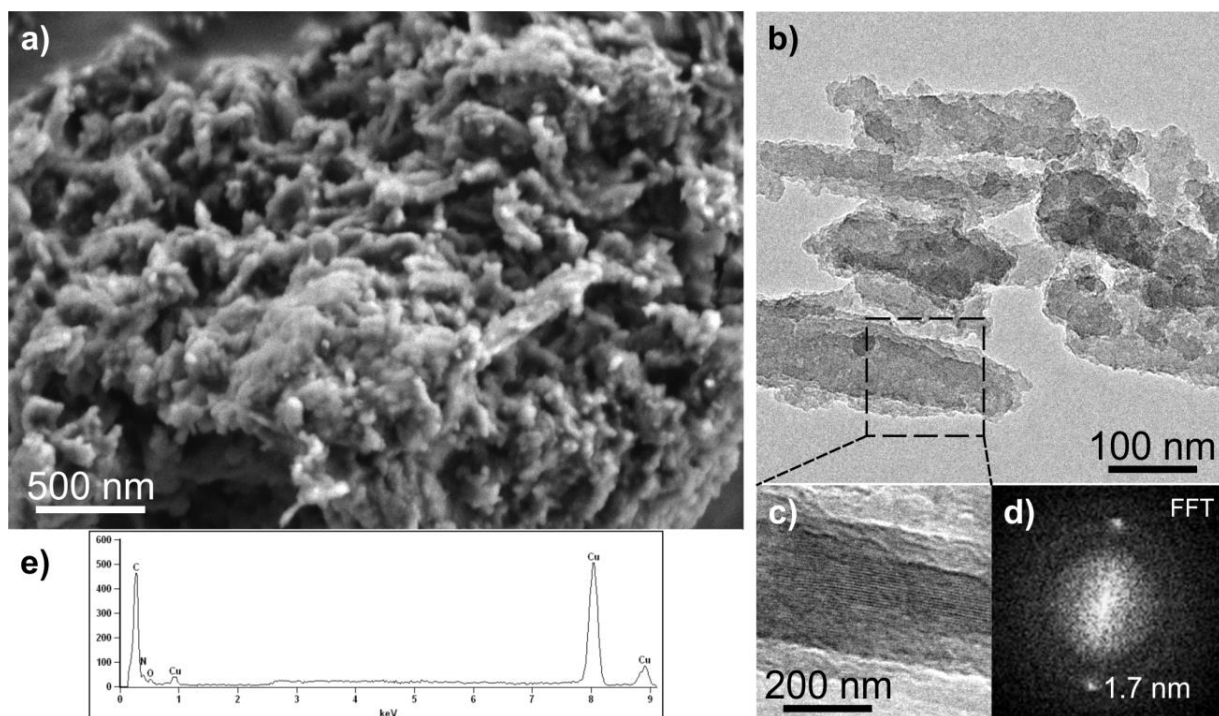
Figure S49. (a)-(c) SEM (left) and TEM micrographs/analysis of A-TE**N**PY showing multiflake agglomerates and platelets. (d) FFT of the enlarged area in (c) showing a distance of 1.7 nm close to the pore diameter. EDX (e) analysis shows the presence of C,N,O and copper (TEM grid).

O.   XPS of the COFs
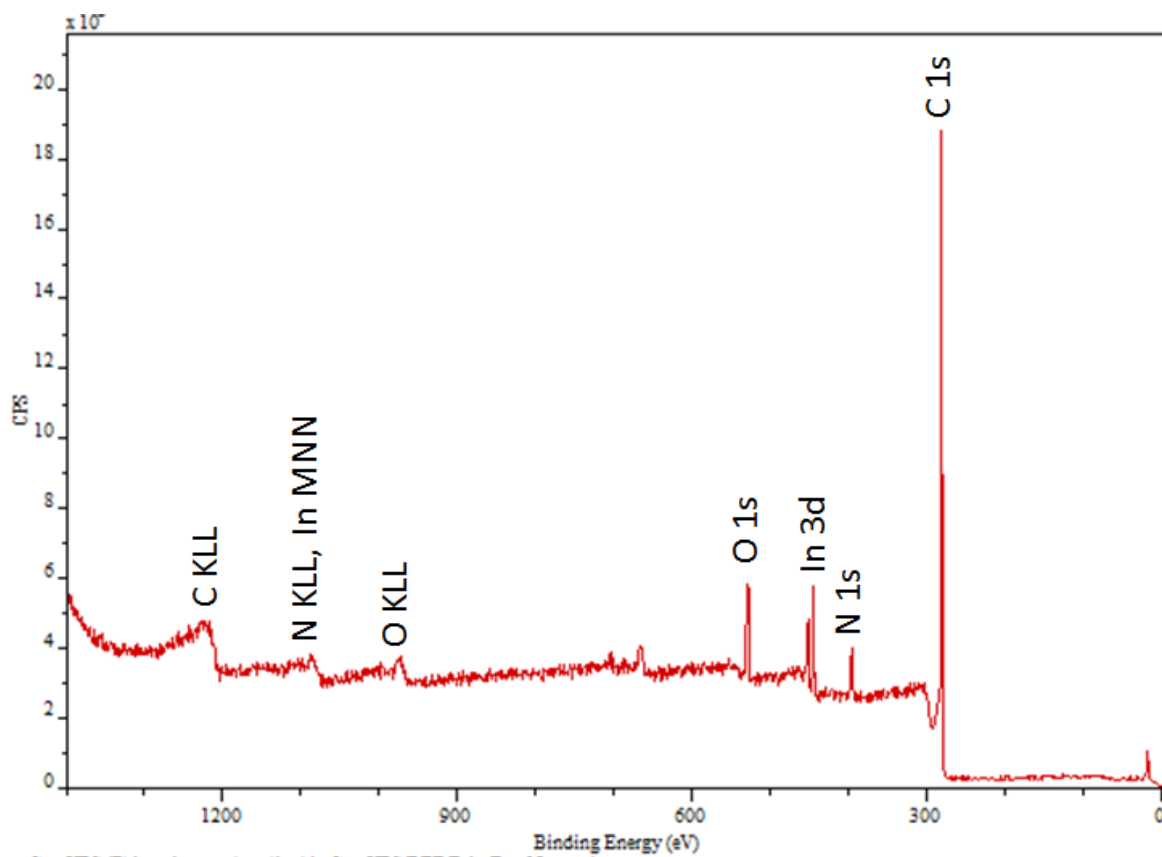
Figure S50. XPS of A-TE**B**PY COF on an indium substrate. Oxygen might be present due to surface oxidation of the indium substrate or terminating aldehyde groups or adsorption of water.
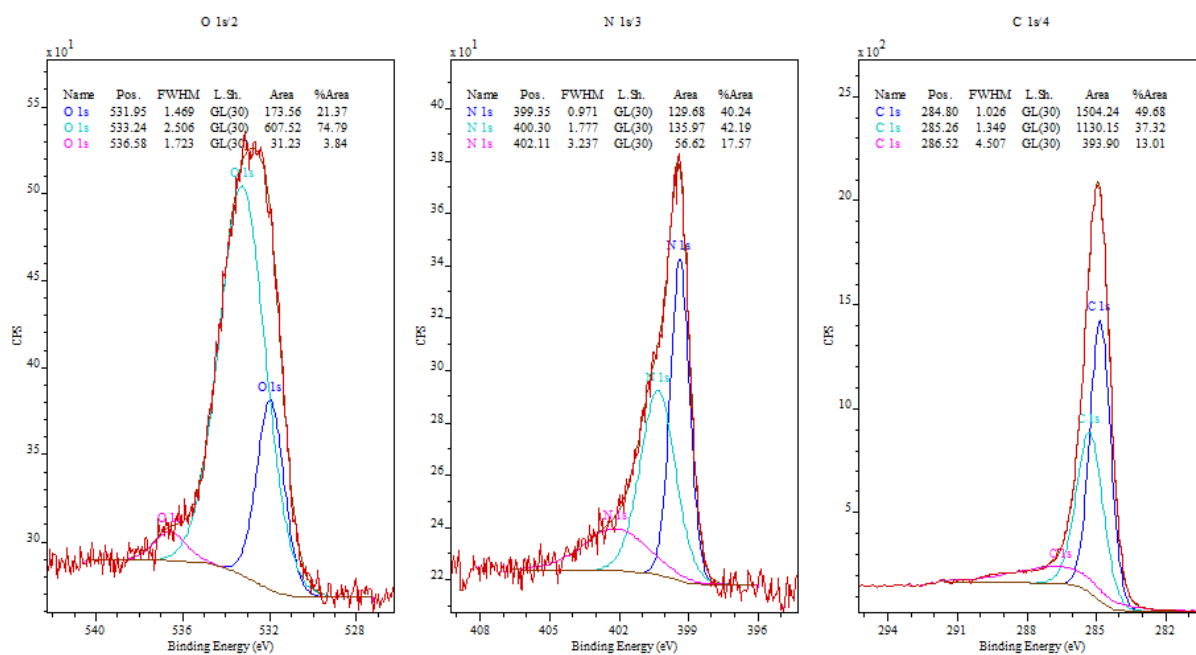
Figure S51. XPS detailed view of the O, N, and C 1s spectra of A-TE**B**PY COF on an indium substrate. Oxygen might be present due to surface oxidation of the indium substrate or terminating aldehyde groups, or adsorption of water.
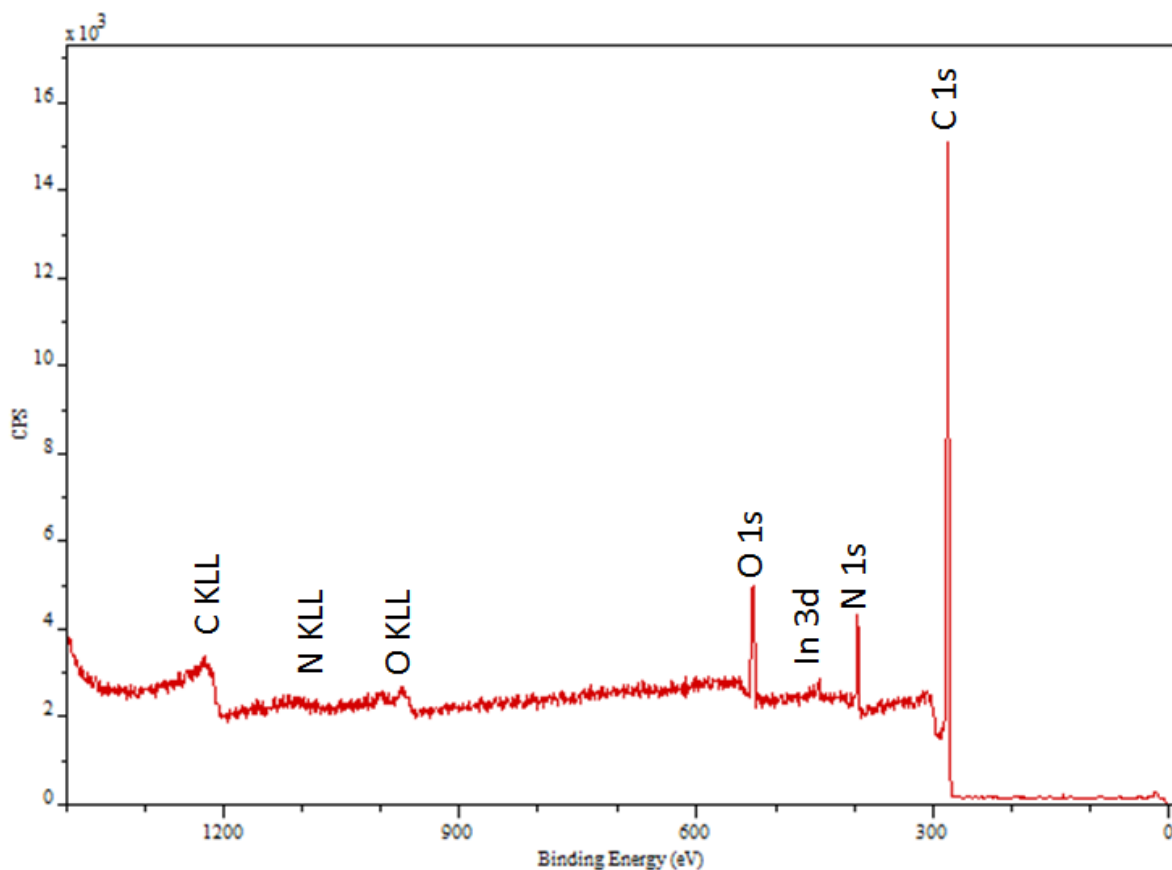
Figure S52. XPS of A-TE**N**PY COF on an indium substrate. Oxygen might be present due to surface oxidation of the indium substrate or terminating aldehyde groups or adsorption of water.

Figure S53. XPS detailed view of the O, N, and C 1s spectra of A-TE**N**PY COF on an indium substrate. Oxygen might be present due to surface oxidation of the indium substrate or terminating aldehyde groups, or adsorption of water.

Figure S54. XPS of A-TE**P**PY COF on an indium substrate. Oxygen might be present due to surface oxidation of the indium substrate or terminating aldehyde groups or adsorption of water. Fluorine is an impurity from the starting material of 2-chloropyrimidine-5-carboxaldehyde which has not reacted.

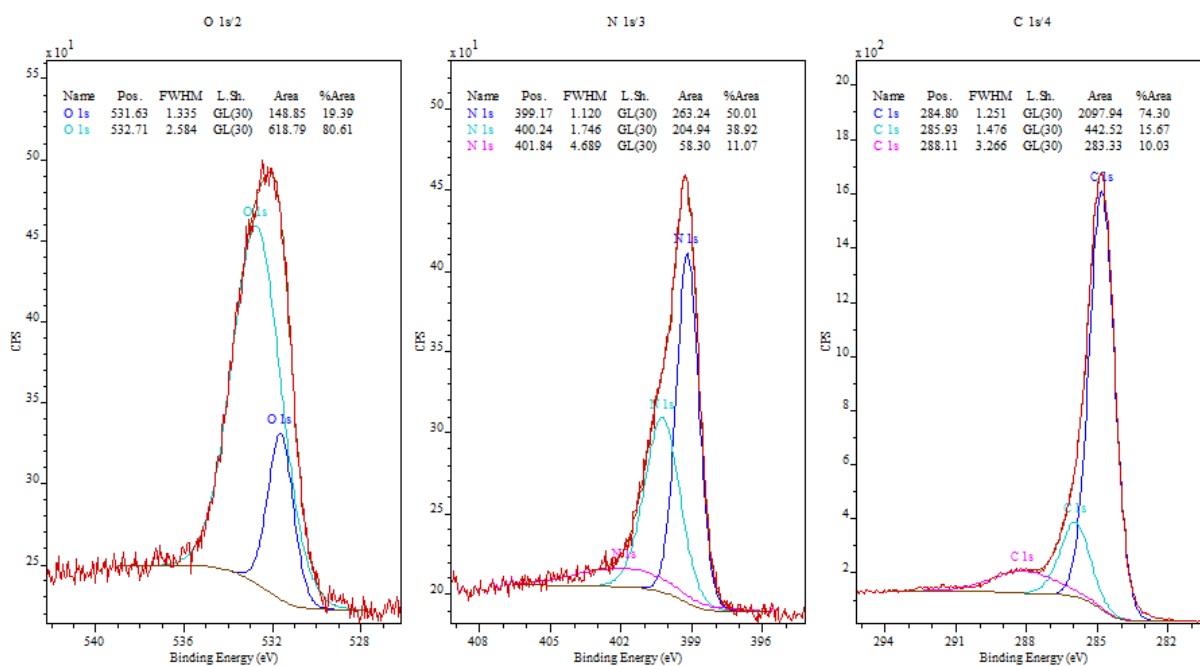**Figure S55.** XPS detailed view of the O, N, and C 1s spectra of A-TE**P**PY COF on an indium substrate. Oxygen might be present due to surface oxidation of the indium substrate or terminating aldehyde groups, or adsorption of water.
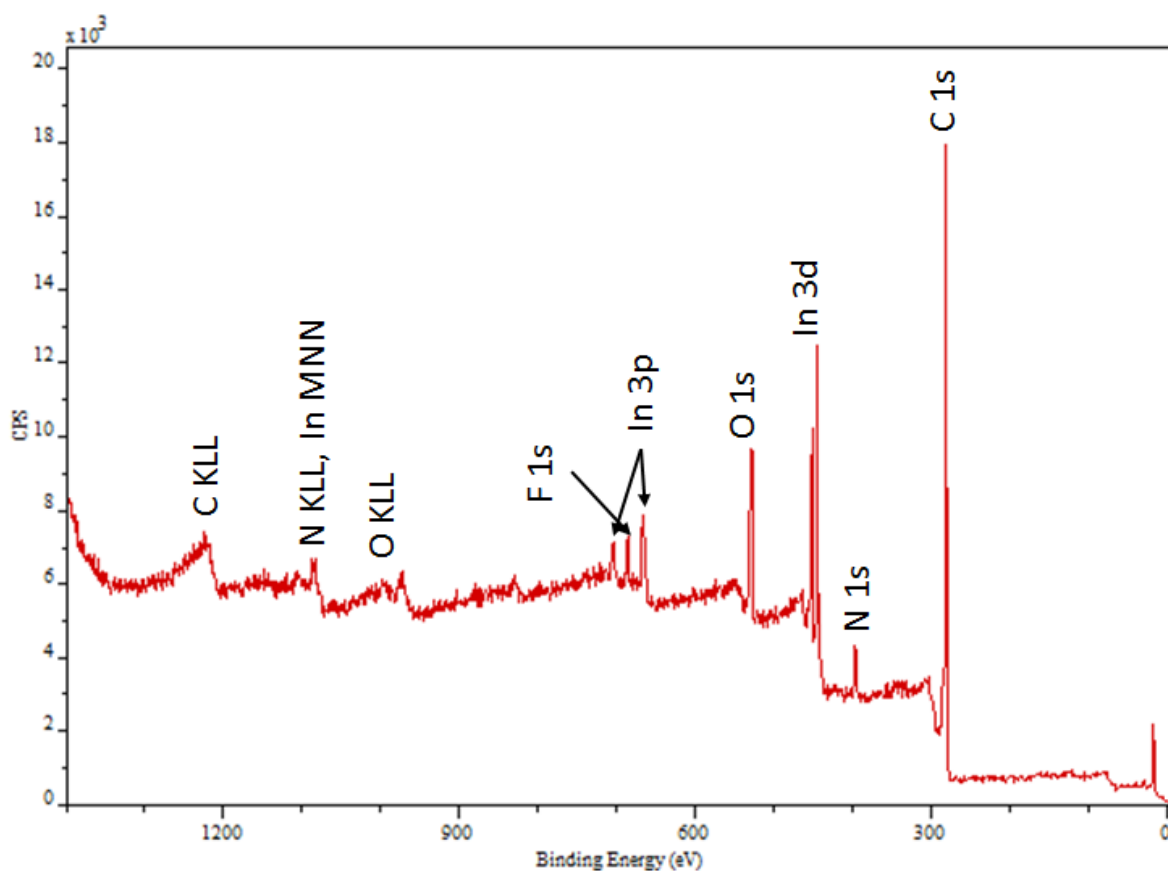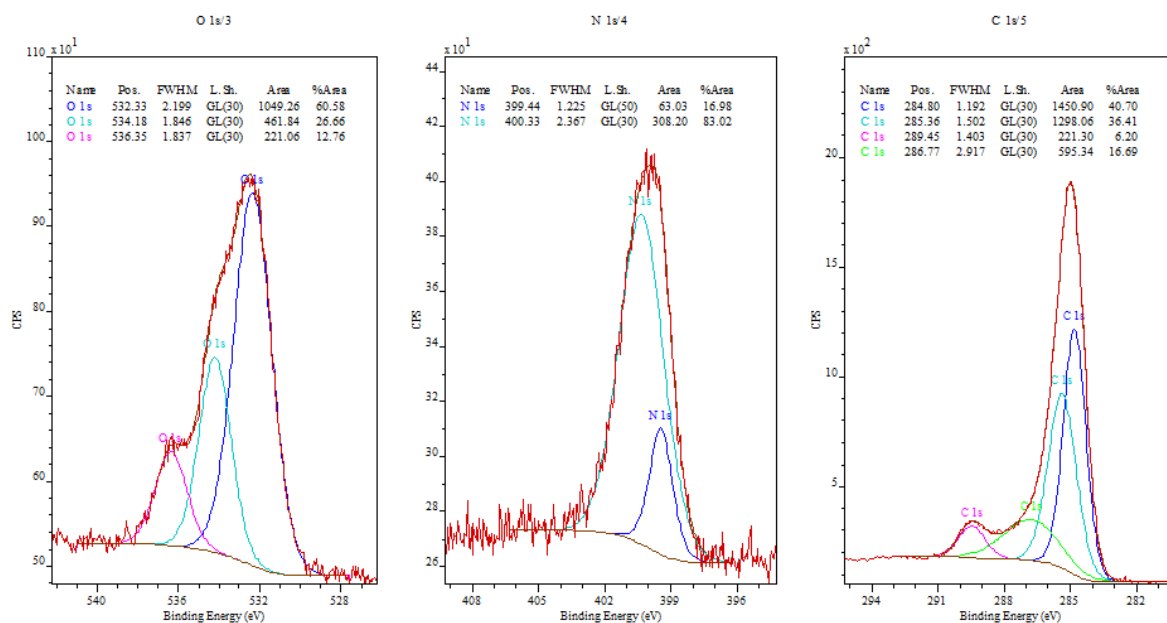
P.   References

[1]   J. C. de Mello, H. F. Wittmann, R. H. Friend, *Adv. Mater.* **1997**, *9*, 230–232.

[2]   C. Adamo, V. Barone, *The Journal of Chemical Physics* **1999**, *110*, 6158–6170.

[3]   M. Ernzerhof, G. E. Scuseria, *The Journal of Chemical Physics* **1999**, *110*, 5029–5036.

[4]   S. Grimme, J. Antony, S. Ehrlich, H. Krieg, *The Journal of Chemical Physics* **2010**, *132*, 154104.

[5]   S. Grimme, S. Ehrlich, L. Goerigk, *J. Comput. Chem.* **2011**, *32*, 1456–1465.

[6]   F. Weigend, R. Ahlrichs, *Phys. Chem. Chem. Phys.* **2005**, *7*, 3297–3305.

[7]   Y. Zhao, D. G. Truhlar, *Theoretical Chemistry Accounts* **2008**, *120*, 215–241.

[8]   a) J. Kussmann, C. Ochsenfeld, *J. Chem. Theory Comput.* **2015**, *11*, 918–922; b) J. Kussmann, C. Ochsenfeld, *J. Chem. Phys.* **2013**, *138*, 134114.

[9]   H. Vollmann, H. Becker, M. Corell, H. Streeck, *Justus Liebigs Ann. Chem.* **1937**, *531*, 1–159.

[10] S. Bernhardt, M. Kastler, V. Enkelmann, M. Baumgarten, K. Müllen, *Chem. - Eur. J.* **2006**, *12*, 6117–6128.

[11] G. Venkataramana, S. Sankararaman, *Eur. J. Org. Chem.* **2005**, *2005*, 4162–4166.

[12] D. D. Medina, V. Werner, F. Auras, R. Tautz, M. Dogru, J. Schuster, S. Linke, M. Döblinger, J. Feldmann, P. Knochel et al., *ACS Nano* **2014**, *8*, 4042–4052.

[13] O. V. Gutov, W. Bury, D. A. Gomez-Gualdron, V. Krungleviciute, D. Fairen-Jimenez, J. E. Mondloch, A. A. Sarjeant, S. S. Al-Juaid, R. Q. Snurr, J. T. Hupp et al., *Chem. - Eur. J.* **2014**, *20*, 12389–12393.

[14] S. Califano, G. Abbondanza, *The Journal of Chemical Physics* **1963**, *39*, 1016–1023.

[15] S. Lowell, J. E. Shields, M. A. Thomas, M. Thommes, *Characterization of porous solids and powders: surface area, pore size and density*, Springer Science & Business Media, Dordrecht, Netherlands, **2012**.

[16] S. Diring, F. Camerel, B. Donnio, T. Dintzer, S. Toffanin, R. Capelli, M. Muccini, R. Ziessel, *J. Am. Chem. Soc.* **2009**, *131*, 18177–18185.

[17] Z. Chen, H. N. Dinh, E. Miller, *Photoelectrochemical water splitting. Standards, experimental methods, and protocols*, Springer, New York, **2013**.

[18] a) P. Quaino, F. Juarez, E. Santos, W. Schmickler, R. J. Behm, *Beilstein Journal of Nanotechnology* **2014**, *5*, 846–854; b) T. F. Jaramillo, K. P. Jørgensen, J. Bonde, J. H. Nielsen, S. Horch, I. Chorkendorff, *Science* **2007**, *317*, 100–102; c) J. Greeley, T. F. Jaramillo, J. Bonde, I. Chorkendorff, J. K. Norskov, *Nat Mater* **2006**, *5*, 909–913.

A.3 Supporting Information for Publication 3

ADVANCED MATERIALS

Supporting Information

Toward an Aqueous Solar Battery: Direct Electrochemical Storage of Solar Energy in Carbon Nitrides

Filip Podjaski, Julia Kröger, and Bettina. V. Lotsch*

Supplementary Information

Towards an Aqueous Solar Battery: Direct Electrochemical Storage of Solar Energy in Carbon Nitrides

F. Podjaski,[ab] J. Kröger[ac] and B. V. Lotsch[acde*]

[a.] *Max Planck Institute for Solid State Research, Heisenbergstraße 1, 70569 Stuttgart, Germany, E-mail:* b.lotsch@fkf.mpg.de
[b.] *Ecole Polytechnique Fédérale de Lausanne, Station 12, 1015 Lausanne, Switzerland*
[c.] *Department of Chemistry, University of Munich (LMU), Butenandtstraße 5-13, 81377 München, Germany*
[d.] *Nanosystems Initiative Munich (NIM), Schellingstraße 4, 80799 München, Germany*
[e.] *Center for Nanoscience, Schellingstraße 4, 80799 München, Germany*

1. Experimental

NCN-PHI synthesis
All chemicals used are reagent grade purity. Potassium containing NCN-PHI was prepared following published procedures.[1, 2]

NCN-PHI ion exchange for CV control experiments
For the ion exchange with Li^+ ions potassium containing NCN-PHI (200 mg) was dispersed in a LiCl solution (1 M, 20 ml). To avoid protonation, LiOH solution (1 M,) was added until a pH of 9-10. After several hours of stirring the product was separated from the solution by centrifugation and multiple washing with water until a neutral washing solution was obtained. This procedure (i.e. stirring in LiCl solution with a pH of 9-10 and washing of the product) was repeated two more times. The final yellow solid was dried at 60°C in vacuum overnight.

Sample and electrode preparation
Nanosheets of NCN-PHI were obtained by sonicating the pristine powder in deionized water for 2 h. The sheets were separated from the bulk material by two centrifugation steps (353 RCF, 25 min and 795 RCF, 40 min) in a SIGMA 3-30k centrifuge. Subsequently, the nanosheet supernatant was separated by centrifugation for 90 min (35329 RCF), yielding dense dispersions in the range of 1-5 mg/ml.

Electrode substrates were prepared by contacting SIGMA ALDRICH FTO slides (surface resistivity: 7 Ohm/sq), cut to 5×7 mm, to isolated copper wires with silver paste. The contact was sealed with epoxy (3 M Scotch-Weld DP410), leaving an exposed electrode area of approximately 5x5 mm². After plasma cleaning, an equivalent of the nanosheet suspension, usually 10 µg of NCN-PHI, was drop cast on the electrodes and dried on a hot plate at 60°C for at least 2 h. For spin-coated electrodes, 25 µg of material was used for every spin coating step (ramp: 1200 rpm/s; 60 s spin coating; 10 min drying at 60°C in-between the steps; rotation frequency and amount of steps depends on sample and is described in the respective figures). The mass loading of spin-coated electrodes could not be determined due to the low specific weight of NCN-PHI with respect to the electrode (<20 µg) and the roughness of the substrate, which is beneficial for adhesion but disadvantageous for thickness or volume determination. The mass was therefore determined from the drop-casted samples by calculation of the used sample concentration and by using a quartz microbalance (SARTORIUS ME36S).

Photoelectrochemical measurements

Photoelectrochemical measurements were performed in a self-made closed glass reactor equipped with a quartz window for side illumination. 1 M Na-based phosphate buffer solution (containing NaH_2PO_4 (57.2 g, 0.48 mol) and Na_2HPO_4 (74.2 g, 0.52 mol) in water (1 l)) at pH=7 or aqueous KCl solution (1 M) were used as electrolyte. An Ag/AgCl reference electrode with saturated KCl (+0.197 V vs. NHE) was used as reference electrode and a glassy carbon rod as counter electrode. The electrolyte was purged with >99% pure N_2 or Ar prior to every measurement through a porous glass frit to remove dissolved oxygen. The dissolved oxygen content was monitored to be <5 ppb with a PRESENS Fibox 3 Trace optic oxygen meter together with a PSt6 sensor spot being placed on the inside of the reactor. Electrochemical measurements were recorded and analyzed using an IVIUM CompactStat potentiostat and the IviumSoft software. Simulated sunlight was provided by a SCIENCETECH LightLine A4 solar simulator (class AAA) fitting the ASTM standard G138 (AM 1.5G). The intensity of the illumination was measured by a calibrated THORLABS S310C thermal power meter and further confirmed by a calibrated OCEAN OPTICS USB4000 spectrometer.

Hydrogen evolution in phosphate buffer and 4-MBA

The photocatalytic experiments were performed in a glass photoreactor with a quartz window on the top. The whole reactor was thermostated at 25°C, as described in our previous works.[1, 2] All glassware used for the experiments were soaked overnight in *aqua regia* for cleaning. A standard experiment for hydrogen evolution involved irradiating the reactor under AM 1.5G conditions. As a light source a xenon lamp (Newport, 300 W) equipped with a water filter and a full spectrum mirror (2000 nm >λ>200 nm) was used. The headspace of the photoreactor was evacuated and backfilled with argon several times prior to the experiment in order to provide an oxygen free environment. During illumination, the headspace of the reactor was periodically sampled and the components were quantified by gas chromatography (Thermo Scientific TRACE GC Ultra, equipped with a TCD detector) using argon as carrier gas.

IR

ATR-IR spectra were collected with a PerkinElmer UATR TWO spectrometer equipped with a diamond crystal. Characterization of NCN-PHI nanosheets by IR showed no changes in the structure of the samples being measured either immediately, after drying of a fresh and a 3 week old nanosheet suspension (Fig. S1.1), respectively.
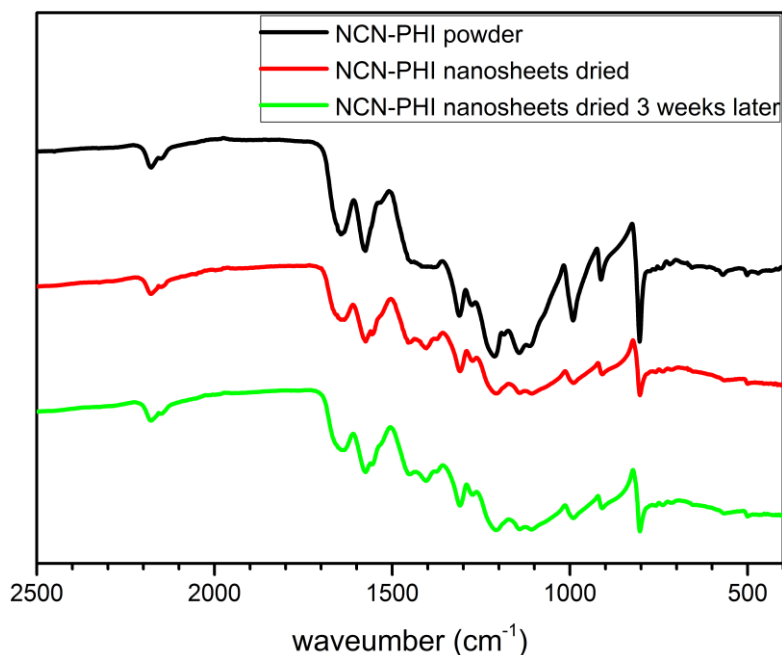
Figure S1.1: IR spectra of the pristine NCN-PHI powder and of dried nanosheets that were suspended in aqueous solution in a fresh or a 3 week old suspension. While some band intensities change compared to the measurements of the pristine nanosheets, the dominant band structure remains the same and the NCN-signal at 2180 cm^{-1} stays unchanged. It is thus unlikely that hydrolysis occurs. Longer suspending times do not lead to additional changes.

ICP-OES

ICP measurements were performed on the powder before sonication and on the dried sheet dispersions to determine the amount of potassium which is present in the structure. The bulk NCN-PHI powder contained 9.55 wt% K while the sheets have a slightly higher K content of 10.22 wt%, corresponding to a relative amount of 0.55 (0.60) potassium atoms per heptazine unit (assumed molecular mass of the heptazine unit of 208.7 g/mol), resulting in an overall average molecular mass of 231(2) g/mol per potassium containing heptazine unit. The charge of the potassium ions is most likely balanced by deprotonated imide-bridges between the heptazine units and the NCN functional groups (Fig. 6).

TEM characterization

Transmission electron microscopy (TEM) was performed with a Philips CM30 ST (300 kV, LaB$_6$ cathode). The samples were suspended in water and drop-cast onto a lacey carbon film (Plano). The TEM images show highly crystalline flakes with a lateral size of 30-60 nm, with a characteristic spacing of approximately 3.0 Å corresponding to the XRD stacking peak and 11 Å corresponding to the in-plane pore-to-pore distance. Note that a slight contraction of the pores is induced by the electron beam exposure.
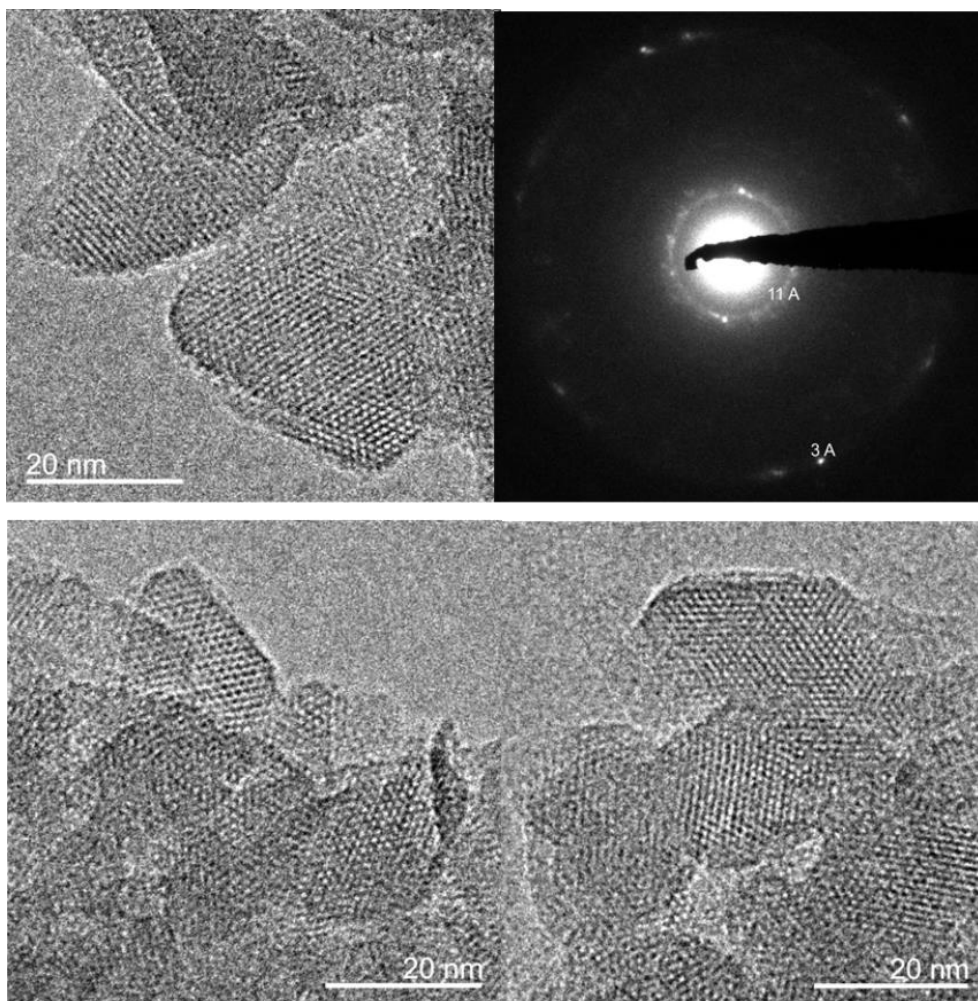
Figure S1.2: TEM images of nanosheets after exfoliation, showing lateral dimensions of 30-60 nm. Top row: TEM image and corresponding SAED of multiple exfoliated flakes of NCN-PHI. Bottom row: Further TEM images showing the sharp contours of the crystalline nanoflakes along with the hexagonal pore system shown schematically in Fig. 6.

Optical band gap

The optical band gap of dried NCN-PHI nanosheets was determined using an Agilent Cary 5000 UV-Vis spectrophotometer.[3] The absorbance was determined in analogy to the measurements reported in references [1] and [2].
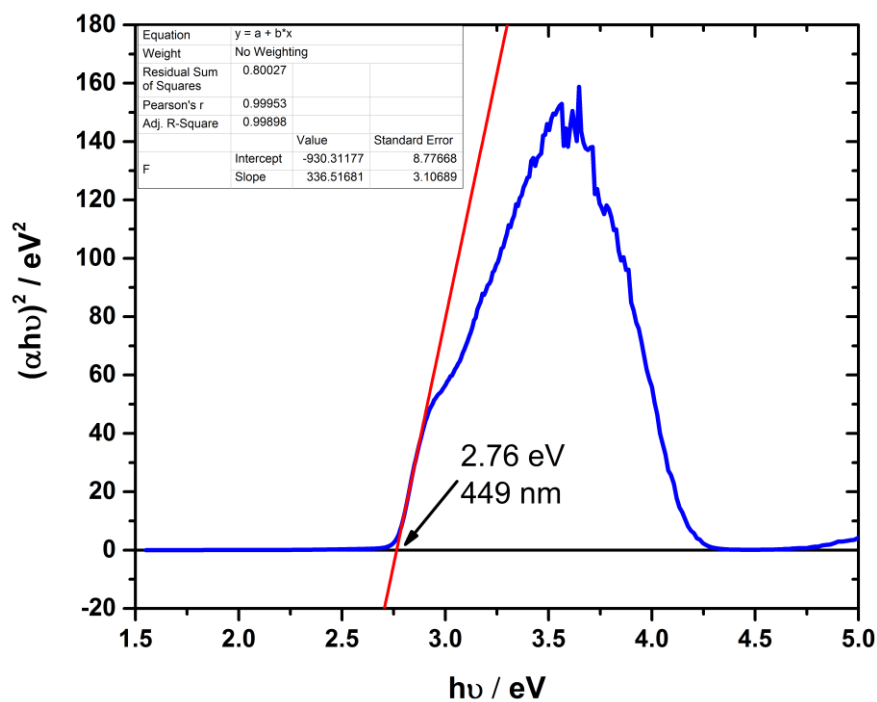
Figure S1.3: UV-VIS diffuse reflectance measurement of dried NCN-PHI nanosheets. The Tauc plot reveals a band gap of 2.76 eV.

Zeta potential

Zeta potential was measured on a Malvern Zetasizer Nano ZS. The NCN-PHI sample was suspended at concentration of 1.0 mg/ml. The measurements were intended to estimate the surface charge and thus a hydrodynamic radius of the dispersed nanosheets. The yellow ground state as well as the blue, excited state in the presence of 4-MBA after illumination were investigated. Since the blue color decayed due to the measurement influence and both measurements resulted in a Zeta potential of -20 mV and, a correlation between the blue state and the surface charge cannot be made by this invasive measurement.

2. Photo-electrochemical measurements

2.1 Solar battery discharge characteristics
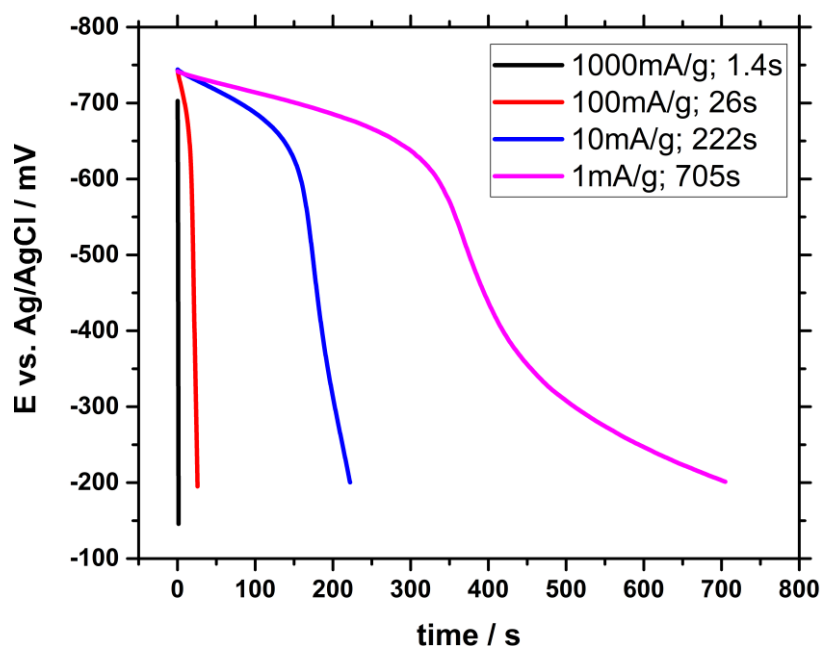
Figure S2.1. NCN-PHI (solar) battery half-cell characteristics of electrodes with 10 µg NCN-PHI in 1M phosphate buffer + 5 mM 4-MBA showing the discharge profile directly after 1 min of 1 sun illumination with current densities varying from 1 mA/g to 1 A/g. The specific capacity maximum is obtained at 100 mA/g for loadings of 10 µg, leading to the most complete discharge within 26 s only, corresponding to a C-rate of 139 for the charge available (2.6 C/g) in this electrode after 1 min of illumination.
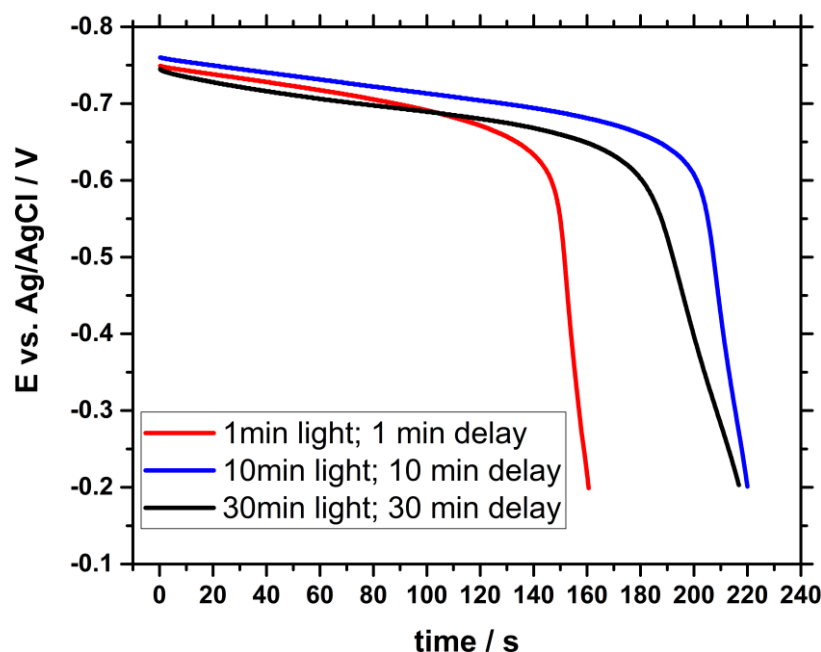
Figure S2.2. NCN-PHI (solar) battery half-cell characteristics summarizing the discharge properties (100 mA/g) of electrodes with 10 µg NCN-PHI after 1 sun illumination in 1 M phosphate buffer + 5 mM 4-MBA, showing the discharge profile after 1 min illumination and 1 min delayed discharge, 10 min illumination and 10 min delayed discharge as well as 30 min illumination and 30 min delayed discharge. The total charge extracted was used in comparison to the measurements in Fig. 2 b to construct Fig. 2 d.

6

2.2 Discussion of decay channels of the photoelectrodes

Decay via the FTO substrate

A decay in the extracted charge after illumination in phosphate buffer and 4-MBA was observed when the discharge was delayed. This is attributed to faradaic currents from the FTO substrate to the electrolyte. We have shown in Fig. 4 b that a blank FTO substrate has a stable current of -110 nA at -700 mV vs. Ag/AgCl and -180 nA at -800 mV. As the electrode potentials after photocharging are in that region, an average decay current of -145 nA can be assumed. Electrons stored on the NCN-PHI-photoelectrodes are in electrical contact with the partially uncovered FTO and thus allow a charge transfer via the FTO substrate to the electrolyte (a direct charge transfer to the electrolyte is negligible as discussed in Section S2.2: Decay via hydrogen evolution by NCN-PHI: these currents are smaller than 1 pA). As we can observe in Fig. 2 c, the extracted charge decays by 4.2 C/g after a waiting time of 600 s (10 min illumination case) and by 1.2×10^{-5} C after a delay time of 1800 s (30 min illumination case). The average resulting loss currents are 70 nA for 10 min and 67 nA for 30 min delay, respectively. This corresponds to 48% and 45%, respectively, of the faradaic currents from a blank substrate in this potential window. The estimated average decay currents for the longer delay are slightly smaller as the material in contact to the FTO has attained a less negative potential due to decay during the delay time. As one can see in Fig. S2.3, the FTO substrates are only partially covered by the NCN-PHI (especially in the drop cast case) and the uncovered part can thus well explain the reason for this decay. For the drop cast samples NCN-PHI is detached partially during measurement (Fig. S2.3 b and c). More homogeneous deposition techniques should allow decreasing these decay currents and likely make our photoelectrodes more stable.

SEM characterization

Scanning electron microscopy (SEM) was performed on a Zeiss Merlin electron microscope.
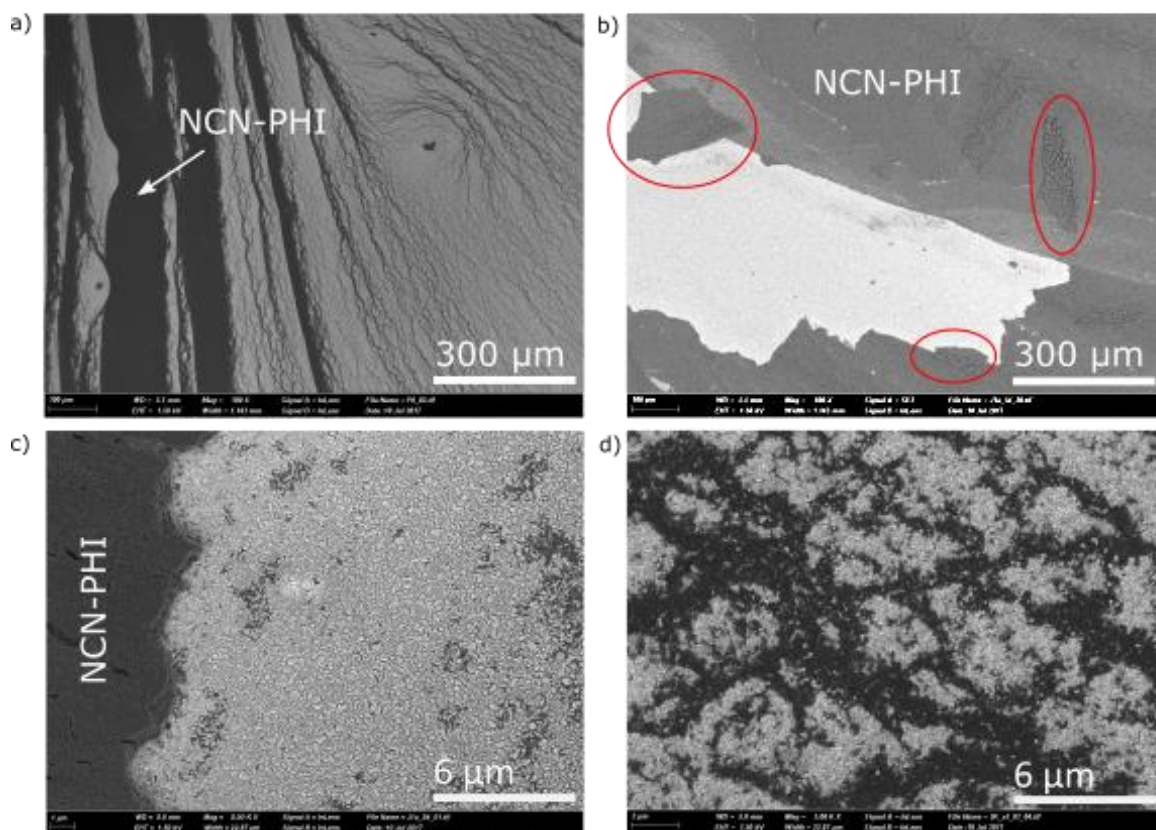

Figure S2.3: SEM images of NCN-PHI@FTO electrodes with FTO substrate being bright(er) and the active NCN-PHI dark due to the back scattered electrons' contrast. a) Image of a drop cast electrode (10 µg on 0.25 cm²) showing the sample border with thick black parts (NCN-PHI) and sparsely covered or uncovered parts of the FTO-electrode after drop casting NCN-PHI and drying. b) Image of a homogeneously covered part (grey) and an uncovered area (white) after measuring discharge curves in phosphate buffer. The red circles highlight flakes of NCN-PHI that detached from the FTO substrates and re-deposited on top of the homogeneous NCN-PHI layer after drying the electrode after the measurement. c) Enlargement of an area after detachment of NCN-PHI during the measuring process (can be seen on the right side in comparison to the left side, where the sample still adheres to the substrate). d) Spin coated electrode (3 krpm, 5x) after cycling in phosphate buffer.

Decay via hydrogen evolution by NCN-PHI

The photocatalytic activity of NCN-PHI (20 mg) was measured for a suspension of the catalyst in phosphate buffer (20 ml, pH7) with donor 4-MBA (24 mg, equivalent to a concentration of 10 µM). The same measurement was done for a suspension of NCN-PHI in water (20 ml) or an aqueous solution of KCl (1 M, 20 ml), each in the presence of 4-MBA (24 mg, equivalent to a concentration of 10 µM).

The results of these three experiments showed that no detectable amount of hydrogen is evolved after 23-27 h of illumination. Within each measurement the amount of total produced hydrogen was below 2 ppm (which is equal to 0.9 µmol/g). Note that a reliable distinction between signal and noise is not possible in this low range. In the case of maximal deviation of 2 ppm, a ratio of hydrogen evolution of 0.03-0.04 µmol/(h×g) is observed. Since every molecule of hydrogen is generated by two electrons the maximal reaction current corresponds to 0.06-0.08 µmol/(h×g) of electrons, or $1.6\text{-}2.1\times10^{-6}$ A/g. Based on the mass loading of NCN-PHI electrodes (10 µg), this corresponds to a hydrogen generation

current of 1.6-2.1 pA which is negligible compared to the currents measured in the experiments (usually in the range of 1 μA).
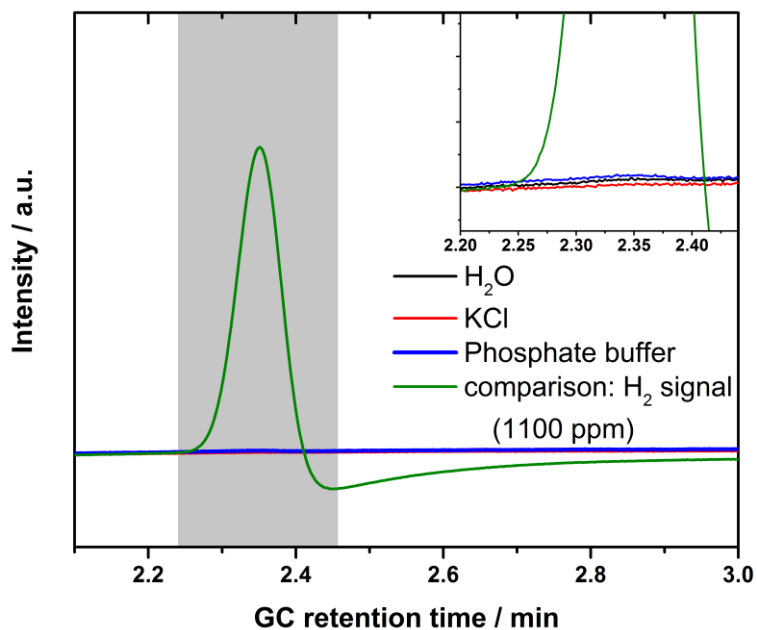
Figure S2.4: Gas chromatogram (GC) plot of the hydrogen evolved by NCN-PHI in water, KCl and phosphate buffer (no signal) after 24h of continuous illumination (1 sun) in the presence of 4-MBA, and a reference signal showing 1100 ppm H_2, which is the amount of hydrogen expected for an average NCN-PHI sample evolving hydrogen in the presence of Pt as a cocatalyst within 3h.

2.3 Electrode stability
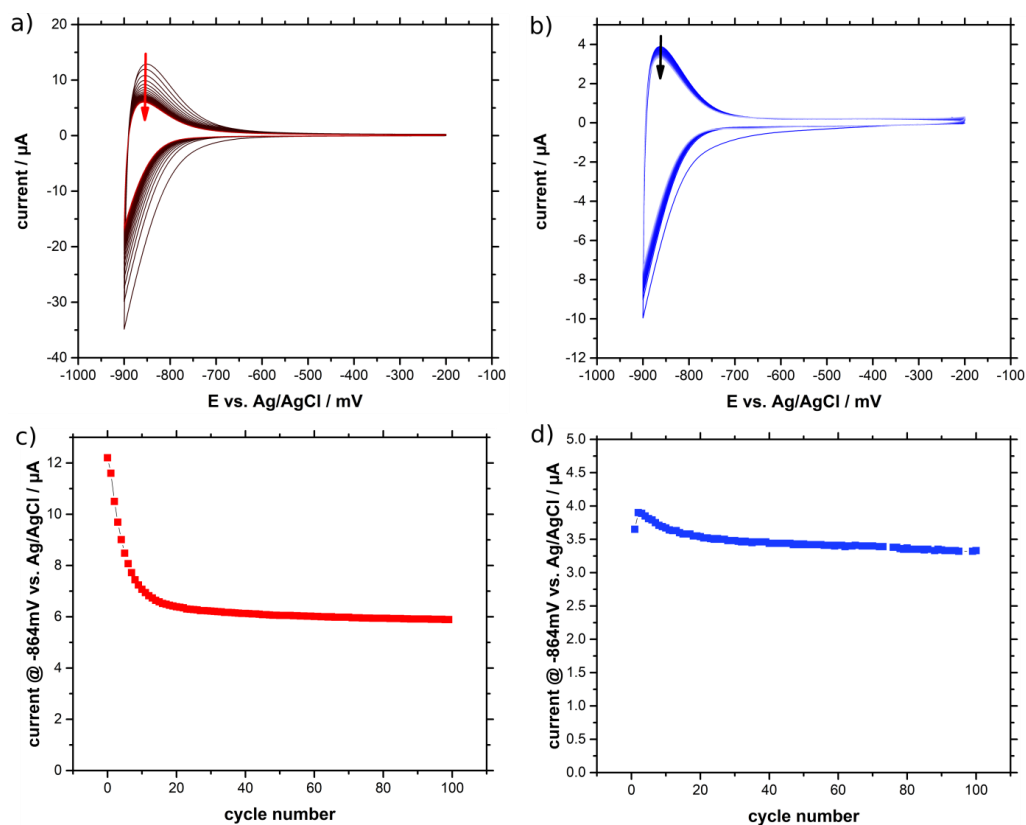
Figure S2.5: CVs of spin coated NCN-PHI electrodes (50 mV/s) in 1 M KCl solution and the analysis of their stability. a) Electrode after 20 spin coating cycles at 2000 rpm. b) Electrode after 5 spin coating cycles at 3000 rpm; c) and d) show the decay of the peak currents of a) and b), respectively.

As seen from the measurements above, the stability of the material on the electrode depends sensitively on the deposition technique and amount of material deposited. The stability is thus limited by cohesion and adhesion. While the most stable electrodes were achieved by spin coating NCN-PHI at 3000 rpm, they could not be used for the measurements reported in the main text since the mass loading could not be precisely determined.

Measurements in phosphate buffer (Figure S2.6) show a decreased stability for both drop cast and spin coated electrodes with respect to the measurements in KCl. The thin spin-coated electrodes at 3000 rpm (blue curve) are somewhat more stable than drop cast ones and thick ones from spin-coating (red curves). If one compares the CVs in Fig. S2.5 and S2.6, a slightly positively shifted potential of maximum current can be observed for spin-coated electodes measured in phosphate buffer compared to electrodes measured in KCl (-860 mV vs. Ag/AgCl in KCl vs. -760 mV in phosphate buffer for the same scan rate of 50 mV/s). The peak shift is attributed to faster diffusion kinetics in KCl due to the smaller hydrodynamic radius of K^+ vs. Na^+ as discussed in the main text. Still, phosphate buffer was used to analyze the (solar) battery capacity values due to better absolute current values compared to KCl for electrodes that were prepared similarly. The reason for the different decay properties in KCl and phosphate buffer is not known yet but is attributed to different adhesion and wetting properties, different surface potentials, or different ion kinetics. As the observed decay in electrode performance is only accelerated by cycling but still present without, these results also affect long-term electrode stability in the electrolyte and explain a decrease in performance in terms of storable charge and shape of the discharge curves (decay after 12 h illumination after hours in the electrolyte, e.g. Fig. 2 b).
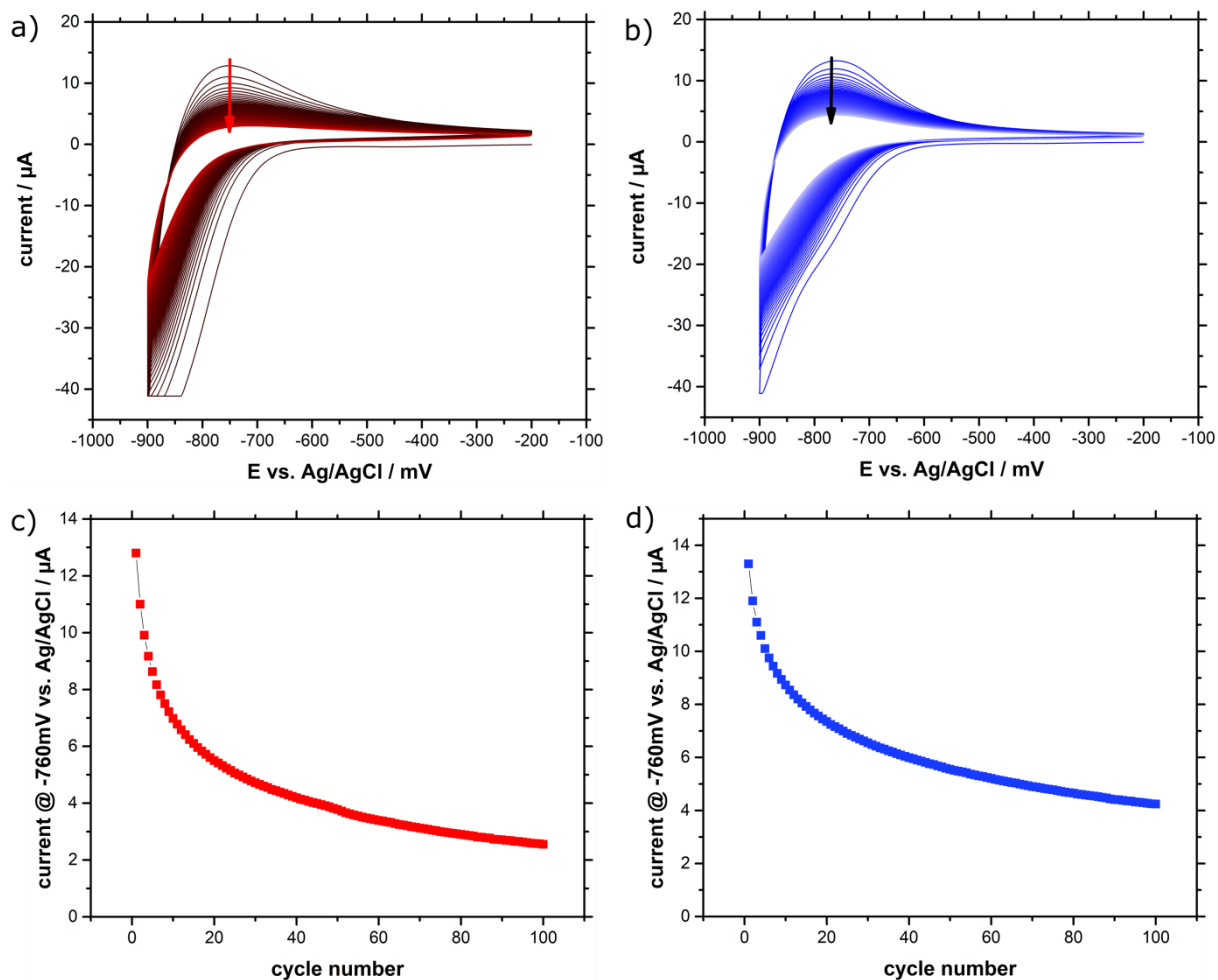
Figure S2.6: CVs of spin coated NCN-PHI electrodes (50 mV/s) in 1 M phosphate buffer solution and the analysis of their stability. a) Electrode after drop casting 10 µg and subsequent drying on a hot plate. b) Electrode after 5 spin coating cycles at 3000 rpm; c) and d) show the decay of the peak currents of a) and b), respectively.

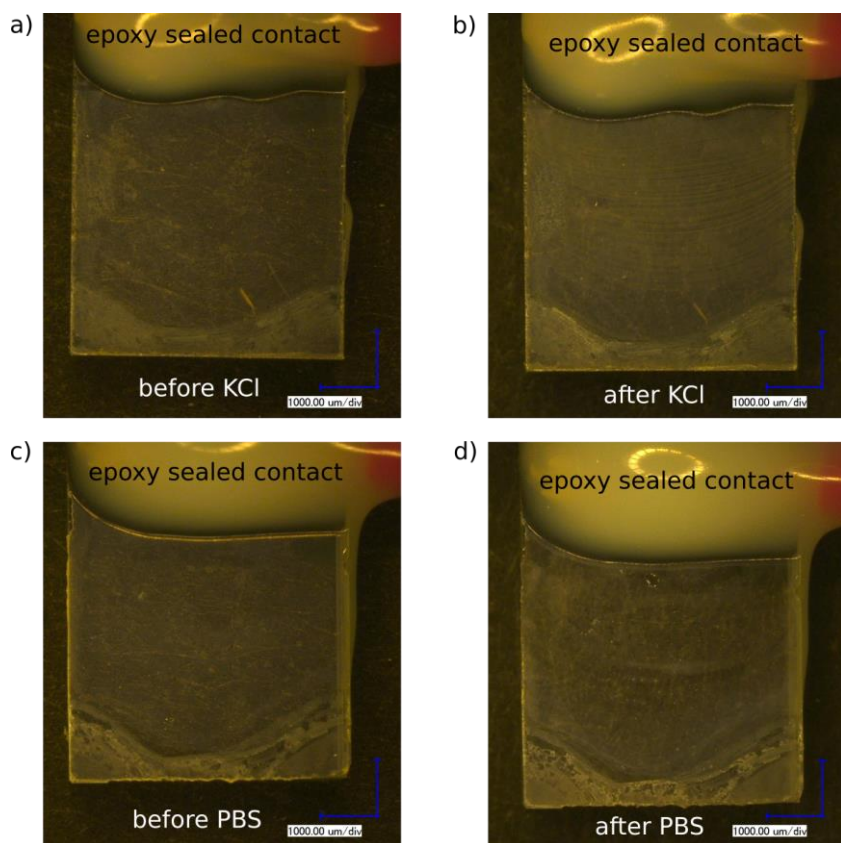**Optical electrode characterization**

Figure S2.7: Optical images of NCN-PHI electrodes spin coated at 3000 rpm before and after CV measurements in KCl and phosphate buffer (from Fig. S2.5 and S2.6), showing the macroscopic homogeneity of the material in the central part of the electrodes before and after measuring as well as its apparent macroscopic adhesion to the FTO substrate, which is best visible on the bottom of the electrodes where more material has been deposited. A quantification of material on the FTO substrate is difficult by this technique.

2.4 Long term OCP stability after illumination
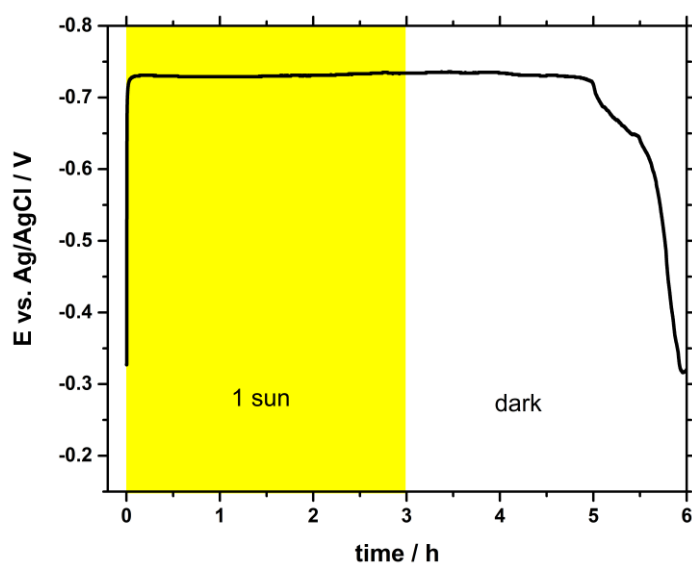
2.5 Capacitance analysis by CV

CVs in KCl
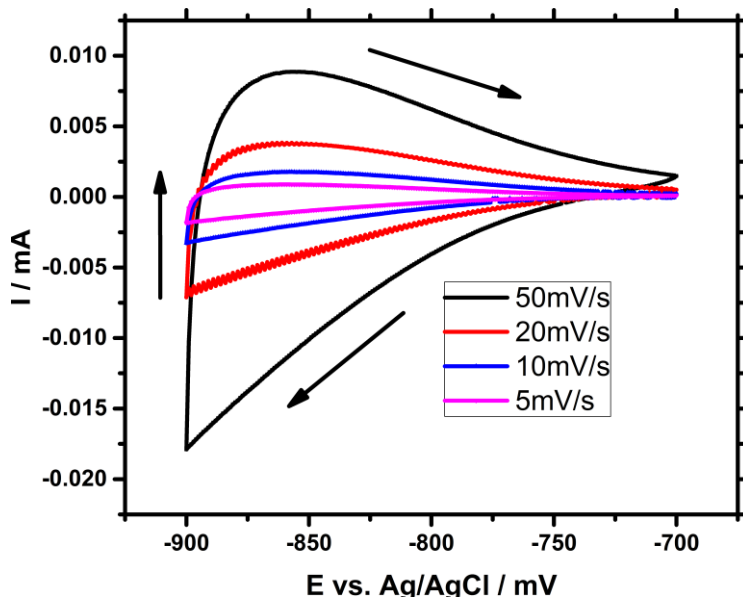
Figure S2.9: CVs in the dark of NCN-functionalized NCN-PHI drop cast on FTO electrodes in oxygen free 1 M KCl solution after the first cycle with varying scan rates (only the respective 2nd cycle is shown). The presence of a capacitive process is visible by the fact that the negative scan leads to negative currents that subsequently are extracted in the forward scan (positive currents), see Fig. 4 b and c and their discussion. The asymmetric curve indicates different charging and discharge kinetics. An increase in scan rate leads to increased currents. The relation between scan rate and current is used to determine the kind of capacitive process[4], as evaluated and discussed in Fig. S2.10 and S2.11..

Capacitance behavior of NCN-PHI
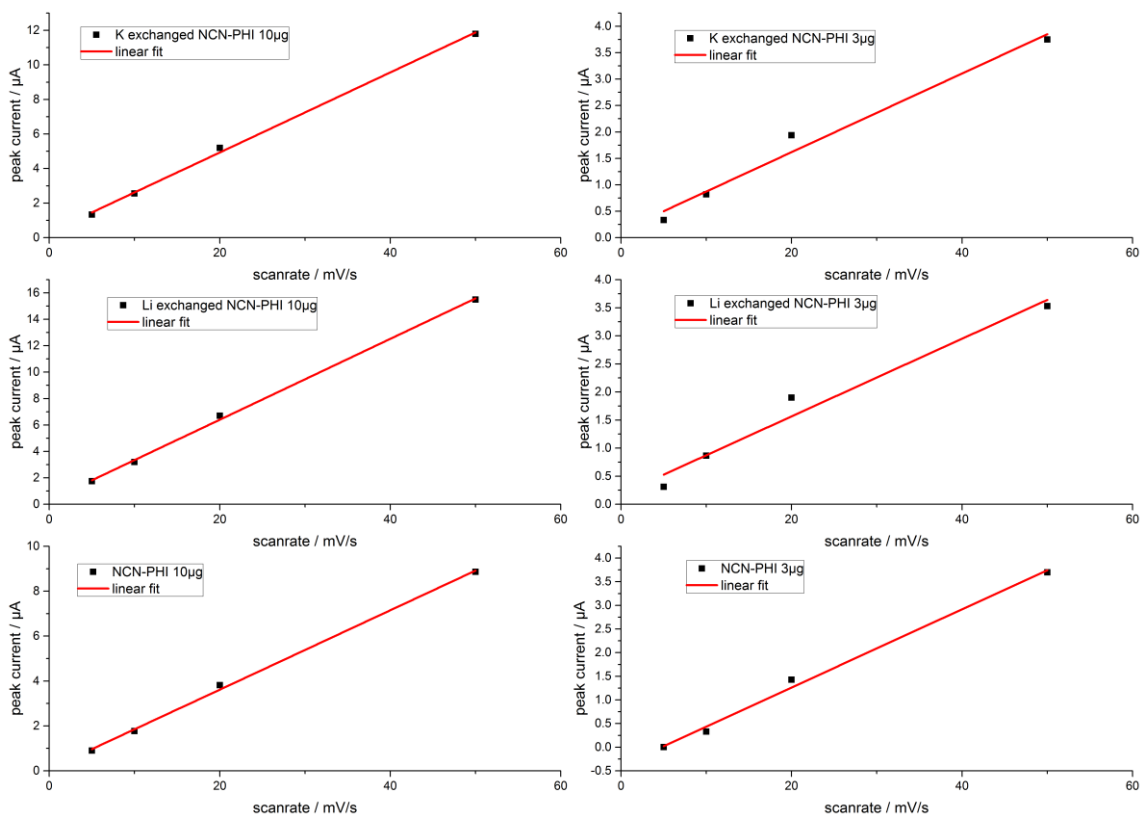
Figure S2.10: Linear fits of the peak currents for the capacitance evaluation with loadings of 10 µg (left) and 3 µg (right) for NCN-PHI nanosheets and Li$^+$ ion-exchanged derivates to probe the role of the intrinsic ion (K$^+$) and the exchange process (exchanging K$^+$ for Li$^+$). The top row represents the measurements on NCN-PHI, (a) evaluates the data from Fig. S2.9), the middle row those after Li$^+$-exchange and the bottom row the pristine sample synthesized from KSCN, containing K$^+$. The linearity of the fit proves that the capacitance follows a surface controlled reaction process and is one type of pseudocapacitance as further explained in Fig. S2.11.
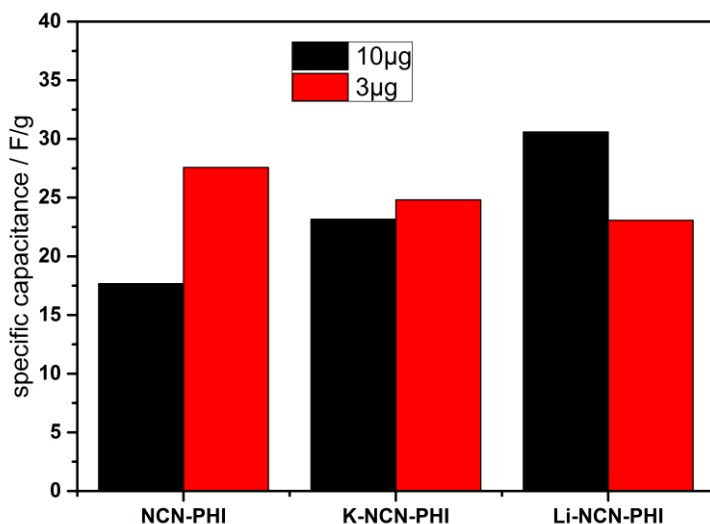
Figure S2.11: Specific capacitance extracted from the linear fits in Fig. S2.10 following the equation I = C × v, with I being the current, v the scan rate and C the pseudocapacitance which is equivalent to the slope.[4, 5] The average capacitance value lies around 25 F/g. The slight variation between different samples and loadings is attributed to inhomogeneous NCN-PHI particle distributions after drop casting and drying, leading to different amounts of material in electrical contact to the electrode and the surrounding electrolyte.

The capacitance extracted from the scan rate-dependent measurements (Fig. S2.10) yields approx. 25 F/g on average and is hence smaller than previously reported for melon-type carbon nitrides (71 F/g for bulk CN$_x$ and 275 F/g for highly structured nanofibers measured in Na$_2$SO$_4$.[6-8] However, the

14

underlying processes leading to capacitive behavior in these systems are fundamentally different among these materials: The processes observed here are measured at very negative potentials vs. Ag/AgCl under neutral conditions and describe NCN-PHI as electron storage material; those measured on melon-type carbon nitrides in the literature are exclusively measured at far more positive potential windows in 6 M KOH or Na_2SO_4, measuring the capacitance in the positive scan direction, thus extracting electrons from the system rather than supplying them. A direct comparison thus cannot be made as the storage processes in our system is fundamentally different from the ones reported beforehand in aqueous electrolytes.

CVs in TBA-Cl
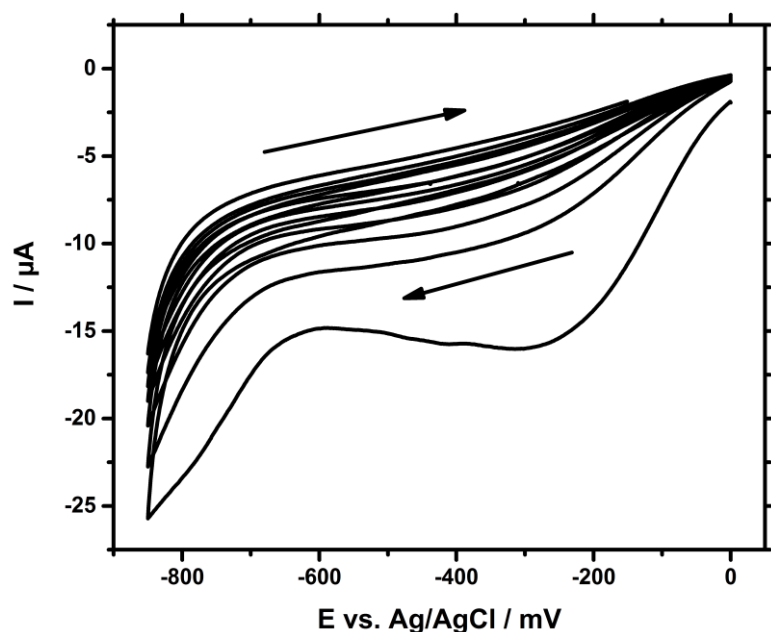
Figure S2.12: CV scans of NCN-PHI electrodes in oxygen free 1 M TBA-Cl solution at 50 mV/s. The absence of a positive discharge current or capacitive feature as observed in Fig. 4 c, S2.9 or S2.13 highlights the crucial role of an appropriate alkali metal cation for the capacitive properties. The TBA cation is too large to penetrate the structural pores and to allow for pseudocapacitive charge storage. The decay of the curve is due to detachment of the material.

CVs in phosphate buffer + 4-MBA including illumination
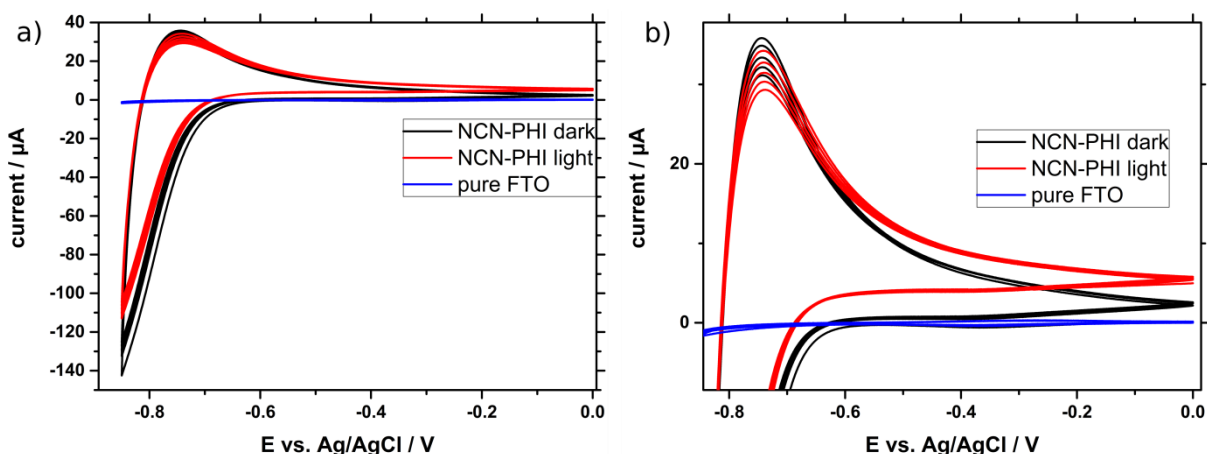
Figure S2.13: CVs of the NCN-PHI electrodes in 1 M phosphate buffer and 50 mM 4-MBA in the dark and under 1 sun illumination a); b) shows a close-up of the relevant region.

The selected voltage region corresponds to the potentials being accessible by photo-charging in the presence of a donor. The absence of new redox peaks with a donor present shows that there is no oxidation of the donor due to the applied potential during CV scans. The black curve measured in the dark already shows a capacitance similar to Fig. 4 c when the charged, blue state is reached at -800 mV. The current decay occurring during cycling is attributed to material loss due to non-optimized adhesion from drop cast aqueous suspensions (see SI Section 2.2). The illuminated, red curve was measured afterwards on the same sample. A decreased negative peak current can be attributed to the same adhesion problem. As seen more clearly in the close-up (Fig. S2.13 b), the illuminated CV is shifted to more positive currents. This evidences that the charge which has been created within the material due to illumination is extracted with a kinetic delay. Furthermore, we observe a shift in the equilibrium potential after discharging (point of zero current), which is explained by an enhanced charge uptake capability under illumination as well as by delayed charge extraction (compare Fig. 4 a).

2.6. Impedance measurements

Dark and illuminated in 1 M KCl solution + 5mM 4-MBA

Table S2.14: Fitting results of the impedance measurements shown in Fig. 5 a in the dark and the charged state when illuminated in the presence of a donor (4-MBA). To evaluate the capacitance C_x of every RQ-element, the equation $C_x=(RQ_x)^{1/n}/R$ was used. As the fit of the resistive element R_C describing the inner half circle in the Nyquist plot does not converge, the resistance values extracted from Fig. 5 b were used and fixed. In the dark measurement, the contribution of the pseudocapacitance is very small. As such, the inner half-circle is not visible. The relatively large error for the double layer capacitance parameters in the dark measurement results from missing lower frequency data (< 10 mHz) resulting in a more pronounced half-circle. This data could not be recorded due to decreasing electrode stability during this long term measurement and increasing noise.

OCP in dark (-24 mV vs. Ag/AgCl)				OCP 1 sun (-850 mV vs. Ag/AgCl)			
Parameter	Value	Error/%	Unit	Parameter	Value	Error/%	Unit
R_S	1.48E+01	2.41	Ohm	R_S	1.37E+01	2.34	Ohm
R_C	2.70E+07	fixed	Ohm	R_C	6.00E+05	fixed	Ohm
Q_P	1.51E-06	7.61	-	Q_P	3.47E-04	2.48	-
$n(Q_P)$	9.98E-01	4.19	-	$n(Q_P)$	7.58E-01	2.51	-
R_{CT}	2.63E+04	551.28	Ohm	R_{CT}	6.56E+02	4.55	Ohm
Q_{DL}	5.33E-05	448.21	-	Q_{DL}	2.46E-05	7.95	-

16

$n(Q_{DL})$	7.70E-01	36.12	-	$n(Q_{DL})$	7.83E-01	1.33	-
C_P	1.52E-01		F/g	C_P	1.91E+02		F/g
C_{DL}	5.90E+00		F/g	C_{DL}	7.84E-01		F/g

3. Supplementary discussion on the influence of oxygen

The photoelectrochemical experiments were performed in an oxygen free environment to avoid side reactions, i.e. the scavenging of electrons from photoreduced NCN-PHI by the electron acceptor dioxygen. The effect of this side reaction can be seen already at low concentrations of oxygen (in the ppb range) (Fig. S3.1).
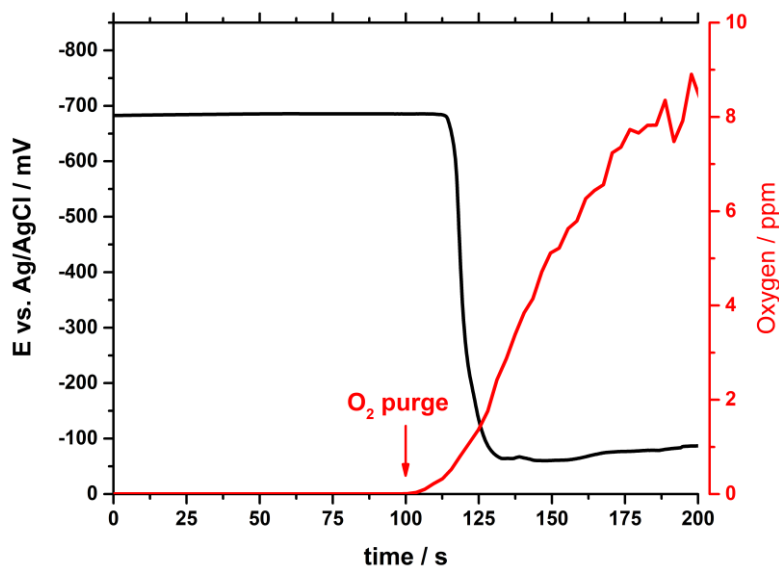
Figure S3.1: Evolution of the OCP of an NCN-PHI electrode (after excitation with light in phosphate buffer + 4-MBA to -700mV vs. Ag/AgCl) when the electrolyte is purged with oxygen at 100 s. The OCP decays within 30 s after the beginning of the purging process. The oxygen content was measured *in situ*.

The standard redox potentials (RHE) for oxygen decomposition reactions are listed in Table S3.2.[9] Since we used neutral conditions for our measurements and Ag/AgCl as a reference electrode the potentials are given at pH 7 vs. Ag/AgCl. In general, the standard redox potential is dependent on the pH of the electrolyte, following the Nernst equation (E^0/ V = E^0 (at pH 0) - 0.059 × pH). Besides the potential of the reaction $O_2 + e^- \rightarrow O_2^-$ which is pH independent, all other RHE's can be calculated using this equation with respect to the relative pH value. The exception for O_2 is due to the independence from the pH value of this reaction.[10]

Table S3.2: Standard redox potentials (RHE) at pH 7 and potentials vs. Ag/AgCl at pH 7 for different oxygen decomposition reactions.

Reaction	Potential vs. RHE at pH 7 / V	Potential vs. Ag/AgCl at pH 7 / V
$O_2 + e^- \rightarrow O_2^-$	- 0.33	- 0.53
$O_2 + e^- + H^+ \rightarrow HO_2^{\bullet}$	- 0.46	- 0.66
$O_2 + 2e^- + 2H^+ \rightarrow H_2O_2$	+ 0.29	+ 0.09
$O_2 + 4e^- + 4H^+ \rightarrow 2H_2O$	+ 0.82	+ 0.62
$O_2 + 2e^- + H_2O \rightarrow HO_2^{\bullet} + OH^-$	+ 0.34	+ 0.15
$O_2 + 4e^- + 2H_2O \rightarrow 4OH^-$	+ 0.83	+ 0.62

The excited OCP of -700 mV vs. Ag/AgCl for an oxygen free environment drops to the ground state potential of -100 mV vs. Ag/AgCl by quenching with oxygen (Fig. S3.1), which is a strong indication of a side reaction caused by oxygen. Within the scanning range of -800 – 0 mV vs. Ag/AgCl in our

experiments all of the shown reactions are possible, in principle. However, which of these reactions is taking place in particular is not clear, but in general reactions with only one electron transfer are kinetically preferred.

4. Supplementary discussion on the influence of the variable conductivity on the discharge curves

The difference in conductivity that is observed between the (light induced) charged state and the discharged state also influences the discharge behavior of NCN-PHI electrodes. During the illumination process, excited electrons are created and distributed rather homogeneously over the electrode. When the illumination is stopped and the material is discharged quickly, electrons near the substrate are extracted to the FTO first, leaving behind a thin depleted layer which has a lower conductivity than the rest of the NCN-PHI electrode that is still in the excited state. The percolation of electrons from the outer parts of the sample (i.e. closer to the electrolyte) to the substrate is hindered due to an increased IR drop and their potential will not be sensed by the effective voltage measured at the NCN-PHI contact. This configuration is schematically illustrated in Fig. 6. As a consequence, it is possible that the apparent, measured potential rises again after discharge, which is what we observed in the case of too fast discharge measurements. Hence, it is possible and crucial to adjust the film thickness and morphology in order to optimize the charge percolation pathways. When used as battery material, a lot of charge per surface and total mass must be stored, resulting in thicker films and slower discharge capability, while supercapacitors with a high-power density will best be realized with thin films.

References

1. V. W. H. Lau, I. Moudrakovski, T. Botari, S. Weinberger, M. B. Mesch, V. Duppel, J. Senker, V. Blum and B. V. Lotsch, *Nature Communications*, 2016, 7, 12165.
2. V. W. Lau, D. Klose, H. Kasap, F. Podjaski, M. C. Pignie, E. Reisner, G. Jeschke and B. V. Lotsch, *Angew Chem Int Ed Engl*, 2017, 56, 510-514.
3. Z. Chen, H. N. Dinh and E. Miller, *Photoelectrochemical water splitting*, 2013.
4. V. Augustyn, J. Come, M. A. Lowe, J. W. Kim, P. L. Taberna, S. H. Tolbert, H. D. Abruna, P. Simon and B. Dunn, *Nature Materials*, 2013, 12, 518-522.
5. H. Angerstein-Kozlowska, J. Klinger and B. E. Conway, *Journal of Electroanalytical Chemistry*, 1977, 75, 45-60.
6. M. Tahir, C. B. Cao, F. K. Butt, F. Idrees, N. Mahmood, Z. Ali, I. Aslam, M. Tanveer, M. Rizwan and T. Mahmood, *Journal of Materials Chemistry A*, 2013, 1, 13949-13955.
7. M. Tahir, C. B. Cao, N. Mahmood, F. K. Butt, A. Mahmood, F. Idrees, S. Hussain, M. Tanveer, Z. Ali and I. Aslam, *Acs Applied Materials & Interfaces*, 2014, 6, 1258-1265.
8. Y. T. Gong, M. M. Li and Y. Wang, *Chemsuschem*, 2015, 8, 931-946.
9. A. J. Bard, R. Parsons and J. Jordan, *Standard potentials in aqueous solution*, CRC press, 1985.
10. P. M. Wood, *Biochemical Journal*, 1988, 253, 287-289.

Bibliography

[1] CO_2 Emissions from Fuel Combustion 2018 *Highlights*. Report, International Energy Agency (2018). URL `https://webstore.iea.org/co2-emissions-from-fuel-combustion-2018-highlights`.

[2] *Atlas der Globalisierung.* Die Welt von morgen (Le Monde Diplomatique / taz Verlags- und VertriebsGmbH, Berlin, 2012).

[3] Schumacher, E. F. *Small is Beautiful: A Study of Economics as if People Mattered* (Blond & Briggs Ltd., 1973).

[4] *Renewable Energy Sources - a Survey* (Wiley-VCH, 2013). URL `https://onlinelibrary.wiley.com/doi/abs/10.1002/9783527671342.ch1`.

[5] Lewis, N. S. & Nocera, D. G. Powering the planet: Chemical challenges in solar energy utilization. *Proceedings of the National Academy of Sciences* **103**, 15729–15735 (2006). URL `https://www.pnas.org/content/pnas/103/43/15729.full.pdf`.

[6] Jacobson, M. Z. Review of solutions to global warming, air pollution, and energy security. *Energy & Environmental Science* **2**, 148–173 (2009). URL `http://dx.doi.org/10.1039/B809990C`.

[7] Jacobson, M. Z. & Delucchi, M. A. A path to sustainable energy by 2030. *Sci. Am.* **301**, 58–65 (2009). URL `https://www.ncbi.nlm.nih.gov/pubmed/19873905`.

[8] Jacobson, M. Z. & Delucchi, M. A. Providing all global energy with wind, water, and solar power, Part I: Technologies, energy resources, quantities and areas of infrastructure, and materials. *Energy Policy* **39**, 1154–1169 (2011). URL `https://EconPapers.repec.org/RePEc:eee:enepol:v:39:y:2011:i:3:p:1154-1169`.

[9] Delucchi, M. A. & Jacobson, M. Z. Providing all global energy with wind, water, and solar power, Part II: Reliability, system and transmission costs, and policies. *Energy Policy* **39**, 1170–1190 (2011). URL `https://EconPapers.repec.org/RePEc:eee:enepol:v:39:y:2011:i:3:p:1170-1190`.

[10] Banerjee, A. *et al.* Photochemical Nitrogen Conversion to Ammonia in Ambient Conditions with FeMoS-Chalcogels. *Journal of the American Chemical Society* **137**, 2030–2034 (2015). URL `https://doi.org/10.1021/ja512491v`.

[11] Sun, Z., Ma, T., Tao, H., Fan, Q. & Han, B. Fundamentals and Challenges of Electrochemical CO_2 Reduction Using Two-Dimensional Materials. *Chem* **3**, 560–587 (2017). URL `https://doi.org/10.1016/j.chempr.2017.09.009`.

[12] Edwards, P. P., Kuznetsov, V. L., David, W. I. F. & Brandon, N. P. Hydrogen and fuel cells: Towards a sustainable energy future. *Energy Policy* **36**, 4356–4362 (2008). URL `http://www.sciencedirect.com/science/article/pii/S0301421508004503`.

[13] Melaina, M., Sozinova, O. & Penev, M. *Blending Hydrogen into Natural Gas Pipeline Networks: A Review of Key Issues* (2013). URL `https://www.energy.gov/sites/prod/files/2014/03/f11/blending_h2_nat_gas_pipeline.pdf`.

[14] Pinaud, B. A. *et al.* Technical and economic feasibility of centralized facilities for solar hydrogen production via photocatalysis and photoelectrochemistry. *Energy & Environmental Science* **6**, 1983–2002 (2013). URL `http://dx.doi.org/10.1039/C3EE40831K`.

[15] Nordås, R. & Gleditsch, N. P. Climate change and conflict. *Political Geography* **26**, 627–638 (2007). URL `http://www.sciencedirect.com/science/article/pii/S0962629807000856`.

[16] Koh, L. P. & Ghazoul, J. Biofuels, biodiversity, and people: Understanding the conflicts and finding opportunities. *Biological Conservation* **141**, 2450–2460 (2008). URL http://www.sciencedirect.com/science/article/pii/S0006320708002954.

[17] Perez-Alonso, F. J. *et al.* The effect of size on the oxygen electroreduction activity of mass-selected platinum nanoparticles. *Angewandte Chemie* **124**, 4719–4721 (2012). URL https://onlinelibrary.wiley.com/doi/abs/10.1002/ange.201200586.

[18] Du, P. & Eisenberg, R. Catalysts made of earth-abundant elements (Co, Ni, Fe) for water splitting: Recent progress and future challenges. *Energy & Environmental Science* **5**, 6012–6021 (2012). URL http://dx.doi.org/10.1039/C2EE03250C.

[19] Weber, D. *et al.* IrOOH nanosheets as acid stable electrocatalysts for the oxygen evolution reaction. *Journal of Materials Chemistry A* **6**, 21558–21566 (2018). URL http://dx.doi.org/10.1039/C8TA07950A.

[20] Luo, M. & Guo, S. Strain-controlled electrocatalysis on multimetallic nanomaterials. *Nature Reviews Materials* **2**, 17059 (2017). URL http://dx.doi.org/10.1038/natrevmats.2017.59.

[21] Vyas, V. S., Lau, V. W.-h. & Lotsch, B. V. Soft Photocatalysis: Organic Polymers for Solar Fuel Production. *Chemistry of Materials* **28**, 5191–5204 (2016). URL https://doi.org/10.1021/acs.chemmater.6b01894.

[22] Zhang, G., Lan, Z.-A., Lin, L., Lin, S. & Wang, X. Overall water splitting by Pt/g-C_3N_4 photocatalysts without using sacrificial agents. *Chemical Science* **7**, 3062–3066 (2016). URL https://www.ncbi.nlm.nih.gov/pubmed/29997797.

[23] Fujishima, A. & Honda, K. Electrochemical Photolysis of Water at a Semiconductor Electrode. *Nature* **238**, 37 (1972). URL https://doi.org/10.1038/238037a0.

[24] Khaselev, O. & Turner, J. A. A Monolithic Photovoltaic-Photoelectrochemical Device for Hydrogen Production via Water Splitting. *Science* **280**, 425–427 (1998). URL http://science.sciencemag.org/content/sci/280/5362/425.full.pdf.

[25] Licht, S. *et al.* Efficient Solar Water Splitting, Exemplified by RuO$_2$-Catalyzed AlGaAs/Si Photoelectrolysis. *The Journal of Physical Chemistry B* **104**, 8920–8924 (2000). URL `https://doi.org/10.1021/jp002083b`.

[26] Grätzel, M. Photoelectrochemical cells. *Nature* **414**, 338 (2001). URL `https://doi.org/10.1038/35104607`.

[27] Jia, J. *et al.* Solar water splitting by photovoltaic-electrolysis with a solar-to-hydrogen efficiency over 30%. *Nature Communications* **7**, 13237 (2016). URL `https://doi.org/10.1038/ncomms13237`.

[28] Wang, X. *et al.* A metal-free polymeric photocatalyst for hydrogen production from water under visible light. *Nature Materials* **8**, 76 (2008). URL `https://doi.org/10.1038/nmat2317`.

[29] Banerjee, T. *et al.* Single-Site Photocatalytic H$_2$ Evolution from Covalent Organic Frameworks with Molecular Cobaloxime Co-Catalysts. *Journal of the American Chemical Society* **139**, 16228–16234 (2017). URL `https://doi.org/10.1021/jacs.7b07489`.

[30] Lau, V. W.-h. *et al.* Dark Photocatalysis: Storage of Solar Energy in Carbon Nitride for Time-Delayed Hydrogen Generation. *Angewandte Chemie International Edition* **56**, 510–514 (2017). URL `https://onlinelibrary.wiley.com/doi/abs/10.1002/anie.201608553`.

[31] Cao, S., Low, J., Yu, J. & Jaroniec, M. Polymeric Photocatalysts Based on Graphitic Carbon Nitride. *Advanced Materials* **27**, 2150–2176 (2015). URL `https://onlinelibrary.wiley.com/doi/abs/10.1002/adma.201500033`.

[32] Ong, W.-J., Tan, L.-L., Ng, Y. H., Yong, S.-T. & Chai, S.-P. Graphitic Carbon Nitride (g-C$_3$3N$_4$)-Based Photocatalysts for Artificial Photosynthesis and Environmental Remediation: Are We a Step Closer To Achieving Sustainability? *Chemical Reviews* **116**, 7159–7329 (2016). URL `https://doi.org/10.1021/acs.chemrev.6b00075`.

[33] Yu, M. Z. *et al.* Solar-powered electrochemical energy storage: an alternative to solar fuels. *Journal of Materials Chemistry A* **4**, 2766–2782 (2016). URL `http://dx.doi.org/10.1039/C5TA06950E`.

[34] Sun, Y. & Yan, X. Recent Advances in Dual-Functional Devices Integrating Solar Cells and Supercapacitors. *Solar RRL* **1**, 1700002–n/a (2017). URL `http://dx.doi.org/10.1002/solr.201700002`.

[35] Tributsch, H. Photo-intercalation: Possible application in solar energy devices. *Applied physics* **23**, 61–71 (1980). URL `https://doi.org/10.1007/BF00899572`.

[36] Betz, G. & Tributsch, H. Energy conversion and storage using insertion materials. *Progress in Solid State Chemistry* **16**, 195–290 (1985). URL `http://www.sciencedirect.com/science/article/pii/0079678685900056`.

[37] Lotsch, B. *et al.* Unmasking Melon by a Complementary Approach Employing Electron Diffraction, Solid-State NMR Spectroscopy, and Theoretical Calculations-Structural Characterization of a Carbon Nitride Polymer. *Chemistry – A European Journal* **13**, 4969–4980 (2007). URL `https://onlinelibrary.wiley.com/doi/abs/10.1002/chem.200601759`.

[38] Savateev, A. *et al.* Potassium Poly(heptazine imides) from Aminotetrazoles: Shifting Band Gaps of Carbon Nitride-like Materials for More Efficient Solar Hydrogen and Oxygen Evolution. *ChemCatChem* **9**, 167–174 (2017). URL `https://onlinelibrary.wiley.com/doi/abs/10.1002/cctc.201601165`.

[39] Savateev, A., Pronkin, S., Willinger, M. G., Antonietti, M. & Dontsova, D. Towards Organic Zeolites and Inclusion Catalysts: Heptazine Imide Salts Can Exchange Metal Cations in the Solid State. *Chemistry - An Asian Journal* **12**, 1517–1522 (2017). URL `https://doi.org/10.1002/asia.201700209`.

[40] Becquerel, A.-E. Recherches sur les effets de la radiation chimique de la lumière solaire au moyen des courants électriques. *C.R. Acad. Sci* **9**, 145–149 (1839).

[41] Baur, E. & Rebmann, A. Über versuche zur Photolyse des Wassers. *Helvetica Chimica Acta* **4**, 256–262 (1921). URL `https://onlinelibrary.wiley.com/doi/abs/10.1002/hlca.19210040124`.

[42] Nozik, A. J. Photoelectrochemistry: Applications to solar energy conversion. *Annual Review of Physical Chemistry* **29**, 189–222 (1978). URL `https://www.annualreviews.org/doi/abs/10.1146/annurev.pc.29.100178.001201`.

[43] Rajeshwar, K. *Fundamentals of Semiconductor Electrochemistry and Photoelectrochemistry* (Wiley-VCH, 2007). URL `https://onlinelibrary.wiley.com/doi/abs/10.1002/9783527610426.bard060001`.

[44] Walczak, M. M., Dryer, D. A., Jacobson, D. D., Foss, M. G. & Flynn, N. T. ph Dependent Redox Couple: An Illustration of the Nernst Equation. *Journal of Chemical Education* **74**, 1195 (1997). URL `https://doi.org/10.1021/ed074p1195`.

[45] Chen, Z., Dinh, H. N. & Miller, E. *Photoelectrochemical Water Splitting*. SpringerBriefs in Energy, New York (2013).

[46] Morales-Guio, C. G., Stern, L.-A. & Hu, X. Nanostructured hydrotreating catalysts for electrochemical hydrogen evolution. *Chemical Society Reviews* **43**, 6555–6569 (2014). URL `http://dx.doi.org/10.1039/C3CS60468Chttps://pubs.rsc.org/en/content/articlepdf/2014/cs/c3cs60468c`.

[47] Takanabe, K. Photocatalytic Water Splitting: Quantitative Approaches toward Photocatalyst by Design. *ACS Catalysis* **7**, 8006–8022 (2017). URL `https://doi.org/10.1021/acscatal.7b02662`.

[48] Hu, S., Xiang, C., Haussener, S., Berger, A. D. & Lewis, N. S. An analysis of the optimal band gaps of light absorbers in integrated tandem photoelectrochemical water-splitting systems. *Energy & Environmental Science* **6**, 2984–2993 (2013). URL `http://dx.doi.org/10.1039/C3EE40453F`.

[49] Nozik, A. J. & Memming, R. Physical Chemistry of Semiconductor-Liquid Interfaces. *The Journal of Physical Chemistry* **100**, 13061–13078 (1996). URL `https://doi.org/10.1021/jp953720e`.

[50] Zhang, Z. & Yates, J. T. Band Bending in Semiconductors: Chemical and Physical Consequences at Surfaces and Interfaces. *Chemical Reviews* **112**, 5520–5551 (2012). URL `https://doi.org/10.1021/cr3000626`.

[51] Yang, J., Wang, D., Han, H. & Li, C. Roles of Cocatalysts in Photocatalysis and Photoelectrocatalysis. *Accounts of Chemical Research* **46**, 1900–1909 (2013). URL `https://doi.org/10.1021/ar300227e`.

[52] Zhao, H. *et al.* Atomic single layer graphitic-C_3N_4: fabrication and its high photocatalytic performance under visible light irradiation. *RSC Advances* **4**, 624–628 (2014). URL `http://dx.doi.org/10.1039/C3RA45776A`.

[53] Chen, S., Takata, T. & Domen, K. Particulate photocatalysts for overall water splitting. *Nature Reviews Materials* **2**, 17050 (2017). URL `https://doi.org/10.1038/natrevmats.2017.50`.

[54] Kichigin, V. I. & Shein, A. B. Influence of hydrogen absorption on the potential dependence of the Faradaic impedance parameters of hydrogen evolution reaction. *Electrochimica Acta* **201**, 233–239 (2016). URL `http://www.sciencedirect.com/science/article/pii/S0013468616307770`.

[55] Erdey-Grúz, T. & Volmer, M. Zur Theorie der Wasserstoff Überspannung (1930). URL `https://www.degruyter.com/view/j/zpch.1930.150.issue-1/zpch-1930-15020/zpch-1930-15020.xml`.

[56] McCrory, C. C. L. *et al.* Benchmarking Hydrogen Evolving Reaction and Oxygen Evolving Reaction Electrocatalysts for Solar Water Splitting Devices. *Journal of the American Chemical Society* **137**, 4347–4357 (2015). URL `https://doi.org/10.1021/ja510442p`.

[57] Montoya, J. H. *et al.* Materials for solar fuels and chemicals. *Nature Materials* **16**, 70 (2016). URL `https://doi.org/10.1038/nmat4778`.

[58] Jaramillo, T. F. *et al.* Identification of Active Edge Sites for Electrochemical H_2 Evolution from MoS_2 Nanocatalysts. *Science* **317**, 100–102 (2007). URL `http://science.sciencemag.org/content/sci/317/5834/100.full.pdf`.

[59] Voiry, D. *et al.* Enhanced catalytic activity in strained chemically exfoliated WS_2 nanosheets for hydrogen evolution. *Nature Materials* **12**, 850 (2013). URL `https://doi.org/10.1038/nmat3700`.

[60] Hammer, B. & Norskov, J. K. Why gold is the noblest of all the metals. *Nature* **376**, 238 (1995). URL `https://doi.org/10.1038/376238a0`.

[61] Nilsson, A. *et al.* The electronic structure effect in heterogeneous catalysis. *Catalysis Letters* **100**, 111–114 (2005). URL `https://doi.org/10.1007/s10562-004-3434-9`.

[62] Greeley, J., Nørskov, J. K., Kibler, L. A., El-Aziz, A. M. & Kolb, D. M. Hydrogen Evolution Over Bimetallic Systems: Understanding the Trends. *ChemPhysChem* **7**, 1032–1035 (2006). URL `https://onlinelibrary.wiley.com/doi/abs/10.1002/cphc.200500663`.

[63] Kibler, L. A., El-Aziz, A. M., Hoyer, R. & Kolb, D. M. Tuning Reaction Rates by Lateral Strain in a Palladium Monolayer. *Angewandte Chemie International Edition* **44**, 2080–2084 (2005). URL `https://onlinelibrary.wiley.com/doi/abs/10.1002/anie.200462127`.

[64] Carmo, M., Fritz, D. L., Mergel, J. & Stolten, D. A comprehensive review on PEM water electrolysis. *International Journal of Hydrogen Energy* **38**, 4901–4934 (2013). URL `http://www.sciencedirect.com/science/article/pii/S0360319913002607`.

[65] Buttler, A. & Spliethoff, H. Current status of water electrolysis for energy storage, grid balancing and sector coupling via power-to-gas and power-to-liquids: A review. *Renewable and Sustainable Energy Reviews* **82**, 2440–2454 (2018). URL `http://www.sciencedirect.com/science/article/pii/S136403211731242X`.

[66] Janzen, A. F. *Solar Energy Conversion 30 - PHOTOELECTROCHEMISTRY I - PHOTOELECTROLYSIS*, 905–921 (Pergamon, 1979). URL `http://www.sciencedirect.com/science/article/pii/B9780080247441500358`.

[67] Ng, C. H. *et al.* Potential active materials for photo-supercapacitor: A review. *Journal of Power Sources* **296**, 169–185 (2015). URL `https://doi.org/10.1016/j.jpowsour.2015.07.006`.

[68] Xu, J. T., Chen, Y. H. & Dai, L. M. Efficiently photo-charging lithium-ion battery by perovskite solar cell. *Nature Communications* **6** (2015). URL `https://www.nature.com/articles/ncomms9103`.

[69] Liu, D. *et al.* Reversible Electron Storage in an All-Vanadium Photoelectrochemical Storage Cell: Synergy between Vanadium Redox and Hybrid Photocatalyst. *ACS Catalysis* **5**, 2632–2639 (2015). URL `https://doi.org/10.1021/cs502024k`.

[70] Wei, H. G. *et al.* Energy conversion technologies towards self-powered electrochemical energy storage systems: the state of the art and perspectives. *Journal of Materials Chemistry A* **5**, 1873–1894 (2017). URL `http://dx.doi.org/10.1039/C6TA09726J`.

[71] Hodes, G., Manassen, J. & Cahen, D. Photoelectrochemical Energy-Conversion and Storage Using Polycrystalline Chalcogenide Electrodes. *Nature* **261**, 403–404 (1976). URL `https://www.nature.com/articles/261403a0`.

[72] Parkinson, B. An evaluation of various configurations for photoelectrochemical photovoltaic solar cells. *Solar Cells* **6**, 177–189 (1982). URL `http://www.sciencedirect.com/science/article/pii/0379678782900655`.

[73] Lou, S. N. *et al.* An Operando Mechanistic Evaluation of a Solar-Rechargeable Sodium-Ion Intercalation Battery. *Advanced Energy Materials* **7**, 1700545 (2017). URL `https://onlinelibrary.wiley.com/doi/abs/10.1002/aenm.201700545`.

[74] Andriamiadamanana, C. *et al.* Light-Induced Charge Separation in Mixed Electronic/Ionic Semiconductor Driving Lithium-Ion Transfer for Photo-Rechargeable Electrode. *Advanced Sustainable Systems* **2**, 1700166 (2018). URL `https://onlinelibrary.wiley.com/doi/abs/10.1002/adsu.201700166`.

[75] Kalasina, S., Phattharasupakun, N. & Sawangphruk, M. A new energy conversion and storage device of cobalt oxide nanosheets. *Journal of Materials Chemistry A* **6**, 36–40 (2018). URL `http://dx.doi.org/10.1039/C7TA08736E`.

[76] Arora, Y., Battu, S., Haram, S. & Khushalani, D. Coupling Energy Capture and Storage – Endeavoring to make a solar battery. *Scientific Reports* **8**, 12752 (2018). URL `https://doi.org/10.1038/s41598-018-30728-8`.

[77] Zhu, M. *et al.* Capacitance Enhancement in a Semiconductor Nanostructure-Based Supercapacitor by Solar Light and a Self-Powered Supercapacitor–Photodetector System. *Advanced Functional Materials* **26**, 4481–4490 (2016). URL `https://onlinelibrary.wiley.com/doi/abs/10.1002/adfm.201601260`.

[78] Ahmad, S., George, C., Beesley, D. J., Baumberg, J. J. & De Volder, M. Photo-Rechargeable Organo-Halide Perovskite Batteries. *Nano Letters* **18**, 1856–1862 (2018). URL `https://doi.org/10.1021/acs.nanolett.7b05153`.

[79] Lv, J. *et al.* Direct Solar-to-Electrochemical Energy Storage in a Functionalized Covalent Organic Framework. *Angewandte Chemie International Edition* **57**, 12716–12720 (2018). URL `https://onlinelibrary.wiley.com/doi/abs/10.1002/anie.201806596`.

[80] Antonietti, M., Chen, X., Yan, R. & Oschatz, M. Storing electricity as chemical energy: beyond traditional electrochemistry and double-layer compression. *Energy & Environmental Science* **11**, 3069–3074 (2018). URL `http://dx.doi.org/10.1039/C8EE01723A`.

[81] Conway, B. E. Transition from "Supercapacitor" to "Battery" Behavior in Electrochemical Energy Storage. *Journal of The Electrochemical Society* **138**, 1539–1548 (1991). URL `http://jes.ecsdl.org/content/138/6/1539.abstract`.

[82] Jamnik, J. & Maier, J. Generalised equivalent circuits for mass and charge transport: chemical capacitance and its implications. *Physical Chemistry Chemical Physics* **3**, 1668–1678 (2001). URL `http://dx.doi.org/10.1039/B100180I`.

[83] Maier, J. Pushing Nanoionics to the Limits: Charge Carrier Chemistry in Extremely Small Systems. *Chemistry of Materials* **26**, 348–360 (2014). URL `https://doi.org/10.1021/cm4021657`.

[84] Augustyn, V. *et al.* High-rate electrochemical energy storage through Li^+ intercalation pseudocapacitance. *Nature Materials* **12**, 518–522 (2013). URL `https://www.nature.com/articles/nmat3601`.

[85] Simon, P., Gogotsi, Y. & Dunn, B. Where Do Batteries End and Supercapacitors Begin? *Science* **343**, 1210–1211 (2014). URL `http://science.sciencemag.org/content/sci/343/6176/1210.full.pdf`.

[86] Nitta, N., Wu, F., Lee, J. T. & Yushin, G. Li-ion battery materials: present and future. *Materials Today* **18**, 252–264 (2015). URL `http://www.sciencedirect.com/science/article/pii/S1369702114004118`.

[87] Wu, F. & Yushin, G. Conversion cathodes for rechargeable lithium and lithium-ion batteries. *Energy & Environmental Science* **10**, 435–459 (2017). URL `http://dx.doi.org/10.1039/C6EE02326F`.

[88] Yu, S.-H., Feng, X., Zhang, N., Seok, J. & Abruña, H. D. Understanding Conversion-Type Electrodes for Lithium Rechargeable Batteries. *Accounts of Chemical Research* **51**, 273–281 (2018). URL `https://doi.org/10.1021/acs.accounts.7b00487`.

[89] Winsberg, J., Hagemann, T., Janoschka, T., Hager, M. D. & Schubert, U. S. Redox-Flow Batteries: From Metals to Organic Redox-Active Materials. *Angewandte Chemie International Edition* **56**, 686–711 (2017). URL `https://onlinelibrary.wiley.com/doi/abs/10.1002/anie.201604925`.

[90] Shannon, R. D., Rogers, D. B. & Prewitt, C. T. Chemistry of Noble Metal Oxides. I. Syntheses and Properties of ABO_2 Delafossite Compounds. *Inorganic Chemistry* **10**, 713 (1971). URL `https://doi.org/10.1021/ic50098a011`.

[91] Prewitt, C. T., Shannon, R. D. & Rogers, D. B. Chemistry of Noble Metal Oxides. II. Crystal Structures of $PtCoO_2$, $PdCoO_2$, $CuFeO_2$, and $AgFeO_2$. *Inorganic Chemistry* **10**, 719–723 (1971). URL `https://doi.org/10.1021/ic50098a012`.

[92] Rogers, D. B., Shannon, R. D., Prewitt, C. T. & Gillson, J. L. Chemistry of Noble Metal Oxides. III. Electrical Transport Properties and Crystal Chemistry of ABO_2 Compounds with Delafossite Structure. *Inorganic Chemistry* **10**, 723 (1971). URL `https://doi.org/10.1021/ic50098a013`.

[93] Mackenzie, A. P. The properties of ultrapure delafossite metals. *Reports on Progress in Physics* **80**, 032501 (2017). URL `http://stacks.iop.org/0034-4885/80/i=3/a=032501`.

[94] Daou, R., Frésard, R., Eyert, V., Hébert, S. & Maignan, A. Unconventional aspects of electronic transport in delafossite oxides. *Science and Technology of Advanced Materials* **18**, 919–938 (2017). URL `https://doi.org/10.1080/14686996.2017.1393633`.

[95] Moll, P. J. W., Kushwaha, P., Nandi, N., Schmidt, B. & Mackenzie, A. P. Evidence for hydrodynamic electron flow in $PdCoO_2$. *Science* **351**, 1061–1064 (2016). URL `http://science.sciencemag.org/content/sci/351/6277/1061.full.pdf`.

231

[96] Liebig, J. Über einige Stickstoff - Verbindungen. *Annalen der Pharmacie* **10**, 1–47 (1834). URL `https://onlinelibrary.wiley.com/doi/abs/10.1002/jlac.18340100102`.

[97] Schlomberg, H., Podjaski, F., Kroeger, J. & Lotsch, B. Von der Jahrmarktattraktion zur Energiequelle: Kohlenstoffnitride. *Nachrichten aus der Chemie* **66**, 1157–1161 (2018). URL `https://onlinelibrary.wiley.com/doi/abs/10.1002/nadc.20184065088`.

[98] Xu, J., Zhang, L., Shi, R. & Zhu, Y. Chemical exfoliation of graphitic carbon nitride for efficient heterogeneous photocatalysis. *Journal of Materials Chemistry A* **1**, 14766–14772 (2013). URL `http://dx.doi.org/10.1039/C3TA13188B`.

[99] Merschjann, C. *et al.* Complementing Graphenes: 1D Interplanar Charge Transport in Polymeric Graphitic Carbon Nitrides. *Advanced Materials* **27**, 7993–7999 (2015). URL `https://onlinelibrary.wiley.com/doi/abs/10.1002/adma.201503448`.

[100] Zhang, J. *et al.* Synthesis of a Carbon Nitride Structure for Visible-Light Catalysis by Copolymerization. *Angewandte Chemie International Edition* **49**, 441–444 (2010). URL `https://onlinelibrary.wiley.com/doi/abs/10.1002/anie.200903886`.

[101] Zhao, Z., Sun, Y. & Dong, F. Graphitic carbon nitride based nanocomposites: a review. *Nanoscale* **7**, 15–37 (2015). URL `http://dx.doi.org/10.1039/C4NR03008G`.

[102] Jiang, L. *et al.* Doping of graphitic carbon nitride for photocatalysis: A reveiw. *Applied Catalysis B: Environmental* **217**, 388–406 (2017). URL `http://www.sciencedirect.com/science/article/pii/S0926337317305465`.

[103] Kessler, F. K. *et al.* Functional carbon nitride materials — design strategies for electrochemical devices. *Nature Reviews Materials* **2**, 17030 (2017). URL `https://doi.org/10.1038/natrevmats.2017.30`.

[104] Wirnhier, E. *et al.* Poly(triazine imide) with Intercalation of Lithium and Chloride Ions $[(C_3N_3)_2(NH_xLi_{1-x})_3 \cdot LiCl]$: A Crystalline 2D Carbon Nitride Network. *Chemistry – A European Journal* **17**, 3213–3221 (2011). URL `https://onlinelibrary.wiley.com/doi/abs/10.1002/chem.201002462`.

[105] Schwinghammer, K. *et al.* Triazine-based Carbon Nitrides for Visible-Light-Driven Hydrogen Evolution. *Angewandte Chemie International Edition* **52**, 2435–2439 (2013). URL https://onlinelibrary.wiley.com/doi/abs/10.1002/anie.201206817.

[106] Döblinger, M. *et al.* Structure elucidation of polyheptazine imide by electron diffraction – a templated 2D carbon nitride network. *Chemical Communications* 1541–1543 (2009). URL http://dx.doi.org/10.1039/B820032G.

[107] Lau, V. W.-h. *et al.* Rational design of carbon nitride photocatalysts by identification of cyanamide defects as catalytically relevant sites. *Nature Communications* **7**, 12165 (2016). URL https://doi.org/10.1038/ncomms12165.

[108] Lau, V. W.-h. *et al.* Urea-Modified Carbon Nitrides: Enhancing Photocatalytic Hydrogen Evolution by Rational Defect Engineering. *Advanced Energy Materials* **7**, 1602251 (2017). URL https://onlinelibrary.wiley.com/doi/abs/10.1002/aenm.201602251.

[109] Kasap, H. *et al.* Solar-Driven Reduction of Aqueous Protons Coupled to Selective Alcohol Oxidation with a Carbon Nitride–Molecular Ni Catalyst System. *Journal of the American Chemical Society* **138**, 9183–9192 (2016). URL https://doi.org/10.1021/jacs.6b04325.

[110] Haase, F. *Tuning the Structure and Properties of Nitrogen-rich Covalent Organic Frameworks by Molecular Design and Solid State Reactions*. Thesis (2018).

[111] Côté, A. P. *et al.* Porous, Crystalline, Covalent Organic Frameworks. *Science* **310**, 1166–1170 (2005). URL http://science.sciencemag.org/content/sci/310/5751/1166.full.pdf.

[112] Feng, X., Ding, X. & Jiang, D. Covalent organic frameworks. *Chemical Society Reviews* **41**, 6010–6022 (2012). URL http://dx.doi.org/10.1039/C2CS35157A.

[113] Ding, S.-Y. & Wang, W. Covalent organic frameworks (COFs): from design to applications. *Chemical Society Reviews* **42**, 548–568 (2013). URL http://dx.doi.org/10.1039/C2CS35072F.

[114] Qian, H.-L., Yang, C.-X., Wang, W.-L., Yang, C. & Yan, X.-P. Advances in covalent organic frameworks in separation science. *Journal of Chromatography A* **1542**, 1–18 (2018). URL `http://www.sciencedirect.com/science/article/pii/S0021967318301742`.

[115] Du, Y. *et al.* Experimental and computational studies of pyridine-assisted post-synthesis modified air stable covalent–organic frameworks. *Chemical Communications* **48**, 4606–4608 (2012). URL `http://dx.doi.org/10.1039/C2CC30781B`.

[116] Bunck, D. N. & Dichtel, W. R. Bulk Synthesis of Exfoliated Two-Dimensional Polymers Using Hydrazone-Linked Covalent Organic Frameworks. *Journal of the American Chemical Society* **135**, 14952–14955 (2013). URL `https://doi.org/10.1021/ja408243n`.

[117] Colson, J. W. & Dichtel, W. R. Rationally synthesized two-dimensional polymers. *Nature Chemistry* **5**, 453 (2013). URL `https://doi.org/10.1038/nchem.1628`.

[118] Dogru, M. & Bein, T. On the road towards electroactive covalent organic frameworks. *Chemical Communications* **50**, 5531–5546 (2014). URL `http://dx.doi.org/10.1039/C3CC46767H`.

[119] Huang, N., Wang, P. & Jiang, D. Covalent organic frameworks: a materials platform for structural and functional designs. *Nature Reviews Materials* **1**, 16068 (2016). URL `https://doi.org/10.1038/natrevmats.2016.68`.

[120] Stegbauer, L., Schwinghammer, K. & Lotsch, B. V. A hydrazone-based covalent organic framework for photocatalytic hydrogen production. *Chemical Science* **5**, 2789–2793 (2014). URL `http://dx.doi.org/10.1039/C4SC00016A`.

[121] Vyas, V. S. *et al.* A tunable azine covalent organic framework platform for visible light-induced hydrogen generation. *Nature Communications* **6**, 8508 (2015). URL `http://dx.doi.org/10.1038/ncomms9508`.

[122] Haase, F. *et al.* Tuning the stacking behaviour of a 2D covalent organic framework through non-covalent interactions. *Materials Chemistry Frontiers* **1**, 1354–1361 (2017). URL `http://dx.doi.org/10.1039/C6QM00378H`.

[123] Stegbauer, L. *et al.* Tailor-Made Photoconductive Pyrene-Based Covalent Organic Frameworks for Visible-Light Driven Hydrogen Generation. *Advanced Energy Materials* **8**, 1703278 (2018). URL `https://onlinelibrary.wiley.com/doi/abs/10.1002/aenm.201703278`.

[124] Thote, J. *et al.* A Covalent Organic Framework-Cadmium Sulfide Hybrid as a Prototype Photocatalyst for Visible-Light-Driven Hydrogen Production. *Chemistry – A European Journal* **20**, 15961–15965 (2014). URL `https://onlinelibrary.wiley.com/doi/abs/10.1002/chem.201403800`.

[125] Wang, X. *et al.* Sulfone-containing covalent organic frameworks for photocatalytic hydrogen evolution from water. *Nature Chemistry* **10**, 1180–1189 (2018). URL `https://doi.org/10.1038/s41557-018-0141-5`.

[126] Sick, T. *et al.* Oriented Films of Conjugated 2D Covalent Organic Frameworks as Photocathodes for Water Splitting. *Journal of the American Chemical Society* **140**, 2085–2092 (2018). URL `https://doi.org/10.1021/jacs.7b06081`.

[127] Pachfule, P. *et al.* Diacetylene Functionalized Covalent Organic Framework (COF) for Photocatalytic Hydrogen Generation. *Journal of the American Chemical Society* **140**, 1423–1427 (2018). URL `https://doi.org/10.1021/jacs.7b11255`.

[128] Banerjee, T., Gottschling, K., Savasci, G., Ochsenfeld, C. & Lotsch, B. V. H_2 Evolution with Covalent Organic Framework Photocatalysts. *ACS Energy Letters* **3**, 400–409 (2018). URL `https://doi.org/10.1021/acsenergylett.7b01123`.

[129] Banerjee, T. & Lotsch, B. V. The wetter the better. *Nature Chemistry* **10**, 1175–1177 (2018). URL `https://doi.org/10.1038/s41557-018-0176-7`.

[130] Bhunia, S. *et al.* Electrochemical Stimuli-Driven Facile Metal-Free Hydrogen Evolution from Pyrene-Porphyrin-Based Crystalline Covalent Organic Framework. *ACS Applied Materials & Interfaces* **9**, 23843–23851 (2017). URL `https://doi.org/10.1021/acsami.7b06968`.

[131] Nandi, S. *et al.* Low Band Gap Benzimidazole COF Supported Ni_3N as Highly Active OER Catalyst. *Advanced Energy Materials* **6**, 1601189 (2016). URL `https://onlinelibrary.wiley.com/doi/abs/10.1002/aenm.201601189`.

[132] Aiyappa, H. B., Thote, J., Shinde, D. B., Banerjee, R. & Kurungot, S. Cobalt-Modified Covalent Organic Framework as a Robust Water Oxidation Electrocatalyst. *Chemistry of Materials* **28**, 4375–4379 (2016). URL `https://doi.org/10.1021/acs.chemmater.6b01370`.

[133] Lin, C.-Y., Zhang, D., Zhao, Z. & Xia, Z. Covalent Organic Framework Electrocatalysts for Clean Energy Conversion. *Advanced Materials* **30**, 1703646 (2018). URL `https://onlinelibrary.wiley.com/doi/abs/10.1002/adma.201703646`.

[134] Takatsu, H. *et al.* Roles of High-Frequency Optical Phonons in the Physical Properties of the Conductive Delafossite $PdCoO_2$. *Journal of the Physical Society of Japan* **76**, 104701 (2007). URL `https://doi.org/10.1143/JPSJ.76.104701`.

[135] Williams, D. B. & Carter, C. B. (Springer, 1996).

[136] Almeida, C. M. V. B. & Giannetti, B. F. A new and practical carbon paste electrode for insoluble and ground samples. *Electrochemistry Communications* **4**, 985–988 (2002). URL `http://www.sciencedirect.com/science/article/pii/S1388248102005118`.

[137] Ragone, D. V. Review of Battery Systems for Electrically Powered Vehicles (1968). *SAE Technical Paper 680453* URL `https://doi.org/10.4271/680453`.

[138] Łukaszewski, M., Soszko, M. & Czerwiński, A. *Electrochemical Methods of Real Surface Area Determination of Noble Metal Electrodes – an Overview, International Journal of Electrochemical Science* **11**, 4442-4469 (2016). URL `http://www.electrochemsci.org/papers/vol11/110604442.pdf`.

[139] Zhang, J. *et al.* High catalytic activity of nanostructured Pd thin films electrochemically deposited on polycrystalline Pt and Au substrates towards electro-oxidation of methanol. *Electrochemistry Communications* **9**, 1298–1304 (2007). URL `http://www.sciencedirect.com/science/article/pii/S1388248107000410`.

[140] Huang, X. *et al.* Freestanding palladium nanosheets with plasmonic and catalytic properties. *Nature Nanotechnology* **6**, 28 (2010). URL `https://doi.org/10.1038/nnano.2010.235`.

[141] Kuo, C.-H. *et al.* The Effect of Lattice Strain on the Catalytic Properties of Pd Nanocrystals. *ChemSusChem* **6**, 1993–2000 (2013). URL `https://onlinelibrary.wiley.com/doi/abs/10.1002/cssc.201300447`.

[142] Rahul, R., Singh, R. K., Bera, B., Devivaraprasad, R. & Neergat, M. The role of surface oxygenated-species and adsorbed hydrogen in the oxygen reduction reaction (ORR) mechanism and product selectivity on Pd-based catalysts in acid media. *Physical Chemistry Chemical Physics* **17**, 15146–15155 (2015). URL `http://dx.doi.org/10.1039/C5CP00692A`.

[143] Wolfe, J. P. & Li, J. J. *Chapter 1 An introduction to palladium catalysis*, vol. 26, 1–35 (Elsevier, 2007). URL `http://www.sciencedirect.com/science/article/pii/S146015670780050X`.

[144] Carcia, P. F., Shannon, R. D., Bierstedt, P. E. & Flippen, R. B. O_2 Electrocatalysis on Thin-Film Metallic Oxide Electrodes with the Delafossite Structure. *Journal of the Electrochemical Society* **127**, 1974–1978 (1980). URL `<GotoISI>://WOS:A1980KH19200021`. Kh192 Times Cited:26 Cited References Count:28.

[145] Jana, R., Bhim, A., Bothra, P., Pati, S. K. & Peter, S. C. Electrochemical Dealloying of $PdCu_3$ Nanoparticles to Achieve Pt-like Activity for the Hydrogen Evolution Reaction. *ChemSusChem* **9**, 2922–2927 (2016). URL `https://onlinelibrary.wiley.com/doi/abs/10.1002/cssc.201601081`.

[146] Hollemann, A. F. & Wiberg, N. *Lehrbuch der Anorganischen Chemie* (Walter de Gruyter, Berlin, 2007), 102 edn.

[147] Elam, M. & Conway, B. E. Sorption Behavior of the Overpotential-Deposited H Species in the Cathodic H_2 Evolution Reaction at Pd and Pt-Pd Electroplated Composite Electrodes. *Journal of The Electrochemical Society* **135**, 1678–1685 (1988). URL `http://jes.ecsdl.org/content/135/7/1678.abstract`.

[148] Spitler, E. L. *et al.* A 2D Covalent Organic Framework with 4.7-nm Pores and Insight into Its Interlayer Stacking. *Journal of the American Chemical Society* **133**, 19416–19421 (2011). URL `https://doi.org/10.1021/ja206242v`.

Curriculum vitae Filip Mateusz Podjaski

address:
Seyfferstraße 38
D - 70197 Stuttgart

telephone: +49 (0) 163 / 772 76 73
e-mail: filip@podjaski.de

born October 09, 1986
in Berent (Kościerzyna), Poland

Academic studies

PhD

03/2014 – present   PhD candidate at the MPI for Solid State Research, Stuttgart, Germany and at Ecole Polytechnique Fédérale de Lausanne, Switzerland

Topic of the thesis: *"Investigations into Nanostructured Materials for Water Splitting and Direct Solar Energy Harvesting"*

Master of Science in Physics

11/2011 – 02/2013   Master studies and thesis under Prof. Dr. Michael Seibt at the Institute for Semiconductor Physics, University of Göttingen.
Grade: "very good" (1.1)
Topic of the Master's thesis: *"Preparation and electrical characterization of single $NiSi_2$-precipitates in Silicon"*

09/2010 – 08/2011   Erasmus student at Université Claude Bernard Lyon 1 and Ecole Normale Supérieure de Lyon, France

Bachelor of Science in Physics

10/2007 – 08/2010   Bachelor studies and thesis under Prof. Dr. Christian Jooß at the Institute for Material Physics, University of Göttingen.
Grade: "good" (1.7)
Topic of the Bachelor's thesis: *"Fabrication of a Niob-doped STO sample for photo-induced water splitting with Cobalt ferrite as a catalyst"*

Education

07/2006   University entrance qualification (Abitur), grade: "very good" (1.4)

08/1997 – 07/2006   Ernst-Barlach-Gymnasium, Kiel, Germany

09/2005 – 10/2005   exchange student at Collège Claparède in Geneva, Switzerland

08/2003 – 10/2003   exchange student at Lycée Polyvalent Le Mans Sud, France

Professional experience and internships

05/2015 – 06/2015	Research visit in the Multifunctional Optics Group, Institute of Material Science of Sevilla, Spain
04/2013 – 12/2013	Research assistant at the Institute of Semiconductor Physics, University of Göttingen, Germany
10/2011 – 03/2012	Tutor for physics exercise courses, University of Göttingen
02/2011 – 08/2011	Internship (extended French Master's thesis) at the Laboratory of Condensed Matter Physics and Nanostructures (LPMCN) in Lyon and at the Michelin research center Ladoux in Clermont-Ferrand, France.
04/2009 – 08/2010	Tutor for physics laboratory courses, University of Göttingen
07/2007 – 08/2007	Two voluntary services for Service Civil International in Scotland
10/2006 – 06/2007	Civilian service at the Studentenwerk Schleswig-Holstein as chef's assistant in the university canteen, Kiel, Germany
02/2006 – 03/2006	Internship at the DESY research centre in Hamburg, Germany

Personal skills and competences

Research related competences

(Photo-)electrochemistry and impedance spectroscopy, photocatalysis, photoluminescence, thin film fabrication and characterization, AFM, cleanroom, SEM and EBIC, e-beam lithography, FIB and basic TEM

Computer skills

Microsoft Office package, Origin, C++, Linux, Latex, basic Matlab
material research related software

Language skills

German, Polish: mother tongue

English, French: fluent

Spanish, Russian: intermediate level

Activities, hobbies and honorary posts

	foreign languages and cultures, politics and sociology, environmental science, psychology, badminton, board games
06/2016 – 07/2016	Organization of the Max-Planck – EPFL center workshop on Bioinspired Nanosystems for Energy Conversion
01/2015 – 01/2016	PhD representative for the MPI for Solid State Research and MPI for Intelligent Systems, Stuttgart, Germany
12/2014 – 12/2015	Head of the seminar group, PhDnet, Max Planck Society
09/2011 – 10/2011	6 week language study travel to Moscow, Russia
2007 – 2008	Preparing and co-leading a confirmation course in Kiel, Germany
2001 – 2007	Group leader, preparing and leading holiday camps and meetings in the parish Franz von Assisi in Kiel, Germany
2000 – 2007	Aikido coach at the Budo-Klub Akamon, Kiel, Germany

Appendix
Peer-reviewed publications

[10]   **F. Podjaski**, D. Weber, S. Zhang, L. Diehl, R. Eger, V. Duppel, E. Alarcon-Llado, G. Richter, F. Haase, A. Fontcuberta i Morral, C. Scheu, B. V. Lotsch (*submitted*). Title: "Rational Strain Engineering in Delafossite Oxides for Highly Efficient Hydrogen Evolution Catalysis in Acidic Media"

[9]   S. Laha, Y. Lee, **F. Podjaski,** D. Weber, V. Duppel, L. M. Schoop, F. Pielnhofer, C. Scheurer, K. Müller, U. Starke, K. Reuter, B. V. Lotsch. *Adv. Energy Mater.* **2019**, 1803795*.* Title: "Ruthenium Oxide Nanosheets for Enhanced Oxygen Evolution Catalysis in Acidic Medium"

[8]   D. Weber, L. M. Schoop, D. Wurmbrand, S. Laha, **F. Podjaski**, V. Duppel, K. Müller, U. Starke, B. V. Lotsch. *J. Mater. Chem. A* **2018**, *6*, 21558–21566*.* Title: "IrOOH nanosheets as acid stable electrocatalysts for the oxygen evolution reaction"

[7]   L. Stegbauer, S. Zech, G. Savasci, T. Banerjee, **F. Podjaski**, K. Schwinghammer, C. Ochsenfeld, B.V. Lotsch. *Adv. Energy Mater.* **2018**, *8*, 1703278. Title: "Tailor-made Photoconductive Pyrene-based Covalent Organic Frameworks for Visible-Light Driven Hydrogen Generation"

[6]   T. Wang, H.-K. Kim, Y. Liu, W. Li, J. Griffiths, Y. Wu, S. Laha, K. Fong, **F. Podjaski**, C. Yun, R. Kumar, B.V. Lotsch, A. Cheetham, S. Smoukov. *J. Am. Chem. Soc.* **2018**, *140*, 6130–6136. Title: "Bottom-up Formation of Carbon-based Structures with Multilevel Hierarchy from MOF-guest Polyhedra"

[5]   **F. Podjaski**, J. Kröger, B.V. Lotsch. *Adv. Mater.* **2018**, *30*, 1705477. Title: "Toward an Aqueous Solar Battery: Direct Electrochemical Storage of Solar Energy in Carbon Nitrides"

[4]   C. Ziegler,   T.K. Dennenwaldt,   D. Weber,   V. Duppel,   C. Kamella,   **F. Podjaski**,   B. Tuffy, I. Moudrakovski, C. Scheu, B.V. Lotsch. *Z. Anorg. Allg. Chem* **2017**, *643*, 1668–1680. Title: "Functional engineering of perovskite nanosheets: Impact of lead substitution on exfoliation in the solid solution $RbCa_{2-x}Pb_xNb_3O_{10}$ "

[3]   V.W.-h. Lau, D. Klose, H. Kasap, **F. Podjaski**, M.-C. Pignié, E. Reisner, G. Jeschke, B.V. Lotsch. *Angew. Chem. Int. Ed.* **2017**, *56*, 510–514. Title: "Dark photocatalysis: Storage of solar energy in carbon nitride for time-delayed hydrogen generation**"**

[2]   S. Betzler, **F. Podjaski**, M. Beetz, K. Handloser, A. Wisnet, M. Handloser, A. Hartschuh, B.V. Lotsch, C. Scheu. *Chem. Mater.* **2016**, *28*, 7666. *Title: "*Titanium doping and its effect on the morphology of three-dimensional hierarchical $Nb_3O_7(OH)$ nanostructures for enhanced light-induced water splitting*"*

[1]   V.S. Vyas, F. Haase, L. Stegbauer, G. Savasci, **F. Podjaski**, C. Ochsenfeld, B.V. Lotsch *Nat. Commun.* **2015**, *6*, 8508. Title: *"A tunable azine covalent organic framework platform for visible light-induced hydrogen generation"*

Honours and awads

2018   Graduate Student Award at the E-MRS Spring meeting, Strasbourg, France
2015   1st Poster Prize at the ISF-1 Young, Uppsala, Sweden
2006   Abitur-Prize of the German Physical Society (DPG), Kiel, Germany

---

Selected international conference presentations

03/2019   **Invited talk** at the APS March meeting, Boston, USA. Title: "Recent Advances towards the Development of an Aqueous Direct Solar Battery"

10/2018   **Talk** at the 680. WE-Heraeus-Seminar on Materials Development for Automotive Propulsion, Bad Honnef, Germany. Title: "Toward New Solar Batteries: Graphitic Carbon Nitrides Enabling Direct Solar Energy Storage"

06/2018   **Invited talk** at the E-MRS spring meeting, Strasbourg, France. Title: "Toward a Solar Battery: Direct Solar Energy Storage in Graphitic Carbon Nitrides"

07/2016   **Poster** presentation at the 21st International Conference on Photochemical Conversion and Storage of Solar Energy (IPS-21), St. Petersburg, Russia. Title: *"TMD studies for H_2 Evolution – Nanostructuring or Phase engineering?"*

04/2015   **Poster** presentation at 1st International Solar Fuels Conference (ISF-1), Uppsala, Sweden. Title: "*Coated Nanostructured p-Silicon Photocathodes with Earth Abundant Cocatalysts for Overall Solar Water Splitting in a Z-Scheme*"

01/2015   **Talk and poster** presentation at 39th International Conference and Exposition on Advanced Ceramics, Daytona Beach, Florida, USA. Talk title: *"Combined Semiconductor Nanostructures for Efficient Solar Water Splitting"*. Poster title: "*Visible Light Hydrogen Evolution on Heptazine-and Triazine-based Polymers and Metal Complex Cocatalysts bound to p-Silicon Photocathodes*"

March 10, 2019   Filip Podjaski